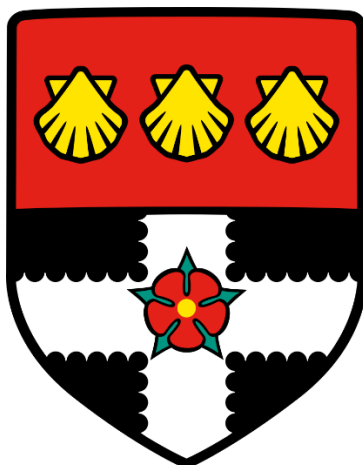


**THE UNIVERSITY OF READING**  
**DEPARTMENT OF CHEMISTRY**



Physical Properties of Atmospheric Aerosol Products  
from the Ozonolysis of Terpenes

A Thesis Submitted in Partial Fulfilment of the Requirements for the  
Degree of Doctor of Philosophy

Matthew Edward Hagreen

September 2017

Supervisor: Dr Christian Pfrang

Co-Supervisor: Prof George Marston

**Declaration**

I confirm that this is my own work and the use of all material from other sources has been properly and fully acknowledged.

Matthew Edward Hagreen

## Abstract

This thesis describes experiments carried out to understand the formation of particles in the reactions of ozone with terpenes, processes that are important in atmospheric chemistry and have an impact on climate change. The main instrument used to study the reactions was a Scanning Mobility Particle Sizer (SMPS), with some experiments using an Electrical Low Pressure Impactor (ELPI+).

The SMPS instrument was used first to study the evolution of aerosol particles formed from the ozonolysis of  $\alpha$ -pinene. A strong dependence on OH scavenger, and the  $[\text{RO}_2] / [\text{HO}_2]$  ratios produced by each, was observed. The effect of relative humidity on the formed aerosol was investigated, and was found to influence both number and size of the particles formed. The relationship between aerosol mass concentration and mass yield was extended beyond the range reported in the literature. A rate constant for the  $\alpha$ -pinene ozonolysis was calculated from the aerosol mass evolution,  $k = 1.05 \pm 0.11 \times 10^{-16} \text{ cm}^3 \text{ molecule}^{-1} \text{ s}^{-1}$ , which agrees well with the literature. Preliminary studies using the ELPI+ instrument were undertaken, and some successful experiments suggested that physical state of the aerosol is independent of relative humidity across the range studied.

An enone derivative of  $\alpha$ -pinene was synthesised to allow for study of one of the  $\alpha$ -pinene Criegee intermediates (CIs) in isolation. A rate constant for its reaction with ozone of  $k = 4.3 \pm 0.9 \times 10^{-17} \text{ cm}^3 \text{ molecule}^{-1} \text{ s}^{-1}$  was determined. Enone mass yields were 5–7 % lower than those of  $\alpha$ -pinene, suggesting that products of CI 2 (enal) contribute more to the total aerosol mass than those of CI 1 (enone). The data suggest that CI 2 is primarily responsible for particle nucleation, and both CIs contribute significantly to their growth.

The ozonolysis of  $\alpha$ -terpinene was investigated using both static chamber experiments and an atmospheric pressure flow tube. This allowed for calculation of upper and lower bounds for the rate constant. The upper bound,  $k = 1.6 \pm 0.29 \times 10^{-14} \text{ cm}^3 \text{ molecule}^{-1} \text{ s}^{-1}$ , is in agreement with the literature. Increasing ozone concentration was noted to have a particularly large impact on the mass of aerosol produced. Mass yields were found to be much higher than for  $\alpha$ -pinene, suggesting an array of very low volatility products. The effect of relative humidity on the initial stages of aerosol formation was studied using the flow tube, and a small effect on the particle size distribution was noted.

## Acknowledgements

I would like to begin by thanking my supervisor, Dr Christian Pfrang, for his guidance and support over the course of the last four years. In particular, my thanks for accepting responsibility for another student, enabling me to continue my work at the University of Reading following the departure of Professor George Marston to Northumbria University.

Heartfelt thanks also to Professor Marston for giving me the opportunity to undertake this PhD project, and whose ideas and advice throughout the course of this project, and especially over these past few months, have been invaluable.

Thanks also to Dr Andy Russell for his assistance during the synthesis of one of the organic compounds used in this work, and for his patience in teaching me new techniques.

I would also like to take this opportunity to gratefully acknowledge funding provided by NERC in the form of a University of Reading Studentship (Award Ref: 1363234). Gratitude also to Dekati Ltd. for their generous loan of an ELPI+ instrument.

My thanks also go to members of the RACER team, past and present. To Ioan Hoare, without whose patience and support I likely would not have undertaken a PhD project at all. To Jana Geßner, Kunal Rastogi and Nathan John, for being good and supportive friends over the whole four years, and for generously assisting me with a whole host of practical tasks. And also to all of the other PhD students in the G15 office, for making my time here more enjoyable. I wish all of you the best in your own studies.

I also extend my thanks to the technical staff in the University of Reading Chemistry department, for providing the framework for this project to take place.

Finally, I would like to thank my family for providing a constant source of support over the past years, and for listening attentively to my ramblings, regardless of how much or how little sense they made. Thank you to all of my friends, both at the University and those further abroad, for all the encouragement and enjoyment you have provided me over the years. I couldn't have done it without you all.

<b>INTRODUCTION</b>	<b>1</b>
<b>1.1 ATMOSPHERE</b>	<b>1</b>
<b>1.2 TERPENES</b>	<b>7</b>
<b>1.3 ATMOSPHERIC OZONE</b>	<b>9</b>
<b>1.4 ATMOSPHERIC OXIDATION</b>	<b>12</b>
<b>1.5 ATMOSPHERIC AEROSOL</b>	<b>15</b>
<b>1.6 GLOBAL SOA BUDGET</b>	<b>21</b>
<b>1.7 FACTORS AFFECTING SOA EVOLUTION</b>	<b>22</b>
1.7.1 TEMPERATURE	22
1.7.2 HUMIDITY	23
1.7.3 SCAVENGER	24
1.7.4 ULTRAVIOLET RADIATION	25
1.7.5 NO <sub>x</sub> PRESENCE	25
<b>1.8 AIMS AND OBJECTIVES</b>	<b>26</b>
<b>1.9 REFERENCES</b>	<b>28</b>
<b>EXPERIMENTAL</b>	<b>34</b>
<b>2.1 APPARATUS SETUP</b>	<b>34</b>
2.1.1 SAMPLE CHAMBER	37
2.1.2 OZONISERS	38
2.1.3 RELATIVE HUMIDITY CONTROL	39
2.1.4 INSTRUMENTATION	40
<b>2.2 REAGENTS</b>	<b>41</b>
<b>2.3 EXPERIMENTAL PROCEDURE</b>	<b>42</b>
2.3.1 SCAVENGERS	43
2.3.2 STATIC CHAMBER PREPARATION	43
2.3.3 OZONE CONCENTRATION CALCULATIONS	45
<b>2.4 SMPS MEASUREMENTS</b>	<b>48</b>
2.4.1 WALL LOSS CORRECTIONS	52
<b>2.5 ELPI+</b>	<b>58</b>
<b>2.6 FLOW TUBE</b>	<b>63</b>
2.6.1 WALL LOSS CORRECTIONS	69
<b>2.7 CALIBRATIONS AND ERROR ESTIMATES</b>	<b>71</b>
<b>2.8 REFERENCES</b>	<b>73</b>
<b>OZONOLYSIS OF A-PINENE</b>	<b>75</b>
<b>3.1 INTRODUCTION</b>	<b>75</b>
<b>3.2 DEVELOPMENT OF A STANDARD FOR DATA PRESENTATION</b>	<b>80</b>
<b>3.3 SYSTEM CHARACTERISATION AND REPRODUCIBILITY</b>	<b>84</b>
<b>3.4 GAS-PHASE KINETICS</b>	<b>87</b>
<b>3.5 AEROSOL MASS AND MASS YIELD</b>	<b>90</b>
<b>3.6 IMPACT OF SCAVENGER</b>	<b>94</b>
<b>3.7 IMPACT OF RELATIVE HUMIDITY</b>	<b>101</b>

3.7.1	HIGH CONCENTRATION CONDITIONS	102
3.7.2	LOW CONCENTRATION CONDITIONS	105
3.7.3	RELATIVE HUMIDITY CONCLUSIONS	109
<b>3.8</b>	<b>PHYSICAL STATE OF AEROSOL</b>	<b>113</b>
<b>3.9</b>	<b>CONCLUSIONS</b>	<b>117</b>
<b>3.10</b>	<b>REFERENCES</b>	<b>119</b>
<b>OZONOLYSIS OF THE A-PINENE ENONE DERIVATIVE</b>		<b>123</b>
<b>4.1</b>	<b>INTRODUCTION</b>	<b>123</b>
<b>4.2</b>	<b>ENONE SYNTHESIS</b>	<b>126</b>
4.2.1	OZONOLYSIS AND SUBSEQUENT PROTECTION AS A DIMETHYL ACETAL	126
4.2.2	REDUCTION AND DEPROTECTION	128
4.2.3	WITTIG OLEFINATION	130
4.2.4	PYRIDINIUM CHLOROCHROMATE OXIDATION	132
<b>4.3</b>	<b>INITIAL INVESTIGATION AND OPTIMISATION OF THE EXPERIMENTAL SETUP</b>	<b>133</b>
<b>4.4</b>	<b>COMPARISON OF THE ENONE TO A-PINENE</b>	<b>140</b>
<b>4.5</b>	<b>GAS-PHASE KINETICS</b>	<b>144</b>
<b>4.6</b>	<b>AEROSOL MASS AND MASS YIELDS</b>	<b>148</b>
<b>4.7</b>	<b>CONCLUSIONS</b>	<b>152</b>
<b>4.8</b>	<b>REFERENCES</b>	<b>154</b>
<b>OZONOLYSIS OF A-TERPINENE</b>		<b>156</b>
<b>5.1</b>	<b>INTRODUCTION</b>	<b>156</b>
<b>5.2</b>	<b>AEROSOL MASS AND MASS YIELDS: INITIAL INVESTIGATION</b>	<b>162</b>
<b>5.3</b>	<b>AEROSOL MASS AND MASS YIELDS: FLOW TUBE INVESTIGATION</b>	<b>164</b>
5.3.1	COMPARISON OF FLOW TUBE AND STATIC CHAMBER TECHNIQUES	164
5.3.2	GAS-PHASE KINETICS	169
5.3.3	AEROSOL MASS AND MASS YIELDS: FLOW TUBE RESULTS	171
<b>5.4</b>	<b>VARYING OZONE EXCESS</b>	<b>174</b>
<b>5.5</b>	<b>AEROSOL MASS AND MASS YIELDS: COMPLETE OXIDATION</b>	<b>181</b>
<b>5.6</b>	<b>IMPACT OF RELATIVE HUMIDITY</b>	<b>183</b>
<b>5.7</b>	<b>CONCLUSIONS</b>	<b>190</b>
<b>5.8</b>	<b>REFERENCES</b>	<b>192</b>
<b>CONCLUSIONS AND FUTURE WORK</b>		<b>194</b>
<b>6.1</b>	<b>CONCLUSIONS</b>	<b>194</b>
<b>6.2</b>	<b>FUTURE WORK</b>	<b>198</b>
<b>APPENDIX</b>		<b>200</b>
<b>A.1</b>	<b>SPECTRA RELEVANT TO CHAPTER 4</b>	<b>200</b>

## List of Acronyms

CI	Criegee Intermediate
CPC	Condensation Particle Counter
DMA	Differential Mobility Analyser
ELPI+	Electrical Low Pressure Impactor
ELVOC	Extremely Low Volatility Organic Compound
IPCC	Intergovernmental Panel on Climate Change
PCC	Pyridinium Chlorochromate
POA	Primary Organic Aerosol
POZ	Primary Ozonide
ppb	Parts per Billion
ppm	Parts per Million
RH	Relative Humidity
SCI	Stabilised Criegee Intermediate
SMPS	Scanning Mobility Particle Sizer
SOA	Secondary Organic Aerosol
VOC	Volatile Organic Compound

# Chapter 1

## Introduction

---

### 1.1 Atmosphere

The atmosphere is the name given to the mixture of gases above the Earth's surface, held in check by the Earth's gravitational pull. The atmosphere is divided into four distinct regions: the troposphere, stratosphere, mesosphere and thermosphere.

The troposphere is the first of these regions, the closest to the ground, and accounts for the majority of atmospheric mass—around 80 %.<sup>1</sup> The troposphere extends from ground level up to 8–16 km from the Earth's surface—higher nearer the Equator and lower at the Earth's poles.<sup>2</sup> As the altitude increases through the troposphere, the temperature decreases. This is simply due to increased distance from the Earth's body—the Earth can be approximated as a black body radiator, which means that it absorbs incident radiation, and emits radiation at a longer wavelength. Whilst only a small proportion of the lower wavelength incident radiation can be absorbed by gases in the atmosphere, the emitted radiation is of a wavelength such that it is readily absorbed by gases in the atmosphere, thus heating the gases surrounding the Earth. This heating effect decays as altitude increases—as the radiation is absorbed, less radiation is therefore able to penetrate higher into the atmosphere, and thus the heating effect decreases. The rate at which temperature decreases is known as the Environmental Lapse Rate (ELR),<sup>3</sup> which is defined by:

$$\text{ELR} = - \frac{\partial T}{\partial z}$$

where,  $T$  is temperature (Kelvin) and  $z$  is height (m).

The temperature gradient across the troposphere greatly influences the chemistry observed since it produces convection currents, whereby the lower, hotter gases are less dense than the colder gases above and so rise through the troposphere. As the gas rises,



the pressure of the surrounding air decreases, and so the rising parcel of gas expands. This expansion means that the parcel of gas is doing work on the surrounding air, and thus loses energy, causing a loss of temperature. By this process, one parcel of air can decrease in temperature through an increase in altitude; this is known as the adiabatic lapse rate. This process repeats, with lower, hotter parcels of air displacing the cooler, higher ones. This results in a large degree of mixing, which is important in allowing the gases to react with one another. The temperature profile of the troposphere, and other regions of the atmosphere, are described in Figure 2.

Tropospheric ozone concentration is very low, and although results vary according to location and time of year, they generally lie around 25–50 parts per billion.<sup>4-7</sup> Ozone concentration in the stratosphere is typically much higher, reaching concentrations of up to 10 parts per million (ppm). However, since volatile organic compounds (VOCs) are generally restricted to the troposphere, the oxidation of these species takes place here, in lower ozone concentrations, rather than in the stratosphere.

The chemistry investigated in this work is that which takes place in the troposphere. The ozone concentration profile of the atmosphere is also described in Figure 2, and the formation processes leading to these ozone concentrations are discussed in section 1.3.

The troposphere is separated from the higher stratosphere by the tropopause. This is defined as the point at which the temperature gradient reverses, and the temperature begins to increase with altitude.

The stratosphere is the region directly above the troposphere, typically beginning at 8–16 km, dependent on the height of the troposphere as described previously. The stratosphere extends up to approximately 50 km above the Earth. The temperature gradient across the stratosphere is positive, and thus the environmental lapse rate is negative. This is because UV radiation from the Sun is absorbed by both O<sub>2</sub> and O<sub>3</sub> as they are photodissociated, causing a temperature increase. In a similar situation to that in the troposphere, this effect is greatest in the region closest to the radiation source (in this case the Sun) as the absorption of radiation means that less can penetrate through into the lower regions of the stratosphere. This causes an increased temperature rise as

altitude increases, as more UV radiation is absorbed. Since a temperature increase is observed across the stratosphere, convection does not take place, as the hotter air is already at greater height. Thus, mixing within this region is poor. Most of the ozone found in the atmosphere is produced in the stratosphere—this is because at high altitudes, air pressure decreases, and less oxygen is available to form ozone. On the other hand, at low altitudes, much of the UV radiation has already been absorbed and so, although O<sub>2</sub> is present in greater volume, very little is photodissociated into atomic oxygen, and thus little ozone is produced. At an altitude low in the stratosphere, these two factors can combine to reach a maximum rate of ozone production, resulting in a maximum concentration of ozone. This region is known as the ozone layer; although ozone is actually found across a wide range of altitudes, reaching up high into the stratosphere, and down into the troposphere, this is the region in which it is most concentrated at up to 10 ppm.

The stratosphere is bounded by the stratopause, which is defined as the point at which the temperature gradient reverses a second time, from positive to negative. This is typically located at an altitude of around 50 km.

The mesosphere is located above the stratopause, and extends from approximately 50 km up to 100 km. The temperature decreases with altitude across the mesosphere, leading to incredibly low temperatures in the highest regions of the mesosphere. This temperature is due almost solely to altitude—little radiation from the Earth is able to penetrate to this height, and thus little energy is absorbed by the chemical species located here. Oxygen is scarce in this region, which further contributes to the low temperatures since absorption of UV by molecular oxygen and ozone is the main source of thermal energy in this region. Again, convection currents in this region contribute to mixing of chemical species.

Between the mesosphere and the higher thermosphere lies the mesopause, which again is defined as the point at which the temperature gradient reverses, from negative to positive. The thermosphere extends from 100 km up to the edge of the Earth's atmosphere, after which point space begins. In this region, temperatures are extremely high, at up to 1700 K. However, because chemical species in this region are found in such

low concentrations, temperature can no longer be relied upon in the same way as it can at ground-level pressure, since collisions between species are far less frequent. Indeed, the mean free path, the average distance a molecule will move through the air before collision, is over  $10^3$  m in the thermosphere.<sup>8</sup> For comparison, the mean free path at ground level is approximately  $10^{-8}$  m. Thus, although temperature as defined is very high, this is relatively meaningless when compared with similar temperatures found at ground-level. Mixing in this region is stagnant, as the positive temperature gradient does not lend itself to convection. Gases in the thermosphere tend to separate out according to their molecular mass, and thus densities, with the heavier species lying lower in altitude than the lighter species. Due to this separation of species, and the low number of particles found in the thermosphere, molecular interactions are infrequent relative to ground-level.

The Earth's atmosphere comprises a mixture of gases in varying concentrations, which are summarised below in Table 1. These concentrations are expressed as a percentage by volume in dry air, and thus are higher than would be expected in the slightly more humid conditions encountered in the atmosphere. However, since the concentration of water vapour may vary substantially, from trace amounts up to 4 % of the atmosphere,<sup>9</sup> expressing concentrations in dry air is more useful than for any specific humidity.

Gas	Volume
Nitrogen	78.08%
Oxygen	20.95%
Argon	0.93%
Carbon Dioxide	0.035%
Neon	0.0016%
Helium	0.0005%
Methane	0.00015%

Table 1: Composition of Earth's Atmosphere (Dry Air).<sup>2</sup>

Other gases are found in the atmosphere in trace concentrations, including carbon monoxide, nitrogen dioxide, volatile organic compounds (VOCs), ozone ( $O_3$ ), hydroxyl radicals (OH) and nitrate radicals ( $NO_3$ ). Although only found in very low concentrations,

the impact of  $O_3$ , OH and  $NO_3$  cannot be overstated as they are highly reactive and participate in a number of important reactions, such as the degradation of organic species. Some of these reactions will be studied in this work.

The first competing oxidant in the atmosphere are OH radicals, which are responsible for the majority of VOC oxidation within the troposphere. The initial step proceeds *via* OH attack onto the VOC, forming an alkyl radical (R), which rapidly reacts with  $O_2$  to form an  $RO_2$  radical.<sup>10</sup>  $RO_2$  may then react with NO, forming either an organic nitrate ( $RONO_2$ ), or an alkoxy radical (RO) and  $NO_2$ .<sup>10</sup> A number of reaction pathways are available to the alkoxy radical. Reaction with  $O_2$  results in formation of a hydroperoxyl radical ( $HO_2$ ) and a carbonyl. The alkoxy radical may also isomerise, or dissociate to form smaller radicals, eventually resulting in formation of  $HO_2$  and a carbonyl. Reaction of the hydroperoxyl radical with NO forms  $NO_2$ , and regenerates the OH radical. Overall, this results in oxidation of the carbonyl, formation of two ozone molecules (through subsequent photolysis of  $NO_2$ ), and regeneration of OH.<sup>10</sup> The general scheme is summarised by a reaction cycle in Figure 1.

The second atmospheric oxidant is  $NO_3$ , which typically reacts with alkene VOCs by addition to the double bond. Resulting compounds include nitrate-substituted peroxy radicals, alkyl and alkoxy radicals.<sup>10</sup> Some of the peroxy radicals may decompose to form  $HO_2$ , similarly to the scheme described in Figure 1, providing a source of night-time OH.<sup>10</sup>

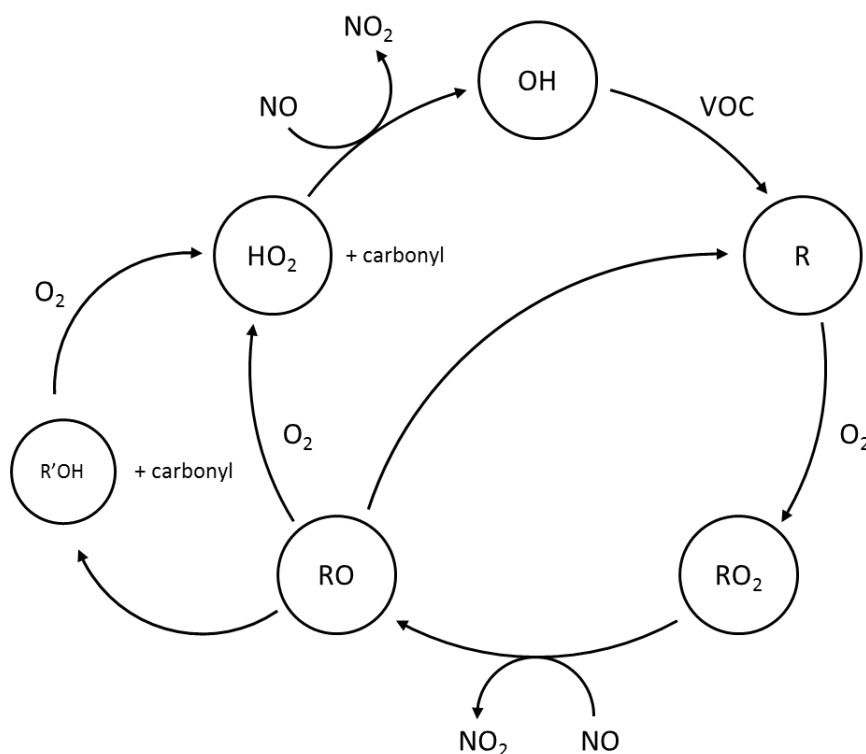


Figure 1: General reaction scheme for OH oxidation, showing regeneration of the OH radical. Adapted from Wayne.<sup>11</sup>

The final competing atmospheric oxidant is ozone, which reacts solely with alkenes *via* concerted attack at both carbons of the double bond. The bond is cleaved, forming a carbonyl and an excited Criegee Intermediate (CI). The CI may either be thermally stabilised to a Stabilised Criegee Intermediate (SCI) which can react with either water or an oxygenated organic molecule, or may decompose, forming alkyl,  $\text{RO}_2$  and  $\text{HO}_2$  radicals. As previously mentioned, and described by the scheme in Figure 1, both  $\text{HO}_2$  and  $\text{RO}_2$  radicals may react with NO, forming  $\text{NO}_2$ , which may subsequently be photolyzed to form  $\text{O}_3$ . In this way, catalytic ozone formation may occur.

Compositions of the troposphere and stratosphere are largely comparable: both regions are made up of approximately 78 % nitrogen, 21 % oxygen and 1 % argon, in addition to other trace gases.  $\text{CO}_2$  concentrations remain constant throughout the troposphere and stratosphere at 370 ppb<sup>12</sup> (different sources in the literature report values from 350–380 ppb). Water vapour concentrations vary hugely between these two regions, with 99 % of atmospheric water vapour contained within the troposphere, and the remaining 1 % found mostly within the stratosphere.<sup>13</sup> Ozone concentrations also differ between the

two, with higher concentrations in the stratosphere (home to the famous ‘ozone layer’), and low concentrations in the troposphere, depicted in Figure 2. These will be discussed in greater depth in section 1.3.

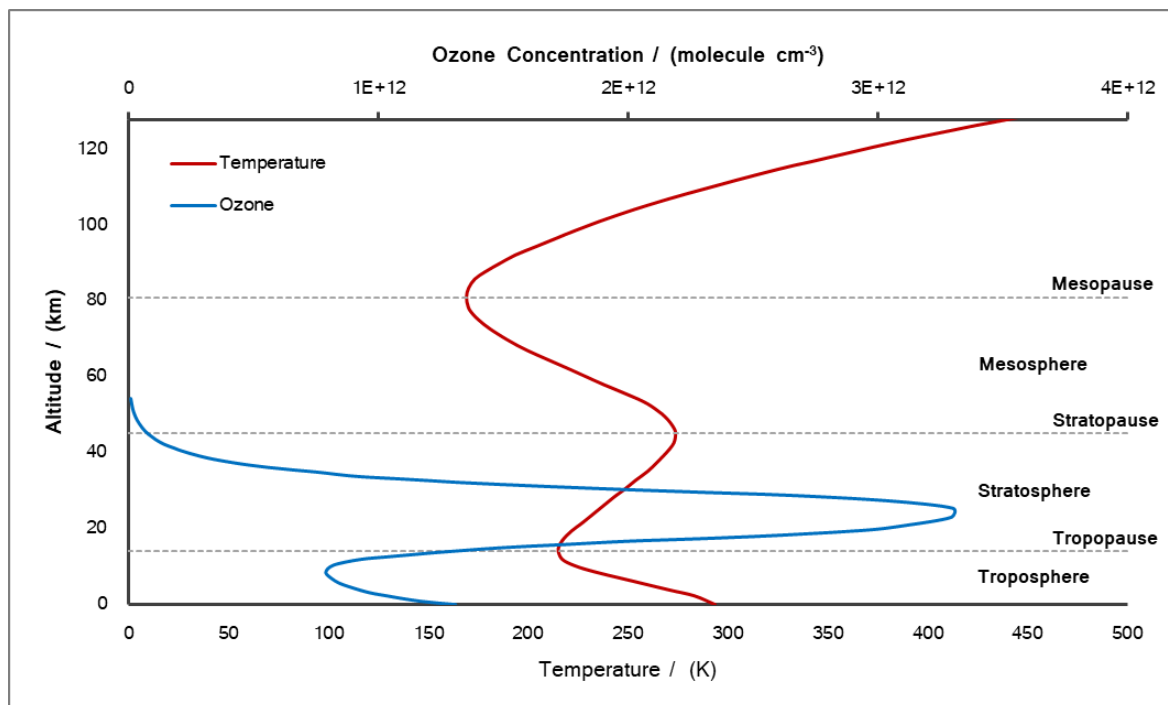


Figure 2: Temperature and Ozone Profiles of the Atmosphere, adapted from Watson *et al.*<sup>14</sup>

## 1.2 Terpenes

Terpenes are a group of organic compounds, composed of one or more isoprene units bonded in either an acyclic or a cyclic formation, where isoprene has the chemical formula  $C_5H_8$ . The simplest terpene is therefore isoprene itself, which is the only member of the sub-category hemiterpenes, defined as those terpenes made up of just one  $C_5H_8$  unit. Molecules comprised of two isoprene units are named monoterpenes, and these are very important in atmospheric chemistry due to their high abundance. Larger sub-categories include sesquiterpenes (3 isoprene units) and diterpenes (4 units). Terpenes derive their name from the chemical mixture turpentine (pine tree resin), of which they are the major component. The structures of some common terpenes have been produced below:

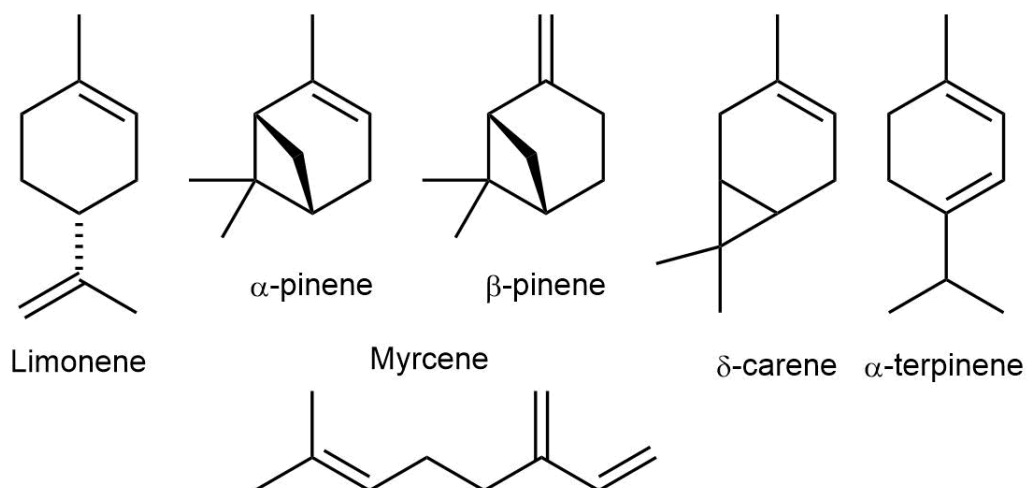


Figure 3: Some common monoterpenes ( $C_{10}H_{16}$ )

The most abundant of all terpenes in the atmosphere is  $\alpha$ -pinene, the major component of pine tree emissions, with estimates placing its global emissions at  $66 \text{ Tg yr}^{-1}$ .<sup>15</sup> Therefore, an understanding of the fate of this compound in the atmosphere is perhaps the most important of all terpenes due to its high abundance. Temperature and light have been shown to play an important role in emission behaviour.<sup>16</sup> Terpene emissions also vary dependent on the season, indicating that a plant's developmental state is a factor in controlling emissions<sup>17</sup>. The highest emissions are observed in the warmer months. Higher emissions encourage cloud seeding—a process by which water vapour condenses onto the surface of a particle, allowing the formation of water droplets on its surface, thereby increasing precipitation during warmer weather—by formation of more particles. Fractional contribution of each terpene to the overall monoterpene emission rate also varies based on the season. This is particularly pronounced in the case of  $\alpha$ -terpinene, emissions of which may increase significantly in pine trees from August to September.<sup>18</sup> The average annual emissions of the monoterpenes in Figure 3 are presented in Table 2, along with their rate constants and lifetimes with respect to each of the three major atmospheric oxidants.

Terpene	Emission Rate (Tg yr <sup>-1</sup> ) <sup>a</sup>	$k_{\text{OH}}$	$k_{\text{NO}_3}$ (cm <sup>3</sup> molecule <sup>-1</sup> s <sup>-1</sup> )	$k_{\text{O}_3}$	$\tau_{\text{OH}}$ <sup>b</sup>	$\tau_{\text{NO}_3}$ <sup>c</sup>	$\tau_{\text{O}_3}$ <sup>d</sup>
$\alpha$ -pinene	50	$5.3 \pm 0.15 \times 10^{-11}$	$6.2 \pm 0.1 \times 10^{-12}$	$9.4 \pm 0.15 \times 10^{-17}$	2.6 h	5 min	4.2 h
$\beta$ -pinene	34	$7.7 \pm 0.44 \times 10^{-11}$ <sup>f</sup>	$2.5 \pm 0.12 \times 10^{-12}$	$1.9 \pm 0.25 \times 10^{-17}$	1.8 h	13 min	21 h
Limonene	34	$1.65 \pm 0.25 \times 10^{-10}$ <sup>g</sup>	$1.2 \pm 0.12 \times 10^{-11}$	$2.1 \pm 0.10 \times 10^{-16}$	51 min	3 min	1.9 h
Myrcene	7	$1.0 \pm 0.02 \times 10^{-10}$	$1.1 \pm 0.12 \times 10^{-11}$	$4.6 \pm 0.2 \times 10^{-16}$	1.4 h	3 min	52 min
$\delta$ -carene	6	$8.7 \pm 0.43 \times 10^{-11}$ <sup>h</sup>	$9.1 \pm 0.12 \times 10^{-12}$	$4.8 \pm 0.20 \times 10^{-17}$	1.6 h	4 min	8.3 h
$\alpha$ -terpinene	1 <sup>e</sup>	$3.5 \pm 0.08 \times 10^{-10}$	$1.8 \pm 0.25 \times 10^{-10}$	$1.9 \pm 0.20 \times 10^{-14}$	24 min	11 s	1 min

Table 2: Emission rates and calculated lifetimes of selected monoterpenes, with respect to OH, NO<sub>3</sub> and O<sub>3</sub>.

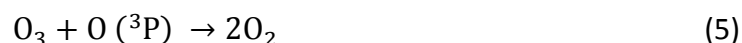
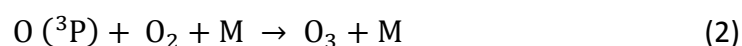
<sup>a</sup> Emission rates calculated from Griffin *et al.*<sup>19</sup> <sup>b</sup> For a 12-h daytime average OH concentration of  $2.0 \times 10^6$  molecule cm<sup>-3</sup>. <sup>c</sup> For a 12-h night-time average NO<sub>3</sub> concentration of  $5 \times 10^8$  molecule cm<sup>-3</sup>. <sup>d</sup> For a 24-h average O<sub>3</sub> concentration of  $7 \times 10^{11}$  molecule cm<sup>-3</sup>. <sup>b,c,d</sup> See Atkinson<sup>20</sup> for oxidant concentrations. <sup>e</sup> Emission rate is for  $\alpha$ - &  $\gamma$ -terpinene. <sup>f</sup> Rate constant from Chuong *et al.*<sup>21</sup> <sup>g</sup> Rate constant from Braure *et al.*<sup>22</sup> <sup>h</sup> Rate constant from Atkinson *et al.*<sup>23</sup> All other rate constants are IUPAC preferred values.<sup>24</sup>

Terpenes as a whole vary in their toxicity, according to the type of contact encountered. Skin contact causes only irritation, but aspiration may lead to more complex health problems, as it may impact on the central nervous system, causing seizures and comas, amongst other symptoms. Few deaths from direct terpene exposure are reported, with three observed in 2009—two from pine oil exposure, and one from turpentine.<sup>25</sup>

### 1.3 Atmospheric Ozone

Ozone is present in low concentrations through the troposphere and stratosphere, as mentioned previously in section 1.1, reaching its peak concentration in the stratosphere. Ozone is produced in the stratosphere via the Chapman mechanism<sup>26</sup>—a series of reactions which account for both production of ozone, and the subsequent removal of ozone from the atmosphere, leading to a steady-state concentration of ozone.





Reaction steps (1) and (5) proceed much more slowly than steps (2), (3) & (4). Therefore, since the reaction of O with O<sub>2</sub> to produce O<sub>3</sub> is much faster than the reaction of O with O<sub>3</sub> to produce 2 O<sub>2</sub>, ozone is only said to be destroyed *via* step (5), as the majority of the O formed in step (3) simply reacts again *via* step (2) to produce ozone again, rather than *via* step (5) to destroy the ozone. Thus, an important concept is odd oxygen, which is the sum of O<sub>3</sub> and O, as the two species interconvert quickly.

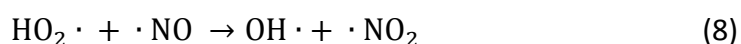
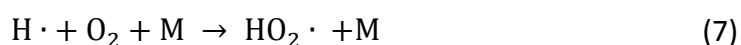
In this scheme, O (<sup>3</sup>P) is an oxygen atom in the ground-level triplet state, O (<sup>1</sup>D) is an oxygen atom in the excited singlet state, and O<sub>3</sub><sup>+</sup> is an excited O<sub>3</sub> molecule. The species M in this scheme is simply any inert molecule, usually N<sub>2</sub> or O<sub>2</sub>, which can collide with O (<sup>1</sup>D) or O<sub>3</sub><sup>+</sup>, absorbing excess energy, which is then lost as heat. In the first case, this allows the O(<sup>1</sup>D) atom, in the excited singlet state, to be converted into the lower energy O(<sup>3</sup>P) ground triplet state. Similarly, in the second case, this allows for the O<sub>3</sub><sup>+</sup> formed to be stabilised to O<sub>3</sub> in step (2).

Since UV radiation of  $\lambda < 240 \text{ nm}$  is required to initiate this reaction scheme, and only a small quantity of radiation of this wavelength penetrates through the stratosphere to the troposphere, this reaction has minimal impact on ozone production in the lower troposphere; below 10 km, its effect on ozone production is considered negligible.<sup>27</sup> However, in regions of the troposphere above 14 km, the Chapman mechanism may influence ozone concentration and is estimated to account for 5–20 ppb O<sub>3</sub> in this region.<sup>27</sup>

Ozone produced in the stratosphere may be transported down to the troposphere through eddy diffusion,<sup>28</sup> and some ozone transport from the troposphere up into the stratosphere also occurs. Net cross-tropopause ozone flux estimates vary between 408–1077 Tg O<sub>3</sub> yr<sup>-1</sup>.<sup>29–31</sup> This is on a similar order of magnitude to tropospheric ozone

formation, which is estimated to contribute between 216–1404 Tg O<sub>3</sub> yr<sup>-1</sup>.<sup>32</sup> Once transported through the tropopause, ozone mixes efficiently throughout the troposphere.<sup>33</sup> This is because most of the ozone transport through the tropopause takes place in the winter and spring, when ozone lifetimes are longer. Ozone originating in the stratosphere accounts for, on average, 40 % of tropospheric ozone, varying at the surface from 10 % in summer to 60 % in winter.<sup>33</sup>

Thus, the remaining 60 % of tropospheric ozone is formed within the troposphere itself. There are a multitude of reaction schemes to account for tropospheric ozone production. However, most of these have minimal impact, and only the photolysis of NO<sub>2</sub> results in a significant production of ozone.<sup>28</sup> This scheme requires the presence of OH radicals for the initiation in step (6) which are regenerated in step (8). The reaction scheme for production of these OH radicals is explained later in this section, in equations (11) & (12). Similarly, NO radicals are regenerated from equations (8) through (9).

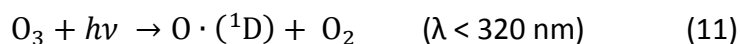


Although this reaction scheme specifies OH and CO as the two initial reactants, the reaction can proceed in a similar way by substituting NO with NO<sub>x</sub>, and CO with any available VOC.

Tropospheric ozone can affect the health of those who breathe it in, causing reduced lung function and complications of existing lung problems, in addition to premature mortality.<sup>34</sup> Since formation of tropospheric ozone requires  $\cdot \text{NO}$  as a reactant, production is higher in more polluted (and generally more populated) areas.

## 1.4 Atmospheric Oxidation

As well as ozone, hydroxyl radicals and NO<sub>3</sub> radicals also act as atmospheric oxidants, in that they also oxidise VOCs to produce secondary organic aerosol (SOA), which will be discussed in section 1.5. OH radicals are produced from ozone via a simple reaction scheme:



It can be seen that ·OH is produced via a photochemical reaction, and thus production of ·OH via this route halts at night-time. This impacts its ability to act as an oxidant in the atmosphere, since ·OH is mostly available to react for 12 hours of the day, approximately.

For OH-initiated oxidation of alkenes, the major reaction pathway proceeds *via* addition of the OH radical to the carbon atoms of the double bond. From here, the 1,2-hydroxyalkyl radical formed may react with molecular oxygen to form a 1,2-hydroxyalkyl peroxy radical.<sup>35</sup> Formation of further products continues analogous to the scheme presented in Figure 1. The minor pathway involves H-abstraction to form H<sub>2</sub>O and an alkyl radical.<sup>36</sup> Formation of further products proceeds *via* reaction with molecular oxygen to form a peroxy radical, and continues according to the scheme presented in Figure 1.

NO<sub>3</sub> radicals are the third competing oxidant present in the atmosphere. NO<sub>3</sub> is rapidly photolyzed by sunlight, and daytime concentrations are as low as 2–5 parts per trillion (ppt), or  $5\text{--}12.5 \times 10^7 \text{ molecule cm}^{-3}$ , rising to up to 31 ppt in the hour before sunset.<sup>37</sup> Whilst this is of high enough concentration to impact ozone concentrations, accounting for  $10 \pm 7 \%$  of ozone destruction during daytime,<sup>37</sup> it is low enough that any reaction involving NO<sub>3</sub> as an oxidant during the day may be considered negligible.

NO<sub>3</sub>-initiated oxidation of alkenes proceeds *via* addition of the NO<sub>3</sub> radical to the carbon atom of the double bond, forming a nitrooxyalkyl radical (O<sub>2</sub>NOR·).<sup>38</sup> The dominant reaction pathway then involves thermal stabilisation of the radical, followed by reaction

with  $O_2$  to form a nitrooxyalkyl peroxy radical ( $O_2NORO_2\cdot$ ).<sup>38</sup> Product formation then proceeds analogous to the scheme described by Figure 1 for OH-initiated oxidation.

Ozonolysis is important within the atmosphere for a number of reasons. It participates in the formation of radicals which may undergo further reactions (e.g. the OH radicals described in equation (12)), damages and restricts growth of vegetation at the ground level, has implications for health, and reacts with VOCs to form acid and highly oxygenated products.<sup>39</sup>

In the  $O_3$ -oxidised reactions presented in this work, the initial step is now widely accepted<sup>40</sup> to proceed via the Criegee mechanism,<sup>41</sup> whereby ozone attacks onto a double bond in the VOC, forming a primary ozonide (POZ), which then decomposes into Criegee intermediates (CIs). Criegee intermediates are often represented as a biradical, but infrared spectroscopy suggests that it is in fact a zwitterion.<sup>42</sup> The general reaction scheme is described by Figure 4:

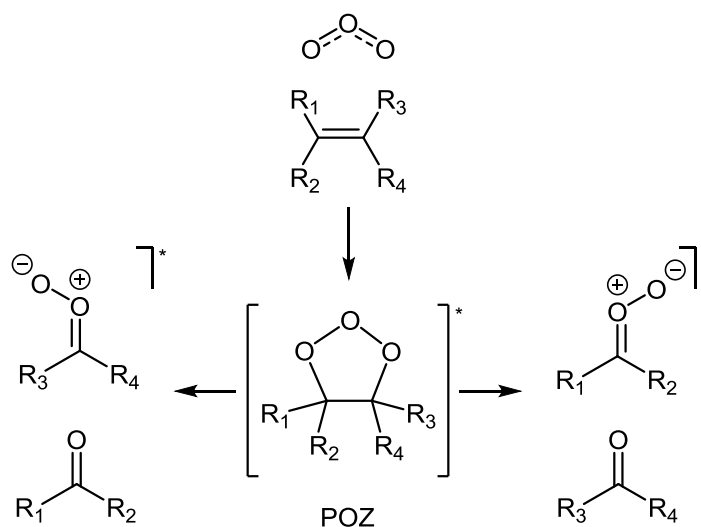


Figure 4: General mechanism for Criegee intermediate formation<sup>41</sup>

To understand the fate of the CIs formed, it is important to make a distinction between unsubstituted, mono-substituted and di-substituted CIs. The unsubstituted CI, of which there is only one ( $\cdot CH_2OO\cdot$ ) is formed through ozonolysis of ethene and terminal alkenes. A number of unimolecular reaction pathways are available to the CI, which are

summarised in Figure 5. Stabilisation of the CI by collision with O<sub>2</sub> or N<sub>2</sub> allows for bimolecular reactions involving CIs, or further unimolecular processes.

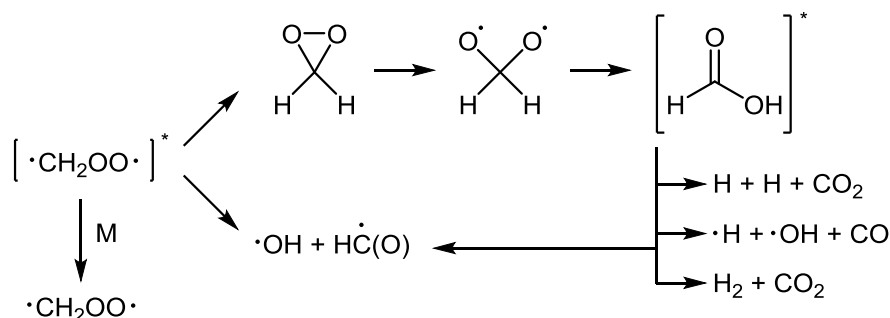


Figure 5: Summary of reaction pathways available to the unsubstituted CI. Reproduced from Johnson and Marston.<sup>40</sup>

In addition to the pathways described by Figure 5, mono- and di-substituted CIs may isomerise to form a vinyl hydroperoxide, which may then decompose to form OH and a vinyloxy radical.<sup>43</sup> These processes are presented in Figure 6:

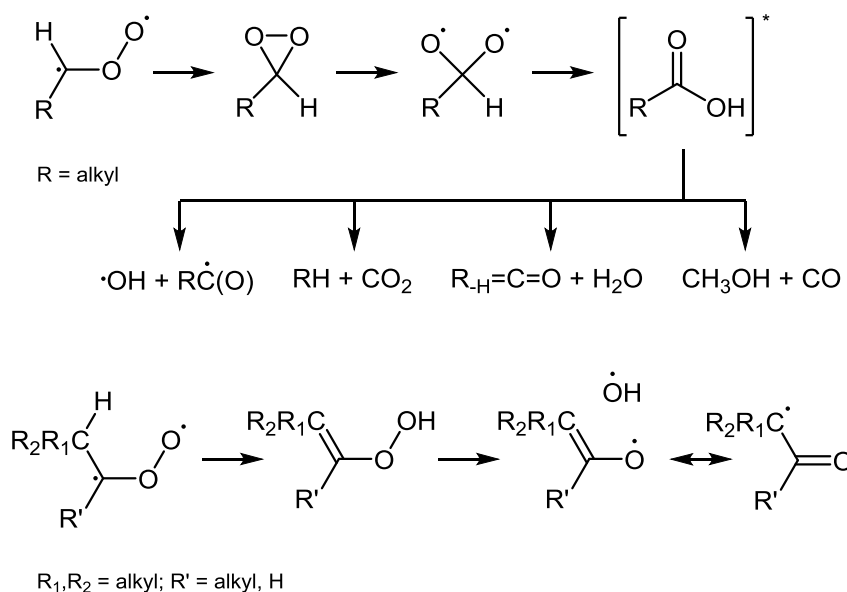


Figure 6: Summary of reaction pathways available to a substituted CI. Reproduced from Johnson and Marston.<sup>40</sup>

Stabilisation of the CIs through collisional quenching (with N<sub>2</sub> or O<sub>2</sub>) allows for the possibility of bimolecular interactions between stabilised CIs (SCIs) and other trace species in the atmosphere.<sup>43</sup> These include, but are not limited to, H<sub>2</sub>O, SO<sub>2</sub> and NO<sub>2</sub>.

Most important amongst these is likely to be HO<sub>2</sub> (forming H<sub>2</sub>O<sub>2</sub> and acidic products), followed by NO<sub>x</sub> in urban areas.<sup>40</sup>

Degradation of VOCs by ozone contributes a significant proportion of atmospheric aerosol product formation (see section 1.5) under environmental conditions, alongside NO<sub>3</sub> and OH.<sup>44</sup> It is the study of these products, and more specifically the aerosol particles which they combine to form, which is the subject of this thesis.

## 1.5 Atmospheric Aerosol

Aerosols are defined as solid or liquid particles suspended in a gas, and thus atmospheric aerosols are simply solid or liquid particles suspended in the atmosphere. Organic atmospheric aerosols may be categorised into two groups: Primary Organic Aerosols (POA) and Secondary Organic Aerosols (SOA).

Primary organic aerosols are those released directly into the atmosphere as aerosols—this is achieved through a combination of mechanical and combustion processes. In general, mechanical processes result in larger, coarse particles of diameter 2.5–10 µm (PM<sub>10</sub>), whilst combustion processes result in fine particles with diameters less than 2.5 µm (PM<sub>2.5</sub>).<sup>45</sup> Both PM<sub>10</sub> and PM<sub>2.5</sub> particulates are known carcinogens when inhaled. The lung cancer rate increases by 22 % per 10 µg m<sup>-3</sup> increase in background levels of PM<sub>10</sub>.<sup>46</sup> An increase in PM<sub>2.5</sub> of 10 µg m<sup>-3</sup> causes the lung cancer rate to increase by 36 %, due to greater penetrative ability of the smaller particles, allowing them to travel further into the lungs.<sup>46</sup>

Sources of POA include: vehicle exhaust fumes—mostly alkanes, alkanoic acids and polycyclic aromatic hydrocarbons;<sup>47, 48</sup> biomass and fossil fuel burning;<sup>49</sup> sea spray—an important source of fatty acids in coastal areas;<sup>50</sup> and also plant waxes from plant abrasion,<sup>51</sup> and alkanoic and alkenoic acids from cooking emissions.

Secondary organic aerosols are those produced in the atmosphere through the reaction of volatile organic compounds (VOCs) to form lower volatility products. In general, the particles produced through this route are fine (< 2.5 µm diameter). It is these reactions,

taking place in the troposphere, which are described in this work. The formation of SOA is comprised of two parts—the first is nucleation (the initial production of a base upon which material can condense to form larger particles), and the second is the growth, or ageing, of this ‘base’.

For the ozonolysis reactions studied in this work, the Criegee intermediates form a range of products dependent on the parent terpene; the products of the individual terpenes investigated in this work will be detailed in future chapters. Due to their low volatility, these products may undergo gas-to-particle conversion, forming a cluster.

Gas-to-particle partitioning relates to the saturation vapour pressure of the compounds present. For the initial nucleation process, any quantity of material present in excess of its saturation vapour pressure will either homogeneously nucleate or condense onto existing seed particles.<sup>52</sup>

Once condensation of organic material has begun, and an organic surface layer has been deposited onto the particle, other products with gas-phase concentrations below their saturation vapour concentrations will partition a proportion of their mass onto the particle.<sup>53</sup> The proportion of product mass which partitions is related to the organic mass concentration and a partitioning co-efficient for the particular species.<sup>53</sup> Condensation of these low volatility vapours allows particles to grow into the Nucleation Mode (3–20 nm). If the concentration of these vapours is too low, the clusters will coagulate, and production of new clusters will halt.<sup>45</sup> Further condensation of low volatility vapours allows the particle to proceed into the Aitken Mode (20–100 nm), and the Accumulation Mode (100 nm–1  $\mu$ m), as shown in Figure 7.<sup>54</sup>

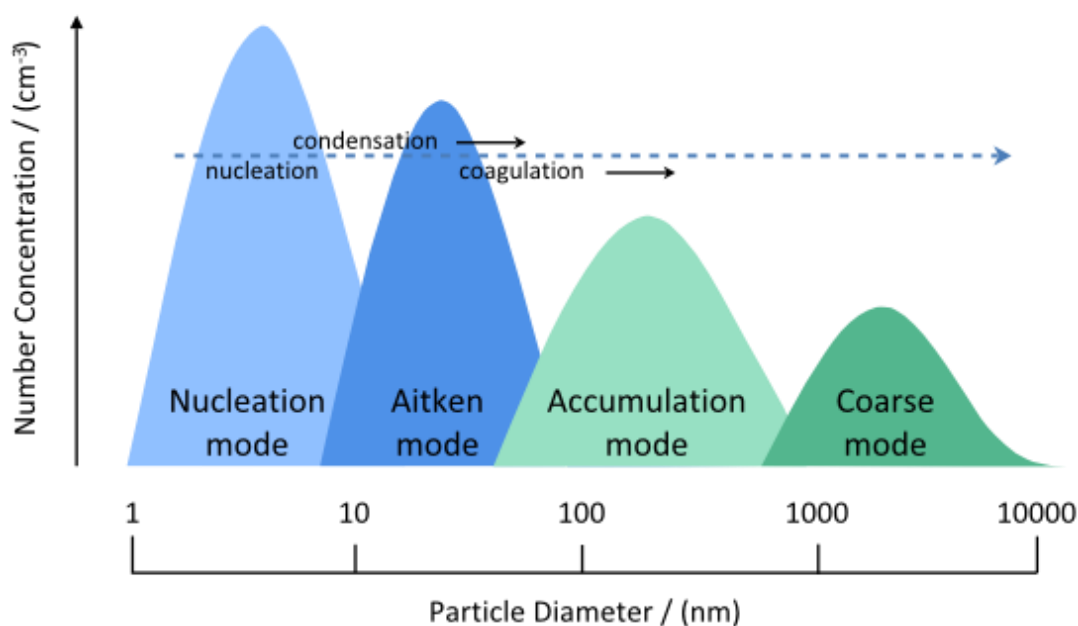


Figure 7: Aerosol Size Modes (not to scale). Diagram adapted.<sup>55</sup>

An important class of compounds for particle nucleation are extremely low volatility organic compounds (ELVOCs).<sup>56</sup> Using high-resolution chemical ionisation mass spectrometry, Ehn *et al.*<sup>57</sup> detected a number of high molecular mass, highly oxygenated products from  $\alpha$ -pinene ozonolysis, which they identified as a number of monomers ( $C_{10}H_{14-16}O_{7-11}$ ) and dimers ( $C_{19-20}H_{28-32}O_{10-18}$ ). They suggest that ELVOC molar yields account for 6–8 % of  $\alpha$ -pinene ozonolysis products, and, due to the high molecular mass of these compounds, 14–18 % of the mass yield. Ehn *et al.* further hypothesise that these ELVOCs are formed from  $RO_2$ , through intramolecular hydrogen abstractions, followed by rapid molecular oxygen additions, yielding products with very high oxygen content. This formation mechanism has been previously proposed;<sup>58</sup> however, the process was believed to terminate before such high O/C ratios as observed by Ehn *et al.* could be achieved. ELVOCs reportedly have vapour pressures orders of magnitude below those of other ozonolysis products, and therefore are believed to contribute significantly to particle formation.

Accretion reactions (reactions of oxidation products that result in an increase in the carbon number) also form low volatility products, due to the high molecular weights



which may be achieved. A number of studies in the literature have observed the uptake of volatile organic species into SOA, and also the formation of high molecular weight products in SOA.<sup>59, 60</sup> Direct evidence and explanation for these observations have been supplied by subsequent experimental studies, which have identified oligomers with molecular weights ranging from 250–1600 Da.<sup>61</sup> Gao *et al.*<sup>61</sup> propose three possible reaction pathways in the particulate phase which may result in oligomer formation: acid dehydration (with loss of a water molecule), aldol reaction between two carbonyls, and *gem-diol* reaction between carbonyls with the participation of water. Due to the resulting high MWs and low volatilities of the oligomer products, accretion reactions may have consequences for the ability of oxidation products to form new particles, and also for the total amount of material which may be incorporated into SOA.

SOA is a component of photochemical smog which has associated health risks—respiratory problems in particular. However, the impact of SOA production is much broader than this. Aerosol particles act as cloud condensation nuclei, where the aerosol particles facilitate the condensation of water vapour in the atmosphere, encouraging the formation of water droplets, which in turn cause increased rainfall.

Perhaps the most interesting consequence of SOA production is the impact that it has on climate change. Incident solar radiation on the Earth has wavelengths of  $\lambda > 300$  nm, such that the radiation is predominantly in the visible and UV regions of the electromagnetic spectrum. While portions of the UV radiation are absorbed by species in the atmosphere, the visible radiation and the remaining UV radiation is able to pass through the atmosphere unhindered, and is absorbed by the Earth. Earth in turn acts as a black body radiator, and emits longer wavelength infrared radiation. This radiation is absorbed by species in the atmosphere, termed ‘greenhouse gases’, thereby increasing the temperature of the atmosphere, and Earth as a whole. This is commonly referred to as ‘global warming’. Species which affect climate change in this way (causing a heating effect) are described as having a positive radiative forcing effect.

Conversely, SOA is known to have a negative radiative forcing effect—that is, SOA contributes a net cooling effect to the atmosphere. This radiative forcing (RF) is comprised of two competing components. The first of these is a cooling effect arising

from the direct scattering of incident sunlight by the aerosol particles, preventing the radiation from directly reaching the Earth. The role of aerosols as cloud condensation nuclei also influences their radiative forcing, since clouds reflect incident sunlight back into space via the albedo effect. Thus, an increase in cloud coverage results in an increase in reflected incident radiation, and a cooling effect. A larger number of aerosol particles provides a larger number of nucleation sites for the formation of cloud droplets, and may result in the formation of more numerous, but smaller droplets. Smaller droplets are known to have a higher albedo (reflectivity)<sup>62</sup> and therefore this increases the cooling effect.

The second of these components is the warming effect caused by presence of black carbon, particularly in anthropogenic aerosols, which absorbs sunlight (Figure 8). Nonetheless, this effect cannot fully offset the cooling effects described above, and thus aerosols contribute a net negative radiative forcing.

The net aerosol radiative forcing in 2011 relative to 1750 was estimated as  $-0.9$  [ $-2.1$  to  $-0.1$ ]  $\text{W m}^{-2}$ .<sup>62</sup> For comparison, change in  $\text{CO}_2$  radiative forcing over the same period is  $+1.68 \text{ W m}^{-2}$ , and net anthropogenic (human-caused) forcing is  $2.29$  [ $1.13$  to  $3.33$ ]  $\text{W m}^{-2}$ .<sup>62</sup> These forcings are presented in Figure 8, along with a “level of confidence”, of which possible levels are: *very high*, *high*, *medium*, *low*, *very low*. This is appraised by a combination of amount of evidence, and to what extent the evidence agrees. More evidence, and better agreement between that evidence, both contribute to a higher confidence level.<sup>62</sup>

From 1950–2011, global temperatures increased by  $0.65 \pm 0.5$  °C. Other anthropogenic forcings, of which aerosol contributions are the dominant part, provided a net contribution of  $-0.25 \pm 0.35$  °C over the same period.<sup>63</sup> Other contributors to “other anthropogenic forcings” include changes in ozone concentrations, land use reflectance changes and other minor terms.

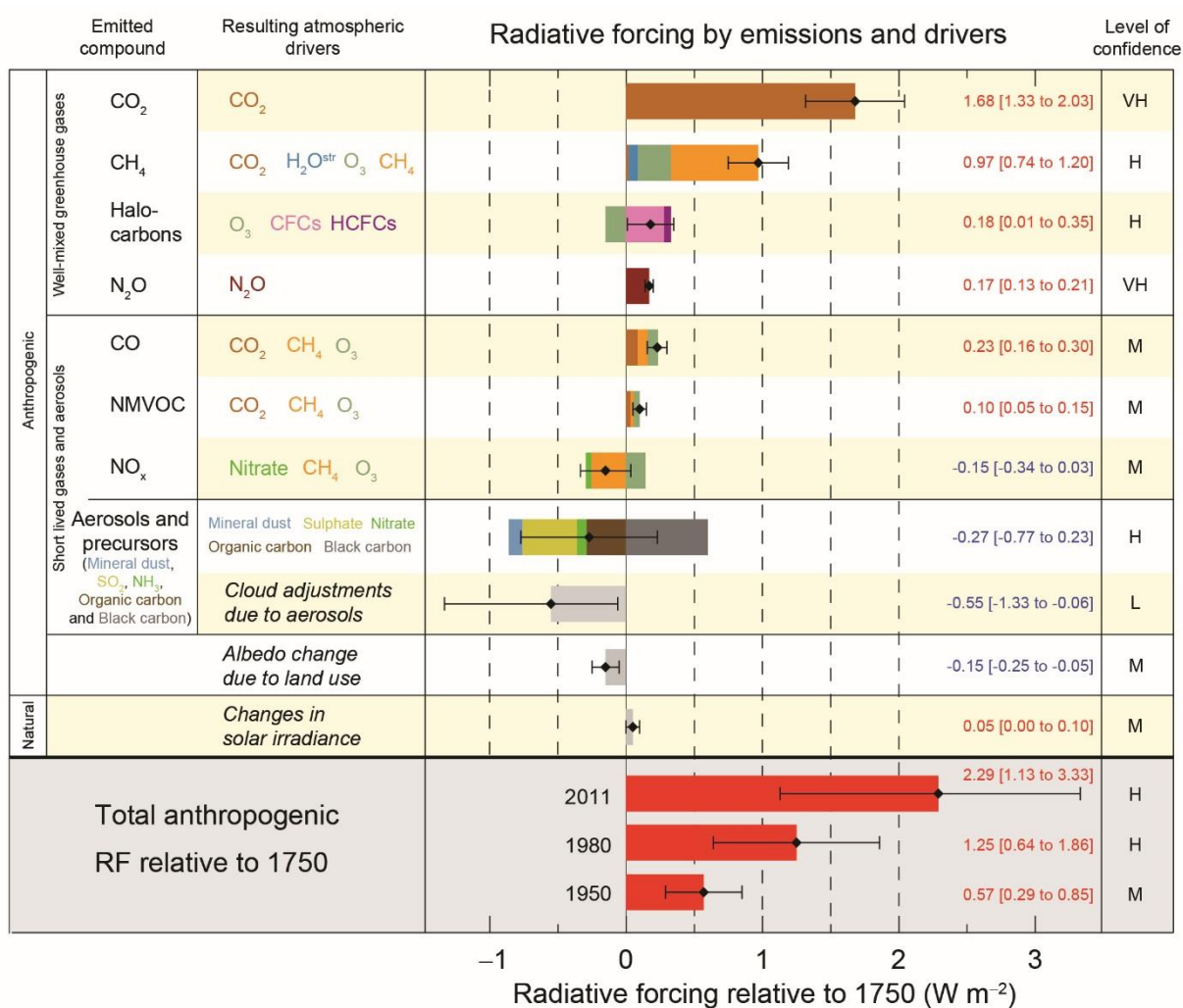


Figure 8: Change in relative forcings of climate change contributors during the period 1750–2011. Reproduced from the IPCC Working Group I Report: Climate Change 2013: The Physical Science Basis.<sup>62</sup> RF = Radiative Forcing. Confidence levels: VH = very high; H = high; M = medium; L = low; VL = very low.

Thus, it is clear both that aerosols play a major role in climate change, and that greater understanding of their properties is required to reduce the uncertainty regarding their contribution. Indeed, the Intergovernmental Panel on Climate Change (IPCC) concludes that, whilst there is “high confidence that the global mean total aerosol radiative forcing has counteracted a substantial portion of radiative forcing from well mixed greenhouse gases... aerosols continue to contribute the largest uncertainty to the total radiative forcing estimate.”<sup>63</sup>

SOA has, until recently, been assumed to be liquid in nature by gas-particle partitioning models.<sup>64, 65</sup> However, studies have shown that particles may be solid in nature.<sup>66</sup> This is a very important discovery since chemical reactions may be inhibited within solid aerosol, due

to the lack of movement of species within the particle, severely constraining reactions within the bulk of the particle, but still allowing reactions on the surface. This would in turn affect the reactivity and lifetime of SOA produced from VOCs.

## 1.6 Global SOA Budget

The global SOA budget is a simple concept, which is essentially an estimate of the mass of SOA produced per year. However, in practice it has proved difficult to produce a definitive value, and estimates vary wildly. There are two methods used to provide estimates of SOA production. Bottom-up methods combine emission data from SOA precursors with laboratory-based yield analyses, within a computational model, to estimate SOA formation. They also calculate an estimate for the rate of SOA removal processes, including wet and dry deposition and photolytic destruction. They combine the calculated formation and removal rates to determine an overall SOA flux.

Top-down methods use calculations constrained by atmospheric observations in an attempt to replicate atmospheric conditions in their models. Measurements of atmospheric aerosols are taken across a range of locations, using an Aerosol Mass Spectrometer (AMS). Within the model, yields of different SOA categories (e.g. biogenic, biomass burning, ageing of POA) are varied until the best fit to the atmospheric observations can be obtained. Another top-down method involves estimating the SOA budget from the sulfate budget. By assuming that organic aerosol is internally mixed with sulfate, the SOA budget can be calculated from the sulfate budget, which is comparatively well understood.<sup>64</sup>

A review of more than 20 state-of-the-art global aerosol models showed that bottom-up estimates of the annual SOA budget vary from 12–119 Tg yr<sup>-1</sup>,<sup>67</sup> with further top-down estimates ranging as widely as 140–910 Tg yr<sup>-1</sup>.<sup>68</sup> Clearly, there is a huge differential between these estimates; however, recently there have been advances in the modelling techniques used, allowing for much-improved estimates.

Recently, Hodzic et al.<sup>69</sup> suggested that both SOA formation rates, as well as deposition rates, have been underestimated in bottom-up models by factors of 3.9 and 3.6 respectively. By incorporating these factors into their model, they have produced a revised estimate of

132.2 Tg yr<sup>-1</sup> SOA, of which 97.5 Tg result from biogenic sources, and the remainder from anthropogenic sources. This tallies remarkably well with the top-down central estimate of 140 Tg yr<sup>-1</sup> derived by Spracklen et al.<sup>70</sup>

It is worthy of note that not all emitted VOCs form SOA; only molecules of sufficiently low volatility are able to be incorporated into aerosol particles. As a general rule, the lower the molecular mass of the molecule, the higher its volatility, and thus molecules with very few carbon atoms (< 7) do not participate in SOA formation under normal conditions.<sup>71</sup> Of course, this is only a general rule, and other factors such as oxygenation of the molecule are important in governing volatility.

## 1.7 Factors Affecting SOA Evolution

Conditions in the atmosphere are highly variable, and evaluating the formation of SOA is not as simple as simply studying the ozonolysis of a terpene under one set of conditions. A whole host of environmental factors affect the nucleation and subsequent evolution of aerosol particles, and understanding these is key to understanding how aerosols may behave in the atmosphere.

### 1.7.1 Temperature

The first, and perhaps simplest determinant of SOA evolution is temperature. Since temperatures within the troposphere are hugely variant, dependent on location and altitude amongst other factors, an understanding of how temperatures affect aerosol yield is important. A number of groups have investigated the effect of changing temperature on aerosol yields. All agree that an increase in temperature correlates with a decrease in aerosol mass yield. The dominant effect is believed to be caused by changes in gas-to-particle partitioning.<sup>64</sup> This is as may be expected, since an increase in temperature correlates with an increase in vapour pressure, making it more favourable for species to remain in the gas phase. A change in temperature is also believed to influence the chemical mechanisms and rate constants, resulting in changes in product yields.<sup>64</sup>

Pathak *et al.*<sup>72</sup> note a significant temperature dependence between 273–288 K; they observed a reduction in mass yield of almost 50 % for the  $\alpha$ -pinene ozonolysis when temperature was raised from 273 to 288 K. A weaker dependence was observed between 288–313 K, resulting in a reduction in mass yield of 10–20 % across this range.

Similarly, Saathoff *et al.*<sup>73</sup> report a significant temperature dependence. An increase from 243–313 K resulted in an 80–90 % decrease in yield for products of the  $\alpha$ -pinene ozonolysis, and an increase from 253–313 K gave a 60 % fall in mass yield for the ozonolysis of limonene.

### 1.7.2 Humidity

Relative humidity (RH) is defined as the partial pressure of water vapour in the air, divided by its vapour pressure at a given temperature, expressed as a percentage. RH in the atmosphere is again hugely variant, depending on local conditions, and thus a solid understanding of how RH affects SOA formation is paramount to better characterising SOA evolutions.

The effect of varying RH on SOA is believed to be considerably more complex than that of varying temperature. One likely consequence of increasing RH is that water may condense onto the surface of particles, thus accelerating their growth. This effect is reportedly minor.<sup>74</sup> The uptake of water into a particle may in turn affect gas-to-particle partitioning, as suggested by Prisle *et al.*<sup>75</sup> By increasing the proportion of water in the particle, the mole fraction of the products is decreased. According to Raoult's law, the partial vapour pressure of a component of a liquid mixture is equal to the vapour pressure of the pure component, multiplied by its mole fraction in the mixture. Thus, by reducing the mole fraction of the organic components, their partial vapour pressures are decreased, and condensation of vapours becomes more favourable.

Numerous groups in the literature have studied the effect of RH on SOA formation for  $\alpha$ -pinene ozonolysis. Jonsson *et al.*<sup>76</sup> report an increase in both number and mass of particles formed under increasing (2–85 %) RH conditions, which they attribute to water uptake and change in product yield distribution. Bonn *et al.*,<sup>77</sup> meanwhile, report an increase in mass yield, but a decrease in particle number, with increasing (0–31 %) RH. Rohr *et al.*,<sup>78</sup> from

their smog chamber experiments, observed no change in either number or mass of particles produced as a result of varying (13–41 %) RH.

Clearly, there is no consensus on the effect of varying RH on aerosol formation, with a number of conflicting results reported in the literature.

### 1.7.3 Scavenger

The oxidation of terpenes is known to form OH radicals as a by-product of the reaction with O<sub>3</sub> (see section 1.4). Once formed, these radicals are known to undergo reaction with the terpene. The products of these reactions can then mix with those of the ozonolysis reaction studied, making it impossible to determine which products were formed as a result of reaction with ozone, and which as a result of reaction with OH<sup>•</sup>.

Thus, scavengers are commonly employed in ozonolysis-based studies of SOA. A scavenger is a molecule which is inert with respect to ozone, but which reacts at a good rate with hydroxyl radicals. A good scavenger must therefore be a saturated organic molecule, as ozone reacts readily with any available double bond. Common examples of scavengers include cyclohexane,<sup>79</sup> carbon monoxide<sup>80</sup> and simple alcohols.<sup>81</sup>

However, as is often the case, employing a scavenger brings with it its own set of complexities. Jonsson *et al.*<sup>82</sup> report that presence of a scavenger may inhibit growth of the aerosol. This suggests that the scavenger may condense onto the aerosol's surface, potentially forming a barrier to further oxidation of products within the particle.

Use of a scavenger can lead to a large decrease in SOA yield,<sup>83</sup> due to inhibition of OH-initiated oxidation. Iinuma *et al.*<sup>83</sup> conclude that reactions of the hydroxyl radical with gas-phase organics are an important step in the formation of high molecular weight products identified in the particle phase.

Presence of a scavenger may also influence the HO<sub>2</sub> / RO<sub>2</sub> ratio, which in turn has consequences for SOA yield.<sup>84, 85</sup> OH and RO<sub>2</sub> radicals are produced as by-products of the ozonolysis of terpenes, and RO<sub>2</sub> radicals are understood to undergo secondary reactions with the Criegee intermediates to form a number of the ozonolysis products.<sup>86, 87</sup> Reactions

of the scavenger with OH results in formation of both HO<sub>2</sub> and RO<sub>2</sub> radicals, in different ratios, dependent on the nature of the scavenger.<sup>84</sup> Similarly to RO<sub>2</sub>, HO<sub>2</sub> may also undergo reaction with the Criegee intermediates to form low volatility products. The scavenger thus influences yield of the aerosol by governing HO<sub>2</sub> / RO<sub>2</sub> ratios, and thus influencing product yields.

#### 1.7.4 Ultraviolet Radiation

Ultraviolet light, while not of any significance in the chamber studies performed in this work due to the very weak radiation present in the laboratory, may impact on SOA yields in the upper troposphere. Again, the magnitude of UV radiation is dependent on environmental factors, such as concentration of ozone in the stratosphere, cloud cover and incident angle of sunlight.

Presto *et al.*<sup>88</sup> report a decrease in SOA yields in correlation with an increase in UV radiation, of approximately 20–40 %. This tallies well with a study by Cao and Jang,<sup>89</sup> who also report a decrease in SOA yield of approximately 20 % under highly irradiated conditions.

Both groups attribute this reduction in SOA yield to the gas-phase photolysis of otherwise stable organic species to form a more volatile product distribution, less inclined to form SOA. GC-MS studies suggest that, for the  $\alpha$ -pinene ozonolysis, yields of pinic and pinonic acid, believed to participate in gas-to-particle partitioning, are significantly reduced under high-UV conditions.<sup>88</sup>

#### 1.7.5 NO<sub>x</sub> Presence

NO<sub>x</sub> (the sum of NO & NO<sub>2</sub>) is formed within the atmosphere by the extreme heat of lightning strikes, and is emitted as a product of fossil fuel burning. Thus, levels of NO<sub>x</sub> are elevated in more urban and industrial areas where fossil fuel burning is greater.

SOA yields are known to decrease dramatically in the presence of high-NO<sub>x</sub> concentrations. Indeed, under experimental conditions where initial VOC concentration is not considerably



greater than initial  $\text{NO}_x$  concentration ( $[\text{VOC}]_0/[\text{NO}_x]_0 \leq 4.5$ ), formation of SOA from the  $\alpha$ -pinene ozonolysis system is completely suppressed.<sup>90</sup> Kroll *et al.*<sup>91</sup> and Presto *et al.*,<sup>90</sup> as examples, both observe a significant dependence of SOA yield on  $\text{NO}_x$  concentration, which they attribute to  $\text{RO}_2$  chemistry. At high  $\text{NO}_x$ ,  $\text{NO}$  reacts with peroxy radicals to form small alkoxy radicals, which are likely to fragment, and organic nitrates which are expected to be of higher volatility than the other products.<sup>90, 91</sup> This acts as a sink of  $\text{RO}_2$ , which may otherwise react with  $\text{HO}_2$  to form hydroperoxides, believed to be important components of SOA,<sup>92</sup> and may also react with Criegee intermediates to form a number of low volatility products.<sup>86</sup>

## 1.8 Aims and Objectives

This thesis describes a characterisation of the aerosol produced by ozonolysis of two terpenes. Section 1.7 of this introduction has described some of the complexities which may be encountered when studying aerosol products of these reactions, and identified some uncertainties in the literature. In this work, the effects of varying different experimental conditions on the physical properties of the aerosol formed have been studied in isolation, and consequently inferences have been made regarding the chemistry.

The first system investigated was that of the monoterpene  $\alpha$ -pinene and its ozonolysis products. Chapter 3 describes the aerosol produced by this reaction, and begins by probing the relationship between mass of products and the tendency of those products to be incorporated into aerosol particles. A rate constant for the reaction was determined by comparison of the aerosol evolution profile to a simulated reaction profile. The effects of varying the scavenger on the properties of SOA formed were investigated. The effect of varying humidity was also explored, and additional information on its physical state under varying relative humidities is presented.

An enone derivative of  $\alpha$ -pinene, designed to allow for study of one Criegee intermediate in isolation, was synthesised in Chapter 4, and the ozonolysis products of this compound are the primary focus of the chapter. The SOA evolution profile of the enone ozonolysis products was first compared with that of  $\alpha$ -pinene, and also with an enal derivative not investigated

in this work. A rate constant for the reaction of enone with ozone was calculated through the same method used previously for  $\alpha$ -pinene. Relative contributions of each Criegee intermediate to the total SOA mass yield of  $\alpha$ -pinene are presented, and the effect of local reactant concentrations is discussed.

Chapter 5 concerns the ozonolysis of  $\alpha$ -terpinene, and analysis of the subsequent aerosol. The volatility behaviour of the products was again investigated by exploring the relationship between observed aerosol mass and tendency of products to be incorporated into that aerosol. The flow tube experimental technique was introduced, and comparisons drawn between that and the more standard chamber technique. The flow tube technique was then employed to supplement the work on product incorporation into aerosol. The effect of varying ozone concentration on the aerosol formed was investigated, and the effect of varying humidity on the initial stages of SOA formation also explored. Finally, lower and upper bounds for the reaction rate constant were established, through comparison of experimental to simulated results.

As discussed in section 1.5, aerosols currently contribute the greatest uncertainty to the total radiative forcing estimate. Only by studies of SOA formation such as those described in this work, incorporating a wider range of VOCs over atmospherically relevant concentrations, looking in greater depth at the SOA formation mechanisms of the most abundant VOCs, and investigating the effect of varying environmental factors, may we begin to reduce this uncertainty and better quantify the impact aerosols have on the earth's climate.

## 1.9 References

1. J. P. Friend, A. R. Bandy, J. L. Moyers, W. H. Zoller, R. E. Stoiber, A. L. Torres, W. I. Rose, M. P. McCormick and D. C. Woods, *Geophys. Res. Lett.*, 1982, **9**, 1101-1104.
2. B. Pani, I.K. International Publishing House Pvt. Limited, 2007, Structure of the Atmosphere, pp. 169-170.
3. S. Ackerman and J. Knox, *Meteorology: Understanding the Atmosphere*, 3rd edn., Jones and Bartlett Learning, 2012.
4. D. Jaffe, H. Price, D. Parrish, A. Goldstein and J. Harris, *Geophys. Res. Lett.*, 2003, **30**, 4.
5. P. G. Simmonds, R. G. Derwent, A. L. Manning and G. Spain, *Atmos. Environ.*, 2004, **38**, 4769-4778.
6. P. Pochanart, S. Kato, T. Katsuno and H. Akimoto, *Atmos. Environ.*, 2004, **38**, 1325-1336.
7. K. E. Percy, E. H. Legge and S. V. Krupa, *Air Pollution, Global Change and Forests in the New Millennium*, Elsevier, 2003, vol. 3, 4, p. 85.
8. C. D. Ahrens and R. Henson, *Meteorology Today: An Introduction to Weather, Climate and the Environment*, 11th edn., Cengage Learning, 1999.
9. S. Solomon, K. H. Rosenlof, R. W. Portmann, J. S. Daniel, S. M. Davis, T. J. Sanford and G.-K. Plattner, *Science*, 2010, **327**, 1219-1223.
10. M. S. Waring and J. R. Wells, *Atmos. Environ.*, 2015, **106**, 382-391.
11. P. Wayne, *Chemistry of Atmospheres, An Introduction to the Chemistry of Atmospheres of Earth, the Planets and their Satellites*, 1 edn., Oxford Clarendon Press, 1991.
12. J. T. Emmert, M. H. Stevens, P. F. Bernath, D. P. Drob and C. D. Boone, *Nature Geosci.*, 2012, **5**, 868-871.
13. K. Mohanakumar, *Stratosphere Troposphere Interactions: An Introduction*, Springer, 2008.
14. R. T. Watson, M. A. Geller, R. S. Stolarski and R. F. Hampson, *NASA Reference Publication 1162*, NASA, Washington, D.C., 1986, 20.
15. A. B. Guenther, X. Jiang, C. L. Heald, T. Sakulyanontvittaya, T. Duhl, L. K. Emmons and X. Wang, *Geosci. Model Dev.*, 2012, **5**, 1471-1492.
16. T. Dindorf, U. Kuhn, L. Ganzeveld, G. Schebeske, P. Ciccioli, C. Holzke, R. Köble, G. Seufert and J. Kesselmeier, *Biogeosciences Discuss.*, 2005, **2005**, 137-182.
17. C. Holzke, T. Dindorf, J. Kesselmeier, U. Kuhn and R. Koppmann, *J. Atmos. Chem.*, 2006, **55**, 81-102.
18. N. C. Bouvier-Brown, R. Holzinger, K. Palitzsch and A. H. Goldstein, *Atmos. Environ.*, 2009, **43**, 389-401.

19. R. J. Griffin, D. R. Cocker, J. H. Seinfeld and D. Dabdub, *Geophys. Res. Lett.*, 1999, **26**, 2721-2724.
20. R. Atkinson, *Atmos. Environ.*, 2000, **34**, 2063-2101.
21. B. Chuong, M. Davis, M. Edwards and P. S. Stevens, *Int. J. Chem. Kinet.*, 2002, **34**, 300-308.
22. T. Braure, Y. Bedjanian, M. N. Romanias, J. Morin, V. Riffault, A. Tomas and P. Coddeville, *J. Phys. Chem. A*, 2014, **118**, 9482-9490.
23. R. Atkinson, S. M. Aschmann and J. N. Pitts, *Int. J. Chem. Kinet.*, 1986, **18**, 287-299.
24. R. Atkinson, D. L. Baulch, R. A. Cox, J. N. Crowley, R. F. Hampson, R. G. Hynes, M. E. Jenkin, M. J. Rossi and J. Troe, *Atmos. Chem. Phys.*, 2006, **6**, 3625-4055.
25. A. C. Bronstein, D. A. Spyker, L. R. J. Cantilena, J. L. Green, B. H. Rumack and S. L. Giffin, *Clin. Toxicol. (Phila.)*, 2010, **48(10)**, 979-1178.
26. S. Chapman, *A Theory of Upper-atmospheric Ozone*, Edward Stanford, 1930.
27. M. J. Prather, *Geophys. Res. Lett.*, 2009, **36**, L03811.
28. R. Atkinson and J. Arey, *Atmos. Environ.*, 2003, **37**, **Supplement 2**, 197-219.
29. A. Ebel, H. Elbern and A. Oberreuter, *Coupling Processes in the Lower and Middle Atmosphere*, eds. E. V. Thrane, T. A. Blix and D. C. Fritts, Springer Netherlands, Dordrecht, 1993, pp. 49-65.
30. H. Levy, J. D. Mahlman, W. J. Moxim and S. C. Liu, *J. Geophys. Res.-Atmos.*, 1985, **90**, 3753-3772.
31. D. M. Murphy and D. W. Fahey, *J. Geophys. Res.-Atmos.*, 1994, **99**, 5325-5332.
32. World Meteorological Organization 1995, *Scientific assessment of depletion: 1994*, Global ozone research and monitoring project, **37**, Geneva, Switzerland.
33. G.-J. Roelofs and J. Lelieveld, *Tellus B Chem. Phys. Meteorol.*, 1997, **49**, 38-55.
34. M. Lippmann, *J Expo Anal Environ Epidemiol*, 1993, **3**, 103-129.
35. R. Atkinson, *J. Phys. Chem. Ref. Data*, 1997, **26**, 215-290.
36. E. C. Tuazon, S. M. Aschmann, M. V. Nguyen and R. Atkinson, *Int. J. Chem. Kinet.*, 2003, **35**, 415-426.
37. A. Geyer, B. Alicke, R. Ackermann, M. Martinez, H. Harder, W. Brune, P. di Carlo, E. Williams, T. Jobson, S. Hall, R. Shetter and J. Stutz, *J. Geophys. Res.-Atmos.*, 2003, **108**, 4368.
38. R. Atkinson and J. Arey, *Chemical Reviews*, 2003, **103**, 4605-4638.
39. J. Fuhrer, L. Skärby and M. R. Ashmore, *Environ. Pollut.*, 1997, **97**, 91-106.
40. D. Johnson and G. Marston, *Chem. Soc. Rev.*, 2008, **37**, 699-716.
41. R. Criegee, *Angew. Chem. Int. Ed. Engl.*, 1975, **14**, 745-752.
42. Y.-T. Su, Y.-H. Huang, H. A. Witek and Y.-P. Lee, *Science*, 2013, **340**, 174-176.

- 
43. J. G. Calvert, R. Atkinson, J. A. Kerr, S. Madronich, G. K. Moortgat, T. J. Wallington and G. Yarwood, *The Mechanisms of Atmospheric Oxidation of the Alkenes*, Illustrated edn., Oxford University Press, UK, 2000.
44. T. Hoffmann, J. R. Odum, F. Bowman, D. Collins, D. Klockow, R. C. Flagan and J. H. Seinfeld, *J. Atmos. Chem.*, 1997, **26**, 189-222.
45. T. Hoffmann and J. Warnke, *Volatile Organic Compounds in the Atmosphere*, ed. R. Koppmann, Blackwell Publishing, Oxford, 1st edn., 2007, vol. 1, 9, pp. 342-387.
46. O. Raaschou-Nielsen, Z. J. Andersen, R. Beelen, E. Samoli, M. Stafoggia, G. Weinmayr, B. Hoffmann, P. Fischer, M. J. Nieuwenhuijsen, B. Brunekreef, W. W. Xun, K. Katsouyanni, K. Dimakopoulou, J. Sommar, B. Forsberg, L. Modig, A. Oudin, B. Oftedal, P. E. Schwarze, P. Nafstad, U. De Faire, N. L. Pedersen, C.-G. Östenson, L. Fratiglioni, J. Penell, M. Korek, G. Pershagen, K. T. Eriksen, M. Sørensen, A. Tjønneland, T. Ellermann, M. Eeftens, P. H. Peeters, K. Meliefste, M. Wang, B. Bueno-de-Mesquita, T. J. Key, K. de Hoogh, H. Concin, G. Nagel, A. Vilier, S. Grioni, V. Krogh, M.-Y. Tsai, F. Ricceri, C. Sacerdote, C. Galassi, E. Migliore, A. Ranzi, G. Cesaroni, C. Badaloni, F. Forastiere, I. Tamayo, P. Amiano, M. Dorronsoro, A. Trichopoulou, C. Bamia, P. Vineis and G. Hoek, *Lancet Oncol.*, 2013, **14**, 813-822.
47. W. F. Rogge, L. M. Hildemann, M. A. Mazurek, G. R. Cass and B. R. Simoneit, *Environ. Sci. Technol.*, 1993, **27**, 636-651.
48. J. J. Schauer, M. J. Kleeman, G. R. Cass and B. R. Simoneit, *Environ. Sci. Technol.*, 2002, **36**, 1169-1180.
49. B. T. Simoneit, *Environ. Sci. & Pollut. Res.*, 1999, **6**, 159-169.
50. M. Mochida, Y. Kitamori, K. Kawamura, Y. Nojiri and K. Suzuki, *J. Geophys. Res.-Atmos.*, 2002, **107**, 4325.
51. W. F. Rogge, L. M. Hildemann, M. A. Mazurek, G. R. Cass and B. R. Simoneit, *Environ. Sci. Technol.*, 1993, **27**, 2700-2711.
52. T. D. Vaden, C. Song, R. A. Zaveri, D. Imre and A. Zelenyuk, *Proc. Natl. Acad. Sci. U.S.A.*, 2010, **107**, 6658-6663.
53. J. F. Pankow, *Atmos. Environ.*, 1994, **28**, 189-193.
54. M. Kulmala, H. Vehkamäki, T. Petäjä, M. Dal Maso, A. Lauri, V. M. Kerminen, W. Birmili and P. H. McMurry, *J. Aerosol. Sci.*, 2004, **35**, 143-176.
55. D. Wetterdienst, (2018),  
[https://www.dwd.de/EN/research/observing\\_atmosphere/composition\\_atmosphere/aerosol/cont\\_nav/particle\\_size\\_distribution\\_node.html](https://www.dwd.de/EN/research/observing_atmosphere/composition_atmosphere/aerosol/cont_nav/particle_size_distribution_node.html),

56. N. M. Donahue, J. H. Kroll, S. N. Pandis and A. L. Robinson, *Atmos. Chem. Phys.*, 2012, **12**, 615-634.
57. M. Ehn, J. A. Thornton, E. Kleist, M. Sipilä, H. Junninen, I. Pullinen, M. Springer, F. Rubach, R. Tillmann, B. Lee, F. Lopez-Hilfiker, S. Andres, I.-H. Acir, M. Rissanen, T. Jokinen, S. Schobesberger, J. Kangasluoma, J. Kontkanen, T. Nieminen, T. Kurtén, L. B. Nielsen, S. Jørgensen, H. G. Kjaergaard, M. Canagaratna, M. D. Maso, T. Berndt, T. Petäjä, A. Wahner, V.-M. Kerminen, M. Kulmala, D. R. Worsnop, J. Wildt and T. F. Mentel, *Nature*, 2014, **506**, 476.
58. L. Vereecken, J. F. Muller and J. Peeters, *Phys. Chem. Chem. Phys.*, 2007, **9**, 5241-5248.
59. M. Jang, N. M. Czoschke, S. Lee and R. M. Kamens, *Science*, 2002, **298**, 814-817.
60. A. Limbeck, M. Kulmala and H. Puxbaum, *Geophys. Res. Lett.*, 2003, **30**, n/a-n/a.
61. S. Gao, N. L. Ng, M. Keywood, V. Varutbangkul, R. Bahreini, A. Nenes, J. He, K. Y. Yoo, J. L. Beauchamp, R. P. Hodyss, R. C. Flagan and J. H. Seinfeld, *Environ. Sci. Technol.*, 2004, **38**, 6582-6589.
62. Myhre, G., D. Shindell, F.-M. Bréon, W. Collins, J. Fuglestad, J. Huang, D. Koch, J.-F. Lamarque, D. Lee, B. Mendoza, T. Nakajima, A. Robock, G. Stephens, T. Takemura and H. Zhang, 2013: Anthropogenic and Natural Radiative Forcing. In: *Climate Change 2013: The Physical Science Basis. Contribution of Working Group I to the Fifth Assessment Report of the Intergovernmental Panel on Climate Change*, [Stocker, T.F., D. Qin, G.-K. Plattner, M. Tignor, S.K. Allen, J. Boschung, A. Nauels, Y. Xia, V. Bex and P.M. Midgley (eds.)]. Cambridge University Press, Cambridge, United Kingdom and New York, NY, USA.
63. IPCC, 2014: *Climate Change 2014: Synthesis Report. Contribution of Working Groups I, II and III to the Fifth Assessment Report of the Intergovernmental Panel on Climate Change* [Core Writing Team, R.K. Pachauri and L.A. Meyer (eds.)]. IPCC, Geneva, Switzerland, 151 pp.
64. M. Hallquist, J. C. Wenger, U. Baltensperger, Y. Rudich, D. Simpson, M. Claeys, J. Dommen, N. M. Donahue, C. George, A. H. Goldstein, J. F. Hamilton, H. Herrmann, T. Hoffmann, Y. Iinuma, M. Jang, M. E. Jenkin, J. L. Jimenez, A. Kiendler-Scharr, W. Maenhaut, G. McFiggans, T. F. Mentel, A. Monod, A. S. H. Prévôt, J. H. Seinfeld, J. D. Surratt, R. Szmigielski and J. Wildt, *Atmos. Chem. Phys.*, 2009, **9**, 5155-5236.
65. J. L. Jimenez, M. R. Canagaratna, N. M. Donahue, A. S. H. Prevot, Q. Zhang, J. H. Kroll, P. F. DeCarlo, J. D. Allan, H. Coe, N. L. Ng, A. C. Aiken, K. S. Docherty, I. M. Ulbrich, A. P. Grieshop, A. L. Robinson, J. Duplissy, J. D. Smith, K. R. Wilson, V. A. Lanz, C. Hueglin, Y. L. Sun, J. Tian, A. Laaksonen, T. Raatikainen, J. Rautiainen, P. Vaattovaara, M. Ehn, M. Kulmala, J. M. Tomlinson, D. R. Collins, M. J. Cubison, E., J. Dunlea, J. A. Huffman, T. B. Onasch, M. R. Alfarra, P. I. Williams, K. Bower, Y. Kondo, J. Schneider, F. Drewnick, S. Borrmann, S. Weimer, K.

- Demerjian, D. Salcedo, L. Cottrell, R. Griffin, A. Takami, T. Miyoshi, S. Hatakeyama, A. Shimono, J. Y. Sun, Y. M. Zhang, K. Dzepina, J. R. Kimmel, D. Sueper, J. T. Jayne, S. C. Herndon, A. M. Trimborn, L. R. Williams, E. C. Wood, A. M. Middlebrook, C. E. Kolb, U. Baltensperger and D. R. Worsnop, *Science*, 2009, **326**, 1525-1529.
66. A. Virtanen, J. Joutsensaari, T. Koop, J. Kannosto, P. Yli-Pirilä, J. Leskinen, J. M. Mäkelä, J. K. Holopainen, U. Pöschl, M. Kulmala, D. R. Worsnop and A. Laaksonen, *Nature*, 2010, **467**, 824-827.
67. K. Tsigaridis, N. Daskalakis, M. Kanakidou, P. J. Adams, P. Artaxo, R. Bahadur, Y. Balkanski, S. E. Bauer, N. Bellouin, A. Benedetti, T. Bergman, T. K. Berntsen, J. P. Beukes, H. Bian, K. S. Carslaw, M. Chin, G. Curci, T. Diehl, R. C. Easter, S. J. Ghan, S. L. Gong, A. Hodzic, C. R. Hoyle, T. Iversen, S. Jathar, J. L. Jimenez, J. W. Kaiser, A. Kirkevåg, D. Koch, H. Kokkola, Y. H. Lee, G. Lin, X. Liu, G. Luo, X. Ma, G. W. Mann, N. Mihalopoulos, J. J. Morcrette, J. F. Müller, G. Myhre, S. Myriokefalitakis, N. L. Ng, D. O'Donnell, J. E. Penner, L. Pozzoli, K. J. Pringle, L. M. Russell, M. Schulz, J. Sciare, Ø. Seland, D. T. Shindell, S. Sillman, R. B. Skeie, D. Spracklen, T. Stavrakou, S. D. Steenrod, T. Takemura, P. Tiitta, S. Tilmes, H. Tost, T. van Noije, P. G. van Zyl, K. von Salzen, F. Yu, Z. Wang, Z. Wang, R. A. Zaveri, H. Zhang, K. Zhang, Q. Zhang and X. Zhang, *Atmos. Chem. Phys.*, 2014, **14**, 10845-10895.
68. M. Kanakidou, J. H. Seinfeld, S. N. Pandis, I. Barnes, F. J. Dentener, M. C. Facchini, R. Van Dingenen, B. Ervens, A. Nenes, C. J. Nielsen, E. Swietlicki, J. P. Putaud, Y. Balkanski, S. Fuzzi, J. Horth, G. K. Moortgat, R. Winterhalter, C. E. L. Myhre, K. Tsigaridis, E. Vignati, E. G. Stephanou and J. Wilson, *Atmos. Chem. Phys.*, 2005, **5**, 1053-1123.
69. A. Hodzic, P. S. Kasibhatla, D. S. Jo, C. D. Cappa, J. L. Jimenez, S. Madronich and R. J. Park, *Atmos. Chem. Phys.*, 2016, **16**, 7917-7941.
70. D. V. Spracklen, J. L. Jimenez, K. S. Carslaw, D. R. Worsnop, M. J. Evans, G. W. Mann, Q. Zhang, M. R. Canagaratna, J. Allan, H. Coe, G. McFiggans, A. Rap and P. Forster, *Atmos. Chem. Phys.*, 2011, **11**, 12109-12136.
71. J. H. Seinfeld and S. N. Pandis, *Atmospheric Chemistry and Physics: From Air Pollution to Climate Change*, 3 edn., Wiley-Interscience, New York, 1998.
72. R. K. Pathak, A. A. Presto, T. E. Lane, C. O. Stanier, N. M. Donahue and S. N. Pandis, *Atmos. Chem. Phys.*, 2007, **7**, 3811-3821.
73. H. Saathoff, K. H. Naumann, O. Möhler, Å. M. Jonsson, M. Hallquist, A. Kiendler-Scharr, T. F. Mentel, R. Tillmann and U. Schurath, *Atmos. Chem. Phys.*, 2009, **9**, 1551-1577.
74. G. J. Engelhart, L. Hildebrandt, E. Kostenidou, N. Mihalopoulos, N. M. Donahue and S. N. Pandis, *Atmos. Chem. Phys.*, 2011, **11**, 911-920.

- 
75. N. L. Prisle, G. J. Engelhart, M. Bilde and N. M. Donahue, *Geophys. Res. Lett.*, 2010, **37**, L01802.
  76. Å. M. Jonsson, M. Hallquist and E. Ljungström, *Environ. Sci. Technol.*, 2006, **40**, 188-194.
  77. B. Bonn, G. Schuster and G. K. Moortgat, *J. Phys. Chem. A*, 2002, **106**, 2869-2881.
  78. A. C. Rohr, C. J. Weschler, P. Koutrakis and J. D. Spengler, *Aerosol Sci. Tech.*, 2003, **37**, 65-78.
  79. R. Winterhalter, P. Neeb, D. Grossmann, A. Kolloff, O. Horie and G. Moortgat, *J. Atmos. Chem.*, 2000, **35**, 165-197.
  80. R. Wegener, T. Brauers, R. Koppmann, S. Rodríguez Bares, F. Rohrer, R. Tillmann, A. Wahner, A. Hansel and A. Wisthaler, *J. Geophys. Res.-Atmos.*, 2007, **112**, n/a-n/a.
  81. C. O. Stanier, R. K. Pathak and S. N. Pandis, *Environ Sci Technol*, 2007, **41**, 2756-2763.
  82. Å. M. Jonsson, M. Hallquist and E. Ljungström, *Environ. Sci. Technol.*, 2008, **42**, 5938-5944.
  83. Y. Iinuma, O. Boge, Y. Miao, B. Sierau, T. Gnauk and H. Herrmann, *Faraday Discuss.*, 2005, **130**, 279-294.
  84. M. D. Keywood, J. H. Kroll, V. Varutbangkul, R. Bahreini, R. C. Flagan and J. H. Seinfeld, *Environ Sci Technol*, 2004, **38**, 3343-3350.
  85. K. S. Docherty and P. J. Ziemann, *Aerosol Sci. Technol.*, 2003, **37**, 877-891.
  86. Y. Ma, A. T. Russell and G. Marston, *Phys. Chem. Chem. Phys.*, 2008, **10**, 4294-4312.
  87. Y. Ma, R. A. Porter, D. Chappell, A. T. Russell and G. Marston, *Phys. Chem. Chem. Phys.*, 2009, **11**, 4184-4197.
  88. A. A. Presto, K. E. Huff Hartz and N. M. Donahue, *Environ. Sci. Technol.*, 2005, **39**, 7036-7045.
  89. G. Cao and M. Jang, *Atmos. Environ.*, 2007, **41**, 7603-7613.
  90. A. A. Presto, K. E. Huff Hartz and N. M. Donahue, *Environ. Sci. Technol.*, 2005, **39**, 7046-7054.
  91. J. H. Kroll, N. L. Ng, S. M. Murphy, R. C. Flagan and J. H. Seinfeld, *Environ. Sci. Technol.*, 2006, **40**, 1869-1877.
  92. K. S. Docherty, W. Wu, Y. B. Lim and P. J. Ziemann, *Environ. Sci. Technol.*, 2005, **39**, 4049-4059.



# Chapter 2

## Experimental

---

### 2.1 Apparatus Setup

Aerosol particles were produced through two different techniques in this work: the static chamber method, described in section 2.3.2, and the flow tube method, introduced in section 2.6. Subsequent analysis of SOA was performed using either a Scanning Mobility Particle Sizer (SMPS) instrument (section 2.4) or an Electrical Low Pressure Impactor (ELPI+) instrument (section 2.5).

The experimental approach used in this work combined these techniques in three ways. The typical approach employed the static chamber method of SOA production in tandem with the SMPS instrument. This approach is widespread within the literature.<sup>1-3</sup> The second linked the flow tube with the SMPS to allow for study of shorter reaction times. This approach has seen some use in the literature.<sup>4, 5</sup> The final approach involved use of the static chamber method in combination with the ELPI+ instrument. This again has seen some use in the literature.<sup>6</sup>

The apparatus used in this work is described by Figure 9, and is composed of a Pyrex vacuum line, a static sample chamber, and the SMPS instrument. As mentioned above, in some cases a flow tube may be used to supplement the work, and this is described in section 2.6.

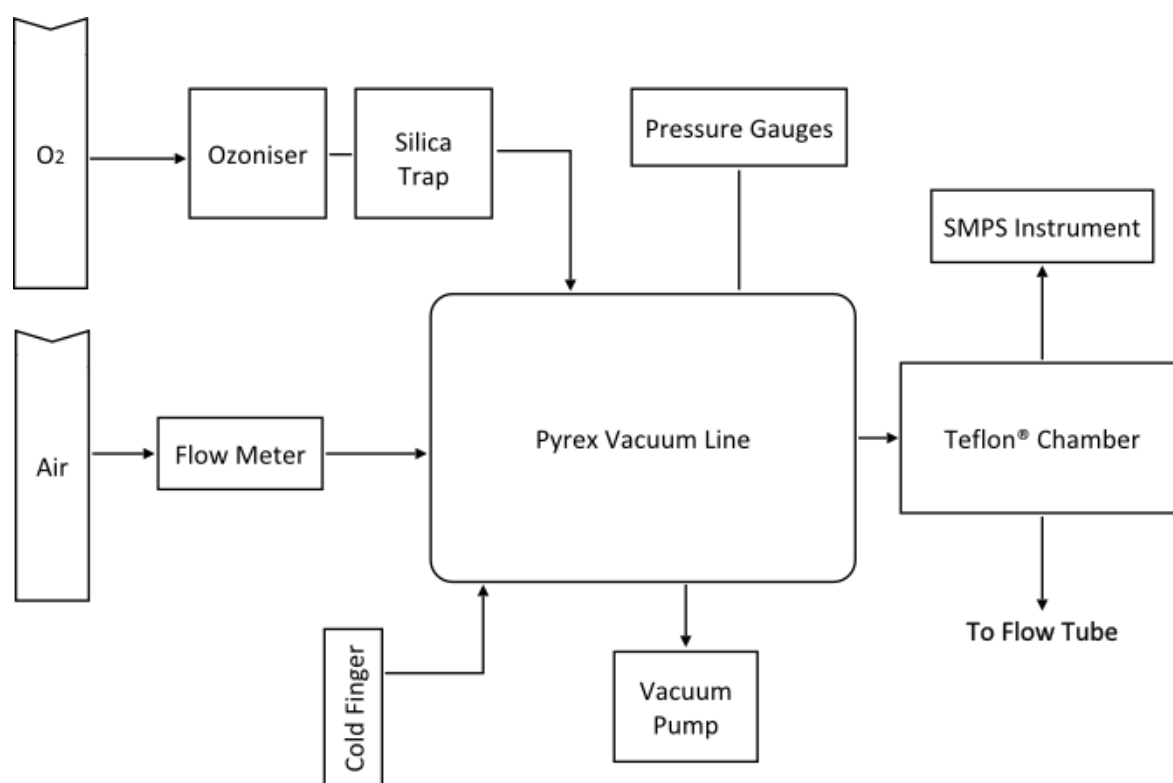


Figure 9: Schematic of the experimental setup

As shown in Figure 9, samples were prepared using a Pyrex vacuum line (“the rig”), connected to an Edwards rotary pump which allowed for pressures down to  $8 \times 10^{-3}$  Torr to be reached. A Leybold CM1000 Capacitron was used in tandem with a Leybold Thermovac 20 pressure gauge to allow for accurate measurement of pressures. A photograph of the rig is presented, along with a schematic, in Figure 10 and Figure 11.

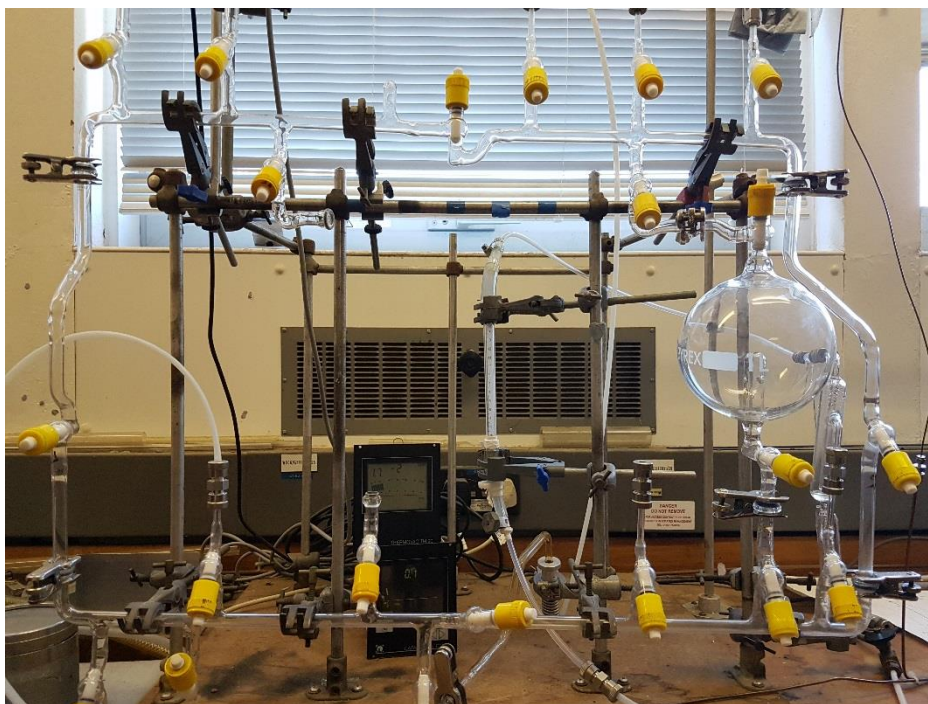


Figure 10: Vacuum line used for sample preparation

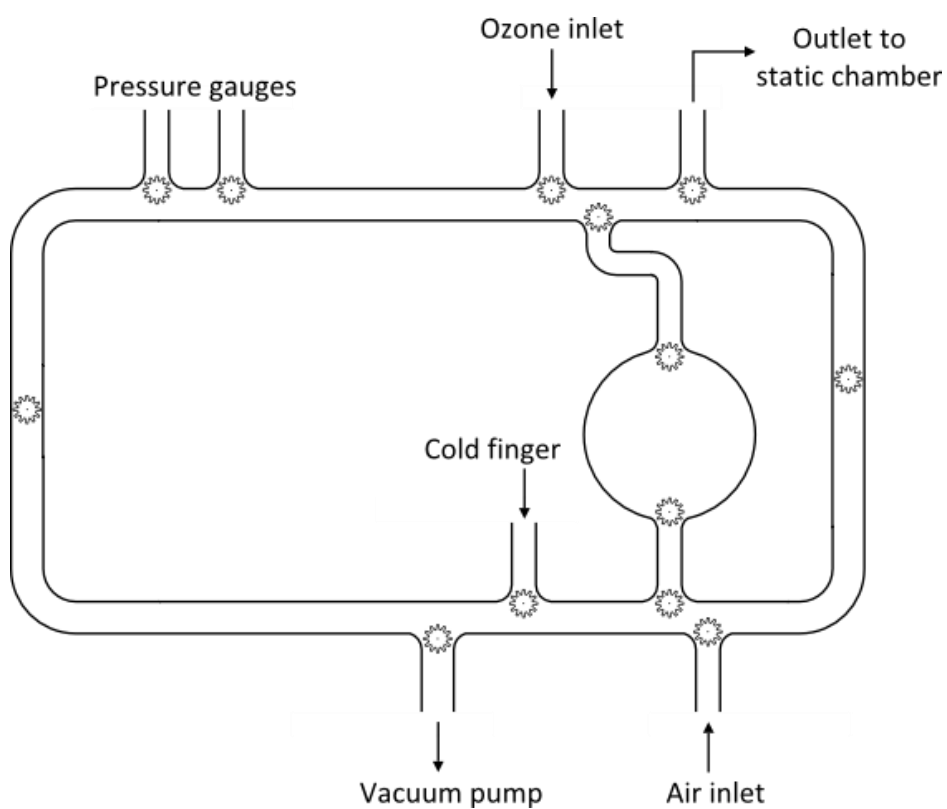


Figure 11: Schematic of vacuum line

Young's greaseless taps, represented by the cogs in Figure 11, allow for the isolation of different parts of the rig, enabling different sections to be evacuated or filled

independently of one another. The rig also houses a 1 L Pyrex bulb, where samples can be diluted prior to being admitted to the static chamber.

### 2.1.1 Sample Chamber

The sample chambers used in these experiments are 100 L capacity fluorinated ethylene propylene (FEP) ‘bags’, supplied by Adtech Polymer Engineering Ltd., equipped with a single  $\frac{1}{4}$ " PTFE connector. Both FEP and PTFE are fully fluorinated structures, resulting in non-reactive properties. They also boast low coefficients of friction, which help to reduce particles losses to the chamber walls during experimental work. The chamber is fully supported by a metal framework during experiments to minimise stress. The chamber itself is connected to the rig by a short length of  $\frac{1}{4}$ " PTFE tubing, and connections are secured at both ends by  $\frac{1}{4}$ " Swagelok® Ultra-Torr connectors. This setup is displayed in Figure 12.

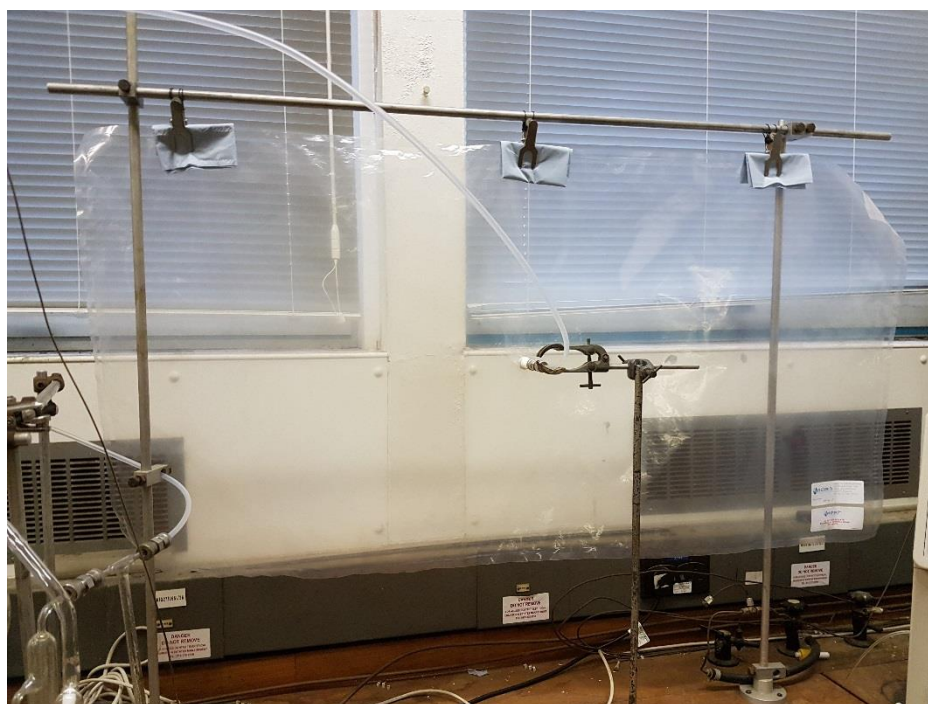


Figure 12: FEP Static Chamber

After completion of each experiment, the static chamber was thoroughly cleaned by purging with synthetic air—the chamber was filled, left for a few minutes, and then evacuated. This procedure was repeated at least three times, depending on the

concentrations of precursors used in the particular experiment. Tests of the resultant aerosol concentration after cleaning showed that this was sufficient to bring the total particle number concentration below  $100 \text{ cm}^{-3}$ , when filled with synthetic air to 67 L (the standard volume used throughout).

### 2.1.2 Ozonisers

Ozone was prepared by two different procedures. For time-resolved experiments performed in a static chamber, where the progress of the reaction was monitored over time as the reaction proceeded, ozone was prepared by use of an A2Z Model 20G Lab ozone generator. Oxygen was flowed through the ozone generator, where an electrical discharge was applied across it, producing ozone at purity ranging from 2–10 % in oxygen. A 'silica trap' was prepared by filling a glass trap with silica gel (Figure 13), and cooling this to  $-78^\circ\text{C}$  by immersion in an acetone-solid  $\text{CO}_2$  slurry. The oxygen-ozone mixture was flowed through the silica trap, and ozone adsorbed onto the silica. The flow was then directed across a Hopcalite<sup>®</sup> catalyst (supplied by Premier Chemicals Ltd.) at  $160^\circ\text{C}$ , ensuring destruction of any residual ozone.

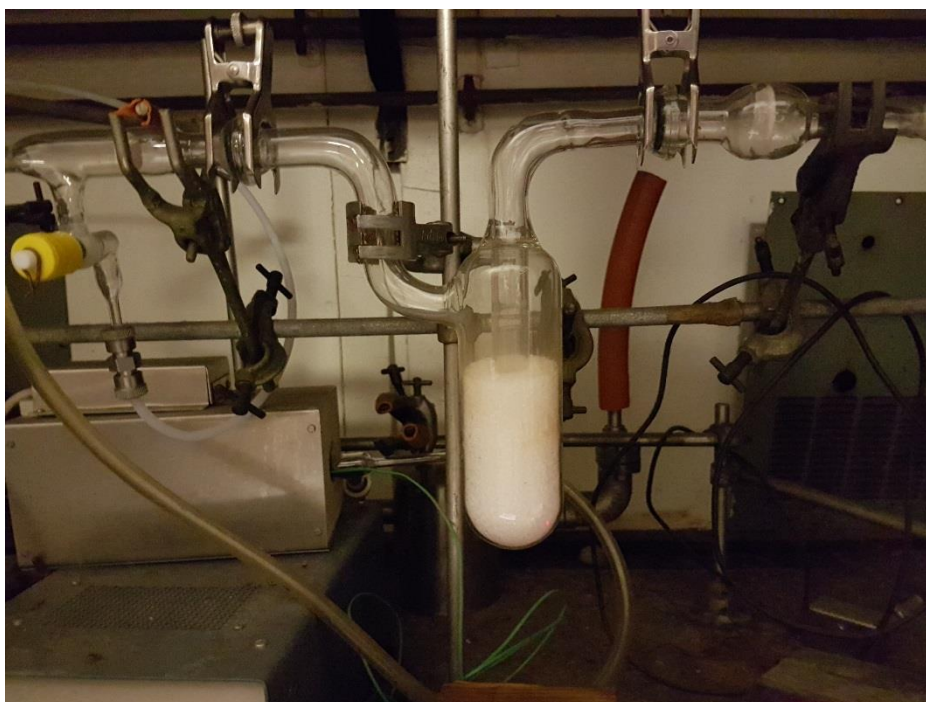


Figure 13: Silica trap used to store ozone



The second procedure for ozone preparation used a UVP SOG-1 model ozone generator. This was used for the flow tube experiments, rather than for those in the static chamber. The UVP ozone generator is equipped with a Pen-Ray® mercury discharge lamp, which provides a stable source of 185 nm radiation. Oxygen was simply flowed through the in-line UVP ozone generator, and exposure to the mercury lamp resulted in dissociation of  $O_2$ , and ultimately production of  $O_3$  at mixing ratios of approximately a few ppm.

### 2.1.3 Relative Humidity Control

Relative humidity in these experiments was controlled by the use of a triple-Dreschler bottle setup, as shown in Figure 14. Synthetic air flow directed through this setup achieved 100 % relative humidity (RH), and control of the overall humidity within the chamber was achieved by mixing air at 0 % and 100 % RH in the required volumes.



Figure 14: Triple-Dreschler bottle setup used to control RH

#### 2.1.4 Instrumentation

An SMPS instrument (Figure 15) was used to classify and quantify the aerosol produced. This is composed of two parts—the first, a TSI 3080 Differential Mobility Analyser (DMA), sorts the particles according to their Stokes equivalent diameter, defined as the diameter of a spherical particle of equivalent volume. The second, a TSI 3775 Condensation Particle Counter (CPC) counts the particles in each size category. The sample input, whether it be *via* a static chamber or flow tube, is connected to the SMPS via  $\frac{1}{4}$ " PTFE tubing, and a Swagelok® connector.



Figure 15: SMPS instrument comprising DMA (left) and CPC (right)

An atmospheric pressure flow tube was used for some experimental sets, enabling the study of aerosol formation in the early stages of a reaction. The flow tube consists of a 1 m length, 10 cm diameter glass tube, with 3 inlet ports at the rear—two equipped for  $\frac{1}{4}$ " tubing, and the other housing a sliding injector. The front of the tube has one port connected to a pump, and another with an available connection for the SMPS instrument. The centre of the tube is equipped with a Thermovac TM 101 Data Logger, providing a pressure readout. Flow rates were regulated by two MKS Type 1179A General Purpose Mass-Flo® Controllers and one MKS Type 179A All-Metal Mass-Flo® Meter.

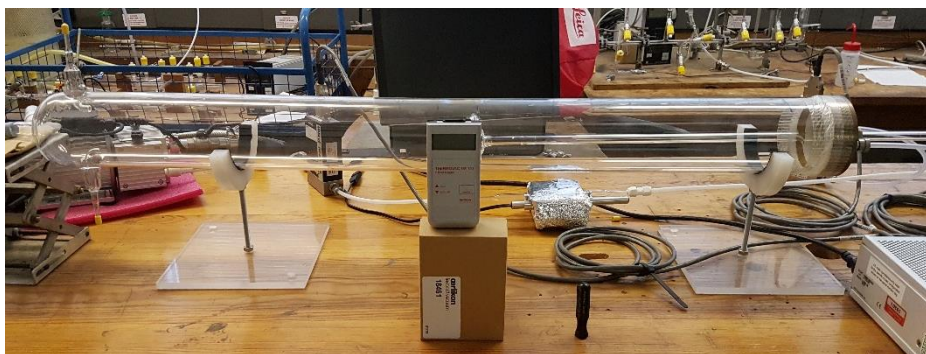


Figure 16: Flow tube showing inlets (right) and outlets (left)

## 2.2 Reagents

All chemicals used throughout this work were of high purity (Table 3) and from reputable sources.

Chemical	Supplier	Purity
$\alpha$ -Pinene	Aldrich	> 98 %
$\alpha$ -Terpinene	Sigma Aldrich	> 95 %
Cyclohexane	ACROS Organics	> 99.80 %
n-Butanol	Sigma Aldrich	> 99 %
Ethanol	Sigma Aldrich	> 99.5 %
Synthetic Air	Air Liquide	CO < 1 ppm, CO <sub>2</sub> < 0.1 ppm, NO <sub>x</sub> < 50 ppb, THC < 50 ppb, H <sub>2</sub> O < 0.5 ppm
Oxygen	Air Liquide	> 99.5 %
Dimethyl Sulfide	Sigma Aldrich	> 99 %
Methanol	Sigma Aldrich	> 99.8 %
NH <sub>4</sub> Cl	Sigma Aldrich	> 99.5 %
NaOMe	Sigma Aldrich	95 %
PCC	Aldrich	98 %
NaBH <sub>4</sub>	Aldrich	98 %
Methyltriphenyl-phosphonium Bromide	Aldrich	98 %

Table 3: Chemicals used in this work

Each liquid was stored in a glass ‘cold finger’ (Figure 17) and was thoroughly de-gassed before use by undergoing multiple freeze-pump-thaw cycles. Simply, the sample was



frozen using liquid N<sub>2</sub>, the headspace evacuated, and the sample then slowly warmed using a water bath (ca. 30 °C). Freeze-pump-thaw cycling was repeated until no gas was seen to bubble through during the warming process, and then for an additional four cycles.



Figure 17: Cold Finger used for storage of liquid samples

### 2.3 Experimental Procedure

All experiments undertaken in this work involved preparation of a mixture of the studied terpene and an  $\cdot\text{OH}$  scavenger within a PTFE chamber, filled to a known volume with synthetic air. Dependent on the type of experiment undertaken, ozone may either be added to the chamber to allow oxidation to occur *in situ*, or may be introduced to the terpene-scavenger mixture at a later point. Analysis of the resultant aerosol was carried out using either an SMPS or Electrical Low Pressure Impactor (ELPI+).

### 2.3.1 Scavengers

As described previously in section 1.7.3, scavengers are often employed in ozonolysis studies of SOA, to allow the reaction with O<sub>3</sub> to be isolated from that with OH. To this end, a scavenger was present for all reactions undertaken herein, such that ≥ 95 % of OH radicals were scavenged. Determining the minimum concentration needed requires a simple calculation, according to equation (13) below, taking into account the rate coefficients of the reactions of both the terpene and the scavenger with ·OH<sup>7</sup> (Table 4).

$$C_{scav.} = 19 \times \frac{k_{terpene,OH}}{k_{scavenger,OH}} \times C_{terpene} \quad (13)$$

where  $C$  is the mixing ratio (ppm) and  $k$  is the rate coefficient (cm<sup>3</sup> molecule<sup>-1</sup> s<sup>-1</sup>).

Scavenger	$k_{OH}$ (cm <sup>3</sup> molecule <sup>-1</sup> s <sup>-1</sup> )
Cyclohexane <sup>a</sup>	$6.97 \pm 1.20 \times 10^{-12}$
2-Butanol <sup>b</sup>	$18.7 \pm 0.15 \times 10^{-12}$
Ethanol <sup>b</sup>	$3.2 \pm 0.06 \times 10^{-12}$

Table 4: Rate constants for the reaction of OH with each scavenger used in this work. Rate constants are recommended values from: <sup>a</sup> IUPAC evaluation,<sup>8</sup> <sup>b</sup> Atkinson.<sup>9</sup>

In addition to inhibiting reactions between the terpene and OH, the use of a scavenger may also inhibit ageing of the aerosol<sup>10</sup> and affect product yields, as discussed in section 1.7.3. However, since it is necessary to use a scavenger in these reactions, this is an unavoidable side effect, but also one that cannot simply be ignored.

### 2.3.2 Static Chamber Preparation

For all experiments, samples were first prepared in the static chamber, according to the procedure: the sample-containing cold finger was attached to the rig *via* Swagelok® connector. The rig was evacuated, and the Young's tap leading to the pump closed. The cold finger was opened slightly to allow a small pressure ( $P_1$ ) of terpene into the rig. The 1 L bulb was isolated, and the remainder of the rig evacuated. The rig was filled with

synthetic air, and once the pressure equilibrated to atmospheric pressure ( $P_{atm}$ ), the 1 L bulb was opened, and this too was raised to atmospheric pressure. The bulb was closed, and the remainder of the rig evacuated. The pump was closed, and the 1 L bulb opened to allow the terpene-air mixture to equilibrate across the rig. The sample was then evacuated until the pressure was brought down to the desired value ( $P_2$ ). The bulb was isolated once again, and the rig remainder evacuated. To achieve very low concentrations, the procedure was simply repeated for one further dilution cycle.

To introduce the sample into the static chamber, the rig (excluding the isolated bulb) was filled with synthetic air. The two side-taps, as shown in Figure 11, were closed. This ensured that, once the bulb taps were opened, the only available path for the air flow would be through the bulb itself. The air flow was adjusted to the correct flow rate (see section 2.7 for calibration), and both taps on the bulb, as well as the tap to the static chamber were opened. The air inlet exhaust was blocked by a cork, causing a small pressure gradient between the rig and the static chamber, which forced the air flow through the bulb and into the chamber. After the desired time had passed, the cork was removed and the chamber tap closed.

The total chamber volume for *in situ* static chamber experiments was typically 67 L, and for flow tube experiments was 76 L. 67 L was easily sufficient to run the static chamber experiments for enough time to see the evolution of the aerosol, whilst being low enough to not put undue stress on the chamber. The volume was increased to 76 L for the flow tube experiments to maximise the amount of data collected. The required partial pressure of terpene in the bulb ( $P_{gas}$ ) to give the correct concentration in the PTFE chamber was determined by equation (14). The required pressure of the terpene-air mixture ( $P_2$ ) to give the correct partial pressure of terpene ( $P_{gas}$ ) was, in turn, calculated by equation (15):

$$P_{gas} = \frac{C \times P_{atm} \times V_{chamber}}{V_{bulb} \times 10^6} \quad (14)$$

$$P_2 = \frac{P_{gas} \times P_{atm}}{P_1} \quad (15)$$

where  $C$  is the required mixing ratio of terpene in the chamber (ppm),  $P_{gas}$  is the partial pressure of terpene required in the bulb (Torr),  $V_{bulb}$  is the volume of the mixing bulb (1 L),  $P_{atm}$  is atmospheric pressure (Torr),  $V_{chamber}$  is the chamber volume (L),  $P_1$  is the initial pressure of terpene (Torr) and  $P_2$  is the pressure of the terpene-air mixture (Torr).

In the same way, the scavenger was then introduced to the rig, diluted, and transferred to the chamber. The required mixing ratio of scavenger was determined by equation (13), as previously mentioned.

### 2.3.3 Ozone Concentration Calculations

For the static chamber experiments, ozonolysis of the reactive species was carried out within the chamber itself, and to do so required knowledge of the precise purity of ozone, since it is produced as a component within an  $O_2/O_3$  mixture.

To determine the concentration of ozone in oxygen, a procedure similar to that outlined in section 2.3.2 was followed, with the additional proviso that, when introducing the ozone sample to the 1 L bulb, it was also allowed into a 10 cm glass cell with  $CaF_2$  windows (supplied by Pike Technologies, shown in Figure 18).



Figure 18: Gas cell used to measure ozone purity

Introduction of the ozone to both the bulb and the cell at the same time ensured that the purity was constant across both. This purity was then determined by UV spectroscopy (using a Varian Cary 300 Bio UV-Visible Spectrophotometer), and manipulation of the Beer-Lambert Law:

$$Abs = \sigma cl = \ln(I_0/I) \quad (16)$$

where  $Abs$  is absorbance at 254 nm,  $\sigma$  is the absorption cross section of  $O_3$ ,  $c$  is concentration (molecules  $cm^{-3}$ ),  $l$  is path length (cm),  $I_0$  is initial intensity and  $I$  is final intensity.

By expressing this in  $\log_{10}$  rather than in natural logs, we get:

$$Abs_{10} = 2.303 \log_{10}(I_0/I) \quad (17)$$

Since concentration can be expressed in terms of moles per unit volume, we can use an arrangement of the Ideal Gas Law to say that:

$$C = n/V = P/RT \quad (18)$$

where  $C$  is concentration ( $\text{mol m}^{-3}$ ),  $n$  is number of moles of  $\text{O}_2/\text{O}_3$ ,  $V$  is volume of the glass cell,  $P$  is pressure (Pa),  $R$  is the ideal gas constant and  $T$  is temperature (K).

Since the Beer-Lambert Law uses units of cm and molecules, and the Ideal Gas Law uses m and moles, it is therefore necessary to convert the units in equation (18) to coincide with those in equation (17). We must also convert from Pascals to Torr, as the equipment used in these experiments gives readings in Torr. Therefore, we find:

$$C = \frac{N_A \times P \times 133.32}{10^6 \times RT}$$

$$C = \frac{6.022 \times 10^{23} \times 133.32 \times P}{10^6 \times 8.314 \times 298} = 3.234 \times 10^{16} \times P \quad (19)$$

where  $C$  is concentration ( $\text{molecule cm}^{-3}$ ),  $N_A$  is Avogadro's number and  $P$  is pressure (Torr).

If we denote ozone purity as  $f$ , the partial pressure of ozone is therefore its purity,  $f$ , multiplied by the pressure of the  $\text{O}_2/\text{O}_3$  mixture,  $P$ . We can therefore deduce that:

$$f = \frac{2.303 \times Abs_{10}}{\epsilon cl}$$

$$f = \frac{2.303 \times Abs_{10}}{1.15 \times 10^{-17} \times 3.234 \times 10^{16} \times P \times 10} = \frac{0.619 \times Abs_{10}}{P} \quad (20)$$

where  $f$  is  $\text{O}_3$  purity,  $Abs_{10}$  is absorbance,  $\epsilon$  is the absorption cross section of  $\text{O}_3$  ( $1.15 \times 10^{-17} \text{ cm}^2 \text{ molecule}^{-1}$ ),<sup>11</sup>  $c$  is concentration ( $\text{molecule cm}^{-3}$ ) and  $l$  is path length (cm).

Using equation (20), we can therefore determine the purity of ozone in the glass cell, which is equal to the purity of the ozone in the 1 L mixing bulb. Thus, we can control the final concentration of ozone in the chamber in the same way as for the terpene, but with the proviso that, instead of using pressure  $P_2$  as suggested by equation (12), we use  $P_2 \div f$ .

For example, if the result of equation (15) is that  $P_2 = 1.0$  Torr, and the purity of  $O_3$  was found to be 5.2 %, we must use  $1.0 \div 0.052 = 19.2$  Torr of diluted ozone to deliver the desired amount of ozone.

In the static chamber experiments, ozone was always blown into the chamber for a period of thirty seconds, and the reaction between the terpene and ozone was considered to have started as soon as the flow of ozone into the chamber was begun—this time is considered to be  $t_0$ . The static chamber was attached to the SMPS inlet port via  $\frac{1}{4}$ " PTFE tubing, and sampling began after 60 seconds reaction time.

## 2.4 SMPS Measurements

For the majority of experiments detailed herein, an SMPS instrument was used to describe the time evolution of the aerosol formed. The SMPS instrument itself is composed of two parts: a Differential Mobility Analyser (DMA) which classifies particles according to their size, and a Condensation Particle Counter (CPC) which quantifies the number of particles in each size category.

Upon introduction to the DMA, particles first enter a  $^{85}\text{Kr}$  Bipolar Charger. Here, they are exposed to a high concentration of bipolar ions and, through collisions between the particles and ions, quickly approach a state of charge equilibrium. This charge distribution has been well-defined experimentally by Wiedensohler,<sup>12</sup> the results of which agree well with the theoretical model produced by Fuchs.<sup>13</sup> The charge distribution used in the DMA data reduction (Figure 19) is an approximation of the Fuchs model, developed by Wiedensohler and Fissan,<sup>14</sup> which, in addition to accounting for ion-particle collisions, also includes a correction for the influence of free electrons. A small number of particles may experience a multiple charge, and this is accounted for within the distribution model.

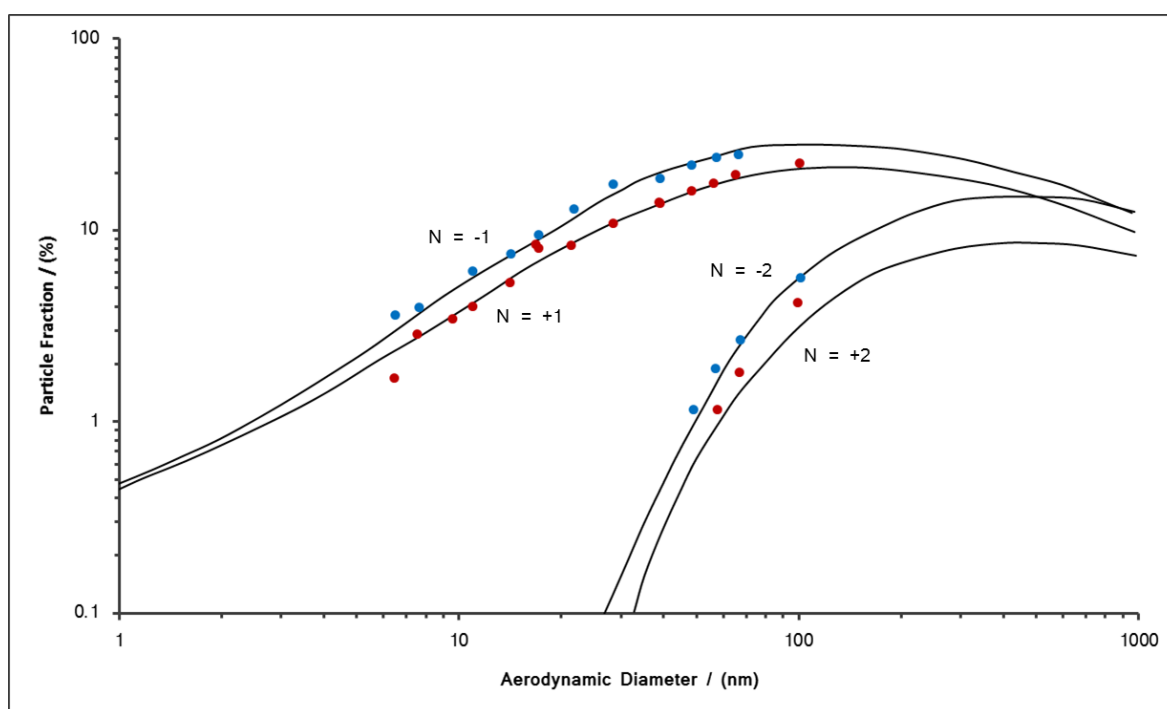


Figure 19: Bipolar particle charge distribution for air, showing the fraction of particles which receive a positive or negative charge. Lines represent theoretical curves; circles represent experimental data: red = positively charged particles, blue = negatively charged particles;  $N$  = charge. Adapted from Wiedensohler and Fissan.<sup>14</sup>

The polydisperse sample flows into the classifier where it is exposed to a strong electrical field, generated by a central high voltage rod, as depicted in Figure 20. The charged particles respond to this electrical field according to particle mobility theory. Only particles whose electrical mobility lies within a specific range, dictated by the voltage of the rod, may exit the DMA, and are collected in corresponding size categories. The remainder are discarded through the exhaust.



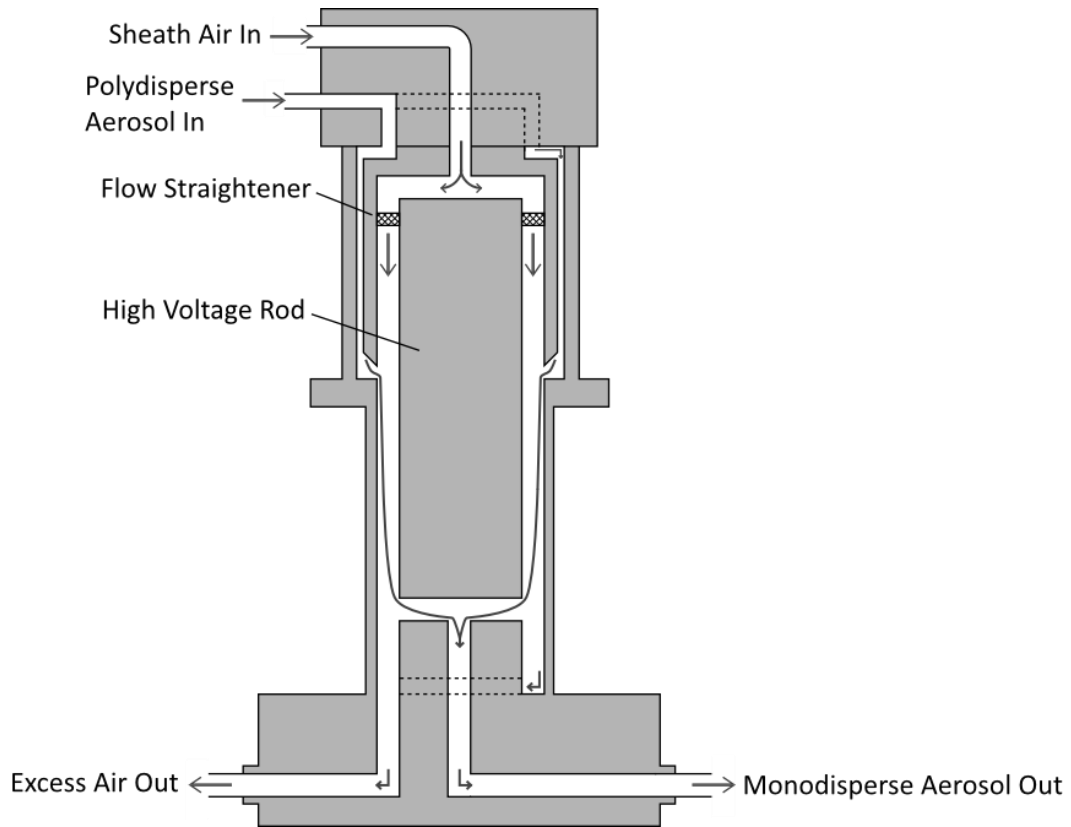


Figure 20: Schematic of electrostatic classifier (DMA), adapted from operating manual<sup>15</sup>

The now-monodisperse sample exits the DMA and enters the Condensation Particle Counter (CPC), where it is exposed to a super-saturated vapour of n-butanol. This condenses onto the surface of the aerosol particles, growing them to such a size that they may be detected by an optical particle counter. Thus, by scanning through a wide range of voltages in the DMA (0–10,000 V), particles may be sorted into size categories, and the number of particles in each category counted.

The aforementioned electrical mobility is defined as the ability of charged particles to move through an electrical field, and is inversely proportional to particle diameter:

$$Z_p = \frac{n e C_c}{3 \pi \eta D_p} \quad (21)$$

where  $Z_p$  is electrical mobility ( $\text{m}^2 \text{V}^{-1} \text{s}^{-1}$ ),  $n$  is number of elementary charges on a particle,  $e$  is elementary charge ( $1.6 \times 10^{-19} \text{ C}$ ),  $C_c$  is the Cunningham correction factor,  $\eta$  is the dynamic viscosity of air ( $\text{kg cm}^{-1} \text{s}^{-1}$ ) and  $D_p$  is Particle diameter (cm).

Thus, we may use electrical mobility as a proxy to sort particles according to their diameter.

Particle concentrations reported by the SMPS are corrected according to their charge distribution (Figure 19), and the reported concentrations are calculated for 100 % charger efficiency.

As shown in Figure 20, the DMA requires a sheath flow input in addition to the sample flow input. This sheath flow forces the sample flow to be correctly oriented parallel to the high voltage rod, and is maintained at 10× the flow rate of the sample. In the experiments recorded here, the sheath and sample flow rates were invariably 3.00 and 0.30 L min<sup>-1</sup> respectively.

In all experiments performed in this work, the SMPS setup was such that one scan through the full range of voltages takes 135 seconds, and allows for the classification of particles from 14–660 nm. A further 45 seconds is allowed after each scan for the voltage to normalise, resulting in data collected every three minutes.

Two corrections are applied to the data by the Aerosol Instrument Manager software. The first of these corrects for large, multiply charged particles, and was described earlier in this section. This generally only applies to particles > 100 nm, and thus has little impact on the data displayed here. The diffusion correction applies for small particles, and is of greater importance for the experiments undertaken in this work. Particle transport losses are size dependent, and are particularly significant for smaller particles. This correction accounts for losses within the SMPS instrument, as well as tubing connections.

Particle mass concentrations in the SMPS are calculated from the particle size distributions by first calculating particle volume, under the assumption that particles are spherical, and then converting this value into a mass concentration by multiplying by the aerosol density. Therefore, knowledge of the particle shape and density is important, since assumptions may introduce significant error. Zelenyuk *et al.*<sup>16</sup> investigated aerosol particles produced by ozonolysis of  $\alpha$ -pinene, both in absence and in presence of cyclohexane scavenger, and found the particles to be spherical in both cases. Abramson *et al.*,<sup>17</sup> in a separate study, investigated SOA particles formed by  $\alpha$ -pinene ozonolysis,

and found that particles formed by coagulation are spherical on relevant experimental timeframes. Zelenyuk *et al.*<sup>16</sup> also found the particles to have a density of approximately  $1.2 \text{ g cm}^{-3}$  in both cases.<sup>16</sup> This is in agreement with other laboratory studies, such as Saathoff *et al.*<sup>3</sup> ( $1.25 \text{ g cm}^{-3}$ ). Thus, for the results presented here, a density of  $1.2 \text{ g cm}^{-3}$  is assumed for calculation of all SOA mass profiles.

#### 2.4.1 Wall Loss Corrections

A large source of error in the static chamber experiments was due to wall loss of SOA; that is, SOA particles sticking to the walls of the Teflon® chamber, thus reducing the observed number and mass concentrations. To quantify this effect, static chamber experiments were undertaken according to the method described in section 2.3.2, with  $[\alpha\text{-pinene}] = 1 \text{ ppm}$  and  $[\text{O}_3] = 0.29 \text{ ppm}$ . Once the reaction had reached completion, plots were produced to determine  $k_L$ , the particle loss rate constant, with respect to both number and mass concentrations.

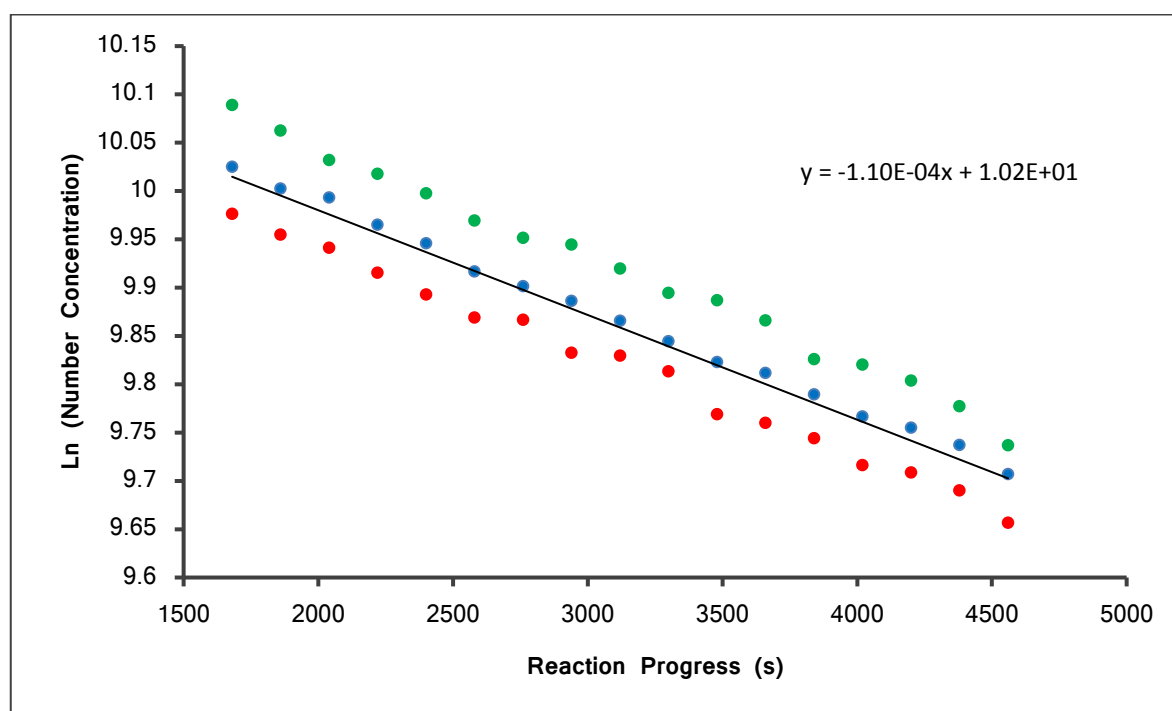


Figure 21: Ln(Number Concentration) vs. time. Gradient gives wall loss rate constant,  $k_L$  (#). Colours represent three separate experimental repeats.

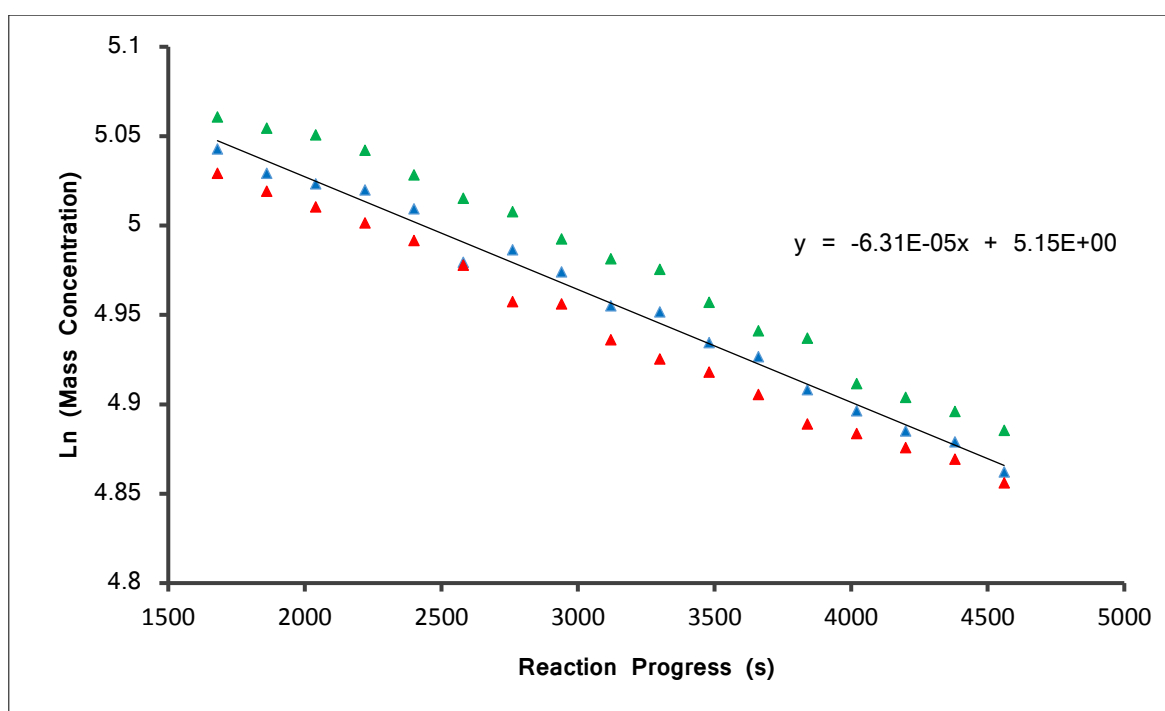


Figure 22: Ln(Mass Concentration) vs. time. Gradient gives wall loss rate constant,  $k_{L(m)}$ . Colours represent three separate experimental repeats.

Since wall loss is a first order decay process, the wall loss rate constants with respect to both mass and number concentrations can be determined simply from the gradients of these plots. Thus, particle loss rate constant with respect to number concentration,  $k_{L(\#)} = 1.10 \pm 0.03 \times 10^{-4} \text{ s}^{-1}$  and particle loss rate constant with respect to mass concentration,  $k_{L(m)} = 6.31 \pm 0.14 \times 10^{-5} \text{ s}^{-1}$ .

However, it is important to note that, while we do calculate wall loss as a constant across all particle diameters measured, this is simply an average of the wall losses experienced across these diameters. Furthermore, our calculation of wall loss has made the assumption that the reaction between  $\alpha$ -pinene and ozone has reached completion. While this is a safe assumption, the system is not stagnant after this point, since we have not accounted for the coagulation of smaller particles to form larger ones, and condensation of vapours onto smaller particles to grow them into larger size categories. While this coagulation would have no impact on  $k_{L(m)}$ , since coagulation of particles would be expected to conserve the mass of those particles involved, it may impact on  $k_{L(\#)}$ , since coagulation of a number of particles into one will reduce the number of particles in the system, whilst no loss of particles to the walls has taken place.

To observe the coagulation / condensation effect, we may calculate  $k_L$ , the particle loss rate constant, as a function of particle size. This is calculated with respect to particle number concentration, and is a measure of all particle losses combined—including both wall and coagulation losses. Whilst it is also possible to calculate the particle loss rate constant with respect to mass concentration, these values are not significant within the scope of this work, since particle mass concentration is a function of size, density and number concentration. Since density is constant, and we are regulating particle size according to the size categories (see section 2.4), mass concentration will be directly proportional to number concentration. Thus,  $k_L$  is displayed in Figure 23 as a function of mean particle diameter:

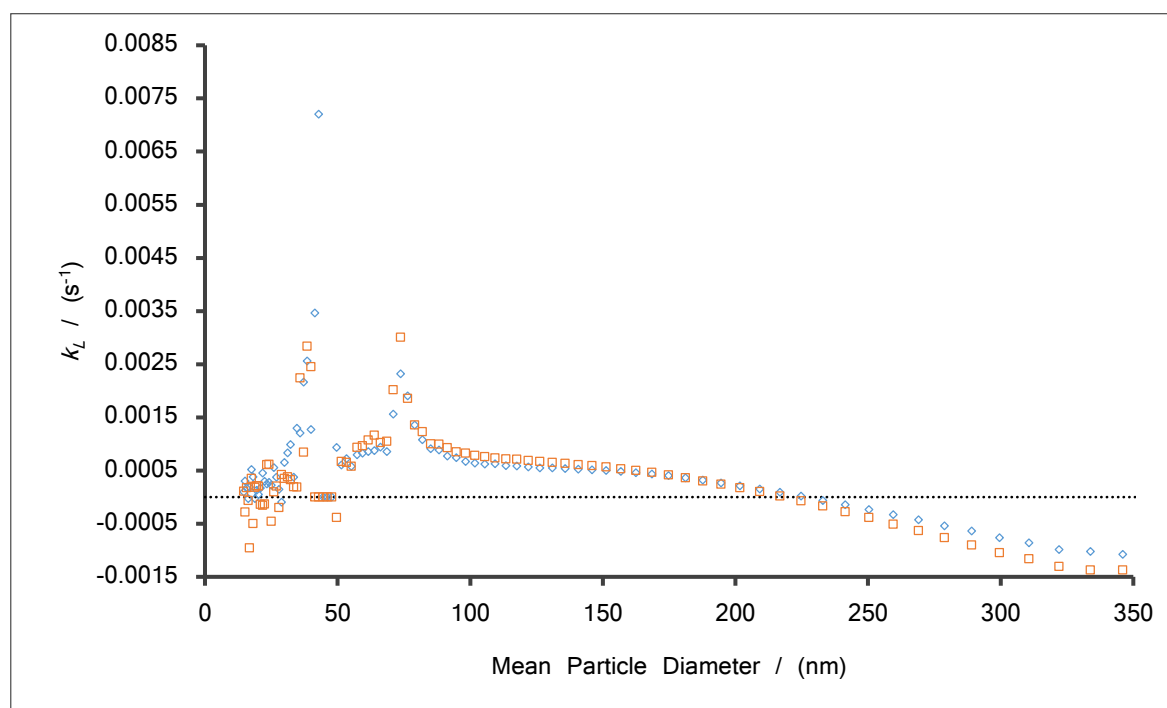


Figure 23: Wall loss and coagulation rate constant relative to number concentration, as a function of particle diameter. Red and blue data points refer to two separate repeats.

Interestingly, as shown in Figure 23,  $k_L$  takes both positive and negative values when plotted as a function of particle diameter. As expected, lower mean particle diameters have higher values of  $k_L$ , as the loss of these particles has contributions from both wall loss and coagulation into larger particles. Conversely, higher mean particle diameters show negative values of  $k_L$ , meaning that their formation via coagulation of smaller

particles, and condensation of low-volatility vapours onto smaller particles, outstrips the loss of these larger diameter particles to walls.

Clearly, the plot displayed in Figure 23 does show a number of peculiarities, and these are addressed below.

The first of these is the particularly noisy region below approximately 35 nm, and above the instrument cut-off diameter of 14.6 nm. After 60 seconds reaction time, some products, on the order of magnitude  $10^3$  particles  $\text{cm}^{-3}$ , are observed in this region, and these persist in the same order of magnitude until 240 seconds. However, by 420 seconds, the number of particles observed has fallen by an order of magnitude to  $< 100 \text{ cm}^{-3}$ . Some background noise then persists throughout the remainder of our data collection period, and this varies, though never rises above 100 particles  $\text{cm}^{-3}$ . This variation in background noise leads to a wide variation in  $\ln(\text{number concentration})$ , and thus causes the wide variation in the values of  $k_L$  observed in Figure 23. Therefore, since the experiments undertaken here do not produce aerosol particles of this size in significant concentrations, and those that are produced have very short lifetimes before aggregating into larger particles, we can disregard this region entirely.

This conclusion is further reinforced by the region at 40–50 nm, where we frequently note a  $k_L$  value of  $0 \text{ s}^{-1}$ . This is because those particles which cause the background noise observed over the lower diameter results are of insufficient size to be collected in the 40–50 nm range, and the aerosol produced by our reaction is of too large a size to be collected in this region. Thus, we see no particles collected, and the rate constant is indeterminate.

The final peculiarity observed is the peak at 73.7 nm. This appears to be due to some anomaly in the collection of particles in the 4 size categories in the range of 71–79.1 nm. In general, the number concentration of particles collected in each of these bins is not dissimilar to those which lie on either side of the range, until reaction progress reaches 1140 s. After this time, the number of particles collected in these size bins decreases at a faster rate than those which lie on either side (thus resulting in a larger  $k_L$  value). However, the concentration of particles collected in this region after 1140 s reaction

progress is again below  $10^3$  particles  $\text{cm}^{-3}$ , suggesting that the variation in number concentration is insignificant, and serves only to distort the  $k_L$  value. Alternatively, everything below this size may be anomalous due to low signal, and we may expect very high loss rates at small diameters.

A new plot was therefore produced, as shown in Figure 24, seeking to rectify these peculiarities. For the size bins from 71–79.1 nm,  $k_L$  was therefore recalculated, excluding the data collected after 1140 s. The region where mean particle diameter < 50 nm was also excluded for clarity, since no aerosol was observed in this region.

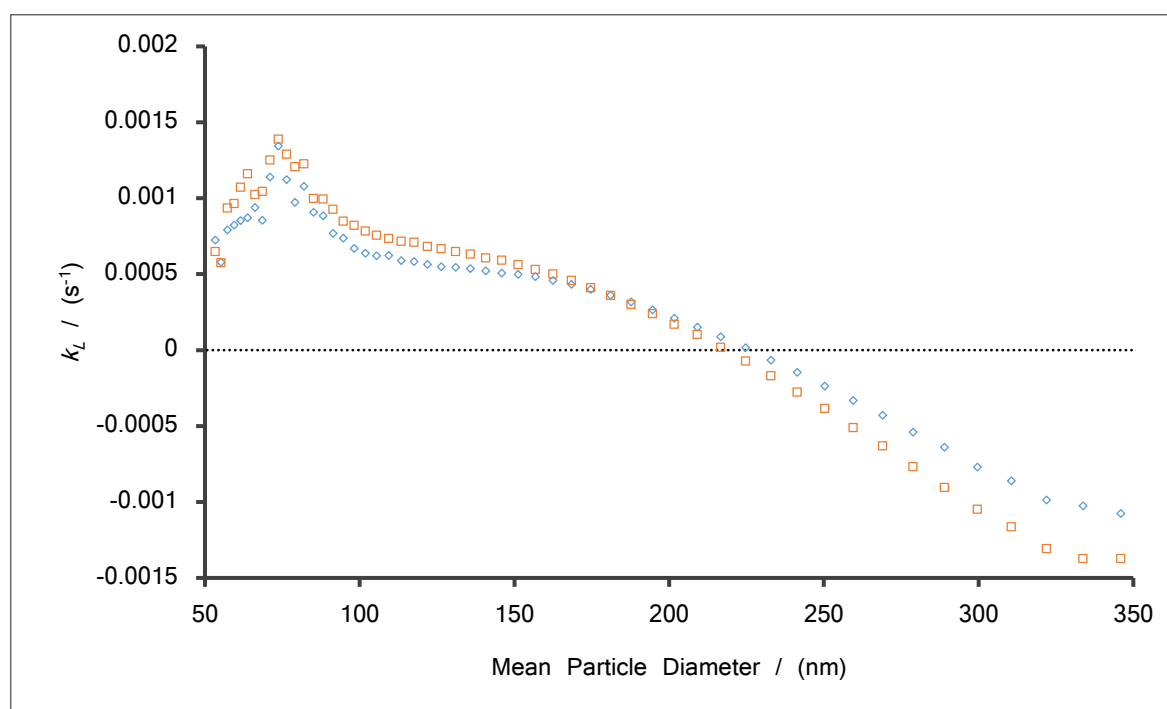


Figure 24: Refined wall loss and coagulation rate constant relative to number concentration, as a function of particle diameter, including a correction for the region 71–79.1 nm. Red and blue data points refer to two separate repeats.

The values calculated for the diameter-specific  $k_L$  are not useful when correcting mass concentrations for the purpose of finding the mass yield, since the system-wide value of  $k_{L(m)}$  is appropriate for this. It is, however, an interesting way of observing the coagulation of the SOA. The large variation observed in  $k_L$  values across the range of particle diameters makes it clear that applying a wall loss correction to number concentrations is inappropriate. Since it is not possible to distinguish particles lost to the walls from particles lost to coagulation, an accurate value for the wall loss rate constant with respect

to number concentration is unobtainable. A wall loss correction for mass concentration is still relevant and accurate, since we may expect particle mass to be conserved throughout any particle coagulation, and any loss of mass may be safely attributed to wall loss. Thus, the particle loss rate constant for mass concentration,  $k_{L(m)}$ , can be said to be equivalent to the wall loss rate constant for mass concentration,  $k_{w(m, SC)} = 6.31 \pm 0.14 \times 10^{-5} \text{ s}^{-1}$ . This is on the same order of magnitude as the wall loss rate constant obtained by I. Hoare,<sup>7</sup> a previous Ph.D. student within the University of Reading atmospheric laboratory ( $9.69 \times 10^{-5} \text{ s}^{-1}$ ; no errors reported). Due to differences in the Teflon® chambers used, a more direct comparison of absolute values would not be appropriate.

While it is not possible to distinguish wall losses from coagulation losses using the data in Figure 24, it is also not possible to conclude that size dependence is not a factor. That is,  $k_w$  may or may not be affected by particle diameter. Therefore, it seems reasonable to assume that there may be a dependence, and thus recognise that we may need to recalculate our system-wide  $k_w$  for each set of conditions investigated. This is because the use of different conditions may produce aerosol particles of very different diameters, and thus their tendency to be lost to walls may also differ.

Nomura *et al.*<sup>18</sup> studied, in detail, deposition losses of particles within a chamber, and the variation of such deposition with varying particle diameter and ventilation rate. Absolute values of a wall loss (or deposition) rate constant depend on the nature of the particle, flow characteristics inside the chamber, and the nature of the chamber walls.<sup>18</sup> However, the typical trend is a positive linear correlation between deposition coefficient and ventilation rate. Nomura *et al.*<sup>18</sup> noted a negative correlation between particle diameter and deposition coefficient across the range of particle diameters studied in this work, indicating that a higher wall loss rate constant would be expected at lower particle diameters. This is in agreement with the trend observed here, suggesting that the chamber is behaving in the expected manner. Indeed, the trend observed by Nomura *et al.* reverses at approximately 400–500 nm, which may explain the increasing gradient observed in Figure 24 between 300–350 nm. However, since the particles studied in this work are typically considerably below this diameter, this should not impact the data presented here.



Particle mass concentrations may be corrected wall loss according to equation (22):

$$\text{mass}_{\text{corr}} = \text{mass}_{\text{raw}} \cdot e^{t \cdot k_w(m, sc)} \quad (22)$$

where  $\text{mass}_{\text{corr}}$  corresponds to particle mass concentration corrected for wall loss ( $\mu\text{g m}^{-3}$ ),  $\text{mass}_{\text{raw}}$  is the raw particle mass concentration ( $\mu\text{g m}^{-3}$ ),  $t$  is time (s) and  $k_w(m, sc)$  corresponds to the wall loss rate constant for mass ( $\text{s}^{-1}$ ).

## 2.5 ELPI+

The Electrical Low Pressure Impactor (ELPI+) is a type of cascade impactor which allows for the size classification and quantification of aerosol samples, in a similar fashion to the SMPS, albeit with a worse size resolution. The ELPI+ is, however, able to characterise a wider aerosol size range and may be used at higher flow rates than the SMPS. Due to the characteristics of the instrument, whereby particles have a tendency to behave differently dependent on their physical state, it is now being employed in studies to determine the physical state of those aerosol particles.<sup>6</sup>



Figure 25: ELPI+ apparatus (left) and impactor stages (right)

Aerosol samples are first introduced to the ELPI+ via non-conductive tubing, where particles are exposed to a corona charger which generates small, positively charged ions through corona discharge.<sup>19</sup> The ELPI+ uses a unipolar corona, whereby an electrode at

high potential induces an electrical discharge into the surrounding fluid—in this case, air. Unipolar coronas in particular have very confined ionisation regions, so only those particles surrounding the corona are charged.<sup>20</sup> The ions produced via this process then transfer charge to the aerosol particles.

The aerosol flow is directed through a cascade impactor, which consists of 15 stages stacked above one another. A schematic of impactor plates and their operating principle is given in Figure 26. Each impactor stage has two plates—the jet plate on top, and the collection plate below. The aerosol flow passes through nozzles in the jet plate at high speed, which straightens the aerosol flow. It then makes a sharp turn to flow around the collection plate. Particles above a set diameter are unable to negotiate the sharp turn, and instead impact on the collection plate. The nozzle diameter and plate-to-plate distance decrease on each consecutive stage, changing the cut-off diameter, and allowing particles to be sorted by size.

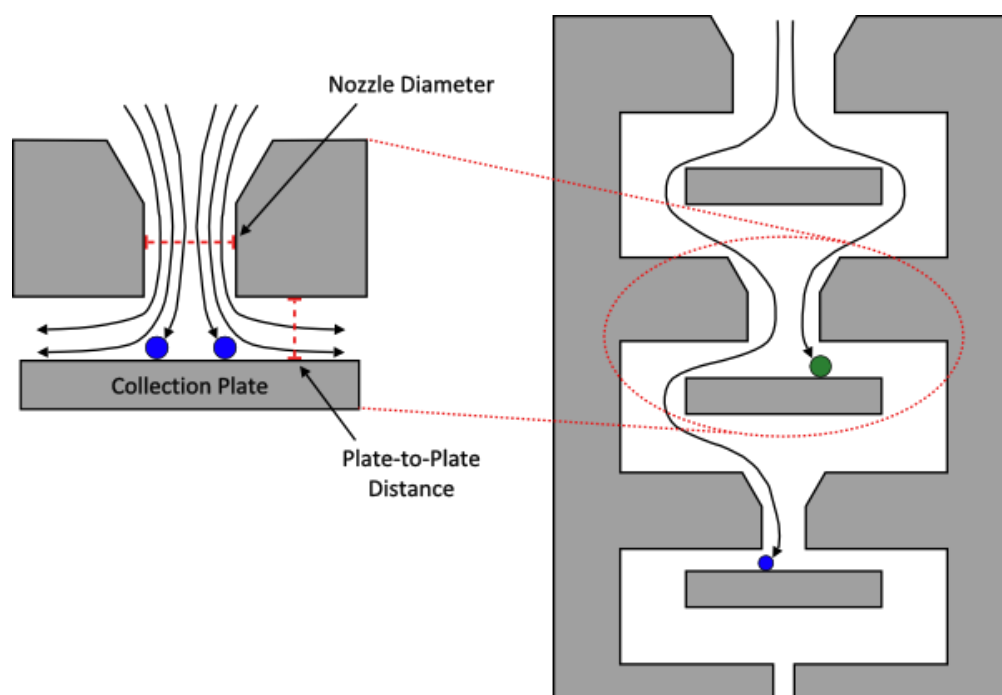


Figure 26: Schematic of ELPI+, adapted from operating manual<sup>21</sup>

Each impactor stage is connected to an electrometer, which measures the current passed by the particles impacting on each stage. The current is proportional to the number of particles, and so the number of particles in each size category can therefore be

calculated. The ELPI+ operates at a flow rate of  $10 \text{ L min}^{-1}$ , and due to this high flow velocity, some particles may impact on one stage, bounce, and be collected on a lower stage, causing an artificial inflation of the current observed on the lower stage. By these means, the number of smaller particles may be overrepresented by the results, and vice versa for larger particles.

Each ELPI+ collection plate is covered with a thin aluminium foil on which particles are collected (non-greased impactor plates). By replacing this foil with another, greased foil, particle bounce may be minimised as particles adhere more readily to the oil surface than to the aluminium surface (Figure 27). However, when working with high number concentrations, the greased plates may become saturated with particles and thus particle bounce will continue to be observed.<sup>19</sup> A solution to this is to use sintered plates, which are composed of porous metal filled with vacuum oil. When particles impact on this surface, the oil seeps up, allowing any further particles to also impact on a liquid surface and thus 'stick' to the plate more effectively. These plates effectively eliminate any particle bounce in higher number concentrations.

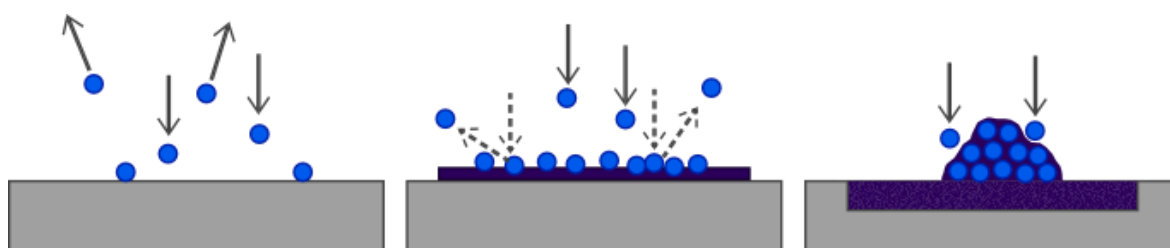


Figure 27: Visual representation of different ELPI+ impactor plates. From the left: non-greased Al plates; greased Al plates; sintered plates. Adapted from Dekati Ltd.<sup>19</sup>

When a particle impacts onto a plate, some of its energy will be lost, whilst the rest will be retained as kinetic energy. If the particle's kinetic energy after impactation is greater than the adhesion energy threshold, the particle will bounce. A larger proportion of harder materials will bounce in comparison to softer materials.<sup>22</sup> Higher relative humidity may also decrease the likelihood of a particle bouncing.<sup>23</sup>

By comparing data collected using non-greased, aluminium plates with data collected using the SMPS under identical conditions, it is possible to determine what fraction of the particles have bounced, and thus determine their 'bounce factor':

$$\text{Bounce Factor} = \frac{\sum I_{\leq 27 \text{ nm}} - \sum I_{\leq 27 \text{ nm}}^{id}}{\sum I_{> 27 \text{ nm}}^{id}} \quad (23)$$

where  $I_{\leq 27 \text{ nm}}$  is the observed current for particles  $\leq 27 \text{ nm}$  (fA),  $I_{\leq 27 \text{ nm}}^{id}$  is ideal current for particles  $\leq 27 \text{ nm}$  (fA) and  $I_{> 27 \text{ nm}}^{id}$  is ideal current for particles  $> 27 \text{ nm}$  (fA).

Therefore, a larger bounce factor implies a larger proportion of the particles bouncing, and thus a more solid-like particle.

The general approach to determine ideal current (the current that would be passed in a system with 100 % charger and collection efficiency) in the literature is to compare particle distribution data from the ELPI+ to equivalent data from the SMPS.<sup>6, 24</sup> However, due to inefficiencies in the ELPI+ technique, corrections for charging efficiencies are required to ensure that the data are comparable. This requires a great deal of calibration specific to the individual ELPI+ instrument. The ELPI+ instrument used in this work was only available due to the kind provision of an instrument from Dekati Ltd. for a trial period, and thus time was limited. Therefore, the decision was made to forego this approach, and instead use a new approach—the implementation of sintered impactor substrates to simulate ideal conditions.

The conversion between SMPS and ELPI+ data usually requires a correction for charger efficiency—a 2-part power function dependent on particle size, allowing the SMPS data to be converted to a current for ease of comparison. However, since the same charger is used under identical conditions for all experiments carried out using the ELPI+, charger efficiency should remain constant for each particle size. Thus, by comparing two sets of ELPI+ data, the need for a charger efficiency correction is removed.

As mentioned previously, the use of different impactor substrates allows for the control of particle bounce. The marked difference between the three substrates is evidenced by Figure 28, the results of which will be discussed in chapter 3.

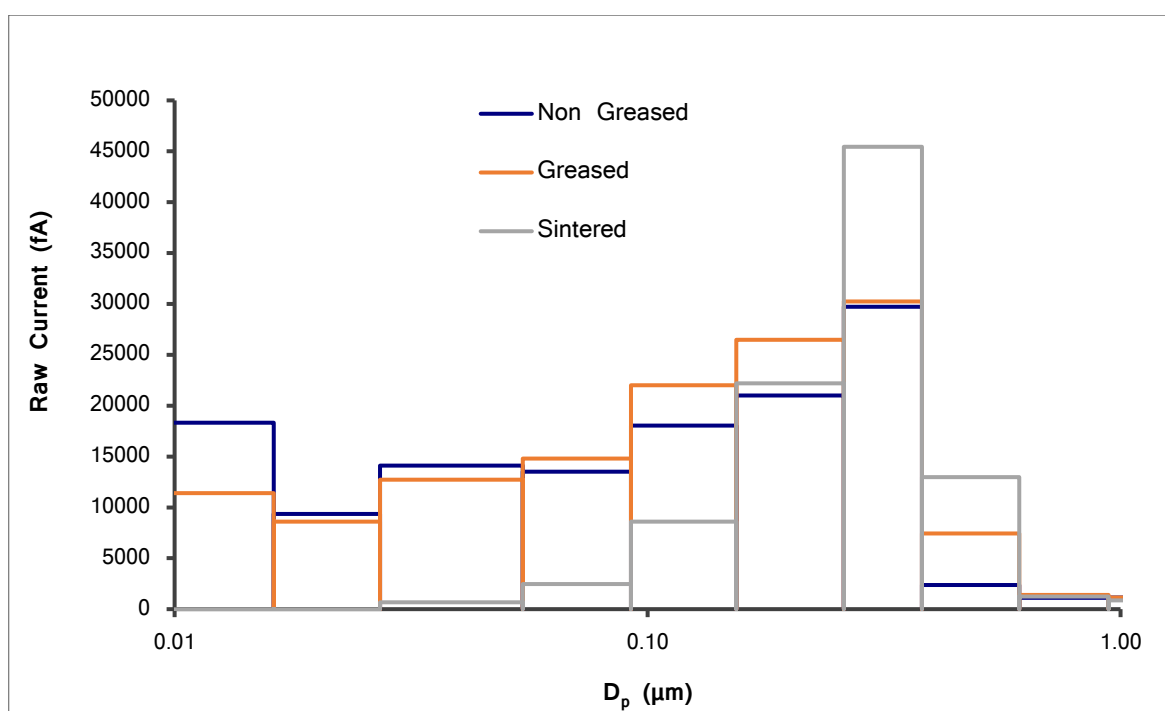


Figure 28: Effect of impactor substrates on particle size distribution (see section 3.8 for full size range)

The difference between non-greased and greased plates, while clearly visible, is not nearly so pronounced as the difference between non-greased and sintered plates. When using non-greased plates, the first three collection plates (corresponding to the three smallest particle size categories) collected 18,300, 9,400 and 14,100 fA respectively. For comparison, sintered plates collected < 100 fA in each of the first two size categories (within background variation), and 700 fA in the third. This reduction of ca. 100 % of particles in the first two categories, as well as 95 % in the third, suggests that the sintered plates are extremely effective in reducing particle bounce. While it is unlikely that substituting non-greased plates for sintered eliminates all particle bounce, there is certainly compelling evidence that it greatly reduces the proportion that bounce on impact. Thus,  $I_{\text{sintered}}$  is assumed to be equivalent to  $I^{\text{id}}$  for the calculations herein.

For experimental sets using the ELPI+, the instrument was first zeroed a minimum of three times by sampling synthetic air until a constant background current of < 100 fA was observed. Samples were prepared using the static chamber method described in section 2.3.2, to give a mixture of terpene and scavenger. Ozone was prepared as described in section 2.3.3, and blown into the chamber for 30 seconds at time,  $t_0$ . The reaction was

considered to have begun as soon as the ozone began to flow into the chamber. The chamber was attached to the ELPI+ instrument via the sample inlet port, with a sample flow of  $10 \text{ L min}^{-1}$ . Analysis of aerosol products began 9 minutes after  $t_0$ , and was halted after a further 6 minutes. Due to the high flow rate required by the instrument, longer sampling times were not feasible.

## 2.6 Flow Tube

Since the SMPS is limited by its ability to scan once every 3 minutes under this setup, another method was required to allow for the study of the early stages of ozonolysis, particularly for fast reactions. For this purpose, an atmospheric flow tube was used—briefly, this allows for the study of specific times during the aerosol's growth, giving a clearer picture of particle nucleation and their initial evolution.

The basic theory behind the atmospheric flow tube is that, by allowing one reactant to enter via the rear of the tube, and the other through a moveable sliding injector, we can access specific timeframes during the aerosol's evolution. Therefore, we may express time as a function of the distance,  $d$ , indicated in Figure 29.

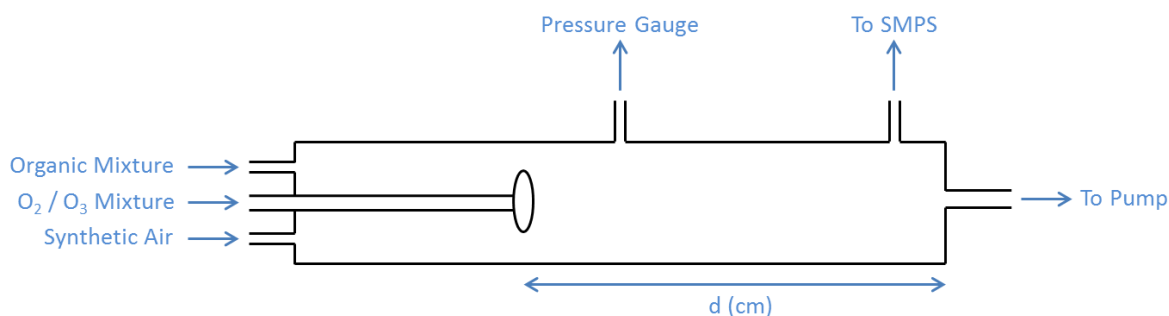


Figure 29: Schematic of flow tube setup

In these experiments, the total flow of all components through the flow tube was  $2 \text{ L min}^{-1}$  unless otherwise stated. The internal diameter of the flow tube was  $10 \text{ cm}$ , so its cross-sectional area could be calculated:

$$\text{Cross – sectional Area} = \pi r^2 = 25\pi \text{ cm}^2 \quad (24)$$

The velocity of the gas flow can therefore be calculated:

$$\text{Velocity} = \frac{\text{Flow}}{\text{Cross – sec Area}} = \frac{2000}{25\pi} = 25.46 \text{ cm min}^{-1} \quad (25)$$

Thus, the relationship between time and distance may be expressed:

$$t = \frac{d}{\text{Flow Velocity}} \quad (26)$$

where  $t$  is time (min),  $d$  is distance from adjustable injector head to end of flow tube (cm) and flow velocity is  $25.46 \text{ cm min}^{-1}$  for a system with total flow volume  $2 \text{ L min}^{-1}$ .

So, by adjusting the position of the injector within the flow tube, it was possible to study multiple specific points during the aerosol's evolution, for each particular sample. The main advantage of this method over the static chamber method was that it allowed better time resolution between results—the time resolution for the static chamber experiments was 3 minutes between data, whereas in this system the time resolution is effectively zero.

There are two distinct types of flow which may exist within a system such as this flow tube: laminar flow and turbulent flow. Laminar flow is described by a system in which there is little to no lateral movement. The species instead tend to move as layers which slide past each other with little interaction. Species at the edges of the tube have lower velocities than those toward the centre, due to frictional interaction with the tube surface. Turbulent flow describes a system in which the flows are irregular, and mixing of the species is therefore encouraged. The distinction between these two flow types can be quantified by introduction of the Reynolds number. A low Reynolds number is characteristic of a laminar flow system, and a high value characteristic of turbulent flow. It has been suggested that for a straight tube such as this one with a circular cross-section, a Reynolds number of 2040 provides a fairly sudden change from laminar flow to

a persistently turbulent flow.<sup>25</sup> This does not suggest that there is no turbulent motion in systems with a lower Reynolds number, but that turbulent motion observed in these systems is transient, and that the flow in these systems is predominantly laminar. It is possible to calculate the Reynolds number for this system using the equation:

$$R_e = \frac{Q D_H}{A v} \quad (27)$$

where  $R_e$  is the Reynolds number,  $Q$  is flow volume ( $\text{cm}^3 \text{s}^{-1}$ ),  $D_H$  is hydraulic diameter (cm),  $A$  is cross-sectional area ( $\text{cm}^2$ ) and  $v$  is kinematic viscosity ( $\text{cm}^2 \text{s}^{-1}$ ).

Hydraulic diameter is defined as four times the cross sectional area divided by the perimeter of the cross-section. For a system with circular cross-section, this is therefore equal to diameter. Kinematic viscosity of air at  $20^\circ\text{C} = 15.11 \times 10^{-2} \text{ cm}^2 \text{s}^{-1}$ .

The Reynolds number for this system can therefore be calculated:

$$R_e = \frac{\frac{2000}{60} \times 10}{\pi \times 5^2 \times 15.11 \times 10^{-2}} \quad (28)$$

$$R_e = 28.10$$

The Reynolds number for this system is thus 28.10, far below the critical value of 2040, and therefore the system can be identified as having laminar flow. This is the preferred flow characteristic for this flow tube, since turbulent flow will result in random motion of species, and thus an inaccurate measure of time spent in the flow tube.

There are some limitations to the flow tube technique, arising from diffusion and flow characteristics. Upon mixing of two gases, it takes a certain distance, calculated by equation (29), for laminar flow conditions to be established.<sup>26</sup> For this flow tube, with a standard flow rate of  $2 \text{ L min}^{-1}$  and Reynolds number of 28.10, this distance is approximately 14 cm.

$$d \approx 0.05 \times D \times R_e \quad (29)$$

where  $d$  is distance (cm),  $D$  is diameter (cm) and  $R_e$  is the Reynolds number.



The injector head used in this flow tube is not a single-point injection, but instead incorporates 16 injection points into a flattened glass head. The glass head has a diameter of approximately 6 cm, and the distance from the outermost injection point to the wall of the flow tube is approximately 3 cm (see Figure 30). Thus, we can calculate a minimum distance to establish laminar flow conditions using equation (29), substituting diameter for twice the distance to the wall, 6 cm. This gives a minimum distance of 8.5 cm.



Figure 30: Multi-port injection head inside the flow tube

It also takes a short period of time before the gaseous species are homogeneously mixed. This can be calculated by equation (30):

$$t_{mix} = \frac{r^2}{5 \times \varphi} \quad (30)$$

where  $t_{mix}$  is time taken to form a homogeneous mixture (s),  $r$  is radius (cm) and  $\varphi$  is diffusion coefficient in air ( $\text{cm}^2 \text{s}^{-1}$ ).

Mixing time for ozone,  $\varphi = 0.137 \text{ cm}^2 \text{s}^{-1}$  in air,<sup>27</sup> equates to 36.5 seconds, or 15.5 cm within the flow tube. Diffusions coefficients for  $\alpha$ -pinene and  $\alpha$ -terpinene may be calculated according to the equation:<sup>28</sup>

$$D_{AB} = \frac{1.00 \times 10^{-8} \times T^{1.75} (1/M_A + 1/M_B)^{1/2}}{P \left[ (\sum_A v_i)^{1/3} + (\sum_B v_i)^{1/3} \right]^2} \quad (31)$$

where  $D_{AB}$  is the binary diffusion coefficient ( $\text{cm}^2 \text{s}^{-1}$ ),  $T$  is temperature (K),  $M_A$  &  $M_B$  are molecular masses ( $\text{g mol}^{-1}$ ),  $P$  is Pressure (atm) and  $v_i$  are atomic diffusion volumes ( $C = 16.5$ ,  $H = 1.98$ ,  $\text{Air} = 20.1$ ; values from Fuller *et al.*<sup>28</sup>; dimensions determined by arbitrary exponent,  $\alpha$ , where in this case  $\alpha = 1/3$ , and thus  $v_i$  are dimensionless).

Where one of the mixture components is air,  $D_{AB} = \varphi$ . Thus, the diffusion coefficient of  $\alpha$ -pinene in air,  $\varphi$ , may be calculated as  $0.06 \text{ cm}^2 \text{s}^{-1}$ , resulting in a mixing time of 83 seconds, or 35 cm. Mixing time of  $\alpha$ -terpinene,  $\varphi = 0.06 \text{ cm}^2 \text{s}^{-1}$ , is also 83 seconds, or 35 cm. These values suggest that, while the reaction may be expected to begin at the point ozone enters the flow tube, at the injector head, homogeneous, laminar flow is not expected to begin until 15 cm afterward. The mixing length of 35 cm for the terpene is not considered to be important, since in these experiments, the injector head was always at least 30 cm from the rear of the flow tube. Thus, the mixing length after the injector head would be 5 cm at most—less than that of the ozone.

The flow through the tube develops a pressure gradient along its length due to the force of the gas.<sup>29</sup> This pressure gradient is described by the Poiseuille Equation:

$$\Delta P / \Delta d = \frac{5.9 \times 10^{-3} \eta v}{R^2} \quad (32)$$

where  $\eta$  is dynamic gas viscosity ( $\text{g cm}^{-1} \text{s}^{-1}$ ),  $v$  is flow velocity ( $\text{cm s}^{-1}$ ) and  $R$  = tube radius (cm).

Dynamic gas viscosity may be calculated using Sutherland's Equation:<sup>30</sup>

$$\eta = \eta_0 \frac{T_0 + C}{T + C} \left( \frac{T}{T_0} \right)^{3/2} \quad (33)$$

where  $\eta_0$  is the reference viscosity ( $\text{g cm}^{-1} \text{s}^{-1}$ ),  $T$  is temperature,  $T_0$  is the reference temperature and  $C$  is Sutherland's constant for the gas.

Assuming that the gas in question is primarily air, we can use reference values of:  $C = 120$  K;  $\eta_0 = 1.827$ ;  $T_0 = 291.15$  K. Average room temperature was  $22 \pm 2$  °C. Thus, we arrive at a dynamic gas viscosity of  $1.85 \text{ g cm}^{-1} \text{ s}^{-1}$ . Substituting this into equation (32), we can calculate a pressure gradient of  $1.85 \times 10^{-4} \text{ Torr cm}^{-1}$ . A slight correction must be applied to account for the injector, which disrupts the velocity profile of the gas.<sup>29</sup> This correction approximately doubles the pressure gradient, to  $3.54 \times 10^{-4} \text{ Torr cm}^{-1}$ . Thus, we can conclude that this pressure gradient is negligible in our system, and no correction need be applied.

A concentration gradient may also develop as the reaction takes place and the number of molecules is altered. However, working at high pressure, and with low concentrations of reactants, makes this effect also negligible.

For experimental sets using the flow tube, a chamber containing the terpene-scavenger mixture was prepared, following the procedure described in section 2.3.2. This chamber was connected to a port at the rear of the flow tube, and its flow regulated by a flow meter. A constant flow of synthetic air was also introduced via a port at the rear of the flow tube. An  $\text{O}_2 / \text{O}_3$  mixture was introduced via a sliding injector inside the tube (Figure 29). A pump was connected at the front of the tube to encourage movement of species along the tube and to control the pressure within it, and a final port at the front of the tube was connected to the SMPS to allow for particle sampling.

Ozone in these experiments was produced via a flow-through ozone generator, described in section 2.1. This allowed for production of ozone at a few ppm, and was controllable by altering the exposure of the oxygen flow to the UV lamp. A calibration curve for the concentration of ozone produced is given in section 2.7.

The pressure gauge is located at the middle of the flow tube, to minimise errors due to the pressure gradient.<sup>29</sup> It is connected at a right angle to the tube, such that it measures only the static pressure—there should be no flow past the gauge.

It is important to note that, because of the dilution of samples when mixed with the carrier gases in the flow tube, the reactant concentrations prior to injection must be

higher. For example, the standard flow component flow rates to make-up 2 L min<sup>-1</sup> total flow were: organic mixture (0.20 L min<sup>-1</sup>); air (1.70 L min<sup>-1</sup>) and O<sub>2</sub> / O<sub>3</sub> mixture (0.10 L min<sup>-1</sup>). Thus, to achieve a concentration of 0.1 ppm terpene within the flow tube, the sample prepared in the chamber must be 10× higher concentration (2÷0.2); i.e. 1 ppm.

### 2.6.1 Wall Loss Corrections

The use of a flow tube as the reaction vessel in place of the static chamber gives rise to its own set of complications. Wall loss must once again be defined for loss of aerosol within the flow tube itself. To quantify particle loss within the flow tube, a static chamber experiment was undertaken, with reactant concentrations of  $\alpha$ -terpinene and ozone both at 0.20 ppm. However, rather than directly connecting the Teflon sample chamber to the SMPS inlet, the sample chamber was instead allowed to sit for 20 minutes to allow sufficient time for the reaction to reach completion. The sample chamber was then connected to the flow tube according to the setup in Figure 29.

In this setup, the sample chamber was connected to the sliding injector, allowing the SOA products to enter the flow tube via the injector at a flow rate of 0.20 L min<sup>-1</sup>. Synthetic air was blown in through the rear of the tube at a rate of 1.80 L min<sup>-1</sup>. By adjusting the position of the injector within the flow tube, the time the SOA products spent within the flow tube could hence be adjusted. The time at which the first result was collected was considered to be  $t_0$ , and results were collected every three minutes after this point. The injector was moved to sample at three different positions within the flow tube.

In the absence of wall loss, and providing that the reaction has reached completion, mass concentration should remain constant; therefore, any decay observed can be attributed to wall loss. However, due to the nature of this experiment, whereby the SOA reservoir is stored in the static chamber, the decay observed was a function of both wall losses from the static chamber and from the flow tube. For all results collected after  $t_0$ , a correction was therefore applied, according to equation (22), to account for wall loss from the static chamber. A typical value for the wall loss rate constant was:  $k_{w(m, SC)} = 1 \times 10^{-4} \text{ s}^{-1}$ .

The corrected mass concentrations may now be used to calculate the wall loss rate constant for the flow tube. The log function of corrected particle mass concentrations are plotted against time spent in the flow tube (calculated using  $d$ , the distance from injector to end of flow tube, in equation (26), resulting in Figure 31.

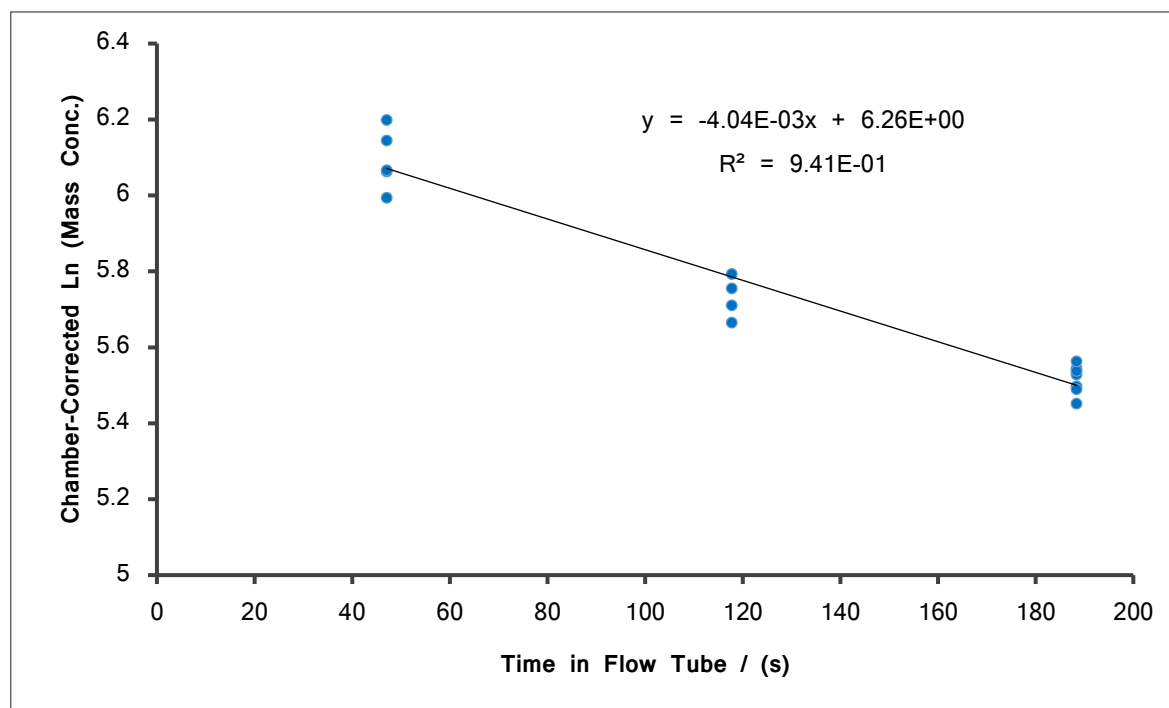


Figure 31: Natural log of mass concentration as a function of time in the flow tube. The negative gradient of a straight line fit corresponds to the wall loss rate constant.

Since wall loss is a first-order decay process, the wall loss rate constant can simply be determined from the negative gradient of the plot, given in Figure 31. Therefore, flow tube wall loss with respect to particle mass concentration,  $k_{w(m. FT)}$ , was found to be  $4.0 \times 10^{-3} \text{ s}^{-1}$ . As expected, wall losses observed within the flow tube itself are significantly larger than those observed within the static chamber, due to the small diameter of the tube. Also, the static chamber is made from FEP, which has a very low co-efficient of friction and is not conducive to trapping particles; on the other hand, the flow tube is made from glass and thus higher wall losses may be expected. Coating options for the flow tube were explored, but a feasible and affordable solution could not be found.

A correction may therefore be applied to all data obtained from the flow tube, according to equation (34):

$$\text{mass}_{\text{corr}} = \text{mass}_{\text{raw}} \cdot e^{t \cdot k_w(m, FT)} \quad (34)$$

where  $\text{mass}_{\text{corr}}$  is the particle mass concentration corrected for wall loss ( $\mu\text{g m}^{-3}$ ),  $\text{mass}_{\text{raw}}$  is the raw particle mass concentration ( $\mu\text{g m}^{-3}$ ),  $t$  is time (s) and  $k_w(m, SC)$  is the wall loss rate constant ( $\text{s}^{-1}$ ).

## 2.7 Calibrations and Error Estimates

The flow meter controlling the synthetic air was calibrated twice during the course of this work to ensure reliability. Both calibrations agreed with one another within error.

Calibrations were carried out by filling a 5 L volumetric flask with water, and upturning into a water-filled tank. The air flow outlet was fed into the volumetric flask, and the flow turned on. The time to displace the water in the flask was recorded, and averaged over three repeats for each flow meter graduation. Both calibrations are presented in Figure 32. Uncertainty associated with this flow, and therefore concentration of components in the chamber, was  $\pm 3\%$ .

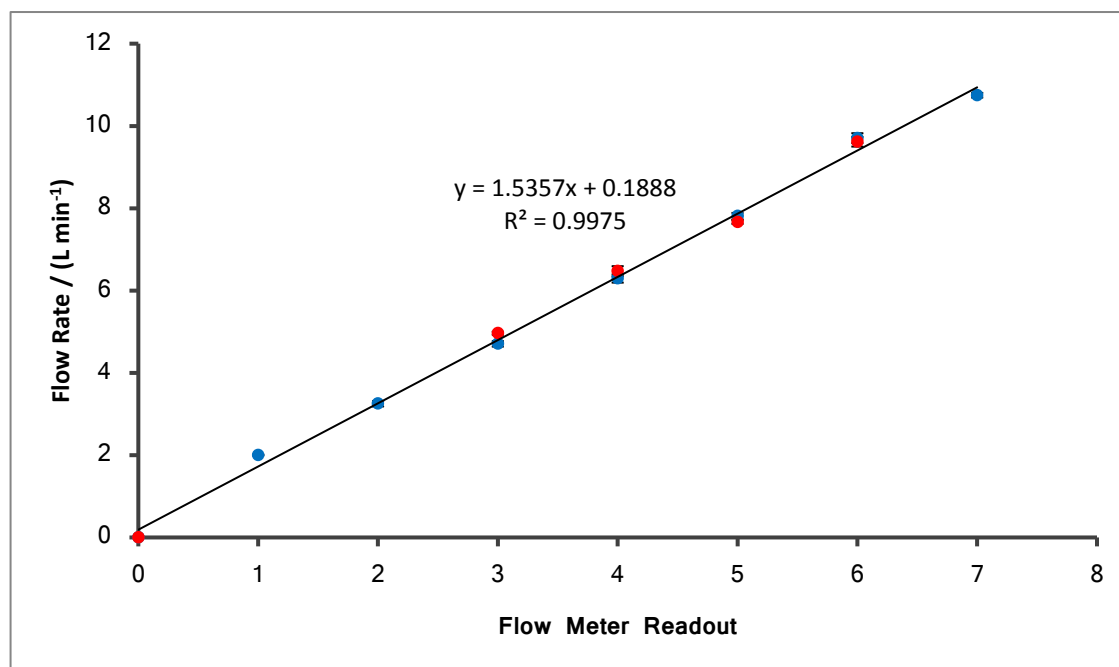


Figure 32: Calibration of synthetic air flow. Different colours correspond to repeats.

The pressure gauges used to regulate pressure within the rig give an uncertainty of 0.05 Torr. To minimise percentage uncertainty in the reagent, initial pressure of the reactants within the bulb were maximised within reason (i.e.  $P_1 \geq 0.8$  Torr). This resulted in an uncertainty in reactant concentrations within the chamber of  $\pm 6\%$ .

The Pen-Ray UV ozone generator was calibrated using UV spectroscopy. The ozoniser was switched on and allowed to warm up for an hour, with the metal cover in place. A gas cell with two connection ports was connected in-line with the ozoniser. Flow of  $O_2$  was controlled via mass-flow controller. The metal cover was retracted to the first graduation, exposing the  $O_2$  flow to UV. After two minutes flow time, the flow was shut off, the ozoniser re-covered, and a UV spectrum was taken of the  $O_2 / O_3$  mixture in the gas cell. This was repeated three times for each graduation, and ozone concentration was calculated according to the method in section 2.3.3. The ozone calibration was repeated for each different flow rate used, since a faster flow rate would reduce the exposure time of the  $O_2$  flow, thus decreasing the ozone concentration. The most common  $O_2$  flow rate used in the flow tube experiments was  $0.1 \text{ L min}^{-1}$ . Calibrations curve for ozone produced at both  $0.1$  and  $0.5 \text{ L min}^{-1}$  are given in Figure 33. Uncertainties in the ozone concentrations used in the flow tube were  $\pm 6.5$  and  $\pm 5.9\%$ , respectively.

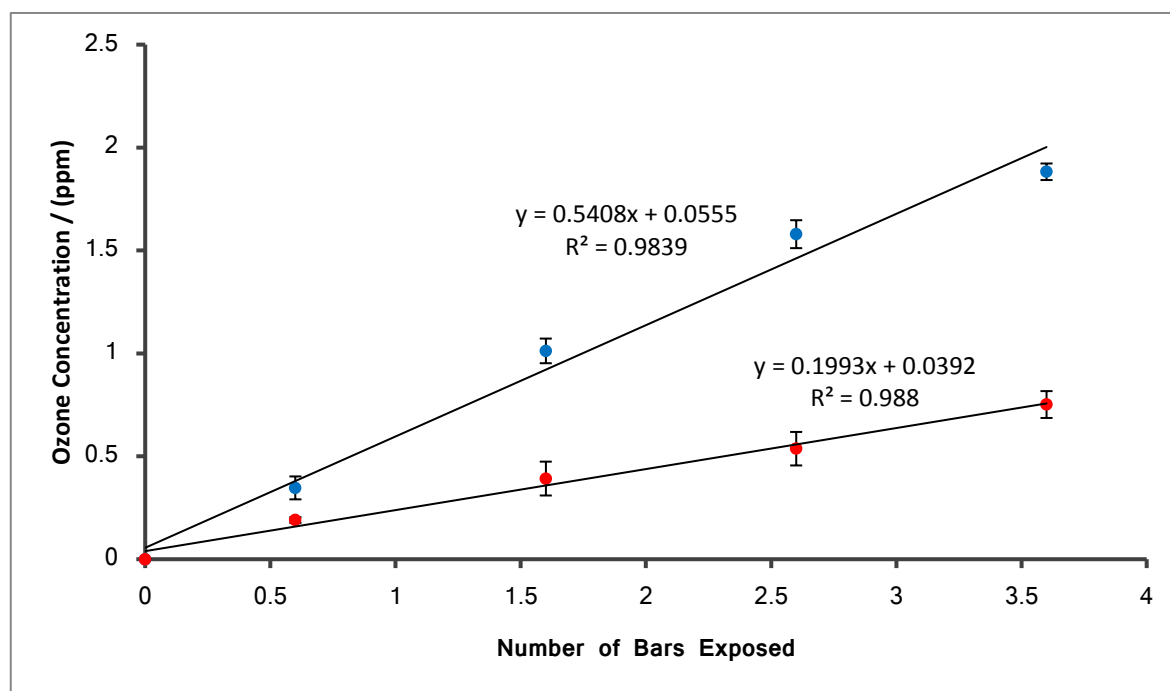


Figure 33: Calibration of Pen-Ray Ozoniser at  $0.1 \text{ L min}^{-1}$  (blue) and  $0.5 \text{ L min}^{-1}$  (red).

## 2.8 References

1. R. K. Pathak, A. A. Presto, T. E. Lane, C. O. Stanier, N. M. Donahue and S. N. Pandis, *Atmos. Chem. Phys.*, 2007, **7**, 3811-3821.
2. N. L. Prisle, G. J. Engelhart, M. Bilde and N. M. Donahue, *Geophys. Res. Lett.*, 2010, **37**, L01802.
3. H. Saathoff, K. H. Naumann, O. Möhler, Å. M. Jonsson, M. Hallquist, A. Kiendler-Scharr, T. F. Mentel, R. Tillmann and U. Schurath, *Atmos. Chem. Phys.*, 2009, **9**, 1551-1577.
4. V. Perraud, E. A. Bruns, M. J. Ezell, S. N. Johnson, Y. Yu, M. L. Alexander, A. Zelenyuk, D. Imre, W. L. Chang, D. Dabdub, J. F. Pankow and B. J. Finlayson-Pitts, *Proc. Natl. Acad. Sci. U.S.A.*, 2012, **109**, 2836-2841.
5. M. P. Tolocka, K. J. Heaton, M. A. Dreyfus, S. Wang, C. A. Zordan, T. D. Saul and M. V. Johnston, *Environ. Sci. Technol.*, 2006, **40**, 1843-1848.
6. A. Virtanen, J. Joutsensaari, T. Koop, J. Kannosto, P. Yli-Pirilä, J. Leskinen, J. M. Mäkelä, J. K. Holopainen, U. Pöschl, M. Kulmala, D. R. Worsnop and A. Laaksonen, *Nature*, 2010, **467**, 824-827.
7. I. D. Hoare, *Physical Properties of Aerosol from the Ozonolysis of  $\alpha$ -Pinene and some of its Synthetic Derivatives*, University of Reading, Ph.D., 2013.
8. R. Atkinson, D. L. Baulch, R. A. Cox, J. N. Crowley, R. F. Hampson, R. G. Hynes, M. E. Jenkin, M. J. Rossi and J. Troe, *Atmos. Chem. Phys.*, 2006, **6**, 3625-4055.
9. R. Atkinson, *Atmos. Chem. Phys.*, 2003, **3**, 2233-2307.
10. Å. M. Jonsson, M. Hallquist and E. Ljungström, *Environ. Sci. Technol.*, 2008, **42**, 5938-5944.
11. J. Viallon, P. Moussay, J. E. Norris, F. R. Guenther and R. I. Wielgosz, *Metrologia*, 2006, **43**, 441.
12. A. Wiedensohler, E. Lütkeemeier, M. Feldpausch and C. Helsper, *J. Aerosol. Sci.*, 1986, **17**, 413-416.
13. N. A. Fuchs, *Geofis. Pura Appl.*, 1963, **56**, 185-193.
14. A. Wiedensohler and H. J. Fissan, *J. Aerosol. Sci.*, 1988, **19**, 867-870.
15. TSI Inc., *Electrostatic Classifiers - Operation and Service Manual*, 2009.
16. A. Zelenyuk, J. Yang, C. Song, R. A. Zaveri and D. Imre, *Environ. Sci. Technol.*, 2008, **42**, 8033-8038.
17. E. Abramson, D. Imre, J. Beranek, J. Wilson and A. Zelenyuk, *Phys. Chem. Chem. Phys.*, 2013, **15**, 2983-2991.



18. Y. Nomura, P. K. Hopke, B. Fitzgerald and B. Mesbah, *Aerosol Sci. Technol.*, 1997, **27**, 62-72.
19. Dekati Ltd., (2007), *Sintered Collection Plates*,  
<http://dekati.com/cms/files/File/PDF/Sintered%20Collection%20platesver2.pdf>, [May 2014]
20. M. Goldman, A. Goldman and R. S. Sigmond, *Pure and Appl. Chem.*, 1985, **57**, 1353-1362.
21. Dekati Ltd., *ELPI+ User Manual*, 2011.
22. L. N. Rogers and J. Reed, *J. Phys. D: Appl. Phys.*, 1984, **17**, 677-689.
23. S. W. Stein, J. B. Turpin, X. Cai, P. F. Huang and P. H. McMurry, *Atmos. Environ.*, 1994, **28**, 1739-1746.
24. M. D. Hays, N. D. Smith, J. Kinsey, Y. Dong and P. Kariher, *J. Aerosol Sci.*, 2003, **34**, 1061-1084.
25. K. Avila, D. Moxey, A. de Lozar, M. Avila, D. Barkley and B. Hof, *Science*, 2011, **333**, 192-196.
26. F. M. White, *Fluid Mechanics*, 4 edn., McGraw-Hill, Boston, MA, 1999.
27. W. J. Massman, *Atmos. Environ.*, 1998, **32**, 1111-1127.
28. E. N. Fuller, P. D. Schettler and J. C. Giddings, *Ind. Eng. Chem.*, 1966, **58**, 18-27.
29. C. J. Howard, *J. Phys. Chem.*, 1979, **83**, 3-9.
30. W. Sutherland, *Phil. Mag.*, 1893, **36**, 507-531.

# Chapter 3

## Ozonolysis of $\alpha$ -pinene

---

### 3.1 Introduction

As previously mentioned in section 1.2,  $\alpha$ -pinene is the most abundant terpene in the atmosphere, with global emissions estimated at 50 Tg yr<sup>-1</sup>.<sup>1</sup> In the atmosphere,  $\alpha$ -pinene reacts with oxidants to form secondary organic aerosol (SOA), yields of which depend heavily on atmospheric conditions. Global production of SOA from all sources has been estimated at 115 Tg yr<sup>-1</sup>, of which 90 Tg yr<sup>-1</sup> are from biogenic sources.<sup>2</sup> Thus, as the most prevalent precursor to SOA, it follows that  $\alpha$ -pinene is considered one of the most important species in the atmosphere, and a better understanding of its contribution to SOA formation, and the nature of that SOA, is paramount.

The growth of SOA as a result of the ozonolysis of  $\alpha$ -pinene has been investigated in this chapter. The system used in these experiments was first characterised by comparing results from our setup to an already well understood system in the literature. Once the reliability of our system had been ascertained, it was possible to move onto other, more interesting variables.

The effects of different scavengers on mass yield and particle size distribution have been examined, in addition to the effect of relative humidity. Reasons for the observed effects have been discussed and compared to results of previous studies by other groups, where possible. Further, the physical state of the SOA formed has been investigated under varying relative humidity conditions, and the results may have implications for the lifetime of SOA droplets in the atmosphere.

The ozonolysis of  $\alpha$ -pinene is understood to proceed initially through attack of the ozone molecule onto the double bond in the  $\alpha$ -pinene, forming a primary ozonide (POZ), which then decomposes into two Criegee intermediates (CIs).<sup>3</sup> Their formation is described by

the reaction scheme in Figure 34. Criegee intermediates are often written as biradicals. However, recently infrared spectroscopy has suggested that their structure is that more of a zwitterion, rather than a biradical.<sup>4</sup>

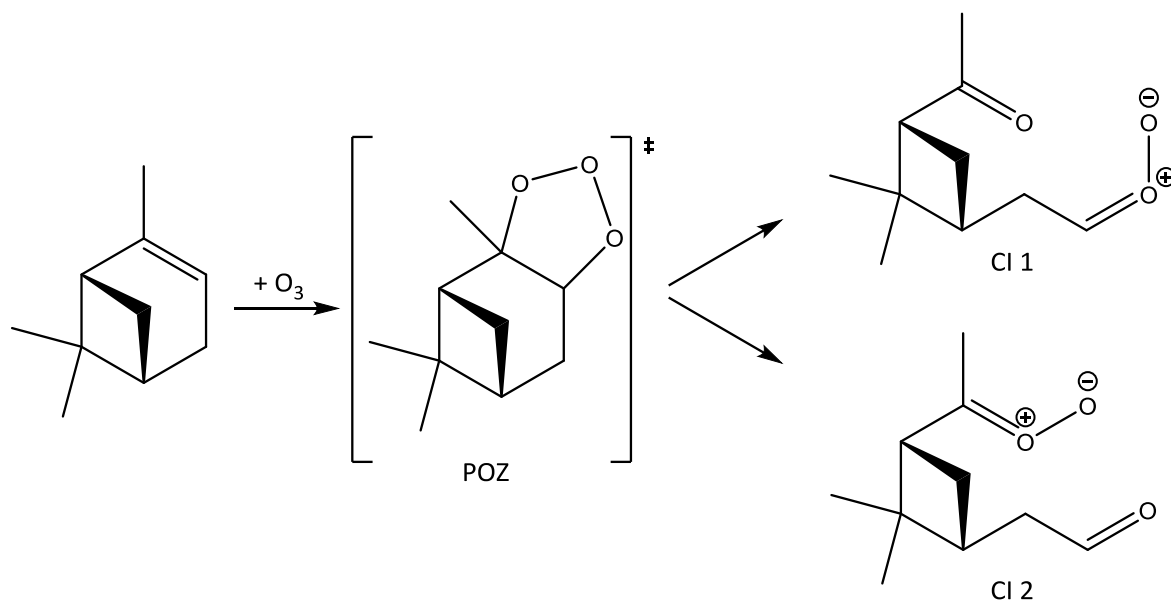


Figure 34: Criegee intermediate formation from the ozonolysis of  $\alpha$ -pinene<sup>5</sup>

The mechanisms by which these two CIs form products are complex and still not fully understood. Figure 35 highlights some of the products formed by each CI, and the initial step in their formation. However, formation of each product is the result of multi-step pathways, which, for clarity, are not presented here. The CIs form a number of acid and carbonyl products,<sup>6</sup> with hydrogen peroxide<sup>7</sup> and formaldehyde<sup>6</sup> formed as by-products.

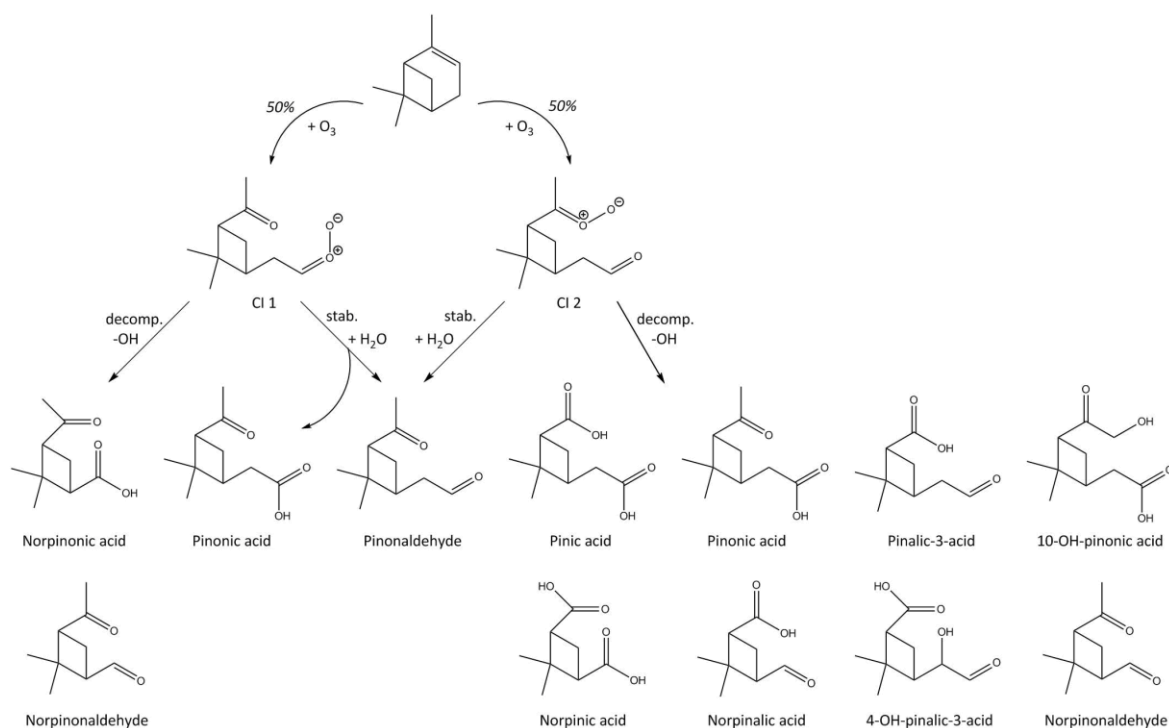


Figure 35: Products of the ozonolysis of  $\alpha$ -pinene, reproduced from Ma *et al.*<sup>6</sup>

Previous groups have suggested that, in isolated chamber experiments such as these, acid products such as pinic acid<sup>8</sup> and pinonic acid<sup>9</sup> may be responsible for the initial gas-to-particle partitioning, resulting in formation of clusters. Dicarboxylic acids in particular, such as pinic acid, are very strong candidates due to their low vapour pressures. Vapour pressures of pinic and pinonic acid have been measured as  $3.2 \times 10^{-5}$  and  $7 \times 10^{-5}$  Pa, respectively.<sup>10</sup> Formation mechanisms for pinic and pinonic acid, suggested in the literature, are reproduced in Figure 36 and Figure 37:

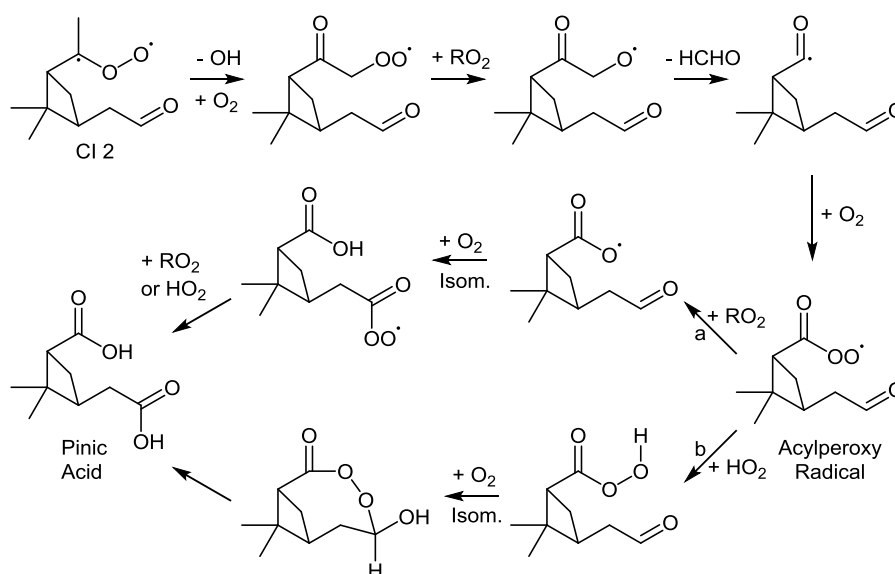


Figure 36: Suggested mechanisms for pinic acid formation from Cl<sub>2</sub>, reproduced from <sup>a</sup> Jenkin *et al.*<sup>11</sup> and <sup>b</sup> Koch *et al.*<sup>12</sup>

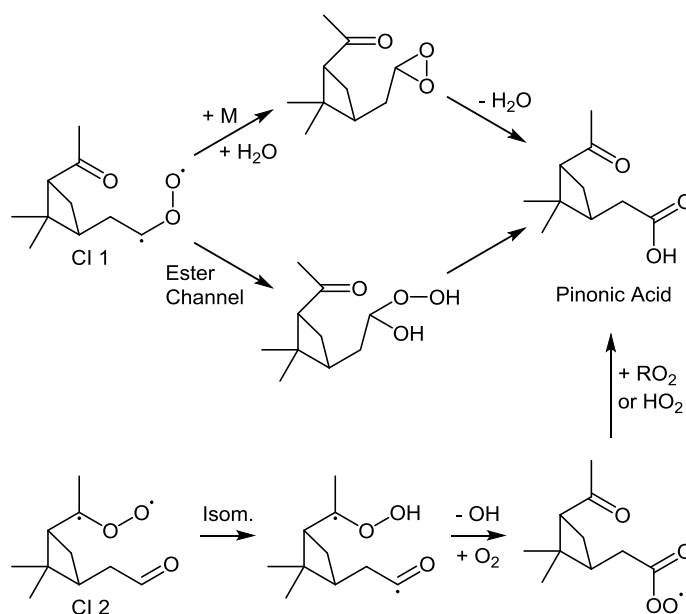
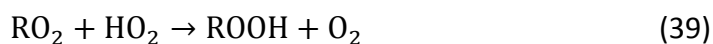


Figure 37: Suggested mechanisms for pinonic acid formation from both Cls, reproduced from Ma *et al.*<sup>6</sup>

An alternative theory is that thermally stabilised Cls are responsible for the formation of new particles.<sup>10</sup> Johnson *et al.*<sup>13</sup> suggested that, for aromatics, hydroperoxides formed by reaction of HO<sub>2</sub> and RO<sub>2</sub> radicals may be important species in SOA formation under low NO<sub>x</sub> conditions, such as those employed here. This was confirmed by Wyche *et al.*,<sup>14</sup> who noted more rapid particle formation under low NO<sub>x</sub> conditions as opposed to high NO<sub>x</sub>. They propose the following reaction scheme:



Since  $\text{NO}_x$  constrains the formation of hydroperoxides, by reacting preferentially with the  $\text{HO}_2$  and  $\text{RO}_2$  precursors (see equations (35) and (36)), faster formation of new particles in its absence suggests that hydroperoxides may be an important species for particle nucleation.

Ziemann<sup>15</sup> identifies diacyl peroxides, with the general formula  $\text{R}_1\text{C}(\text{O})\text{OO}(\text{O})\text{CR}_2$ , as products of the ozonolysis of cyclohexene. These compounds have very low volatilities, with vapour pressures ranging from approximately  $10^{-5}$ – $10^{-8}$  Pa, dependent on composition of the R groups—dialdehydes at the upper end and diacids at the lower. Due to their extremely low volatilities, diacyl peroxides are thought to be important for the nucleation of aerosol particles, although yields are likely to be small<sup>15</sup> and therefore these compounds are only believed to be partially responsible for the formation of particles. The author further identifies diacyl peroxides as products of cyclopentene, cycloheptene and cyclooctene ozonolyses. Zhang *et al.*<sup>16</sup> recently identified, from  $\alpha$ -pinene ozonolysis products, a number of ester dimers which they suggest are decomposition products of diacyl peroxides, thereby providing evidence for the presence of these compounds in  $\alpha$ -pinene SOA.

Other, high molecular weight products may also be important for particle nucleation—particularly those formed through accretion-type reactions discussed previously in section 1.5. These reactions allow formation of dimers and oligomers of significantly increased molecular weight, and therefore significantly decreased volatilities. Volatilities of the products formed can be several orders of magnitude below their constituent monomers.<sup>17</sup> There are numerous possible reaction pathways which may form oligomers from first-generation ozonolysis products. Some of these are highlighted in Figure 38:

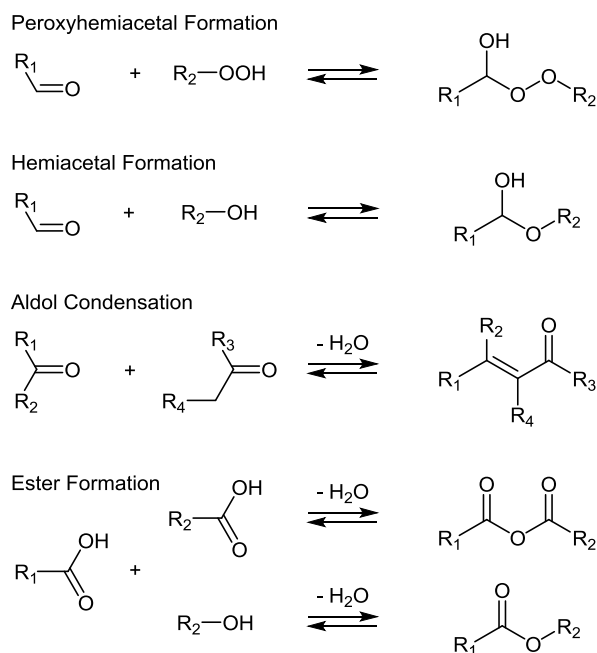


Figure 38: Accretion reaction mechanisms between condensed phase monomers, reproduced from Camredon *et al.*<sup>18</sup>

Whilst these are the likely candidates for particle nucleation in chamber experiments such as those undertaken in this chapter, it is thought highly likely that in the atmosphere ammonium sulfate and other small particles will instead act as seeding particles.<sup>8</sup> Low volatility vapours will tend to condense onto these particles rather than nucleating new ones. Indeed, a number of recent studies have investigated sulfuric acid nucleation,<sup>19, 20</sup> and a large dependency on bases such as ammonia and methyl amine, in addition to sulfuric acid, has been noted.<sup>19-22</sup>

### 3.2 Development of a Standard for Data Presentation

The data obtained from SMPS experiments can be presented in a number of ways, as shown in Figure 39–Figure 42. It was important to develop a standard for data presentation before proceeding, and hence the positives and negatives of each style will be discussed, and the reasons for the choice of style explained. An example of the results obtained for this reaction are illustrated in this section. Note that the results presented at this point are for reference only, and have not been corrected for wall losses.

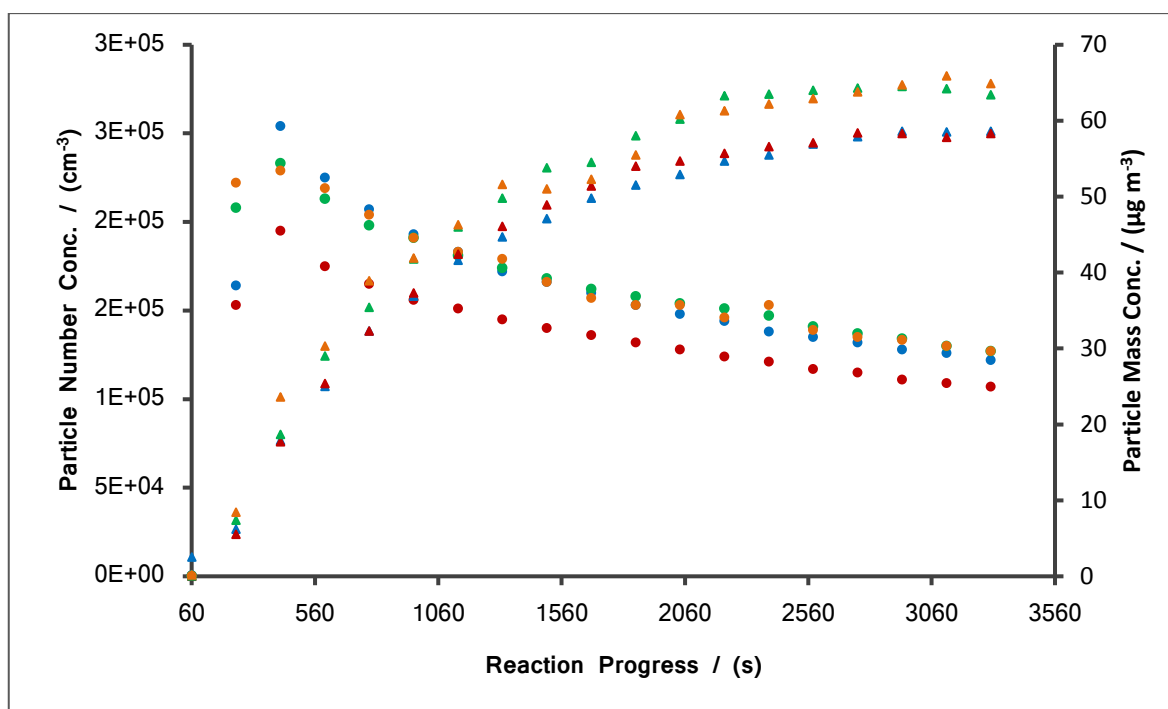


Figure 39: Number & Mass Concentrations vs. time,  $[\alpha\text{-pinene}] = 0.2 \text{ ppm}$ ,  $[\text{O}_3] = 0.1 \text{ ppm}$ . Number concentrations depicted by circles; mass concentrations depicted by triangles. Different colours represent experimental repeats.

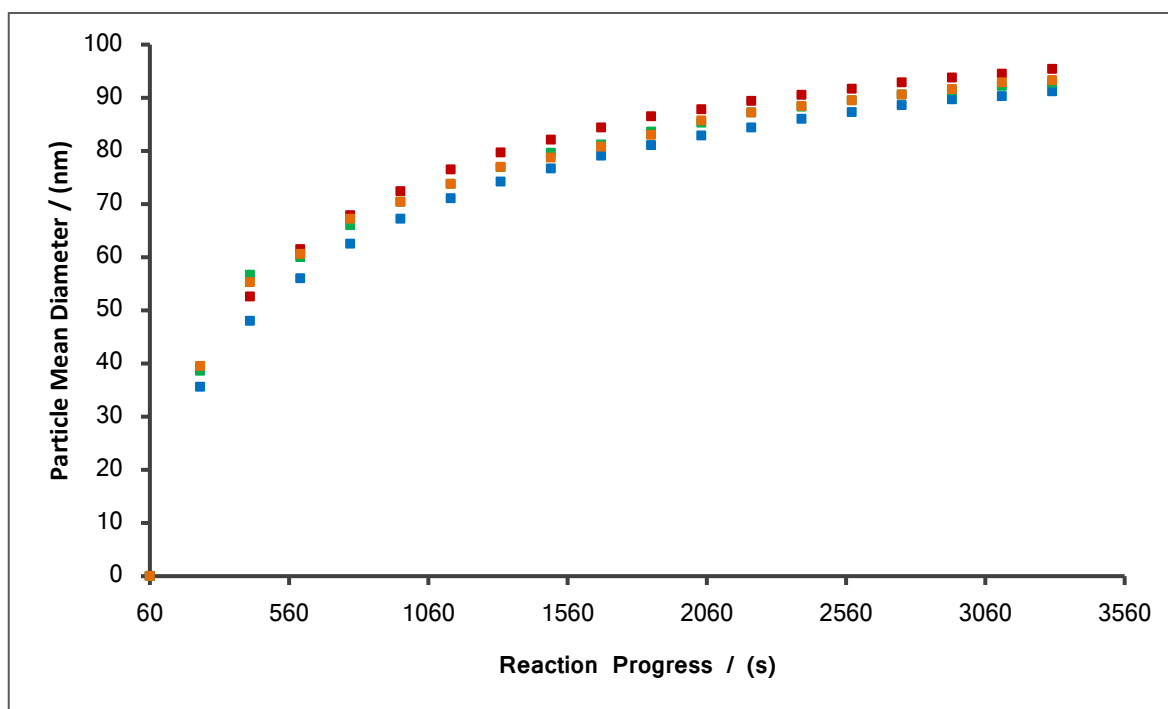


Figure 40: Particle Diameter vs. time,  $[\alpha\text{-pinene}] = 0.2 \text{ ppm}$ ,  $[\text{O}_3] = 0.1 \text{ ppm}$ . Different colours represent experimental repeats.

Both the positives and negatives of the 2-D plots, as demonstrated in Figure 39 & Figure 40, are immediately obvious. Between the two plots, most key information regarding



number and mass concentrations, as well as particle diameter, is displayed. However, it is not possible to view the size distribution of those particles, and the shape of the distribution is assumed to be Gaussian. A further drawback is that, to display all of this information, two separate plots are required, reducing the simplicity of data representation.

The shape of these plots are typical of SOA formation. For number concentration, the initial increase is due to particle nucleation. Particle number concentration then falls due to a combination of particle coagulation and loss of particulate matter to the chamber walls. Particle mass concentration increases throughout the experiment, until such a point where condensation of vapours onto the particulate matter is outstripped by loss of particles to the walls. Mean particle diameter typically increases throughout the course of an experiment, until vapour condensation effectively stops, and a plateau is reached.

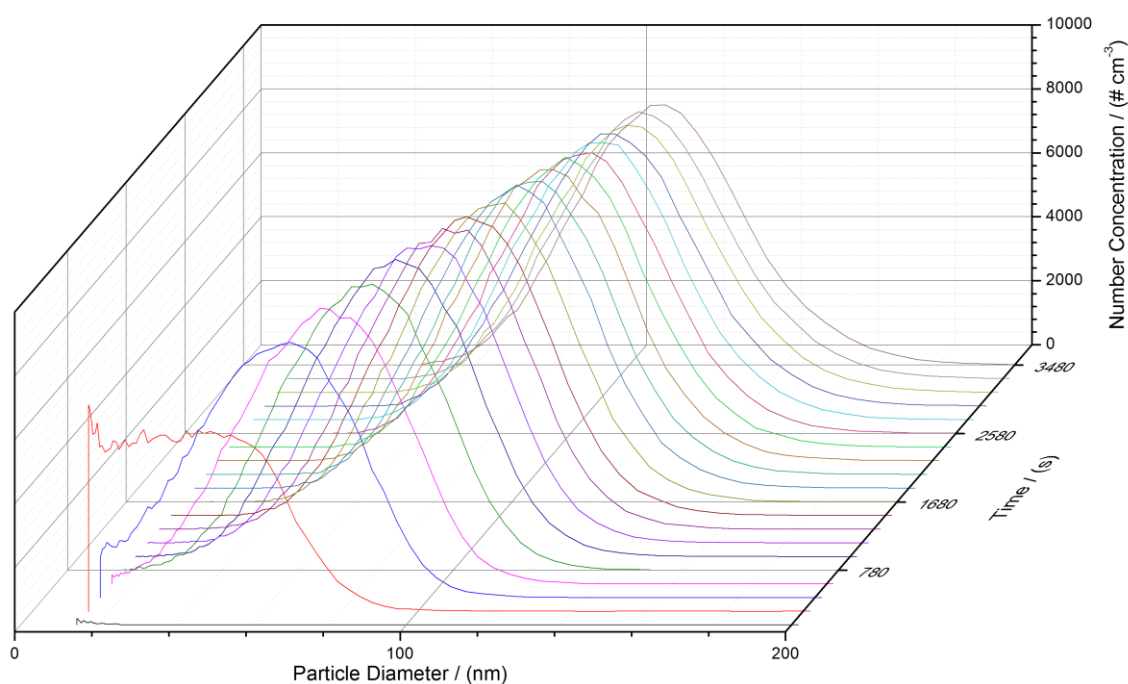


Figure 41: Waterfall plot of SOA Size Distribution vs. time,  $[\alpha\text{-pinene}] = 0.2 \text{ ppm}$ ,  $[\text{O}_3] = 0.1 \text{ ppm}$ .

The size distribution plot in Figure 41 is useful in some regards, with an emphasis on displaying the particle diameter and Gaussian distribution and their evolution over the

course of the experiment. The size distribution plot has a distinct advantage over the 2-D plots with respect to displaying particle diameter, since this allows for representation of all particles in the system, rather than a simple average of those present. However, it is difficult to read particle number concentration from these axes, since to do so would require an integration of the curve, and to display mass concentration would again require a second plot, and result in another unclear axis. Since mass concentration and specifically mass yield are frequently the most interesting results of these experiments, SOA size distribution curves may not be the most appropriate or useful way to represent this data in most circumstances.

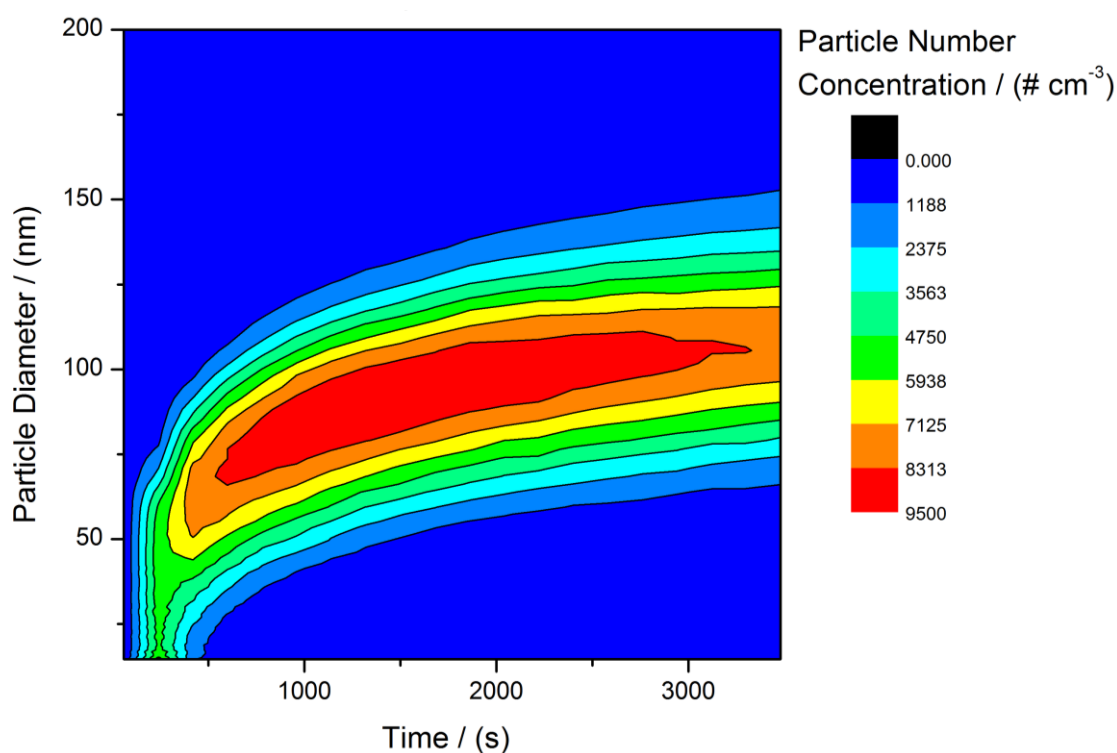


Figure 42: Contour plot of SOA Size Distribution vs. time,  $[\alpha\text{-pinene}] = 0.2 \text{ ppm}$ ,  $[\text{O}_3] = 0.1 \text{ ppm}$ .

The representation of data via a contour plot, as in Figure 42, suffers from a similar problem to the waterfall plot. Whilst the particle diameter and distribution are even more clearly represented, it is again difficult to read total particle number concentration from this plot, and a second plot would again be required to represent mass concentration.

Due to the limitations of the 2-D plots in their inability to present size distribution data, it was decided that, in most cases, data in this work would be presented with contour plots, for ease and clarity of comprehension.

### 3.3 System Characterisation and Reproducibility

The ozonolysis of  $\alpha$ -pinene was first investigated through static chamber experiments, according to the method described in section 2.3.2, with an  $\alpha$ -pinene concentration of 200 ppbv, and ozone concentration of 100 ppbv. This reaction has previously been studied in depth.<sup>23</sup> However, the intention behind investigating this reaction was twofold—first, to ensure that the result was reproducible, and that the system being used for these experiments was identical to that used by I. Hoare, a previous Ph.D. student within the University of Reading atmospheric laboratory, and second to provide a standard, well understood result that any newer results could be compared to. The data obtained from these experiments is that previously presented in Figure 39–Figure 42. Data are the average of three experimental repeats.

After 45 minutes of reaction time, the particle number concentrations observed in these experiments vary from  $1.15 \times 10^5$  to  $1.37 \times 10^5$  particles  $\text{cm}^{-3}$ , with a mean value of  $1.30 \pm 0.160 \times 10^5$  particles  $\text{cm}^{-3}$  (see Figure 39). This corresponds to a deviation of up to approximately 12.5 % from the mean. It was difficult to produce a reliable number concentration across experiments. This is due to the combination of a number of variables which may affect the number concentrations produced. For example, when preparing the sample, a common pressure of  $\alpha$ -pinene introduced into the 1 L mixing bulb was 1.0 Torr. This gives a range of pressures from 0.95 to 1.05 Torr of  $\alpha$ -pinene, and thus alters the final concentration of  $\alpha$ -pinene in the sample by  $\pm 5$  %.

Another variable impacting on the number concentrations observed is the mixing of species in the chamber. The number concentration peaks very early in the reaction, at between 240–420 s for each individual reaction under these conditions, after which it falls off. This suggests that all, or almost all, new particles are formed in the first 7 minutes of the reaction, after which particles are slowly lost due to a combination of

coagulation and wall losses. Therefore, the initial progress of the system is key to the final number concentration observed. Although mixing would be expected to be similar across experiments by the end of the reaction time, it is clearly the initial steps which determine the final number concentration observed, and thus the mixing at the beginning of the reaction is very important. It is impossible with this experimental setup to regulate the mixing of species inside the reaction chamber, and thus the extent of mixing during the initial stages of the reaction is likely to have a large impact on the number concentrations observed. This accounts in part for the large variations between number concentrations observed and, when combined with the smaller effect of experimental limitations discussed previously, and other unavoidable random error, explains the variations between number concentrations.

Observed particle diameters at 45 minutes are the most reproducible of the three results and vary only very slightly, averaging  $90.68 \pm 2.80$  nm (see Figure 40). Under these conditions, there is initially a large discrepancy in mean particle diameters at 60 seconds, which then quickly converge. This is because the SMPS, used under these conditions, can only classify particles of a minimum 14.6 nm diameter. In this case, the bulk of the particles are below this minimum cut-off diameter, and as such the mean particle diameter reported is heavily skewed by those few particles of diameter  $\geq 14.6$  nm. Number concentrations reported at 60 seconds are approximately 3 orders of magnitude below those reported at 240 seconds, emphasising how heavily these few particles may distort the mean diameter. For clarity, where the data is skewed in such a way, mean particle diameters at 60 seconds have therefore been reported as 0 nm in Figure 40, since there is no way of ascertaining the true mean diameter below the cut-off point.

Particle mass concentrations show some variation, averaging  $61.30 \pm 5.33$   $\mu\text{g m}^{-3}$  after 45 minutes (see Figure 39), which constitutes a variation of up to 9 % from the mean. Mass yield was calculated for each result, and is defined as the percentage of reactant converted into the aerosol phase, by process of the reaction:<sup>24</sup>

$$\text{Mass Yield} = \frac{M_{\text{aerosol}}}{M_{\text{initial}} \times f_{\text{conc}}} \quad (40)$$

where  $M_{\text{aerosol}}$  is the maximum mass conc. observed ( $\mu\text{g m}^{-3}$ ),  $M_{\text{initial}}$  is the mass conc. of  $\alpha$ -pinene at  $t_0$  ( $\mu\text{g m}^{-3}$ ),  $f_{\text{conc}}$  is the fraction of  $\alpha$ -pinene reacted, related to concentration of limiting reactant.

The fractional,  $f_{\text{conc}}$ , is equal to the smaller of the concentrations of  $\text{O}_3$  and  $\alpha$ -pinene divided by the larger, and ensures that the concentration of the limiting reagent is reflected in the calculation (assuming that 100 % of the limiting reagent reacts).

$M_{\text{initial}}$ , the mass concentration of  $\alpha$ -pinene, was calculated from the concentration of  $\alpha$ -pinene in the static chamber, in ppm. Assuming  $T = 298 \text{ K}$  and  $P = 101.325 \text{ kPa}$ :

$$PV = nRT$$

$$\frac{n}{V} = \frac{P}{RT}$$

$$\frac{n}{V} = \frac{101325}{8.314 \times 298} \text{ mol m}^{-3}$$

$$\frac{n}{V} = 40.90 \text{ mol m}^{-3}$$

$$M_{\text{initial}} = 40.90 \times C_{\alpha\text{-pinene}} \times M_r \quad (\mu\text{g m}^{-3}) \quad (41)$$

where  $P$  is Atmospheric pressure (Pa),  $V$  is volume ( $\text{m}^3$ ),  $n$  is number of moles,  $R$  is the gas constant ( $\text{J K}^{-1} \text{ mol}^{-1}$ ),  $T$  is temperature (K),  $M_r$  is the molecular mass of  $\alpha$ -pinene ( $\text{g mol}^{-1}$ ) and  $C_{\alpha\text{-pinene}}$  is the concentration of  $\alpha$ -pinene (ppm).

Each individual mass yield can then be determined by substituting equation (41) into equation (40), along with the maximum mass concentration observed for each experiment.

So, for  $[\alpha\text{-pinene}] = 0.2 \text{ ppm}$  and  $[\text{O}_3] = 0.1 \text{ ppm}$ :

$$M_{\text{initial}} = 40.90 \times 0.2 \times 136.23 = 1114.3 \mu\text{g m}^{-3}$$

$$M_{initial} \times f_{conc} = 1114.3 \times \frac{0.1}{0.2} = 557.2 \mu\text{g m}^{-3}$$

The observed mass yield was  $11.00 \pm 0.96 \%$ .

The data presented here suggest that the experimental setup works well, with low experimental uncertainties observed for all three metrics—particle number concentration, mean particle diameter, and particle mass concentration—with particle diameters showing the most reproducibility, and particle number concentrations the least.

### 3.4 Gas-Phase Kinetics

The attack of ozone onto the  $\alpha$ -pinene molecules is expected to be the rate-determining step in these reactions, with subsequent radical-initiated reactions and partitioning to aerosol expected to occur on a much faster timescale. Thus, aerosol mass should prove a good indicator for reaction progress, and may be used as a proxy to allow for calculation of a rate constant. Whilst this experimental setup is not designed to be used for this purpose, it is possible, and relatively straightforward to do.

A simulation method was applied, eliminating the need to assume pseudo-first order conditions as for some other methods (e.g. Guggenheim<sup>25</sup>). According to the literature,<sup>26</sup> the ozonolysis of  $\alpha$ -pinene obeys second order kinetics, and hence, in the method used, reaction rate was initially expressed according to the second order reaction law (equation (42)).

$$\text{Rate} = \frac{\delta[P]}{\delta t} = k[A][B] \quad (42)$$

A correction for wall loss was then applied, yielding:

$$\frac{\delta[P]}{\delta t} = k[A][B] - k_w[P] \quad (43)$$

By integrating over a suitably short timestep,  $[P]$  can thus be approximated according to equation (44).

$$[P]_{t+\delta t} = [P]_t + k[A][B]\delta t - k_w[P]\delta t \quad (44)$$

where  $P$  corresponds to the products,  $A$  &  $B$  are reactants;  $k$  is the reaction rate constant ( $\text{cm}^3 \text{ molecule}^{-1} \text{ s}^{-1}$ ),  $k_w$  is the wall loss rate constant ( $\text{s}^{-1}$ ) and  $t$  is time (s).

A simulated profile of reaction progress can therefore be built up by continuous repeats of equation (44). The wall loss rate constant,  $k_w$ , is calculated from the experimental results according to the method in section 2.4.1. Experimental mass concentrations ( $\mu\text{g m}^{-3}$ ) obtained under the same conditions, i.e. initial reactant concentrations, are converted to molecule  $\text{cm}^{-3}$  by means of a correction factor,  $F$ , which is calculated according to equation (45). The simulated reaction progress is then compared to experimental results, and the reaction rate constant,  $k$ , is varied to produce the best fit, according to the least squares method, to the experimental data.

$$F = \frac{\sum \frac{m_t}{[P]_t}}{n} \quad (45)$$

where  $F$  is a correction factor,  $m_t$  is the observed mass at time  $t$  ( $\mu\text{g m}^{-3}$ ),  $[P]$  is the simulated product concentration at time  $t$  (molecule  $\text{cm}^{-3}$ ) and  $n$  is the number of data points averaged over.

Reactions were carried out between  $\alpha$ -pinene and ozone in a 2:1 ratio, according to the method in 2.3.2, at 298 K, and in the presence of cyclohexane as a scavenger. Each was analysed according to the method described here, to calculate a value for the rate constant,  $k$ . Examples of the comparison between experimental and simulated data are presented in Figure 43.

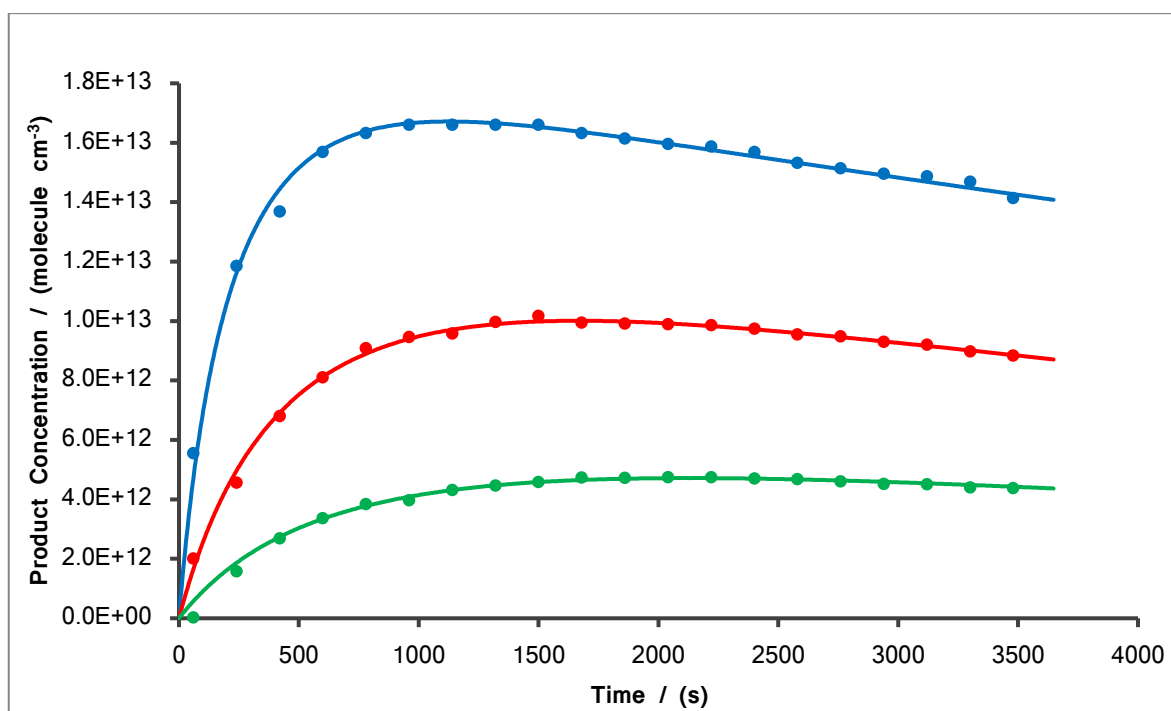


Figure 43: Calculation of a reaction rate constant. Circles represent experimental data; lines represent simulated data. Reactant concentrations: Blue [ $\alpha$ -pinene] = 1.5 ppm; [ozone] = 0.75 ppm; Red [ $\alpha$ -pinene] = 1.0 ppm; [ozone] = 0.50 ppm; Green [ $\alpha$ -pinene] = 0.5 ppm; [ozone] = 0.25 ppm.

The best fits for the data in Figure 43 were achieved for values of  $k = 11.5$ ,  $10.0$  and  $13.5 \times 10^{-17} \text{ cm}^3 \text{ molecule}^{-1} \text{ s}^{-1}$ , in order of decreasing reactant concentration. The data obtained across all experiments performed are summarised in Table 5, and the values obtained from Figure 43 are highlighted. It should be noted that rate analysis of experiments conducted at lower concentrations tend to show poorer fitting in the early stages of the reaction (see e.g. data represented in green in Figure 43). This is because the SMPS only detects particles of diameter  $> 14.6 \text{ nm}$ . Therefore, if all, or a significant proportion of products are below this cut-off, the aerosol mass will not accurately reflect the product concentration.



[Ozone] / (ppm)	[ $\alpha$ -pinene] / (ppm)	$k$ / ( $10^{-17}$ cm <sup>3</sup> molecule <sup>-1</sup> s <sup>-1</sup> )
0.05	0.1	7.5
0.05	0.1	12.0
0.05	0.1	7.5
0.05	0.1	6.5
0.05	0.1	7.1
0.075	0.15	8.0
0.075	0.15	10.9
0.075	0.15	9.2
0.1	0.2	16.1
0.1	0.2	14.8
0.25	0.5	13.5
0.25	0.5	13.7
0.25	0.5	13.0
0.25	0.5	14.7
0.38	0.77	12.5
0.38	0.77	10.6
0.38	0.77	10.5
0.5	1	12.1
0.5	1	12.3
0.5	1	10.1
0.75	1.5	7.3
0.75	1.5	11.4
0.75	1.5	9.9
1	2	8.7
1	2	6.8
1	2	7.3
Average		10.5 $\pm$ 1.1

Table 5: Summary of calculated reaction rate constants for the  $\alpha$ -pinene ozonolysis.

The reaction rate constant,  $k$ , is thus calculated as  $1.05 \pm 0.11 \times 10^{-16}$  cm<sup>3</sup> molecule<sup>-1</sup> s<sup>-1</sup>, and the calculated rate constants range from  $6.5\text{--}14.5 \times 10^{-17}$  cm<sup>3</sup> molecule<sup>-1</sup> s<sup>-1</sup>. This compares well with the preferred IUPAC value of  $9.4 \pm 0.15 \times 10^{-17}$  cm<sup>3</sup> molecule<sup>-1</sup> s<sup>-1</sup>,<sup>27</sup> and lies within the range of room temperature rate coefficients from which the IUPAC preferred value is calculated ( $8.22 \pm 1.24 - 11.3 \pm 1.4 \times 10^{-17}$  cm<sup>3</sup> molecule<sup>-1</sup> s<sup>-1</sup>).<sup>28, 29</sup>

### 3.5 Aerosol Mass and Mass Yield

The relationship between aerosol mass concentration (also called concentration of organic aerosol,  $C_{OA}$ ) and mass yield (also called aerosol mass fraction,  $F$ ) of the  $\alpha$ -pinene ozonolysis has previously been studied by a number of groups in the literature,<sup>30-33</sup> and the results of these are compiled by Hallquist *et al.* in their 2009 review.<sup>2</sup> These studies

comprehensively cover a range of atmospherically relevant aerosol mass concentrations, from 0.1–100  $\mu\text{g m}^{-3}$ , as well as showing some investigation into higher concentrations, up to approx. 300  $\mu\text{g m}^{-3}$ . The resulting plot, showing the relationship between experimentally observed particle mass concentration and mass fraction (or yield) of products which are incorporated into aerosol particles, is reproduced in Figure 44, alongside a basis-set fit produced by Presto and Donahue<sup>31</sup>. The basis-set fit is an empirical method which involves fitting data to a two-product model in which the mass-based yield of each product,  $\alpha_i$ , and the effective gas-phase saturation concentration of that species,  $C_i^*$ , are variables. While  $C_i^*$  is theoretically a constant for each compound, this is, in practice, irrelevant, since the particles studied in these fits are not pure species, but are composites of several compounds.

The shape of the basis-set fit presented in Figure 44 is typical of graphs of this type, and is due to gas-to-particle partitioning, described previously in section 1.5. Once condensation of organic material has begun, other products with gas-phase concentrations below their saturation vapour concentration will partition a proportion of their mass onto the particle, dependent on a partitioning co-efficient specific to each compound.<sup>34</sup> As  $C_{OA}$  increases, this proportion will also increase. The observed shape of the fit in Figure 44 is a consequence of this gradual partitioning behaviour.

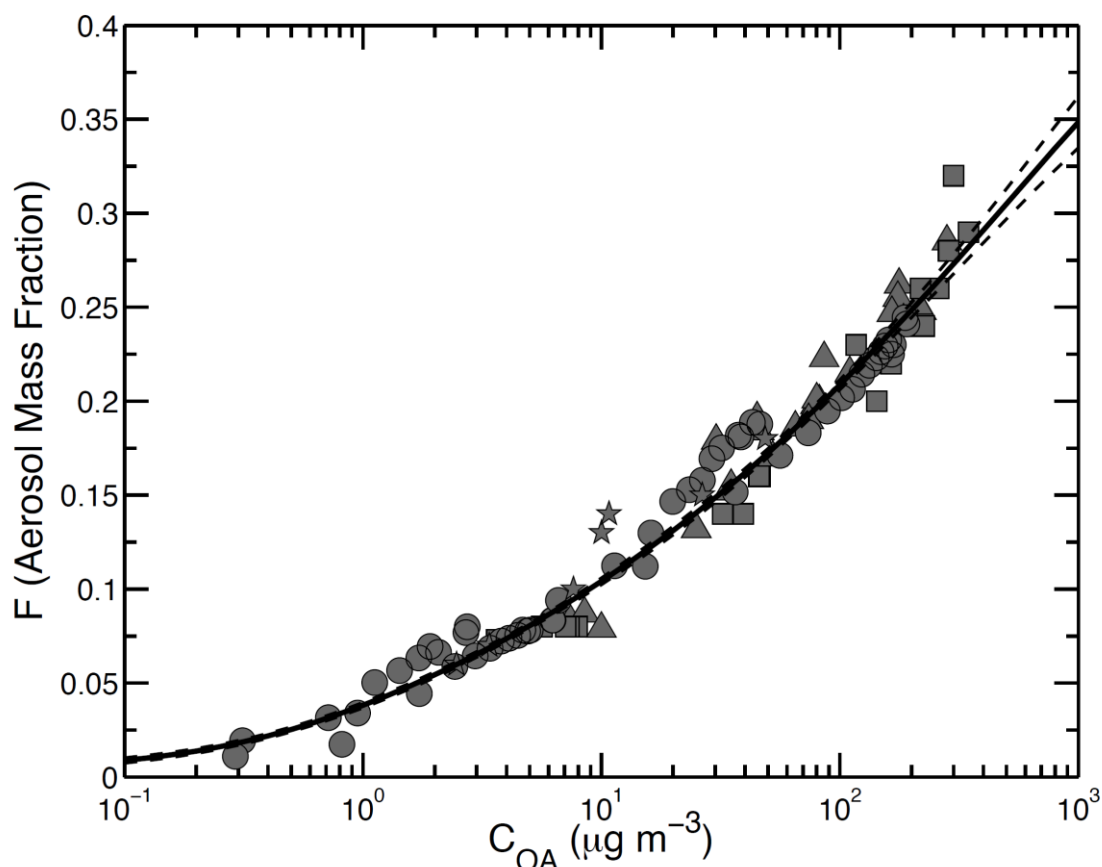


Figure 44: Mass concentration of SOA produced vs. mass yield, reproduced from Hallquist *et al.*<sup>2</sup>

Since creating a fit to the data in this manner is an empirical method, Presto and Donahue<sup>31</sup> make the assertion that basis-set fits should not be trusted for the purpose of extrapolating further data, since this would assume prior knowledge of SOA volatility behaviour outside of the range studied experimentally. Thus, they state, “Additional products, with larger  $C_i^*$  ( $10^3$ – $10^4$   $\mu\text{g m}^{-3}$ ), are required if we wish to ultimately consider the effects of further oxidation of product species, including aerosol ageing.”

In this work, the relationship between mass concentration of produced SOA vs. mass yield was investigated through static chamber experiments, according to the method described in section 2.3.2. Experiments were carried out using concentrations of  $\alpha$ -pinene ranging from 0.05–2.0 ppm, with  $[\text{O}_3]$  typically 50–100 % of  $[\alpha\text{-pinene}]$ . The conversion factor,  $F$ , calculated *via* the simulation method introduced in section 3.4, is representative of both the molecular mass of products and the mass yield.

The molecular mass of  $\alpha$ -pinene is  $136.23 \text{ g mol}^{-1}$ , and therefore:

$$1 \mu\text{g m}^{-3} = 4.42 \times 10^9 \text{ molecule cm}^{-3} \quad (46)$$

Then, mass yields can be calculated according to equation (47):

$$\text{Mass Yield} = \frac{4.42 \times 10^9}{F} \quad (47)$$

Mass yields were thus calculated from each of the experiments undertaken, and plotted alongside the basis-set fit (Figure 44) produced by Presto and Donahue,<sup>31</sup> to give:

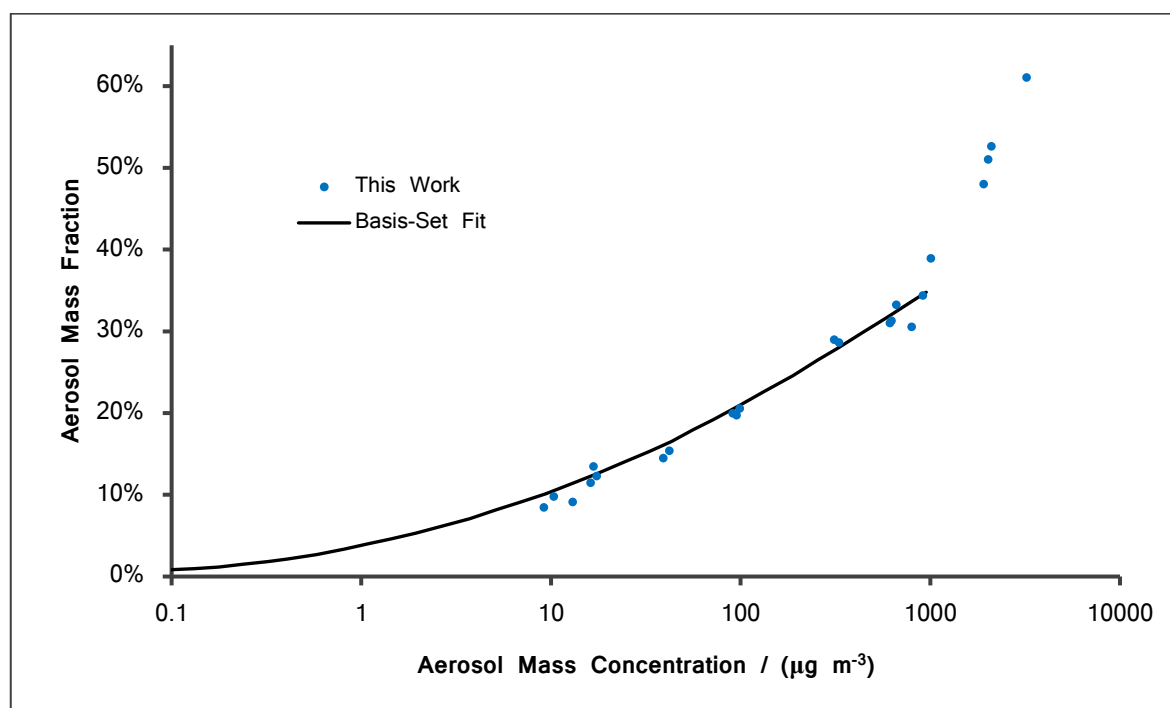


Figure 45: Aerosol mass fraction as a function of observed aerosol mass concentration, plotted against the basis-set fit from Presto and Donahue.<sup>31</sup>

The experiments carried out in this work can therefore be shown to have a good agreement with the literature, within the region interpolated by the basis-set fit.<sup>31</sup> This lends confidence to those data points obtained which lie outside the range previously investigated in the literature. These points suggest a significant proportion of additional products with volatilities in the range 1000–3000  $\mu\text{g m}^{-3}$ , compared to that which might be predicted by extrapolation of the literature fit. It is therefore proposed that the literature fit be amended to better describe products of higher volatilities.

### 3.6 Impact of Scavenger

As previously mentioned in section 1.7.3, scavengers are selected to react preferentially with  $\cdot\text{OH}$ , whilst remaining inert with respect to ozone. Whilst scavenger compounds do not react directly with ozone, previous studies have suggested that SOA yield may be affected by scavenger choice due to differences in  $\text{HO}_2$  /  $\text{RO}_2$  ratios of compounds produced from their reaction with  $\cdot\text{OH}$ .<sup>35</sup> This may be due to either being incorporated directly into aerosol particles, or participating in secondary reactions.

It is known that the use of cyclohexane as an  $\cdot\text{OH}$  scavenger leads almost exclusively to production of  $\text{RO}_2$ , although small quantities of  $\text{HO}_2$  radicals may still be produced from the reaction of the cyclohexyloxy radical with  $\text{O}_2$ .<sup>6</sup> The reactions of  $\cdot\text{OH}$  with both ethanol and 2-butanol proceed *via* similar reaction pathways to form their respective  $\alpha$ -hydroxyalkyl radicals. In the case of 2-butanol, the reaction then proceeds via reaction with  $\text{O}_2$  to form butanone (60–70 %)<sup>36, 37</sup> alongside a  $\text{HO}_2$  radical. In the case of ethanol, the reaction similarly proceeds to form acetaldehyde ( $80 \pm 15$  %)<sup>38</sup> alongside an  $\text{HO}_2$  radical. Reaction schemes for the hydroxyl radical with each of the three scavengers are presented in Figure 46.

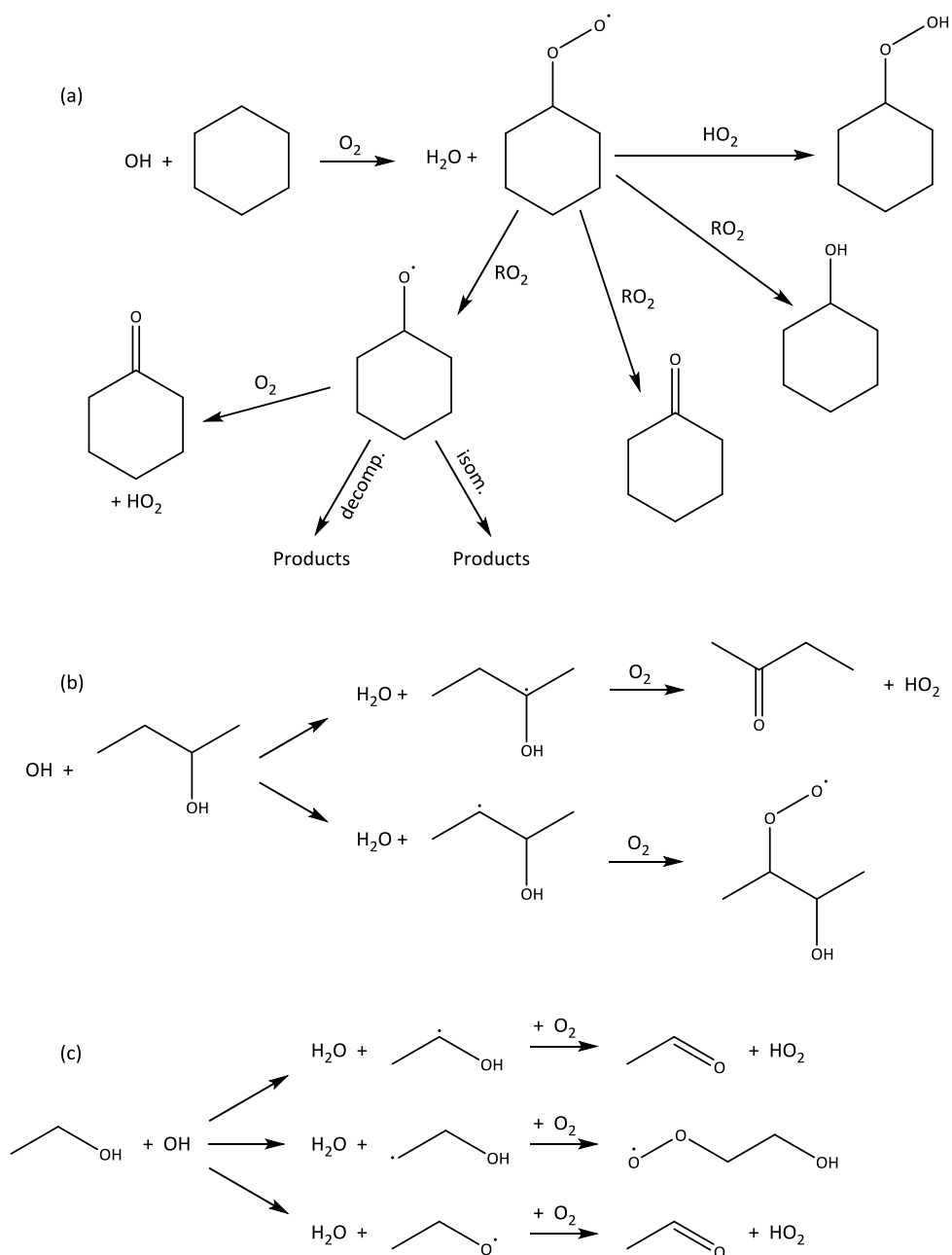


Figure 46: Reaction schemes for the formation of  $\text{HO}_2$  and  $\text{RO}_2$  radicals from the reactions of OH with: (a) cyclohexane;<sup>39, 40</sup> (b) 2-butanol;<sup>39</sup> (c) ethanol.<sup>41</sup>

The major decomposition pathways of the cyclohexoxy radical formed from OH-initiated oxidation of the cyclohexane scavenger (Figure 46a) are presented in Figure 47:

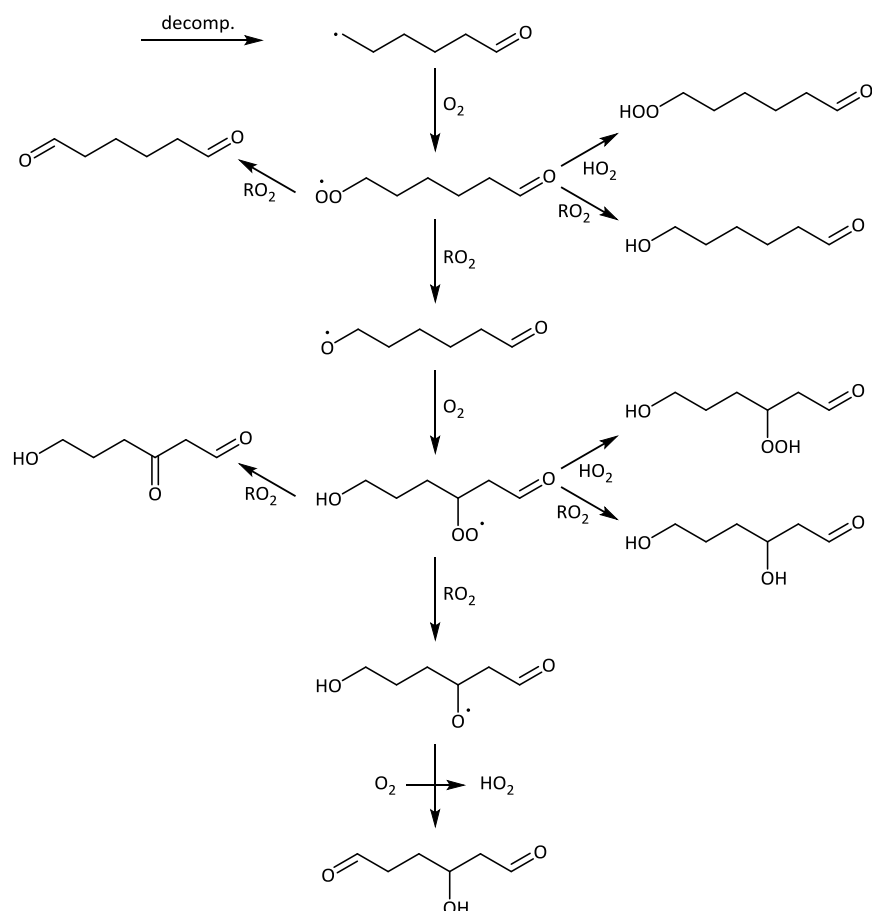


Figure 47: Major decomposition products of the OH-initiated oxidation of cyclohexane, arising from the decomposition pathway highlighted in Figure 46. Reproduced from Alam *et al.*<sup>40</sup>

The HO<sub>2</sub> / RO<sub>2</sub> ratios produced by the scavenger can have significant consequences for the product yields of the ozonolysis.<sup>6</sup> Secondary reactions of these radicals with the Criegee intermediates are responsible for the formation of a large proportion of the products presented in Figure 35. The use of different scavengers to promote either HO<sub>2</sub> or RO<sub>2</sub> has been shown to alter individual product yields by up to 40 %.<sup>6</sup> Note that the scavenger is not the only source of HO<sub>2</sub> and RO<sub>2</sub> radicals—indeed, both may be formed as a result of decomposition of the Criegee intermediates.<sup>6</sup>

Table 6 describes the participation of each radical in the formation of each of the products. This is not to say that the products are formed solely *via* reactions involving HO<sub>2</sub> and RO<sub>2</sub> radicals, but that reactions involving these radicals are known to contribute to their yields. In this table, “RO<sub>2</sub>” or “HO<sub>2</sub>” indicates the participation of that radical in product formation; “both” indicates the participation of both radicals in the same reaction pathway.

Compound	RO <sub>2</sub>	Both	HO <sub>2</sub>
Norpinonic Acid <sup>6</sup>	✓	✓	
Norpinonaldehyde <sup>6</sup>	✓		
Pinonic acid <sup>6</sup>	✓		✓
Pinonaldehyde <sup>6</sup>			
Pinic Acid <sup>34,35</sup>	✓	✓	
Norpinic Acid <sup>6</sup>	✓	✓	
Pinonic Acid <sup>6</sup>	✓		
Norpinalic Acid <sup>6</sup>	✓		
Pinalic-3-Acid <sup>34</sup>	✓		✓
4-OH-Pinalic-3-Acid <sup>6</sup>	✓		
10-OH-Pinonic Acid <sup>34</sup>	✓	✓	
Pinonaldehyde <sup>6</sup>	✓		

Table 6: Participation of the HO<sub>2</sub> & RO<sub>2</sub> radicals in formation of the ozonolysis products. References: <sup>6,11,12</sup>

The effects of 3 different scavengers—cyclohexane, butanol and ethanol—on SOA size distributions and mass yields were investigated. Reactions were carried out in accordance with the method described in section 2.3.2, between  $\alpha$ -pinene [0.20 ppm] and O<sub>3</sub> [0.10 ppm] in the presence of each of these 3 scavengers. Concentrations of cyclohexane, butanol and ethanol were 27.6, 60.5 and 22.7 ppm respectively, such that  $\geq 95\%$  of  $\cdot\text{OH}$  produced as a result of the ozonolysis reacted with the scavenger rather than undergoing further reaction with as-yet unreacted  $\alpha$ -pinene. SOA size evolutions as a function of time are presented in Figure 48, Figure 49 & Figure 50, and are each the average of three separate experiments. Figure 51 presents the average total particle number and mass concentrations of SOA formed from these reactions as a function of time.



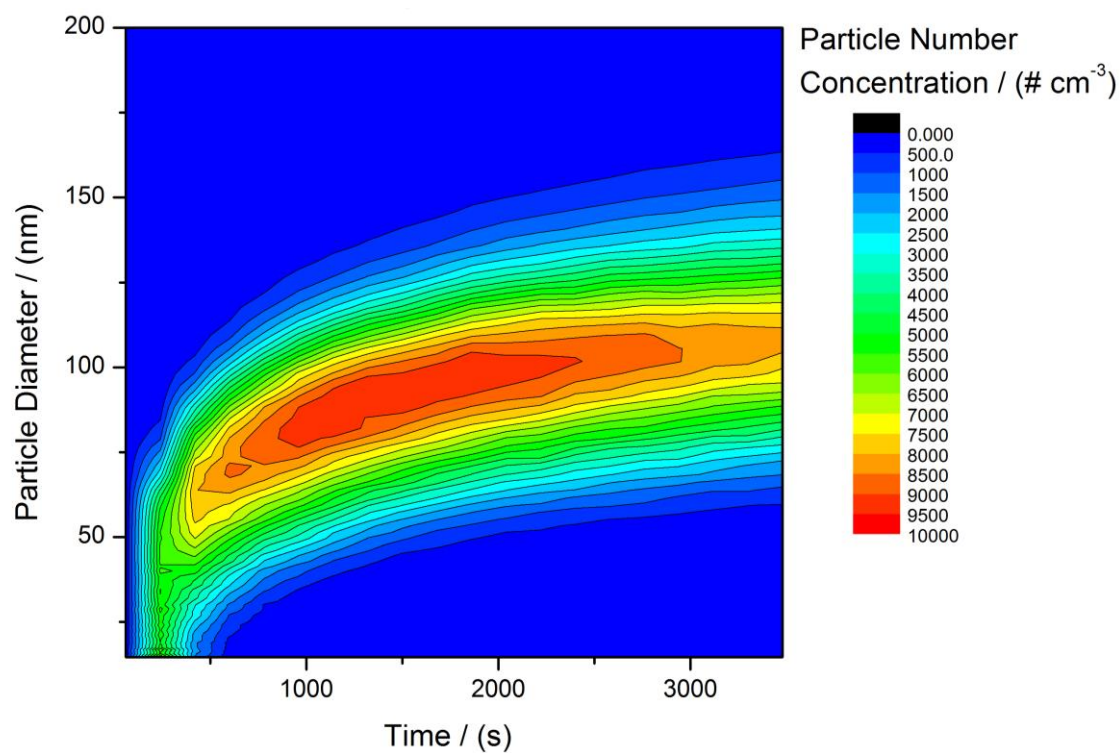


Figure 48: SOA size distribution as a function of time; [ $\alpha$ -pinene] = 0.20 ppm, [ $\text{O}_3$ ] = 0.10 ppm; cyclohexane scavenger.

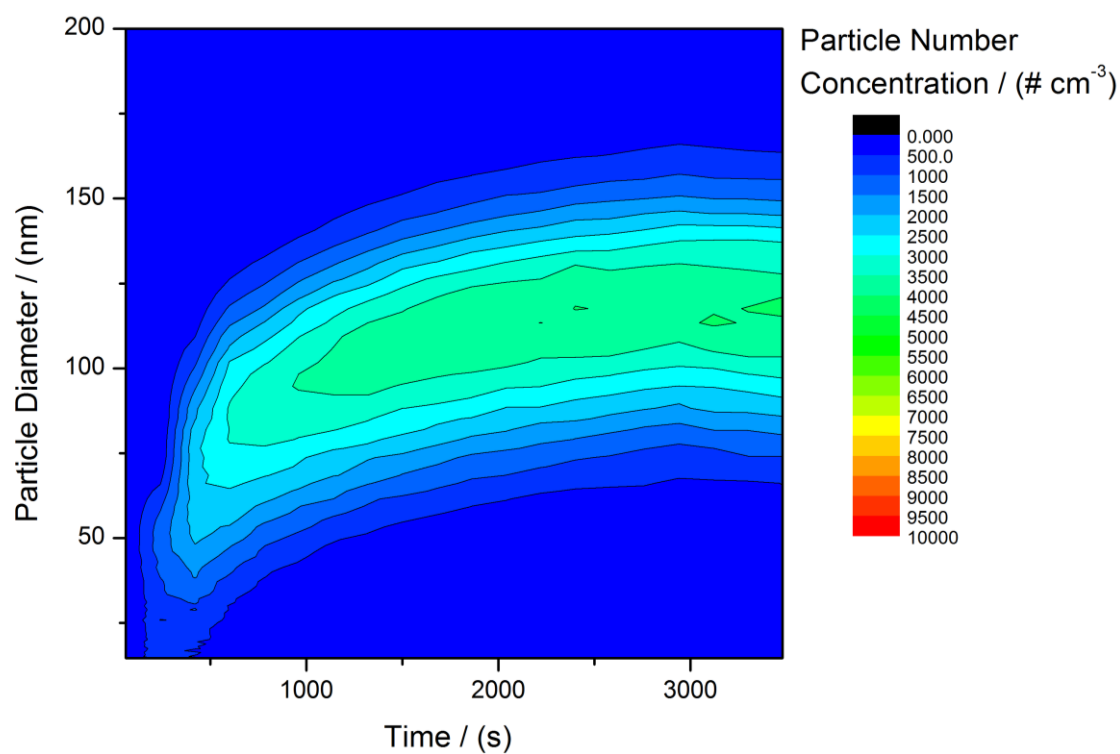


Figure 49: SOA size distribution as a function of time; [ $\alpha$ -pinene] = 0.20 ppm, [ $\text{O}_3$ ] = 0.10 ppm; 2-butanol scavenger.

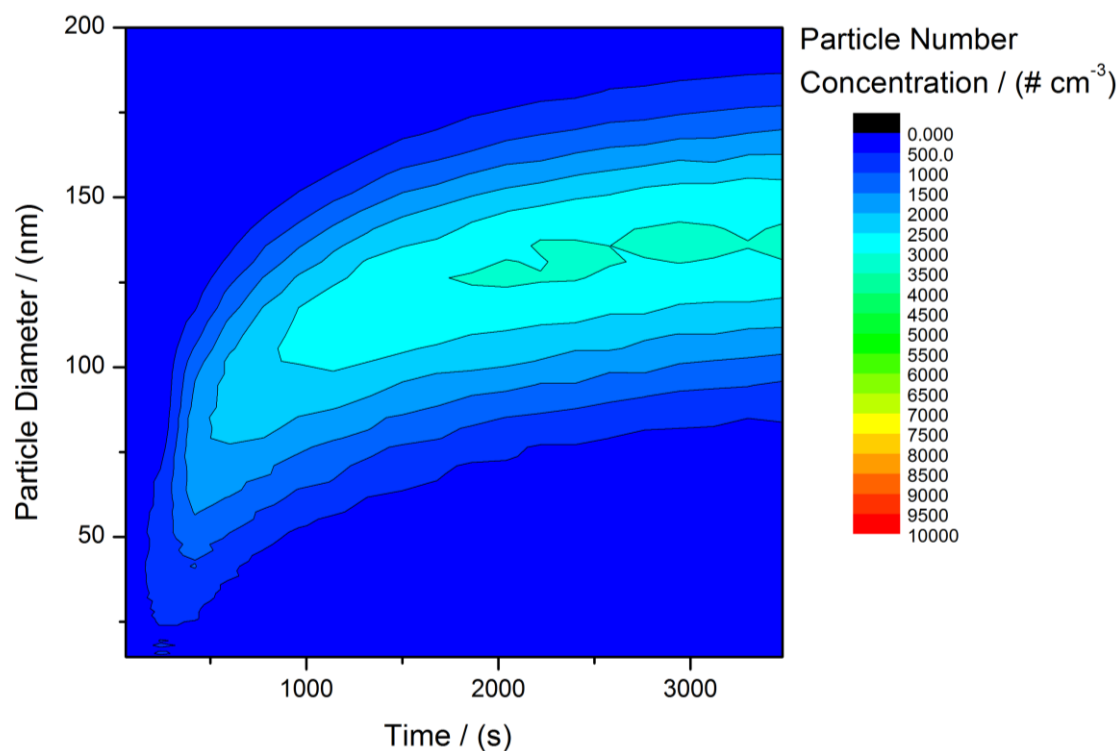


Figure 50: SOA size distribution as a function of time;  $[\alpha\text{-pinene}] = 0.20$  ppm,  $[\text{O}_3] = 0.10$  ppm; ethanol scavenger.

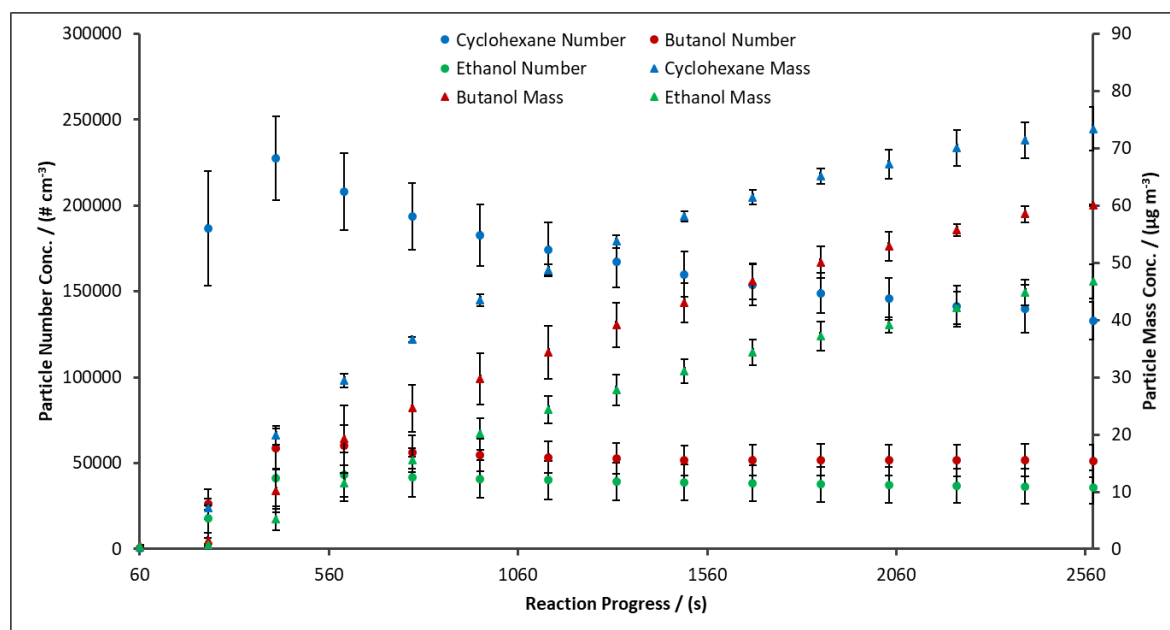


Figure 51: Number and mass concentrations vs. time.  $[\alpha\text{-pinene}] = 0.20$  ppm;  $[\text{ozone}] = 0.10$  ppm. Circles represent number concentrations; triangles represent mass concentrations. Blue = cyclohexane-scavenged experiments; red = butanol-scavenged experiments; green = ethanol-scavenged experiments.

It is clear from these results that the use of cyclohexane as a scavenger, as opposed to either of the alcohol scavengers, contributes to formation of a large number of smaller

particles, compared with a small number of large particles for each of the alcohol scavengers. This effect is slightly more pronounced for ethanol as opposed to butanol. Mean particle diameters 45 minutes after introduction of ozone were  $90.4 \pm 6.5$ ,  $129.4 \pm 7.2$  and  $128.8 \pm 3.5$  nm for cyclohexane, butanol and ethanol respectively, while particle number concentrations were  $1.29 \pm 0.25 \times 10^5$ ,  $5.1 \pm 1.1 \times 10^4$  and  $3.0 \pm 0.5 \times 10^4$   $\text{cm}^{-3}$ , respectively.

Mass yields have been calculated for this reaction in the presence of each of cyclohexane, butanol and ethanol respectively:  $13.55 \pm 0.18$  %,  $10.97 \pm 0.11$  % and  $8.92 \pm 0.57$  %.

These results are summarised in Table 7:

[ $\alpha$ -Pinene] (ppm)	[Ozone] (ppm)	Scavenger	RH (%)	Number Conc. at 45 mins ( $\text{cm}^{-3}$ )	Mass Yield (%)	Mean Dia. at 45 mins (nm)
0.20	0.10	Cyclohexane	0	$1.29 \pm 0.25 \times 10^5$	$13.55 \pm 0.18$	$90.4 \pm 6.5$
0.20	0.10	Butanol	0	$5.1 \pm 1.1 \times 10^4$	$10.97 \pm 0.11$	$129.4 \pm 7.2$
0.20	0.10	Ethanol	0	$3.0 \pm 0.5 \times 10^4$	$8.92 \pm 0.57$	$128.8 \pm 3.5$

Table 7: Summary of experimental conditions and results for experiments with different scavengers.

The trend observed suggests that the use of cyclohexane, a scavenger which yields predominantly  $\text{RO}_2$  radicals, gives rise to a larger mass yield, comprising a significantly increased number of smaller particles. Conversely, the use of ethanol, a scavenger which produces mainly  $\text{HO}_2$  radicals from its reaction with  $\cdot\text{OH}$ , leads to the formation of fewer, larger particles, and a lower mass yield. Finally, the use of 2-butanol as a scavenger again leads to production of fewer, larger particles, albeit in higher number concentration than for ethanol. This corresponds to an increase in mass yield with respect to ethanol, although still significantly below that of cyclohexane-scavenged reactions.

This lends to the conclusion that the secondary reactions of  $\text{RO}_2$  radicals with the Criegee intermediates form products which facilitate particle nucleation to a greater extent than those formed from the similar reaction of  $\text{HO}_2$  radicals. Alternatively, reactions of  $\text{RO}_2$  with the cyclohexyl peroxy radical (see Figure 46) formed from reaction of  $\text{OH} +$  cyclohexane, and subsequent reactions with  $\text{RO}_2$  (see Figure 47), may form compounds more likely to participate in the accretion reactions discussed previously (see Figure 38).

Reactions of the cyclohexylperoxy radical with  $\text{HO}_2$  (Figure 46 & Figure 47) form only hydroperoxides, which may participate in limited accretion reactions—peroxyhemiacetal formation only. It should be noted that reaction with  $\text{RO}_2$  followed by  $\text{HO}_2$  may form compounds with both  $\text{ROH}$  and  $\text{R'OOH}$  moieties, which may participate in other types of reactions (see Figure 38). Reactions with  $\text{RO}_2$ , conversely, produce compounds with suitable moieties that they may participate in all of the accretion reactions highlighted in Figure 38. This increased ability for products of the  $\text{RO}_2$  channel to participate in accretion reactions, thus forming ELVOCs, may account for the large discrepancies observed between the different scavengers.

A modelling simulation previously carried out by Jenkin<sup>35</sup> suggested that the use of 2-butanol as a scavenger in the ozonolysis of  $\alpha$ -pinene produces a lower mass yield than for an identical reaction with cyclohexane as the scavenger. Jenkin attributes this reduction in mass yield to changes in molar yields of low volatility products, particularly highlighting decreased yields of hydroxypinonaldehydes, pinic acid and pinalic-3-acid when employing butanol as a scavenger, since formation of the least volatile products typically rely on  $\text{RO}_2$  chemistry. This is consistent with the data presented here. Conversely, Jonsson *et al.*<sup>42</sup> observed a larger SOA yield with 2-butanol as a scavenger compared to cyclohexane.

### 3.7 Impact of Relative Humidity

The impact of relative humidity (RH) on SOA size distribution and mass yield of the  $\alpha$ -pinene / ozone system was also investigated. Cyclohexane was used as a scavenger for these experiments due to the large number of particles produced compared to the alcohol scavengers (Figure 48). Therefore, any change in particle size distribution would be immediately obvious for this scavenger.

### 3.7.1 High Concentration Conditions

Reactions were carried out in a static chamber between  $\alpha$ -pinene (2.0 ppm) and  $\text{O}_3$  (1.0 ppm), under RH conditions of 0 %, 30 % and 80 %, the results of which are presented in Figure 52–Figure 54. Each is the average of three experiments.

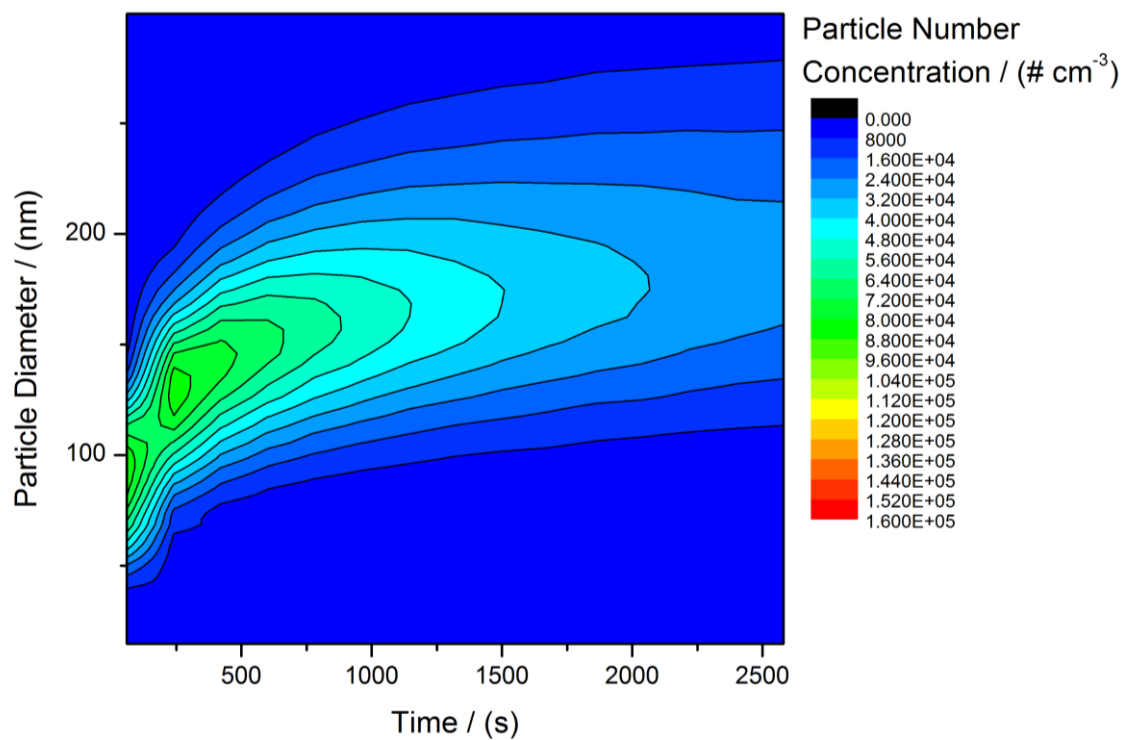


Figure 52: Particle number concentration as a function of particle diameter vs. time, for products of the reaction of  $\alpha$ -pinene [2.0 ppm] with ozone [1.0 ppm] at 0 % RH.

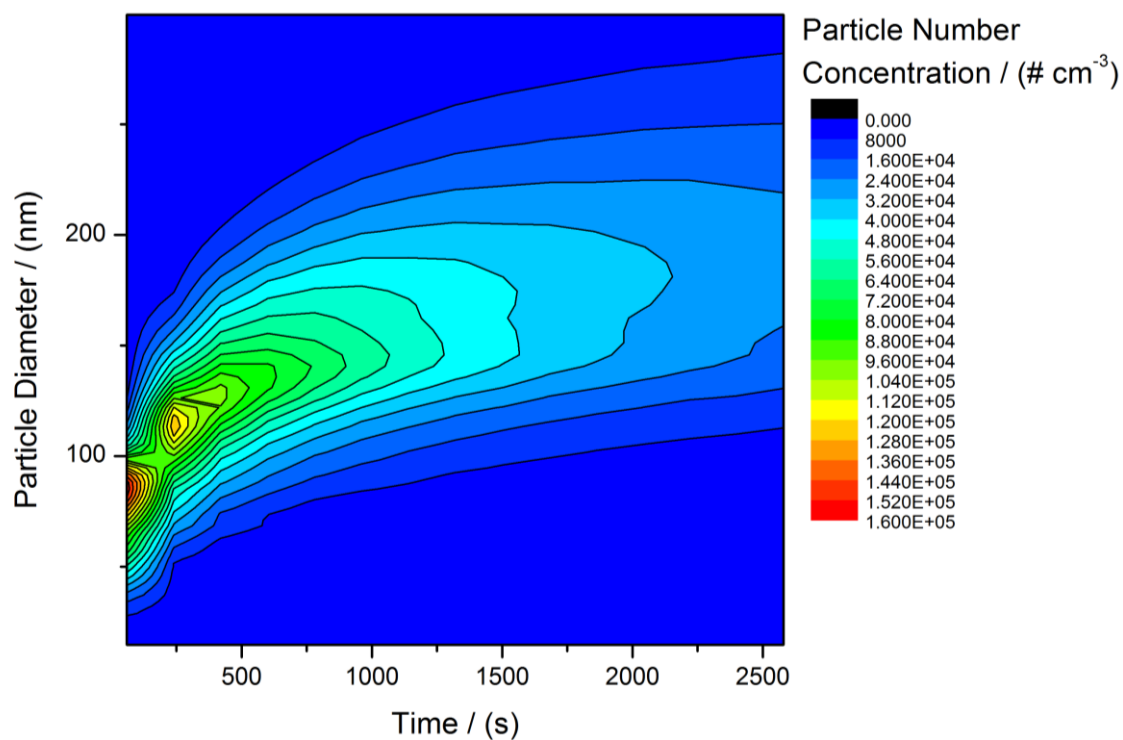


Figure 53: Particle number concentration as a function of particle diameter vs. time, for products of the reaction of  $\alpha$ -pinene [2.0 ppm] with ozone [1.0 ppm] at 30 % RH.

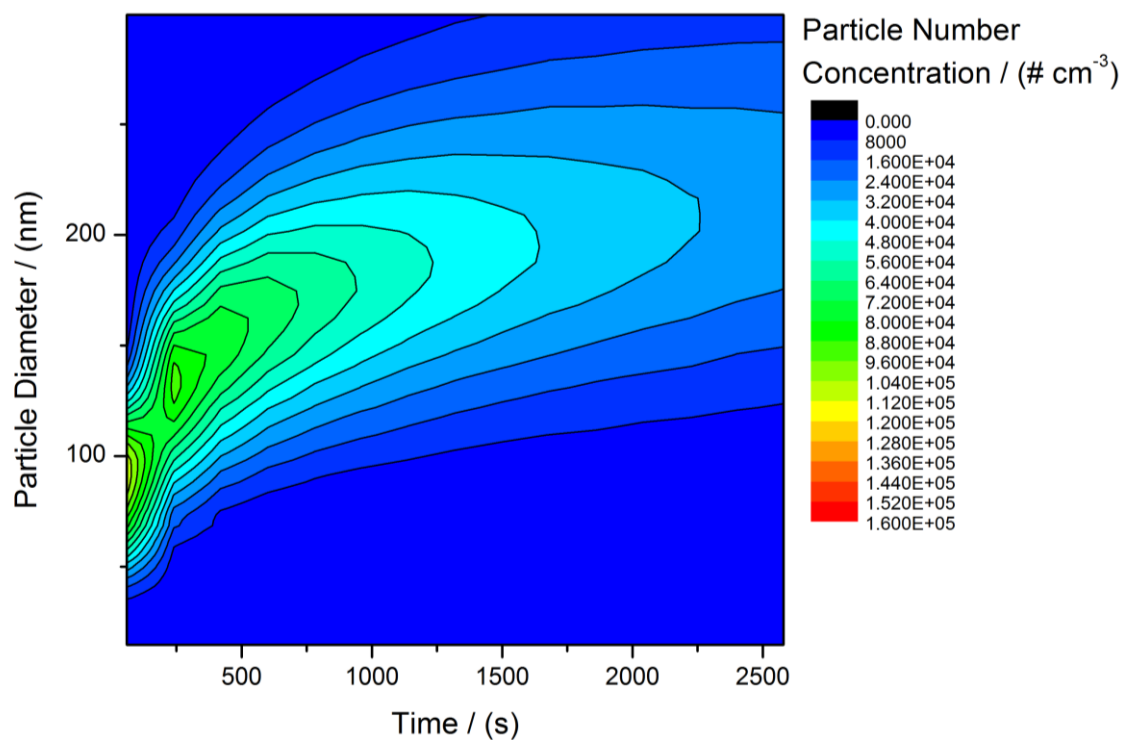


Figure 54: Particle number concentration as a function of particle diameter vs. time, for products of the reaction of  $\alpha$ -pinene [2.0 ppm] with ozone [1.0 ppm] at 80 % RH.

On initial observation, it appears as though there is a large difference between the number concentrations in the initial stages of each reaction. However, this is due to random variation in the mixing of species within the Teflon chamber, and can be disregarded. The effect of this mixing is nullified as SOA formation continues, and is known to have little impact on the mass yield or particle size formation as SOA growth progresses.

45 minutes after the initial introduction of ozone to the chamber, particle number concentrations under 0 % and 30 % RH conditions were  $5.68 \pm 0.24 \times 10^5$  and  $5.72 \pm 0.18 \times 10^5$  particles  $\text{cm}^{-3}$  respectively—well within experimental error. Similarly, mean particle diameters remained within experimental error, at  $200.2 \pm 1.7$  and  $198.8 \pm 1.4$  nm respectively. It can therefore be concluded that an increase from 0 % to 30 % RH has no effect on the particle size distribution of the SOA formed. Maximum observed mass concentrations were  $3.08 \pm 0.15 \times 10^3$   $\mu\text{g m}^{-3}$  and  $2.95 \pm 0.10 \times 10^3$   $\mu\text{g m}^{-3}$ , corresponding to mass yields of  $55.2 \pm 2.6$  % and  $53.0 \pm 1.8$  %, respectively. This provides further support to the conclusion that a small increase from 0 % to 30 % relative humidity has no influence on SOA formation. See Table 8 for a summary of experimental conditions and results. For simple salt systems, a dry particle will only take up water at a critical RH.<sup>43</sup> If this is also the case for more complex organic systems such as this, that would explain the observations reported here.

Upon a further increase from 30 % to 80 % RH, a clear shift in particle size distribution was observed, as demonstrated by the shift ‘upward’ from Figure 53 to Figure 54. 45 minutes after ozone introduction, this corresponds to a significant increase in mean diameter, from  $200.2 \pm 1.7$  to  $219.0 \pm 9.4$  nm. However, particle number concentration remained approximately constant, from  $5.72 \pm 0.18 \times 10^5$  particles  $\text{cm}^{-3}$  to  $5.88 \pm 0.16 \times 10^5$  particles  $\text{cm}^{-3}$ . A combination of these two factors resulted in an increase in particle mass concentration from those at 0 % and 30 % RH. The maximum observed mass concentration was noted to increase from  $3.08 \pm 0.15 \times 10^3$   $\mu\text{g m}^{-3}$  to  $4.12 \pm 0.46 \times 10^3$   $\mu\text{g m}^{-3}$ , while corresponding mass yields increased from  $55.2 \pm 2.6$  % to  $73.9 \pm 8.5$  %. It can therefore be concluded that an increase from 30 % to 80 % relative humidity, whilst having no impact on particle nucleation itself, does accelerate the growth of those

particles already nucleated. The reasons for these observed changes in SOA distribution will be discussed in section 3.7.3. The experimental conditions employed, and key data collected, are summarised in Table 8:

[ $\alpha$ -Pinene] (ppm)	[Ozone] (ppm)	Scavenger	RH (%)	Number Conc. at 45 mins ( $\text{cm}^{-3}$ )	Mass Yield (%)	Mean Dia. at 45 mins (nm)
2.0	1.0	Cyclohexane	0	$5.68 \pm 0.24 \times 10^5$	$55.2 \pm 2.6$	$200.2 \pm 1.7$
2.0	1.0	Cyclohexane	30	$5.72 \pm 0.18 \times 10^5$	$53.0 \pm 1.8$	$198.8 \pm 1.4$
2.0	1.0	Cyclohexane	80	$5.88 \pm 0.16 \times 10^5$	$73.9 \pm 8.5$	$219.0 \pm 9.4$

Table 8: Summary of experimental conditions and results of investigation into RH effect at high reactant concentrations.

The increase in mass yield observed here further lends credibility to the suggestion that there exists a critical RH value for these particles, below which uptake of water does not occur, and that this value lies somewhere between 30–80 %.

### 3.7.2 Low Concentration Conditions

A further set of reactions were carried out to investigate the effect of RH on SOA yield, under the lower concentration conditions of 0.2 and 0.1 ppm,  $\alpha$ -pinene and ozone respectively. Again, these experiments were carried out under 0, 30 and 80 % RH conditions, and the results are presented in Figure 55 – Figure 57.



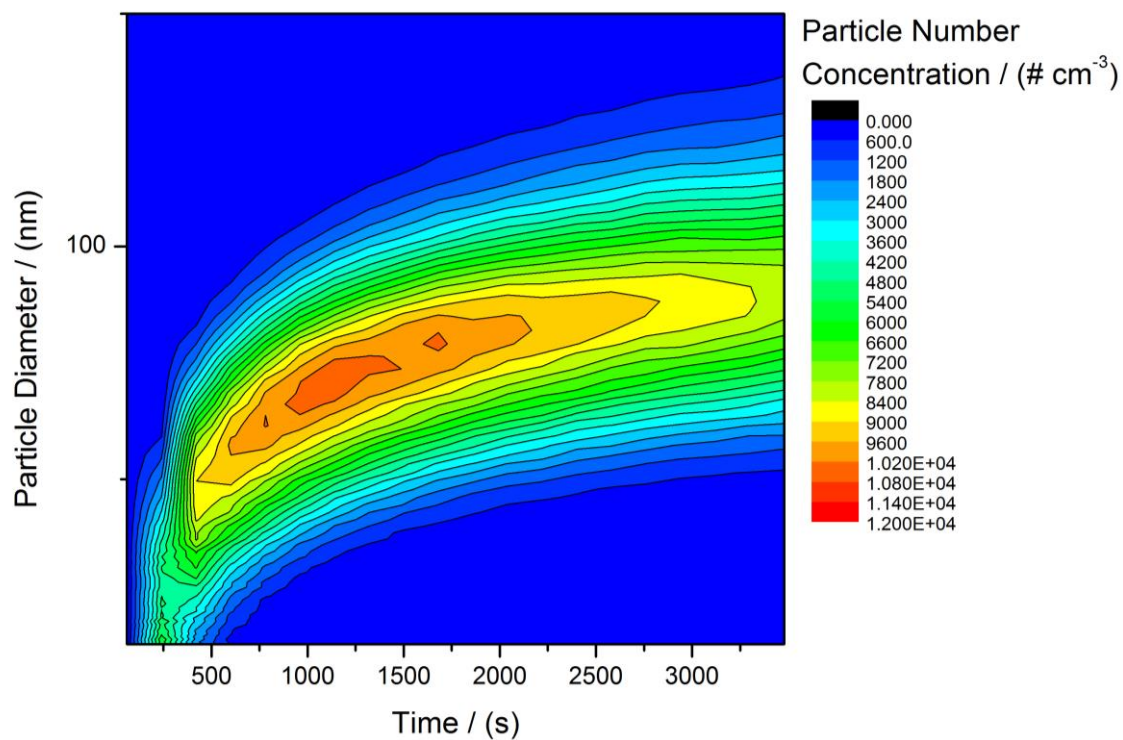


Figure 55: Particle number concentration as a function of particle diameter and time, for products of the reaction of  $\alpha$ -pinene [0.2 ppm] with ozone [0.1 ppm] at 0 % RH.

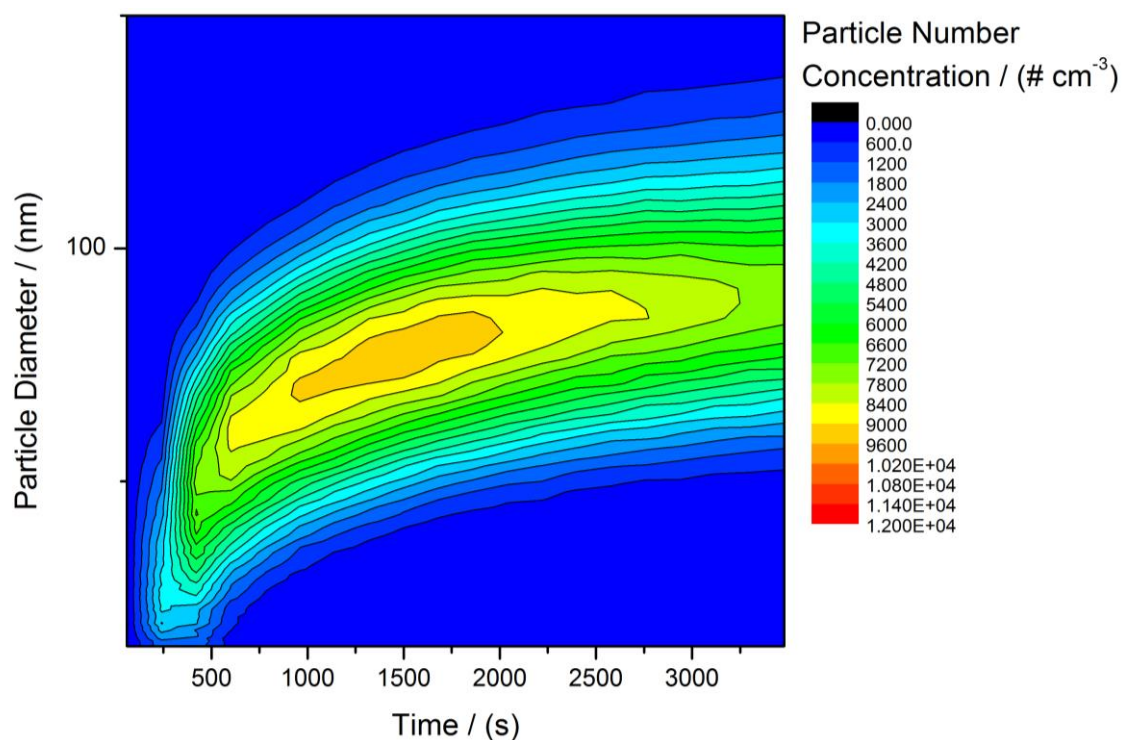


Figure 56: Particle number concentration as a function of particle diameter and time, for products of the reaction of  $\alpha$ -pinene [0.2 ppm] with ozone [0.1 ppm] at 30 % RH.

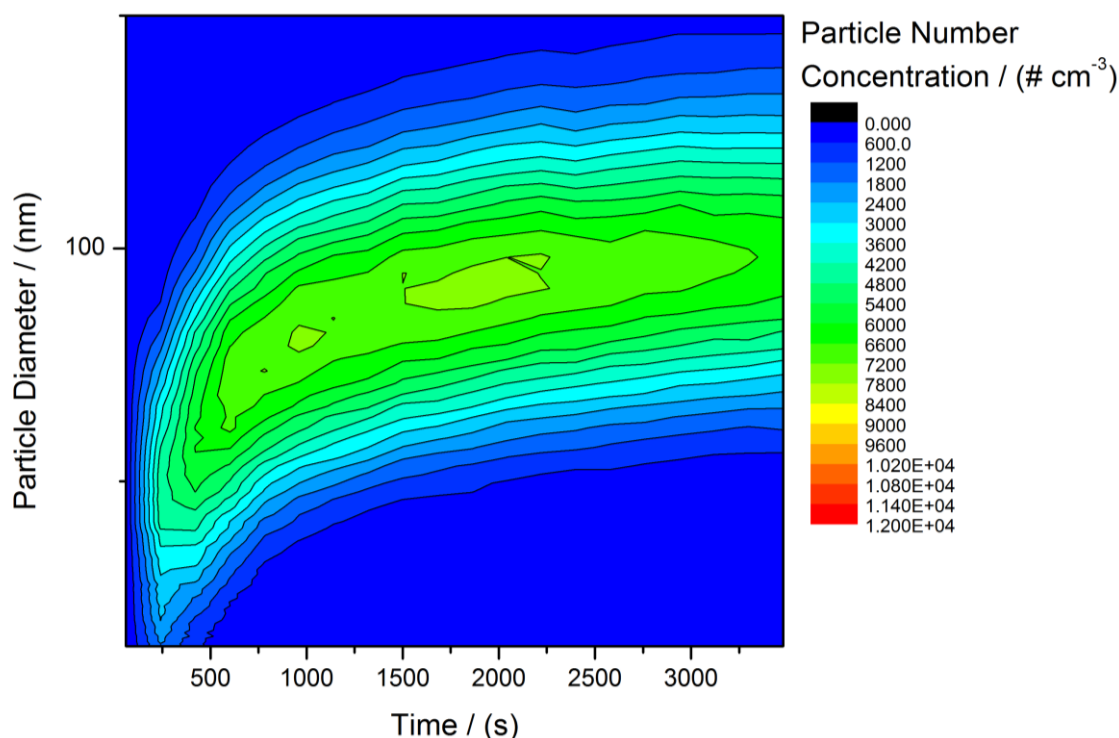


Figure 57: Particle number concentration as a function of particle diameter and time, for products of the reaction of  $\alpha$ -pinene [0.2 ppm] with ozone [0.1 ppm], at 80 % RH.

From observation, there appears to be little difference between the particle concentrations formed under 0 and 30 % RH conditions. Quantitatively, particle number concentrations after 45 minutes at 0 and 30 % RH were  $1.30 \pm 0.16 \times 10^5$  and  $1.26 \pm 0.14 \times 10^5 \text{ cm}^{-3}$ , respectively—i.e. overlapping within experimental error. Mean particle diameters were similarly unchanged, going from  $90.7 \pm 2.8$  to  $89.1 \pm 4.0 \text{ nm}$  with increasing RH—again, within experimental error. Maximum observed mass concentrations were  $69.3 \pm 6.5$  and  $63.8 \pm 6.5 \mu\text{g m}^{-3}$ —again, within experimental error. These corresponded to mass yields of  $13.75 \pm 1.23 \%$  and  $13.07 \pm 1.30 \%$ , under 0 % and 30 % RH, respectively. Thus, the observation that there is little difference between particles formed under 0 % and 30 % RH conditions holds true under low concentration conditions, in addition to the high concentrations discussed in section 3.7.1. See Table 9 for a summary of experimental conditions and results.

Further increasing the RH conditions from 30 to 80 %, as for the higher concentration conditions, resulted in a marked difference in the particle distribution profile. As evidenced by the contrast between Figure 55 and Figure 56 vs. Figure 57, there is a significant decrease in particle number concentration at 45 minutes, from  $1.30 \pm 0.16 \times$

$10^5$  to  $9.85 \pm 1.61 \times 10^5 \text{ cm}^{-3}$ . This is offset by an increase in mean particle diameter from  $90.7 \pm 2.8$  to  $98.4 \pm 3.8 \text{ nm}$ , resulting in little net change in particle mass concentration, from  $69.3 \pm 6.5$  to  $73.4 \pm 5.9 \mu\text{g m}^{-3}$ . This corresponds to a mass yield at 80 % RH of  $14.83 \pm 0.95 \%$ —a slight increase. However, both the mass concentration and mass yield of SOA lie within experimental error of the results obtained under 0 % RH conditions. Thus, we conclude that, under the low concentration conditions studied here, an increase in RH from 0 to 30 % again has little to no impact on the SOA profile. A further increase to 80 % causes a significant decrease in the number of particles formed. However, this is offset by an increase in the diameters of those particles, resulting in no significant net change in SOA yield. Despite this, the change in SOA size distribution may still be significant, since particle diameter is known to impact its properties—e.g. albedo of clouds incorporating these particles. A summary of the experimental conditions employed, and results obtained, is presented in Table 9:

[ $\alpha$ -Pinene] (ppm)	[Ozone] (ppm)	Scavenger	RH (%)	Number Conc. at 45 mins ( $\text{cm}^{-3}$ )	Mass Yield (%)	Mean Dia. at 45 mins (nm)
0.20	0.10	Cyclohexane	0	$1.30 \pm 0.16 \times 10^5$	$13.75 \pm 1.23$	$90.7 \pm 2.8$
0.20	0.10	Cyclohexane	30	$1.26 \pm 0.14 \times 10^5$	$13.07 \pm 1.30$	$89.1 \pm 4.0$
0.20	0.10	Cyclohexane	80	$9.85 \pm 1.61 \times 10^4$	$14.83 \pm 0.95$	$98.4 \pm 3.8$

Table 9: Summary of experimental conditions and results of investigation into RH effect at low reactant concentrations.

The indifference of the SOA yield between 0–30 % RH, followed by an increase from 30–80 %, lends further credibility to the suggestion of a critical RH. Prenni *et al.*<sup>44</sup> studied the water uptake of internally mixed particles containing an inorganic part (ammonium sulfate) and an organic dicarboxylic acid. They note that a high fraction of the dicarboxylic acid results in reduced water uptake. They also observe what appears to be a critical RH at around 80 % RH for their inorganic-organic mixed particles, further supporting this hypothesis. Recently, Järvinen *et al.*<sup>45</sup> observed the presence of a critical RH for  $\alpha$ -pinene SOA, above which water uptake is significantly enhanced. They suggest that this lies at around 35 % RH at  $-10^\circ\text{C}$ , and around 80 % at  $-38^\circ\text{C}$ , although they note that there may be significant uncertainty regarding the exact RH value.

### 3.7.3 Relative Humidity Conclusions

There are several possible consequences resulting from an increase in RH which may influence the formation of SOA, which will be discussed here, and are summarised in Table 10. The first, and simplest, of these is the potential for the water vapour itself to be incorporated into SOA. Water cannot, in the presence of other condensation nuclei, nucleate droplets itself (even in the absence of other condensation nuclei, this is highly unfavourable), and hence no change in number concentration as a direct result of new droplet formation would be expected. However, water vapour may be expected to condense onto existing SOA, potentially causing an increase in particle diameter and mass concentration. As mentioned in section 3.1, calculation of particle mass concentration uses a density of  $1.2 \text{ g cm}^{-3}$ . Therefore, incorporation of water into the aerosol may result in an overestimate of particle mass concentration (and thus mass yield) due to a decrease in average particle density.

A second potential consequence, and perhaps the most interesting, is that the presence of water vapour may influence the  $\text{HO}_2 / \text{RO}_2$  ratios described in section 3.6, causing the production of more  $\text{HO}_2$  than expected.<sup>46</sup> By comparing Figure 48 and Figure 49, it is clear that elevated  $\text{HO}_2 / \text{RO}_2$  ratios cause the formation of larger albeit fewer particles—that is, an increase in particle diameter and a decrease in number concentration—for reasons previously mentioned.

A third possibility is that, according to Raoult's law, and as previously described in section 1.7.2, partial vapour pressure of a component of a liquid mixture is proportional to its mole fraction in the mixture. By incorporating water into the aerosol particle, the mole fraction of each organic component is slightly decreased, resulting in a decrease in their partial vapour pressures, and thus condensation of vapours becomes slightly more favourable. The theoretical predictions of Pankow and Chang<sup>47</sup> suggest a particularly strong Raoult's law effect at low concentrations.

A final suggestion is that, as shown by Ma *et al.*,<sup>6</sup> the initial attack of ozone onto the  $\alpha$ -pinene molecule forms Criegee intermediates, which may then react with water to

form pinonic acid and pinonaldehyde, according to the reaction scheme in Figure 58., where M refers to any inert molecule which can absorb excess energy and stabilise the Cl.

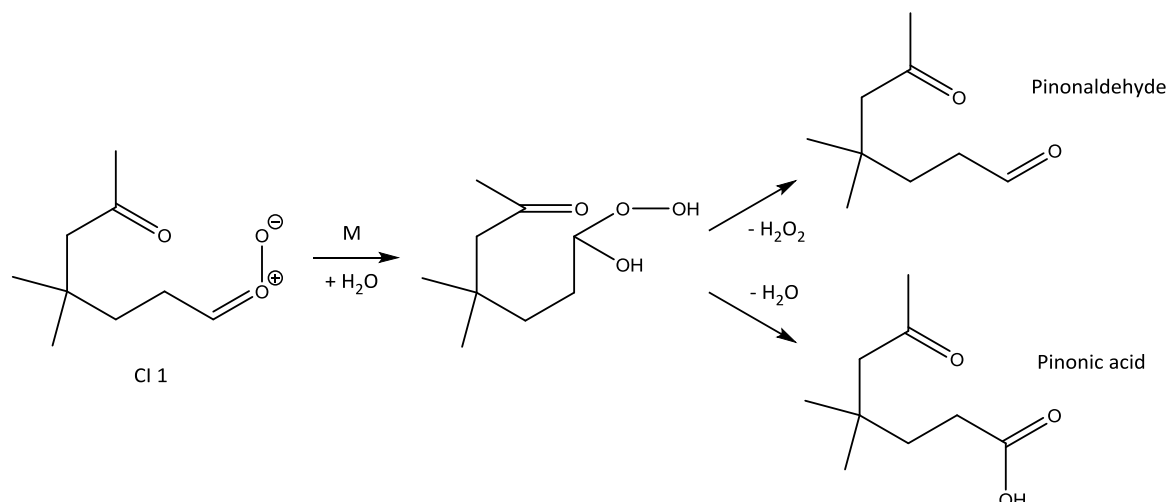


Figure 58: Reaction scheme for formation of pinonaldehyde and pinonic acid, reproduced from Ma *et al.*<sup>6</sup>

Pinonaldehyde is not known to act as a nucleating agent, but will condense onto clusters otherwise formed. Therefore, by increasing the amount of this compound present in the system, the amount of readily available condensable material is increased, allowing particles to grow more quickly. However, as the proportion of pinonaldehyde increases, conversely the proportion of other products must decrease. These include those products responsible for the nucleation of new clusters, and thus, whilst we may observe an increase in particle diameter, this may simultaneously cause a slight decrease in particle number concentration. Pinonic acid, meanwhile, is suspected to play a role in particle nucleation,<sup>9</sup> and thus an increased yield of this compound would result in a slightly increased particle number concentration. The combined effect of these changes in product yields on particle number concentration is not clear, but by increasing the proportion of low volatility products, particle mass concentration is expected to increase.







Effect of Increased Humidity	Expected Change in Number Conc.	Expected Change in Mass Conc.
Direct Water Incorporation	—	
Elevated HO <sub>2</sub> / RO <sub>2</sub> Ratio		
Raoult's Law Effect		
Altered Product Yields	—	

Table 10: Summary of RH influences on SOA profile

Both sets of conditions studied here observed no change in the SOA profile when RH was increased from 0 % to 30 % RH. Both sets of conditions saw an increase in mean particle diameter by approximately 10 %, when RH was further increased to 80 %. However, under low concentration conditions, a decrease in number concentration was also observed, which offset the increase in diameter to cause no significant change in the final mass concentration. Under high concentration conditions, number concentration remained constant, and an increase in mass concentration of approximately 33 % was observed.

Incorporation of water as a component into standard partitioning theories, according to the calculations of Hallquist *et al.*,<sup>2</sup> suggests a greater dependence on RH at low aerosol mass concentrations than at higher concentrations. However, they note that chamber studies often observe a less substantial RH effect since changes in product yields as a result of reaction with water are not accounted for in partitioning models. This is not in agreement with the observed trend in this work, where a greater dependence on RH was observed at high aerosol mass concentration.

Some work has previously been carried out by a number of groups looking into the effect of relative humidity on SOA formation for this system.<sup>23, 32, 48-51</sup> However, the results of these are as yet inconclusive, and thus this work is of particular relevance to better understand the relative humidity effect. Considering the reasons discussed previously for the effect of RH on SOA formation, it is of no surprise that studies have been inconclusive, since the effect is clearly a complex one. The conditions, and results, of studies by other groups are summarised in Table 11.

Study	[ $\alpha$ -pinene] / (ppm)	Scavenger	RH / (%)	Mass Conc.	Number Conc.
Cocker et al. <sup>32</sup>	0.041 - 0.124	2-Butanol	2 - 58	Increase	No mention
Jonsson et al. <sup>50</sup>	0.015, 0.030	2-Butanol	2 - 85	Increase	Increase
Rohr et al. <sup>51</sup>	56 - 266	No mention	13 - 41	No change	No change
Bonn et al. <sup>49</sup>	1.0	Cyclohexane	0.01, 31	No change	No change
	0.05	Cyclohexane	0.01, 31	Increase	Decrease
Berndt et al. <sup>48</sup>	0.049 - 0.713	Cyclohexane	0.2, 40	No mention	Slight decrease
This work	2.0	Cyclohexane	0.01 - 80	Increase	No change
	0.20	Cyclohexane	0.01 - 80	No change	Decrease

Table 11: Summary of previous work into the RH effect on SOA formation. References: <sup>32,49,48,51,50</sup>

The one clear conclusion that can be drawn from the combination of these studies is that an increase in RH seems to cause either no change, or an increase, in particle mass concentration. In this regard, the work described here is in agreement with the literature. The effect of RH on number concentration is where the discrepancies between the literature studies appear. It is interesting to note that, of those studies using 2-butanol as a scavenger, Cocker *et al.*<sup>32</sup> make no mention of any change in number concentration, and Jonsson *et al.*<sup>50</sup> note an increase with increasing RH. As described in section 3.6, the use of 2-butanol is known to increase the HO<sub>2</sub> / RO<sub>2</sub> ratio, and, as mentioned previously, the presence of water vapour may also lead to an elevated HO<sub>2</sub> / RO<sub>2</sub> ratio. However, if the HO<sub>2</sub> concentration is already much higher due to the choice of scavenger, the elevation of the HO<sub>2</sub> / RO<sub>2</sub> ratio by the presence of water vapour may have a smaller impact on number concentration than for other systems with a different scavenger, thus causing a smaller decrease. Therefore, if the decrease in number concentration is normally offset by an increase due to other factors (for cyclohexane-scavenged reactions), the reduction in the magnitude of this effect would hence lead to an increase in number concentration for butanol-scavenged reactions, as suggested by the literature in Table 11.

Thus, it seems logical to compare the results presented in this work predominantly with other cyclohexane-scavenged experiments. In this case, the data presented here agree with the work presented in the literature, which suggest either no change<sup>49, 51</sup> or a decrease<sup>48</sup> in number concentration, with increasing RH. The conclusion, therefore, is that an increase in relative humidity results in an increase in mean particle diameter, and in particle mass concentration. However, the effect of changing RH on number concentration appears to be reliant on the scavenger used, suggesting an RH influence on RO<sub>2</sub> / HO<sub>2</sub> ratios. Cyclohexane-scavenged experiments, such as those presented here, tend to show a decrease in particle number concentration with increasing RH. Butanol-scavenged experiments, meanwhile, appear to show either no change or an increase in particle number concentration with increasing RH.

### 3.8 Physical State of Aerosol

As mentioned previously,  $\alpha$ -pinene SOA is now typically believed to be solid or semi-solid under low RH conditions.<sup>52, 53</sup> The physical state of those particles in higher RH conditions, however, is less established.

Kidd *et al.*<sup>54</sup> studied impaction patterns of  $\alpha$ -pinene SOA under varying RH conditions (25–87 %). They observed that, as RH was increased, the viscosity of particles formed under those conditions decreased. However, even under the highest RH conditions investigated, they note that the aerosol formed were still semi-solid, not liquid particles. Kidd *et al.*<sup>54</sup> also carried out experiments using SOA formed under dry conditions and subsequently humidified (25–85 %). They show that there is a significant difference between particles formed under dry conditions and then exposed to high RH compared to those formed under high RH conditions. The ‘dry’ particles showed no significant change on exposure to the high RH conditions, and as such exhibited higher viscosities than those formed in ‘wet’ conditions. They also continued to behave as solid or semi-solid particles across all RH conditions studied.

Pajunoja *et al.*<sup>53</sup> investigated the physical state of SOA formed from  $\alpha$ -pinene oxidation under varying RH conditions at room temperature, using an Aerosol Bounce Instrument,



which functions similarly to the ELPI+ instrument described in section 2.5. They noted that the fraction of particles that bounced upon contact with the impactor at a given RH had a significant dependence on O:C ratio of the aerosol. An increase in O:C ratio of the SOA, at a given RH, resulted in a reduction in the bounced fraction. For the highest O:C (= 0.7), particles began to behave mechanically as liquids at approximately 65 % RH and above. Meanwhile, even at 90 % RH, particles with the lowest O:C (=0.45) were still observed to behave as solid or semi-solid particles.

In this section, the physical state of aerosol products of the reaction between  $\alpha$ -pinene and ozone were studied through ELPI+ experiments during a 4-week loan period, according to the method described in section 2.5, with [ $\alpha$ -pinene] = 2 ppm and [ $O_3$ ] = 1 ppm. The  $\alpha$ -pinene /  $O_3$  system has previously been studied through ELPI+,<sup>52</sup> though not in great depth. In the work presented here, experiments were carried out at 0 %, 30 % and 80 % relative humidity, on each of non-greased, greased and sintered impactor plates. Cyclohexane was employed as a scavenger for all of the ELPI+ experiments conducted. The results from the ELPI+ experiments are presented in Figure 59, with each data set averaged across 2–3 experiments unless otherwise stated, apart from those using sintered plates, where time constraints meant that no repeats could be performed. Unfortunately, as a result of this, it is not possible to calculate uncertainties of the bounce factors presented in this section, and therefore all results should be treated as preliminary results only.

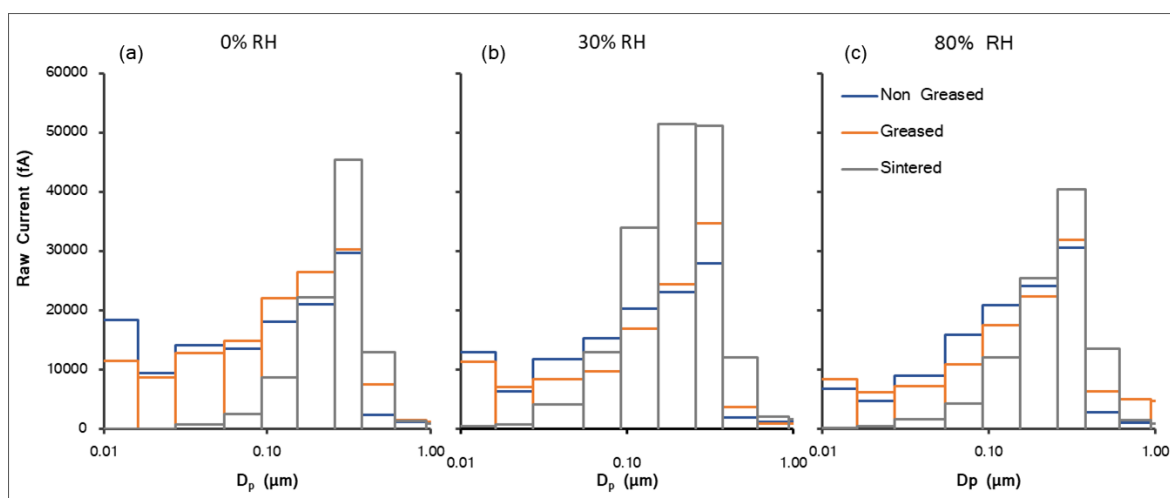


Figure 59: ELPI+ Current Distributions at: (a) 0 % RH; (b) 30 % RH; (c) 80 % RH, for different impactor substrates. Initial reactant concentrations:  $[\alpha\text{-pinene}] = 2 \text{ ppm}$ ,  $[\text{O}_3] = 1 \text{ ppm}$ .

At 0 % RH, it is clear that there is a reduction in the number of small particles observed on the greased plates compared to the non-greased plates, and this effect is mirrored by an increase in the number of larger particles observed. Further comparison to sintered plates confirms that particle bounce has only been reduced, and not eliminated, by introduction of the greased plates.

By assuming complete elimination of particle bounce by the sintered plates, and using equation (23), the bounce factor for aerosol products of the reaction between  $\alpha$ -pinene and  $\text{O}_3$  under 0 % RH conditions can be calculated as 0.209. This can be compared to the bounce factors reported by Virtanen *et al.* for  $\alpha$ -pinene +  $\text{O}_3$ ,<sup>52</sup> which vary from approximately 0.29–0.34, dependent on particle size, with the largest bounce factor observed around 70 nm. For further comparison, amorphous polystyrene has been reported to have a bounce factor varying from 0.3–0.45, dependent on particle size; crystalline  $(\text{NH}_4)_2\text{SO}_4$  as having bounce factor of approximately 0.06–0.13, dependent on particle size, and liquid dioctyl sebacate as having a bounce factor of 0–0.02.<sup>52</sup>

Therefore, the aerosol produced from the reaction of  $\alpha$ -pinene +  $\text{O}_3$  at 0 % RH appears, from this experiment, to behave most like a crystalline solid. However, time limitations meant that the bounce factor from these experiments was only able to be calculated as an average across all particle diameters studied, and thus it is likely that the particles

behave more like amorphous solids at some particle sizes, and more like crystalline solids at others.

When the reaction was performed under 30 % RH conditions (Figure 59 b), a small shift in observed particle diameter was again noted when going from non-greased to greased plates, but the impact of this change appears to be very minor, and is hardly notable.

A comparison to the assumed-ideal current produced by use of sintered plates allows for calculation of a bounce factor of 0.153 for particles formed under 30 % RH conditions.

This is comparable to the bounce factor of 0.06–0.13 for crystalline  $(\text{NH}_4)_2\text{SO}_4$ , suggesting that the aerosol produced is crystalline in nature.

At 80 % RH (Figure 59 c), the current distribution for greased plates is profoundly different to both the non-greased and sintered plate results. This result appears to be anomalous since it shows a higher current than both the non-greased and sintered plates at both low and high particle diameters (see Figure 60 for full size range), and is likely due to a poor zero prior to data collection. Unfortunately, due to time constraints, it was not possible to repeat this experiment.

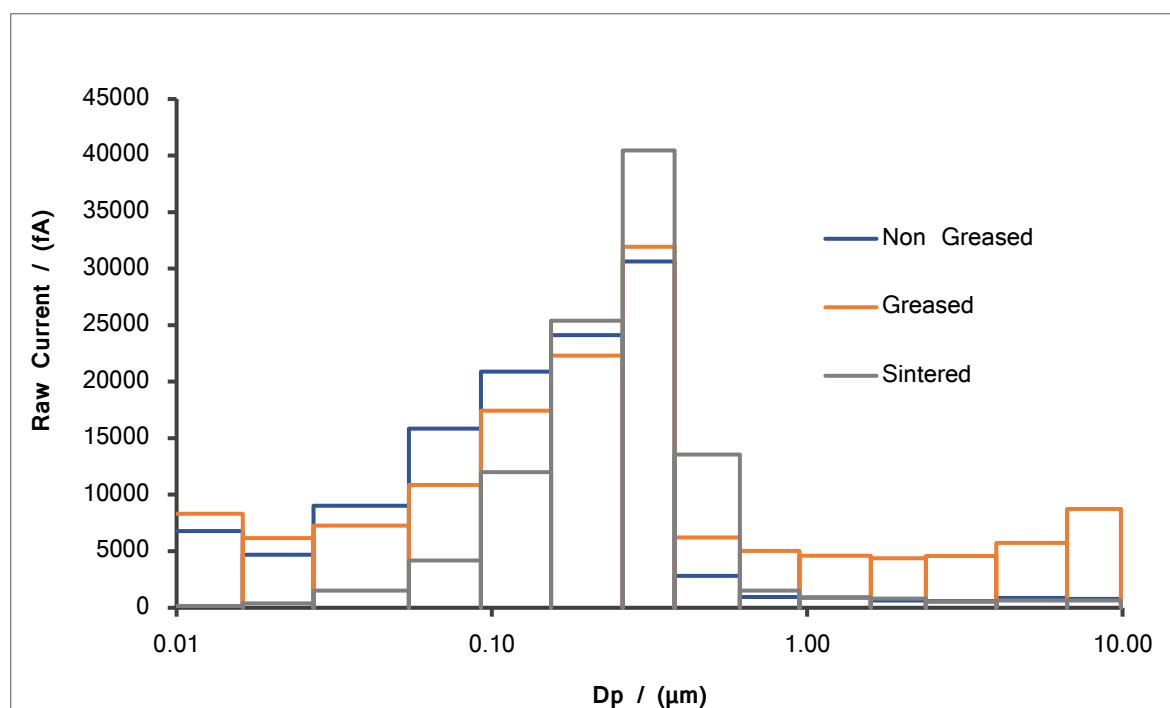


Figure 60: ELPI+ Current Distribution at 80 % RH (full size range).

Again, a comparison between the non-greased and sintered plates shows that the non-greased distribution is heavily skewed towards smaller particles, due to particle bounce, whilst the sintered plate results show  $I_{\leq 27 \text{ nm}} = 500 \text{ fA}$ . Again, whilst this is slightly above the accepted background level of 200 fA, it is still negligible in comparison to the current recorded for non-greased plates, and thus we can assume that sintered plates effectively eliminate particle bounce, and  $I_{\text{sintered}} \equiv I^{\text{id}}$ .

Bounce factor for these aerosol particles, under 80 % RH conditions, can therefore be calculated as 0.096. They can therefore be approximated as crystalline solids in nature.

The bounce factors calculated in this section, the experimental conditions employed, and the indicated phase of SOA formed are summarised in Table 12:

[ $\alpha$ -Pinene] (ppm)	[Ozone] (ppm)	Scavenger	RH (%)	Bounce Factor	Indicated Particle Phase
2.0	1.0	Cyclohexane	0	0.209	Crystalline Solid
2.0	1.0	Cyclohexane	30	0.153	Crystalline Solid
2.0	1.0	Cyclohexane	80	0.096	Crystalline Solid

Table 12: Summary of calculated bounce factors for SOA formed under varying RH conditions, and their indicated phase.

### 3.9 Conclusions

The  $\alpha$ -pinene ozonolysis was thoroughly investigated, and conclusions reached on the effect of a number of variables. The relationship between aerosol mass concentration and aerosol mass fraction—an area extensively reported on in the literature—was revisited, and good agreement was observed between our system and the literature. This lends confidence to future results obtained from more complex systems. The range of concentrations investigated was also extended to look at higher mass concentrations, as suggested by Presto and Donahue.<sup>31</sup>

A rate constant for the reaction of  $\alpha$ -pinene with ozone was determined, by comparison of the SOA evolution profile to a simulated extent of reaction. A value of  $k = 1.05 \pm 0.11 \times$

$10^{-16} \text{ cm}^3 \text{ molecule}^{-1} \text{ s}^{-1}$  was obtained, which is in good agreement with the IUPAC preferred value of  $9.4 \pm 0.15 \times 10^{-17} \text{ cm}^3 \text{ molecule}^{-1} \text{ s}^{-1}$ .<sup>27</sup>

The effect of different scavengers, and the varying  $\text{RO}_2 / \text{HO}_2$  ratios produced by each, was investigated. It was noted that an elevated  $\text{RO}_2 / \text{HO}_2$  ratio gave rise to a large number of smaller particles, and overall showed an increased mass yield. Conversely, a higher  $\text{HO}_2 / \text{RO}_2$  ratio produced fewer, larger particles, and an overall lower mass yield.

The effect of relative humidity was observed to vary, dependent on the initial reactant concentrations. Under high initial concentrations, RH was observed to have no impact on the formation of fresh SOA, but did have a significant impact on SOA growth. No difference was observed in the aerosol size distribution between 0 % and 30 % RH, but an increase to 80 % RH gave rise to a significant increase in particle diameter of ca. 10 %, and thus a rise in mass concentration of approximately 33 %.

Under low initial concentrations, an increase in RH was noted to severely constrain particle formation, causing a reduction of ca. 25 %, when RH was increased to 80 %. This was offset by an increase in particle diameter of approximately 10 %, resulting in no significant difference in mass concentration. Since a wide range of RH conditions are observed within the atmosphere, an understanding of how this affects SOA growth is significant.

The physical state of SOA formed was noted to be independent of relative humidity, remaining crystalline solid under 0 % to 80 % RH conditions. This has strong implications for the lifetime of particles within the atmosphere since, whilst liquid particles might be expected to allow species, such as gas-phase oxidants, to penetrate the surface, a crystalline solid would be expected to be more resistant to penetration by other species, thereby restricting reactions to the surface and extending the lifetime of SOA within the atmosphere, thus increasing its potential to contribute to the net negative radiative forcing associated with aerosols.

### 3.10 References

1. A. Guenther, C. N. Hewitt, D. Erickson, R. Fall, C. Geron, T. Graedel, P. Harley, L. Klinger, M. Lerdau, W. A. McKay, T. Pierce, B. Scholes, R. Steinbrecher, R. Tallamraju, J. Taylor and P. Zimmerman, *J. Geophys. Res.-Atmos.*, 1995, **100**, 8873-8892.
2. M. Hallquist, J. C. Wenger, U. Baltensperger, Y. Rudich, D. Simpson, M. Claeys, J. Dommen, N. M. Donahue, C. George, A. H. Goldstein, J. F. Hamilton, H. Herrmann, T. Hoffmann, Y. Iinuma, M. Jang, M. E. Jenkin, J. L. Jimenez, A. Kiendler-Scharr, W. Maenhaut, G. McFiggans, T. F. Mentel, A. Monod, A. S. H. Prévôt, J. H. Seinfeld, J. D. Surratt, R. Szmigielski and J. Wildt, *Atmos. Chem. Phys.*, 2009, **9**, 5155-5236.
3. R. Criegee, *Angew. Chem. Int. Ed. Engl.*, 1975, **14**, 745-752.
4. Y.-T. Su, Y.-H. Huang, H. A. Witek and Y.-P. Lee, *Science*, 2013, **340**, 174-176.
5. Y. Ma, T. R. Willcox, A. T. Russell and G. Marston, *Chem. Comm.*, 2007, 1328-1330.
6. Y. Ma, A. T. Russell and G. Marston, *Phys. Chem. Chem. Phys.*, 2008, **10**, 4294-4312.
7. X. Zhang, Z. Chen, H. Wang, S. He and D. Huang, *Atmos. Environ.*, 2009, **43**, 4465-4471.
8. T. S. Christoffersen, J. Hjorth, O. Horie, N. R. Jensen, D. Kotzias, L. L. Molander, P. Neeb, L. Ruppert, R. Winterhalter, A. Virkkula, K. Wirtz and B. R. Larsen, *Atmos. Environ.*, 1998, **32**, 1657-1661.
9. J. Zhao, *Experimental and Theoretical Investigation of Nucleation and Growth of Atmospheric Aerosols*, Texas A&M University, Ph.D., 2007.
10. M. Bilde and S. N. Pandis, *Environ Sci Technol*, 2001, **35**, 3344-3349.
11. M. E. Jenkin, D. E. Shallcross and J. N. Harvey, *Atmos. Environ.*, 2000, **34**, 2837.
12. S. Koch, R. Winterhalter, E. Uherek, A. Kolloff, P. Neeb and G. K. Moortgat, *Atmos. Environ.*, 2000, **34**, 4031.
13. D. Johnson, M. E. Jenkin, K. Wirtz and M. Martin-Reviejo, *Environ. Chem.*, 2005, **2**, 35-48.
14. K. P. Wyche, P. S. Monks, A. M. Ellis, R. L. Cordell, A. E. Parker, C. Whyte, A. Metzger, J. Dommen, J. Duplissy, A. S. H. Prevot, U. Baltensperger, A. R. Rickard and F. Wulfert, *Atmos. Chem. Phys.*, 2009, **9**, 635-665.
15. P. J. Ziemann, *J. Phys. Chem. A*, 2002, **106**, 4390-4402.
16. X. Zhang, R. C. McVay, D. D. Huang, N. F. Dalleska, B. Aumont, R. C. Flagan and J. H. Seinfeld, *Proc. Natl. Acad. Sci. U.S.A.*, 2015, **112**, 14168-14173.
17. M. Ehn, J. A. Thornton, E. Kleist, M. Sipilä, H. Junninen, I. Pullinen, M. Springer, F. Rubach, R. Tillmann, B. Lee, F. Lopez-Hilfiker, S. Andres, I.-H. Acir, M. Rissanen, T. Jokinen, S. Schobesberger, J. Kangasluoma, J. Kontkanen, T. Nieminen, T. Kurtén, L. B. Nielsen, S.

- Jørgensen, H. G. Kjaergaard, M. Canagaratna, M. D. Maso, T. Berndt, T. Petäjä, A. Wahner, V.-M. Kerminen, M. Kulmala, D. R. Worsnop, J. Wildt and T. F. Mentel, *Nature*, 2014, **506**, 476.
18. M. Camredon, J. F. Hamilton, M. S. Alam, K. P. Wyche, T. Carr, I. R. White, P. S. Monks, A. R. Rickard and W. J. Bloss, *Atmos. Chem. Phys.*, 2010, **10**, 2893-2917.
19. W. A. Glasoe, K. Volz, B. Panta, N. Freshour, R. Bachman, D. R. Hanson, P. H. McMurry and C. Jen, *J. Geophys. Res.-Atmos.*, 2015, **120**, 1933-1950.
20. J. Kirkby, J. Curtius, J. Almeida, E. Dunne, J. Duplissy, S. Ehrhart, A. Franchin, S. Gagne, L. Ickes, A. Kurten, A. Kupc, A. Metzger, F. Riccobono, L. Rondo, S. Schobesberger, G. Tsagkogeorgas, D. Wimmer, A. Amorim, F. Bianchi, M. Breitenlechner, A. David, J. Dommen, A. Downard, M. Ehn, R. C. Flagan, S. Haider, A. Hansel, D. Hauser, W. Jud, H. Junninen, F. Kreissl, A. Kvashin, A. Laaksonen, K. Lehtipalo, J. Lima, E. R. Lovejoy, V. Makhmutov, S. Mathot, J. Mikkila, P. Minginette, S. Mogo, T. Nieminen, A. Onnela, P. Pereira, T. Petaja, R. Schnitzhofer, J. H. Seinfeld, M. Sipila, Y. Stozhkov, F. Stratmann, A. Tome, J. Vanhanen, Y. Viisanen, A. Vrtala, P. E. Wagner, H. Walther, E. Weingartner, H. Wex, P. M. Winkler, K. S. Carslaw, D. R. Worsnop, U. Baltensperger and M. Kulmala, *Nature*, 2011, **476**, 429-U477.
21. J. H. Zollner, W. A. Glasoe, B. Panta, K. K. Carlson, P. H. McMurry and D. R. Hanson, *Atmos. Chem. Phys.*, 2012, **12**, 4399-4411.
22. C. N. Jen, R. Bachman, J. Zhao, P. H. McMurry and D. R. Hanson, *Geophys. Res. Lett.*, 2016, **43**, 867-873.
23. I. D. Hoare, *Physical Properties of Aerosol from the Ozonolysis of  $\alpha$ -Pinene and some of its Synthetic Derivatives*, University of Reading, Ph.D., 2013.
24. L. Q. Hao, S. Romakkaniemi, P. Yli-Pirilä, J. Joutsensaari, A. Kortelainen, J. H. Kroll, P. Miettinen, P. Vaattovaara, P. Tiitta, A. Jaatinen, M. K. Kajos, J. K. Holopainen, J. Heijari, J. Rinne, M. Kulmala, D. R. Worsnop, J. N. Smith and A. Laaksonen, *Atmos. Chem. Phys.*, 2011, **11**, 1367-1378.
25. E. A. Guggenheim, *The London, Edinburgh, and Dublin Philosophical Magazine and Journal of Science*, 1926, **2**, 538-543.
26. V. G. Khamaganov and R. A. Hites, *J. Phys. Chem. A*, 2001, **105**, 815-822.
27. R. Atkinson, D. L. Baulch, R. A. Cox, J. N. Crowley, R. F. Hampson, R. G. Hynes, M. E. Jenkin, M. J. Rossi and J. Troe, *Atmos. Chem. Phys.*, 2006, **6**, 3625-4055.
28. F. Nolting, W. Behnke and C. Zetzsch, *J. Atmos. Chem.*, 1988, **6**, 47.

29. D. J. Stewart, S. H. Almabrok, J. P. Lockhart, O. M. Mohamed, D. R. Nutt, C. Pfrang and G. Marston, *Atmos. Environ.*, 2013, **70**, 227-235.
30. R. K. Pathak, A. A. Presto, T. E. Lane, C. O. Stanier, N. M. Donahue and S. N. Pandis, *Atmos. Chem. Phys.*, 2007, **7**, 3811-3821.
31. A. A. Presto and N. M. Donahue, *Environ. Sci. Technol.*, 2006, **40**, 3536-3543.
32. D. R. Cocker lii, S. L. Clegg, R. C. Flagan and J. H. Seinfeld, *Atmos. Environ.*, 2001, **35**, 6049-6072.
33. R. J. Griffin, D. R. Cocker, R. C. Flagan and J. H. Seinfeld, *J. Geophys. Res.-Atmos.*, 1999, **104**, 3555-3567.
34. J. F. Pankow, *Atmos. Environ.*, 1994, **28**, 189-193.
35. M. E. Jenkin, *Atmos. Chem. Phys.*, 2004, **4**, 1741-1757.
36. J. S. Baxley and J. R. Wells, *Int. J. Chem. Kinet.*, 1998, **30**, 745-752.
37. A. A. Chew and R. Atkinson, *J. Geophys. Res.-Atmos.*, 1996, **101**, 28649-28653.
38. D. Grosjean, *J. Braz. Chem. Soc.*, 1997, **8**, 433-442.
39. R. H. Schwantes, R. C. McVay, X. Zhang, M. M. Coggon, H. Lignell, R. C. Flagan, P. O. Wennberg and J. H. Seinfeld, *Advances in Atmospheric Chemistry*, 1 edn., World Scientific Publishing Co., 2016.
40. M. S. Alam, M. Camredon, A. R. Rickard, T. Carr, K. P. Wyche, K. E. Hornsby, P. S. Monks and W. J. Bloss, *Phys. Chem. Chem. Phys.*, 2011, **13**, 11002-11015.
41. Y. Ma, R. A. Porter, D. Chappell, A. T. Russell and G. Marston, *Phys. Chem. Chem. Phys.*, 2009, **11**, 4184-4197.
42. Å. M. Jonsson, M. Hallquist and E. Ljungström, *Environ. Sci. Technol.*, 2008, **42**, 5938-5944.
43. G. J. Engelhart, L. Hildebrandt, E. Kostenidou, N. Mihalopoulos, N. M. Donahue and S. N. Pandis, *Atmos. Chem. Phys.*, 2011, **11**, 911-920.
44. A. J. Prenni, P. J. DeMott and S. M. Kreidenweis, *Atmos. Environ.*, 2003, **37**, 4243-4251.
45. E. Järvinen, K. Ignatius, L. Nichman, T. B. Kristensen, C. Fuchs, C. R. Hoyle, N. Höppel, J. C. Corbin, J. Craven, J. Duplissy, S. Ehrhart, I. El Haddad, C. Frege, H. Gordon, T. Jokinen, P. Kallinger, J. Kirkby, A. Kiselev, K.-H. Naumann, T. Petäjä, T. Pinterich, A. S. H. Prevot, H. Saathoff, T. Schiebel, K. Sengupta, M. Simon, J. G. Slowik, J. Tröstl, A. Virtanen, P. Vochezer, S. Vogt, A. C. Wagner, R. Wagner, C. Williamson, P. M. Winkler, C. Yan, U. Baltensperger, N. M. Donahue, R. C. Flagan, M. Gallagher, A. Hansel, M. Kulmala, F. Stratmann, D. R. Worsnop, O. Möhler, T. Leisner and M. Schnaiter, *Atmos. Chem. Phys.*, 2016, **16**, 4423-4438.



46. A. S. Hasson, M. Y. Chung, K. T. Kuwata, A. D. Converse, D. Krohn and S. E. Paulson, *J. Phys. Chem. A*, 2003, **107**, 6176-6182.
47. J. F. Pankow and E. I. Chang, *Environ. Sci. Technol.*, 2008, **42**, 7321-7329.
48. T. Berndt, O. Böge and F. Stratmann, *Atmos. Environ.*, 2003, **37**, 3933-3945.
49. B. Bonn, G. Schuster and G. K. Moortgat, *J. Phys. Chem. A*, 2002, **106**, 2869-2881.
50. Å. M. Jonsson, M. Hallquist and E. Ljungström, *Environ. Sci. Technol.*, 2006, **40**, 188-194.
51. A. C. Rohr, C. J. Weschler, P. Koutrakis and J. D. Spengler, *Aerosol Sci. Tech.*, 2003, **37**, 65-78.
52. A. Virtanen, J. Joutsensaari, T. Koop, J. Kannosto, P. Yli-Pirilä, J. Leskinen, J. M. Mäkelä, J. K. Holopainen, U. Pöschl, M. Kulmala, D. R. Worsnop and A. Laaksonen, *Nature*, 2010, **467**, 824-827.
53. A. Pajunoja, A. T. Lambe, J. Hakala, N. Rastak, M. J. Cummings, J. F. Brogan, L. Hao, M. Paramonov, J. Hong, N. L. Prisle, J. Malila, S. Romakkaniemi, K. E. J. Lehtinen, A. Laaksonen, M. Kulmala, P. Massoli, T. B. Onasch, N. M. Donahue, I. Riipinen, P. Davidovits, D. R. Worsnop, T. Petäjä and A. Virtanen, *Geophys. Res. Lett.*, 2015, **42**, 3063-3068.
54. C. Kidd, V. Perraud, L. M. Wingen and B. J. Finlayson-Pitts, *Proc. Natl. Acad. Sci. U.S.A.*, 2014, **111**, 7552-7557.

# Chapter 4

## Ozonolysis of the $\alpha$ -pinene enone derivative

### 4.1 Introduction

The importance of  $\alpha$ -pinene as a precursor to SOA was discussed in detail in the previous chapter. Section 3.1 introduced the reaction scheme for  $\alpha$ -pinene ozonolysis, which proceeds through two Criegee intermediates (CIs) to form a range of products.<sup>1</sup> Whilst considerable research on SOA formation from  $\alpha$ -pinene ozonolysis has been conducted, both in the literature and in this work, an as yet underexplored avenue is an investigation of the contribution of each Criegee intermediate to aerosol formation, only investigated in the literature in one study by Hoare (Ph.D. thesis).<sup>2</sup>

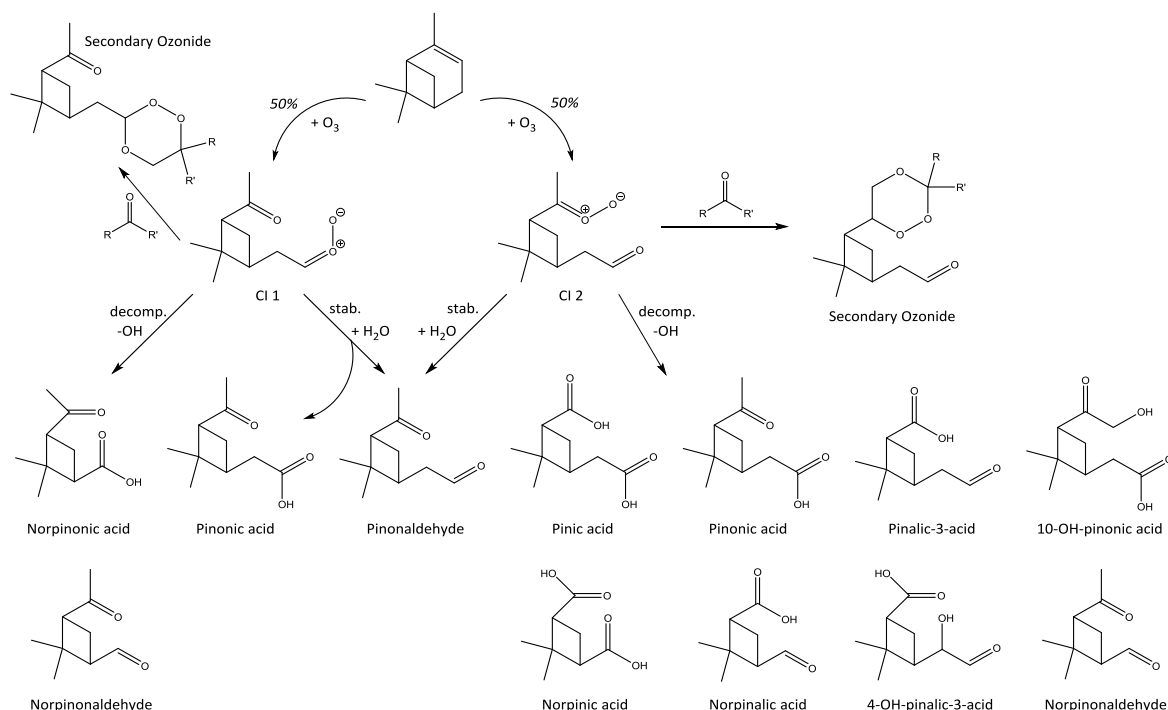


Figure 61: Products of the ozonolysis of  $\alpha$ -pinene, reproduced from Ma *et al.*<sup>1</sup>

In the product scheme published by Ma *et al.*,<sup>1</sup> presented previously in section 3.1 and again here for ease of reference, a number of the ozonolysis products have been

identified, along with which Criegee intermediate they originate from. Their methodology was to synthesise two new organic compounds with structures that, when ozonised, would each result in formation of only one of the CIs, allowing each to be studied in isolation—see Figure 62.

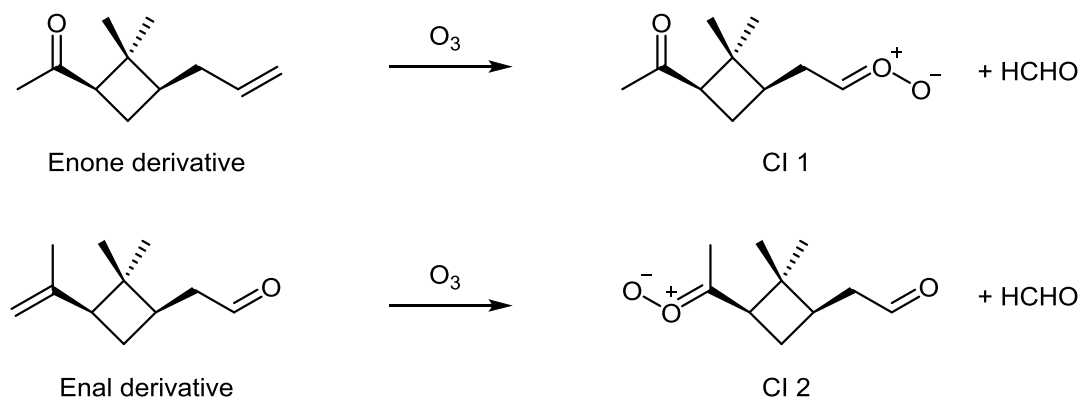


Figure 62: Formation of each Criegee intermediate from the  $\alpha$ -pinene derivatives

This leads to an interesting avenue of enquiry—if the array of products formed from each Criegee intermediate are substantially different, we might expect that each contributes differently to the total SOA yield. Indeed, this question has been addressed previously within the University of Reading atmospheric chemistry laboratory. Hoare<sup>2</sup> noted a marked difference between the SOA-forming capability of each CI.

Ozonolysis of the enal derivative (leading to CI 2) was reported to produce a slightly higher aerosol mass concentration than  $\alpha$ -pinene under the same conditions. Ozonolysis of the enone derivative (leading to CI 1) resulted in perhaps slightly lower mass concentrations than both  $\alpha$ -pinene and the enal. However, whilst the enal data seem reproducible and conclusive, the enone data show a poor degree of reproducibility—indeed, Hoare notes that, due to its low vapour pressure, introduction of the enone into their sample chamber was difficult, resulting in some uncertainty in the concentrations reported. The author further reports that, due to the complexity of its synthesis, only a very limited amount of the enone was available and few experiments were able to be performed. Estimates for the vapour pressures of both the enal and enone were calculated at 298 K and 1 bar. First, boiling point, critical temperature and critical pressure of the parent alkane (replacing the carbonyl group with two hydrogen atoms) were

calculated, according to the group contribution method of Marrero and Gani.<sup>3</sup> Vapour pressure of the parent alkane was then calculated according to the Lee-Kesler Correlation.<sup>4</sup> Finally, vapour pressure of the carbonyl was calculated according to the group contribution method of Capouet and Müller.<sup>5</sup> Estimated saturation vapour pressures for the enal and enone, respectively, are: 0.65 and 0.75 Torr. Uncertainty associated with estimation of the vapour pressure of the parent alkane may be up to  $\pm 50$  %.<sup>3</sup> Vapour pressures predicted by the Capouet and Müller method typically lie within a factor of 2–3 of the experimental values.<sup>5</sup> Therefore, the estimated vapour pressures of the enal and enone are expected to lie within a factor of 6 of the experimental values. Calculated values are summarised in Table 13:

Parameter	Enone	Enal
Boiling Point / (K) <sup>a</sup>	425.5	423.5
Critical Temperature / (K) <sup>a</sup>	605.3	604.6
Critical Pressure / (bar) <sup>a</sup>	22.38	22.32
Vapour Pressure (Parent Alkane) / (bar)	0.00672	0.00777
Vapour Pressure (Carbonyl) / (bar)	0.00086	0.00099

Table 13: Calculated constants for estimation of the vapour pressure of the enal and enone derivatives.

<sup>a</sup> Values refer to the parent alkane

Vapour pressures of the  $\alpha$ -pinene ozonolysis products have been calculated according to this method (using literature data for vapour pressures of the parent alkanes where available) by Capouet and Müller. They suggest that pinic and hydroxy pinonic acid are the least volatile compounds, with estimated vapour pressures of  $3 \times 10^{-6}$  and  $6 \times 10^{-7}$  Torr, respectively. They have calculated other primary products to have vapour pressures ranging from  $10^{-3}$  –  $10^{-5}$  Torr.<sup>5</sup> Vapour pressure of  $\alpha$ -pinene itself at 295 K is 4.75 Torr.<sup>6</sup>

The inconclusive data reported by Hoare, particularly in the case of the enone derivative, clearly warrant further investigation to allow for more reliable conclusions to be drawn with regards to the aerosol products of Cl 1. To this end, a synthesis of the enone derivative was undertaken, and ozonolysis experiments subsequently performed. These will be described within this chapter.

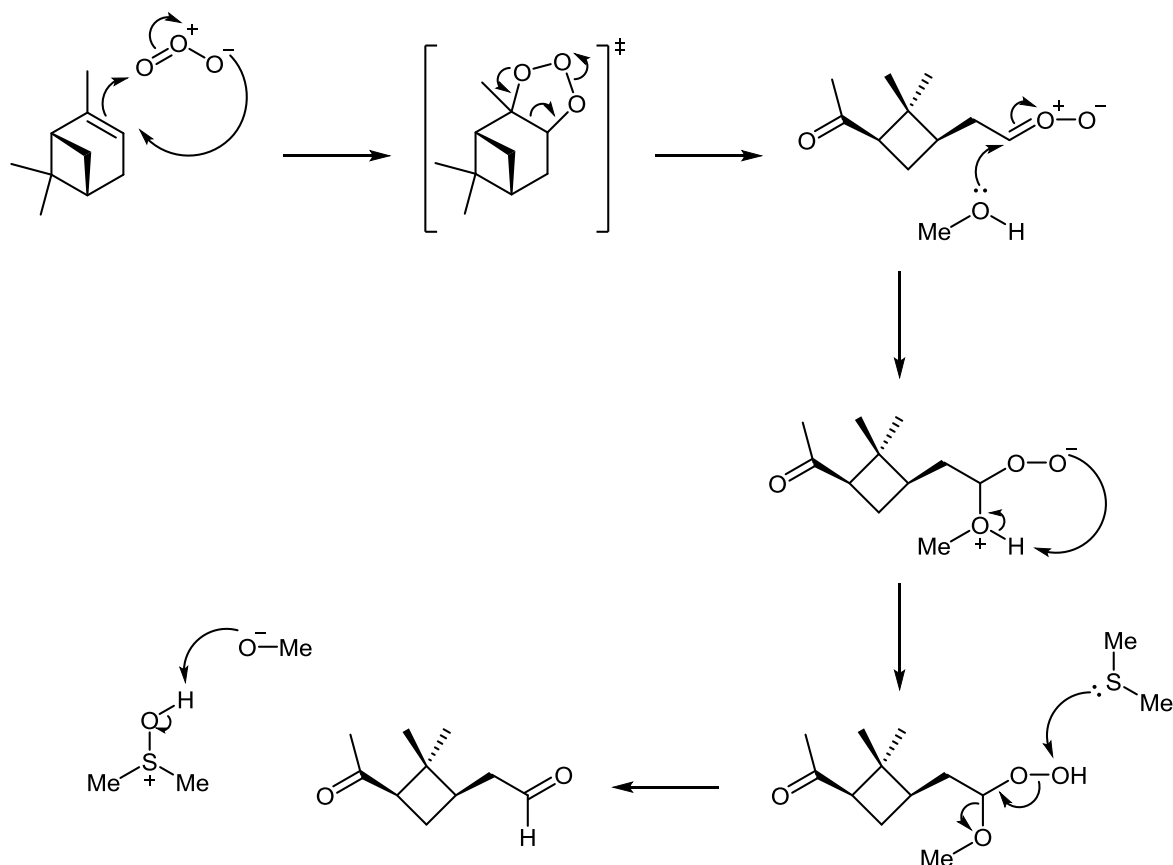
## 4.2 Enone Synthesis

The enone derivative of  $\alpha$ -pinene was prepared *via* a four step organic synthesis, beginning with an ozonolysis of  $\alpha$ -pinene itself, followed by a borohydride reduction, Wittig olefination, and finally a pyridinium chlorochromate (PCC) oxidation to form the desired compound (37 %). Both  $^1\text{H}$  and 2D-COSY- $^1\text{H}$  NMR spectra for each reported compound are provided in the appendix. This synthesis was carried out under the supervision of Dr Andy Russell (University of Reading) in July 2017, since an organic undergraduate project did not yield the desired product. The synthesis method followed was that previously developed by Dr Andy Russell. The synthesis steps are described in detail:

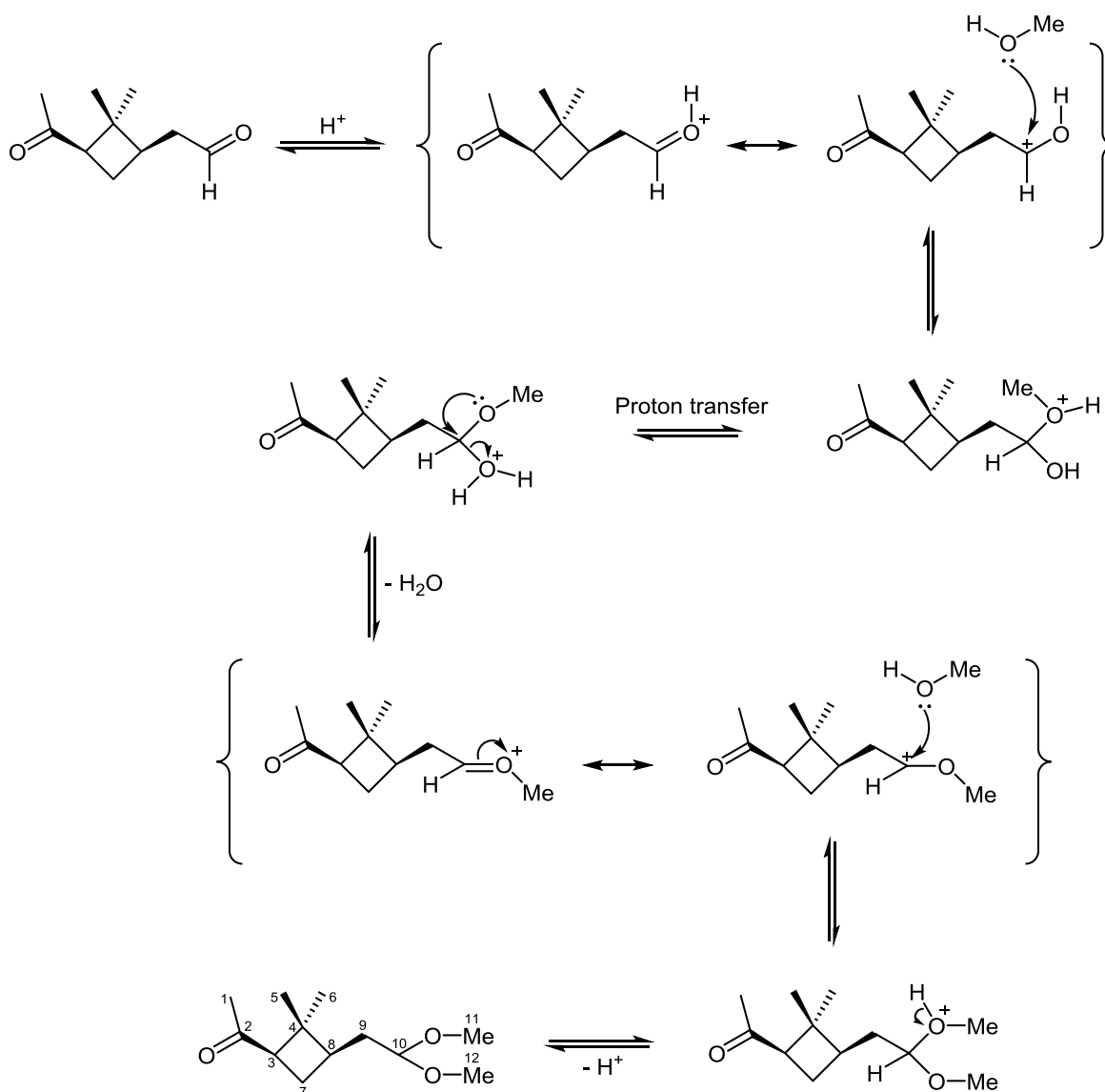
### 4.2.1 Ozonolysis and Subsequent Protection as a Dimethyl Acetal

A mixture of ozone in oxygen (ca. 5 %) was bubbled through a stirring solution of  $\alpha$ -pinene (6 mL, 5.16 g, 39.9 mmol) in DCM / MeOH (1:1, 100 mL), maintained at  $-78\text{ }^\circ\text{C}$  by an acetone-dry ice slush bath. After 40 min, the solution turned a deep blue colour, indicating ozone saturation. The solution was purged with  $\text{O}_2$ , followed by  $\text{N}_2$ . TLC indicated a complete loss of starting material. The reaction mixture was treated with excess dimethyl sulfide, (8.5 mL, 116 mmol), and left to stir overnight at room temperature (Scheme 1).

The bulk of the solvent was removed *via* distillation, and the remainder removed *in vacuo*. The residue was taken into  $\text{Et}_2\text{O}$  (100 mL), and washed with sat.  $\text{NaHCO}_3$  ( $2 \times 30\text{ mL}$ ), followed by brine (30 mL). Petroleum ether (10 mL) was added to the organic fraction, which was subsequently dried over  $\text{MgSO}_4$ , filtered under suction, and the solvent removed *in vacuo*.

Scheme 1: Ozonolysis of  $\alpha$ -pinene and formation of the aldehyde

The residue was taken into MeOH (50 mL), and the solution treated with anhydrous  $\text{NH}_4\text{Cl}$  (0.600 g, 11.16 mmol). The reaction mixture was stirred under  $\text{N}_2$  for 16 h at room temperature. TLC confirmed no change in the mixture composition. NaOMe (0.2 M in MeOH) was added to achieve pH 8–9. The solvent was removed *in vacuo*, and the residue taken into  $\text{Et}_2\text{O}$  (100 mL) and washed with sat.  $\text{NaHCO}_3$  (2 $\times$  30 mL) followed by brine (30 mL). Petroleum ether (10 mL) was added to the organic fraction. The mixture was dried over  $\text{MgSO}_4$ , filtered under suction, and the solvent removed *in vacuo*, yielding the dimethyl acetal as a colourless oil (Scheme 2) (7.49 g, 92 %).  $^1\text{H}$  NMR (400 MHz,  $\text{CDCl}_3$ )  $\delta$  4.29 (1H, t,  $J=6\text{Hz}$ , C(10)H), 3.30 (6H, s, C(11) $\text{H}_3$  & C(12) $\text{H}_3$ ), 2.83 (1H, dd,  $J=10, 7.5\text{Hz}$ , C(3)H), 2.05 (3H, s, C(1) $\text{H}_3$ ), 2.04–1.85 (3H, m, C(7) $\text{H}_2$  & C(8)H), 1.63 (1H, app. dt,  $J=7.5, 6\text{Hz}$ , one of C(9) $\text{H}_2$ ), 1.50 (1H, app. ddd,  $J=14, 8.5, 5\text{Hz}$ , one of C(9) $\text{H}_2$ ), 1.32 (3H, s, C(11) $\text{H}_3$ ), 0.86 (3H, s, C(12) $\text{H}_3$ ).



Scheme 2: Protection of the aldehyde as a dimethyl acetal

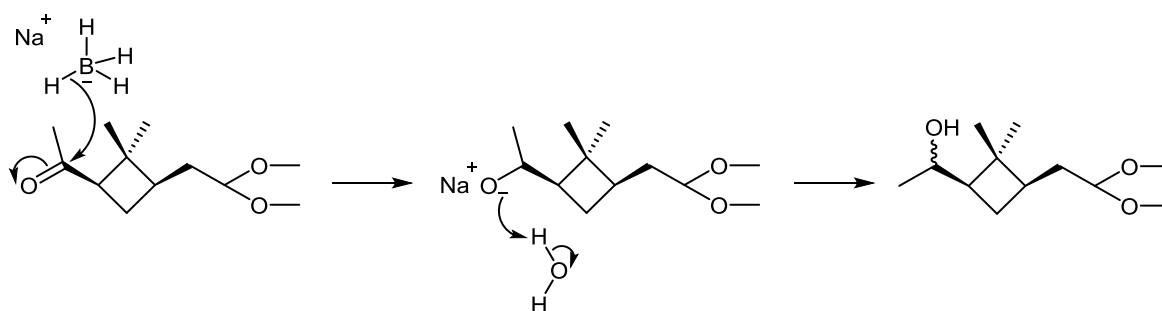
Formation of the dimethyl acetal proceeds *via* specific acid catalysis, whereby protonated solvent is the catalyst, as opposed to general acid catalysis which may result from any acid in the solution. It is noteworthy that no change was observed upon treatment with anhydrous  $\text{NH}_4\text{Cl}$ , suggesting prior formation of the acetal. In the absence of an obvious acid this was, perhaps, surprising.

#### 4.2.2 Reduction and Deprotection

$\text{NaBH}_4$  (3.28 g, 86.7 mmol) was added to a stirring solution of the dimethyl acetal (7.40 g, 34.6 mmol) in MeOH (250 mL) at room temperature. After 45 min, TLC confirmed

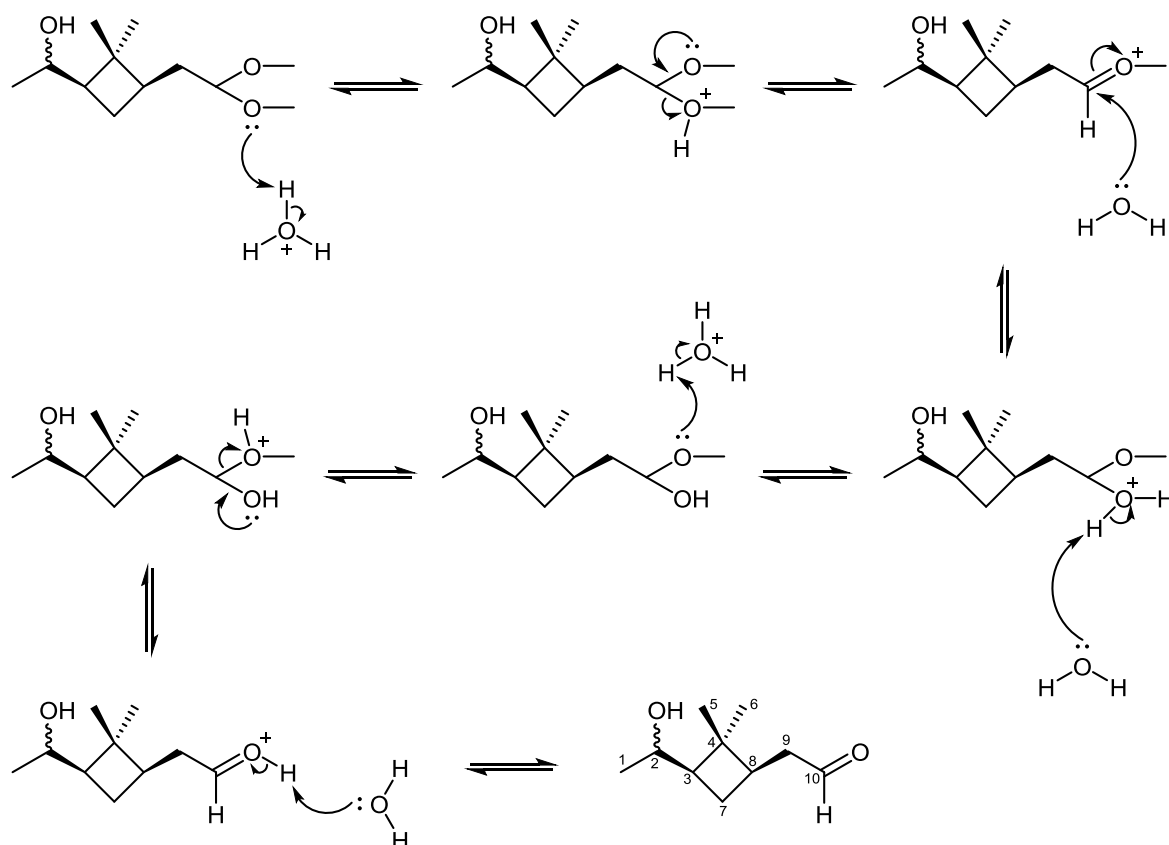
complete loss of starting material (Scheme 3). 1M HCl was added to achieve pH 2. The solution was washed with brine (250 mL), and the aqueous fraction then washed with Et<sub>2</sub>O (2× 200 mL). The organic fractions were combined, and the solvent removed *in vacuo*. The organic residue was then dissolved in acetone (175 mL), treated with 1M HCl (25 mL), and allowed to stir for 16 h at room temperature.

The solvent was removed *in vacuo*, and the resultant residue taken into DCM (400 mL). The solution was washed with sat. NaHCO<sub>3</sub> (3× 100 mL), followed by brine (100 mL). The aqueous fractions were washed with DCM (100 mL). The organic fractions were combined, dried over MgSO<sub>4</sub>, filtered, and the solvent removed *in vacuo*, yielding the aldehyde as a transparent, light-yellow oil (Scheme 4) (5.73 g, 97 %). <sup>1</sup>H NMR (400 MHz, CDCl<sub>3</sub>)  $\delta$  9.71 (1H, s, C(10)H), 3.70 (1H, app. br s, C(2)H), 2.46 (1H, m, one of C(9)H<sub>2</sub>), 2.39–2.17 (2H, m, C(8)H & one of C(9)H<sub>2</sub>), 2.01 (1H, app. q, J=6.5Hz, one of C(7)H<sub>2</sub>), 1.30 (1H, app. q, J=9Hz, C(3)H), 1.22–1.09 (1H, m, one of C(7)H<sub>2</sub>), 1.15 (3H, s, C(5)H<sub>3</sub>), 1.04 (3H, d, J=17.6, C(1)H<sub>3</sub>), 1.01 (3H, s, C(6)H<sub>3</sub>).



Scheme 3: Borohydride reduction of the ketone





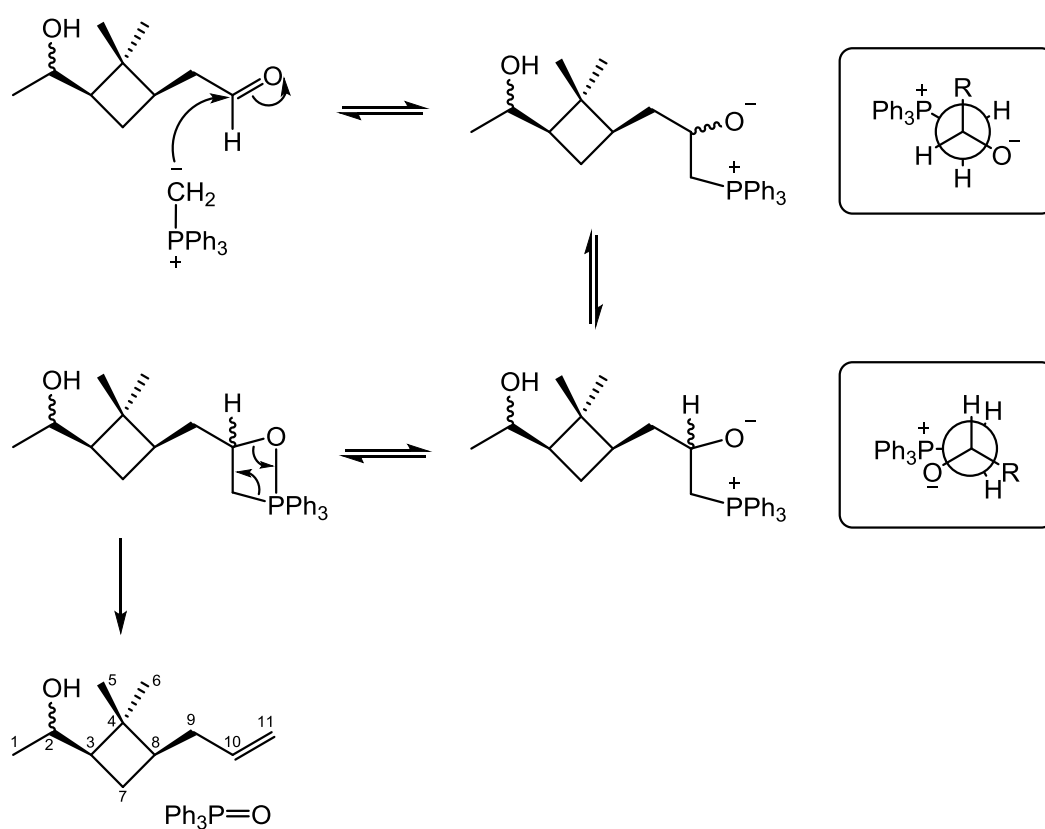
Scheme 4: Deprotection of the aldehyde

### 4.2.3 Wittig Olefination

The ylid was prepared by dropwise addition of MeLi (1.6M in Et<sub>2</sub>O, 24 mL, 38.4 mmol) to a suspension of methyltriphenylphosphonium bromide (15.15 g, 42.4 mmol) in dry THF (38 mL). A solution of the aldehyde (3.03 g, 17.9 mmol) in dry THF (225 mL) was prepared and added dropwise to the stirring ylid solution under N<sub>2</sub> at 0 °C. Stirring continued for 2 ½ h while warming to room temperature. TLC confirmed loss of starting material, and the reaction was quenched upon addition of 1M HCl (150 mL). The bulk of the THF was removed *in vacuo*, and the resultant colourless solution washed with Et<sub>2</sub>O (4× 150 mL). The combined organic fractions were dried over MgSO<sub>4</sub>, filtered, and the solvent removed *in vacuo*.

The resultant oil was taken into n-pentane to remove the triphenylphosphine oxide, filtered, and the solvent removed *in vacuo*. The resulting alkene was purified *via* flash

column chromatography (92:8, petroleum ether:EtOAc), yielding the two diastereoisomers as colourless oils (Scheme 5) (1.5:1, 1.66 g, 55 %).  $^1\text{H}$  NMR (400 MHz,  $\text{CDCl}_3$ )  $\delta$  5.71 (1H, dddd,  $J=21.5, 13, 6.5, 3\text{Hz}$ , C(10)H), 5.00 (1H, d,  $J=17\text{Hz}$ , C(11)H<sub>2</sub> *trans*), 4.96 (1H, d,  $J=11\text{Hz}$ , C(11)H<sub>2</sub> *cis*), 3.68 (1H, dq,  $J=10, 6\text{Hz}$ , C(2)H), 2.10 (1H, app. dt,  $J=14, 7\text{Hz}$ , one of C(9)H<sub>2</sub>), 1.94–1.72 (3H, m, C(8)H, one of C(7)H<sub>2</sub> & one of C(9)H<sub>2</sub>), 1.67 (1H, app. q,  $J=8\text{Hz}$ , C(3)H), 1.12 (3H, s, C(5)H<sub>3</sub>), 1.09–1.07 (1H, m, one of C(7)H<sub>2</sub>), 1.03 (3H, d,  $J=6\text{Hz}$ , C(1)H<sub>3</sub>), 1.02 (3H, s, C(6)H<sub>3</sub>).



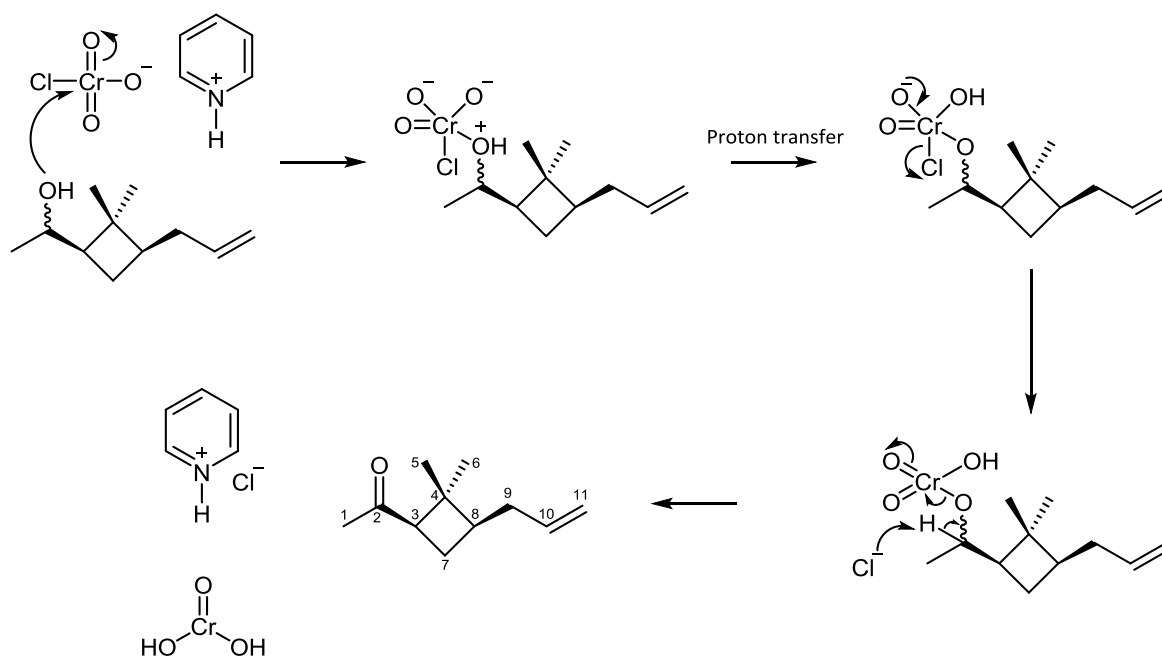
Scheme 5: Formation of the alkene by the Wittig olefination

Although the diastereoisomers were separable *via* flash column chromatography, determination of which was the predominant isomer was beyond the scope of this work.

#### 4.2.4 Pyridinium Chlorochromate Oxidation

The alcohol (1.64 g, 9.75 mmol) was dissolved in DCM (30 mL) and added to a stirring orange solution of PCC (4.21 g, 19.5 mmol) in DCM (150 mL) under  $N_2$  at room temperature. After 1 h 40 min, TLC confirmed loss of starting material. The dark brown solution was diluted with  $Et_2O$  (100 mL) and decanted, leaving behind a thick black residue. The residue was rinsed repeatedly with  $Et_2O$  (5  $\times$  75 mL) and the organic fractions combined.

The brown solution was filtered through a silica pad to remove the remainder of the  $Cr(OH)_2O$ . The solvent was subsequently removed *in vacuo*, yielding the ketone as a colourless oil (Scheme 6) (1.23 g, 7.41 mmol, 76 %).  $^1H$  NMR (400 MHz,  $CDCl_3$ )  $\delta$  5.71 (1H, app. ddd,  $J=17,10,6.5$  Hz, C(10)H), 5.00 (1H, d,  $J=17$  Hz, C(11)H<sub>2</sub> *trans*), 4.93 (1H, d,  $J=10$  Hz, C(11)H<sub>2</sub> *cis*), 2.81 (1H, t,  $J=9.5$  Hz, C(3)H), 2.09 (1H, m, one of C(9)H<sub>2</sub>), 2.03 (3H, s, C(1)H<sub>3</sub>), 2.0–1.91 (3H, m, C(8)H, one of C(7)H<sub>2</sub> & one of C(9)H<sub>2</sub>), 1.80 (1H, m, one of C(7)H<sub>2</sub>), 1.30 (3H, s, C(5)H<sub>3</sub>), 0.86 (3H, s, C(6)H<sub>3</sub>).



Scheme 6: Oxidation of the alcohol

### 4.3 Initial Investigation and Optimisation of the Experimental Setup

In the literature, Hoare notes that, due to its low vapour pressure, coaxing the enone from the liquid phase in the cold finger and into the vacuum line can pose significant challenges.<sup>2</sup> As is always the case with vacuum lines, the rig used here is not a perfectly sealed system, and some leakage occurs. Whilst this is insignificant on the usual timeframe, where introduction of the sample into the rig takes no longer than 30 seconds, it may become an issue with a compound with an extremely low vapour pressure, such as the enone. Therefore, in an attempt to counter the difficulties posed by the enone's low volatility, a specially designed cold finger (Figure 63) was used to store the compound prior to its introduction to the vacuum line. This cold finger differed from the standard type (see section 2.2) by incorporation of a 500 mL bulb just above the sample reservoir. The intention here was to provide a much larger headspace above the liquid, which would allow for a greater quantity of enone vapour in the cold finger. Then, upon introduction of the sample to the vacuum line, the pressure should initially increase more rapidly as the vapour present in the headspace flows into the rig, thus leading to reduced sample introduction times, and a reduced uncertainty in the enone concentration.



Figure 63: Specially designed enone-containing cold finger, incorporating a 500 mL bulb

To further compensate for the very low vapour pressure of the enone, the entire rig, including the cold finger, was heated to  $37 \pm 2$  °C. This was simply achieved by covering the entire rig in a plastic insulating layer, and heating the air inside using a space heater. Temperature was constant in the region surrounding the rig, within the insulating layer, to  $\pm 1$  °C. The aim was to increase the vapour pressure of the enone, again allowing for faster sample introduction times and thus lower uncertainty regarding the final concentration of enone within the chamber. By heating the entire rig, rather than just the cold finger, the potential for condensation of the enone within the rig was minimised.

Since there is no literature data for the rate constant of the enone derivative + OH, a rate constant was calculated from structure activity relationships. This involved calculation of a rate constant for H-abstraction from each alkyl carbon, and also for OH-addition to each alkene carbon. The approach used was that described by Ziemann and Atkinson.<sup>7</sup> H-abstraction partial rate constants were calculated from a group rate constant (Table 14 a), dependent on whether the carbon was primary, secondary or tertiary, multiplied by F(X), a factor dependent on the substituent groups (Table 14 b).

(a)		(b)	
Group Rate Constants / ( $\text{cm}^3 \text{ molecule}^{-1} \text{ s}^{-1}$ )		Substituent Group, X	F(X)
$k_{\text{prim}}$	$1.36 \times 10^{-13}$	$\text{—CH}_3$	1.00
$k_{\text{sec}}$	$9.34 \times 10^{-13}$	$\text{—CH}_2\text{—}$	1.23
$k_{\text{tert}}$	$1.94 \times 10^{-12}$	$\text{>CH—}$	1.23
		$\text{>C<}$	1.23
		$\text{—CHO}$	0.75
		$\text{>C=O}$	0.75
		$\text{=O}$	8.7
		4-Membered ring	0.28

Table 14: (a) Group rate constants for calculation of  $k_{\text{abst}}$ ; (b) Substituent factors, F(X), for calculation of  $k_{\text{abst}}$ . All values from Kwok and Atkinson.<sup>8</sup>

OH-addition partial rate constants were calculated from a group rate constant (Table 15), dependent on whether the radical formed was primary, secondary or tertiary.

Group Rate Constants / ( $\text{cm}^3 \text{ molecule}^{-1} \text{ s}^{-1}$ )	
$k_{\text{prim}}$	$4.5 \times 10^{-12}$
$k_{\text{sec}}$	$3.0 \times 10^{-11}$
$k_{\text{tert}}$	$5.5 \times 10^{-11}$

Table 15: Group rate constants for calculation of  $k_{\text{add}}$ . Values from Peeters *et al.*<sup>9</sup>

A summation of the partial rate constants then yielded an estimate of the overall rate constant for the reaction of OH + enone:  $k_{\text{OH}} = 4.22 \times 10^{-11} \text{ cm}^3 \text{ molecule}^{-1} \text{ s}^{-1}$ . A similar calculation for the enal yielded an estimate of:  $k_{\text{OH}} = 8.89 \times 10^{-11} \text{ cm}^3 \text{ molecule}^{-1} \text{ s}^{-1}$ .

Initial static chamber experiments were carried out according to the method described in section 2.3.2. Whilst the cold finger and rig were heated as described, the static chamber itself was maintained at room temperature (295–298 K). Experiments were carried out under 0 % RH conditions. Cyclohexane was employed as a scavenger; calculation of the required concentration was performed using the estimated rate constant:  $k_{\text{OH}} = 4.22 \times 10^{-11} \text{ cm}^3 \text{ molecule}^{-1} \text{ s}^{-1}$ . Ozone concentration in these experiments was 0.10 ppm, and the enone concentration was initially believed to be 0.20 ppm.

Measurement of the subsequent aerosol evolution was surprising, with a maximum observed mass concentration of  $0.54 \mu\text{g m}^{-3}$ . This compares to a maximum observed mass concentration of  $75.5 \mu\text{g m}^{-3}$  for the ozonolysis of  $\alpha$ -pinene under identical conditions. The data reported by Hoare<sup>2</sup> suggest that, whilst there is some uncertainty regarding the SOA yields resulting from the enone ozonolysis, we would expect to observe a significantly higher aerosol mass. Thus, the suspicion is that the true concentration of enone achieved within the chamber itself was far below the 0.20 ppm originally intended.

Rather than commit more of the limited quantity of enone to repeats under these conditions, the heating system was first improved—specifically, the 0.6" PTFE tubing leading from the rig to the chamber was not entirely inside the heated region, and thus

the temperature along its length was not uniform. This may have resulted in condensation losses of the enone on the walls of the tubing, and thus an overestimation of the true concentration of the enone inside the chamber. To counteract this, the heated region was simply extended so that the tubing was properly heated along its length. During introduction of the enone into the chamber, heat was also specifically applied along the length of the tubing. These measures helped to ensure that any condensation within the tubing was minimised as much as feasibly possible.

Secondly, whilst the design of the cold finger in combination with the heating setup reduced the introduction time of the enone, typical introduction times were still around 3–4 minutes, allowing for a potentially significant leak. Thus, whilst the pressure might increase by, for example, 0.3 Torr within the rig, a significant proportion of this may still be due to air from the laboratory leaking in, rather than the enone. Indeed, a simple test of the leak was carried out by first evacuating the rig, then closing the tap to the vacuum pump and monitoring the change in pressure over time. This suggested a leak of ca.  $0.020 \text{ Torr min}^{-1}$ . This equates to an uncertainty in the enone concentration of 18–24 % due to air leakage alone.

In addition to this, the low vapour pressure of the enone, even under these optimised conditions, meant that realistically achievable initial pressures of the enone within the rig were only up to 0.3 Torr. The resolution of the pressure gauge allowed for measurement of the pressure to only the nearest 0.1 Torr, equating to a further uncertainty of up to 17 % in the final enone concentration. While a longer sample introduction time would have resulted in a higher pressure being achieved, this would also allow more time for the previously discussed leak to have an effect.

To account for the uncertainty in enone concentration within the chamber, further experiments were carried out varying the excess of enone. For these experiments, ozone concentration was 0.10 ppm, and intended enone concentrations ranged from 0.2 to 2.0 ppm. The particle evolutions are presented in Figure 64 – Figure 66. Note that data collected are represented by points on the graphs; lines are drawn between for ease of reading and may not be indicative of the true shapes of the curves.

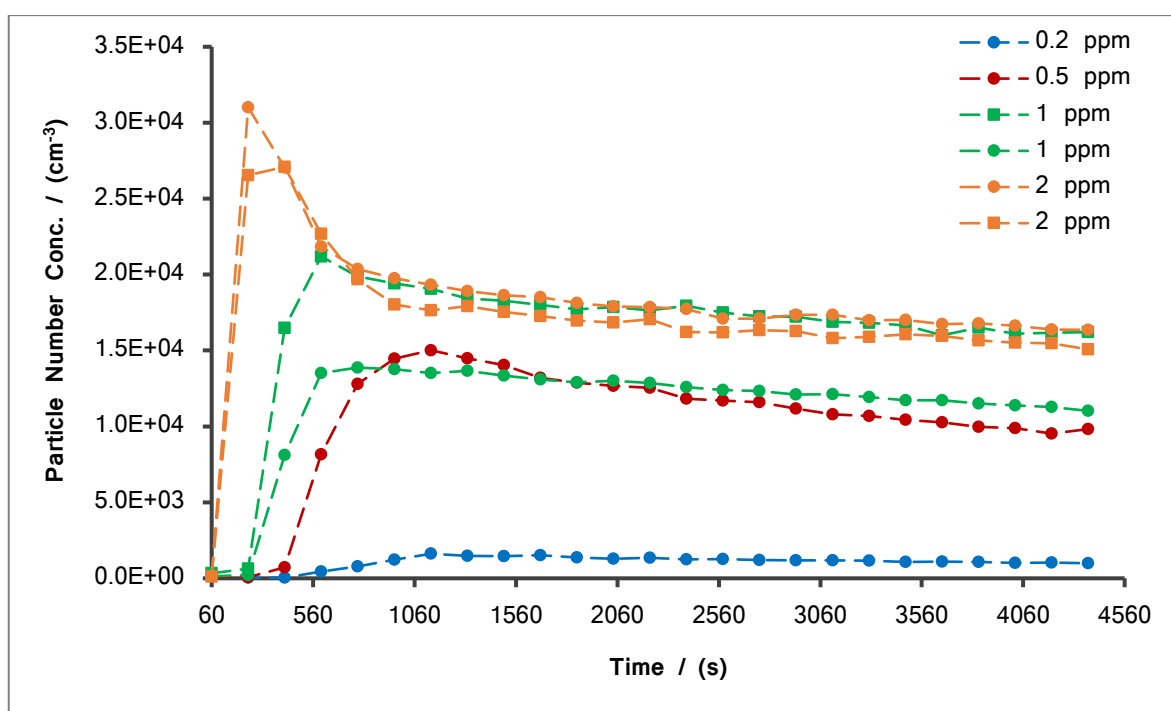


Figure 64: Particle number concentration vs. time; [ozone] = 0.10 ppm; varying enone concentrations detailed by legend.

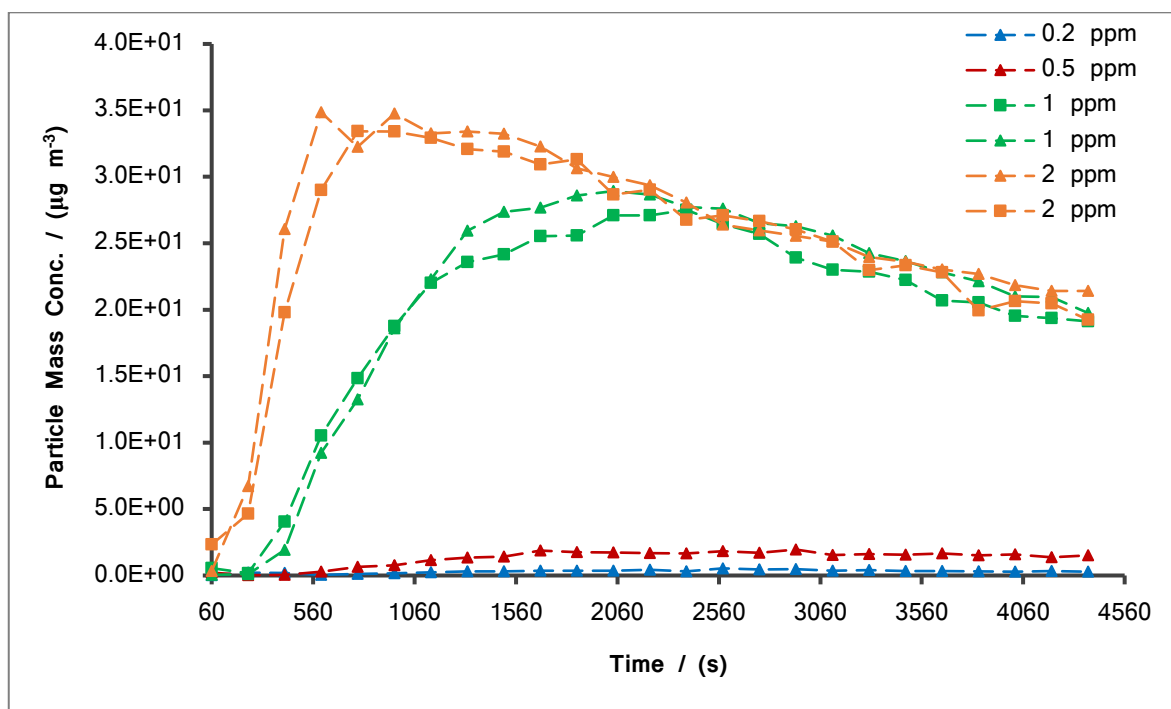


Figure 65: Particle mass concentration vs. time; [ozone] = 0.10 ppm; varying enone concentrations detailed by legend.



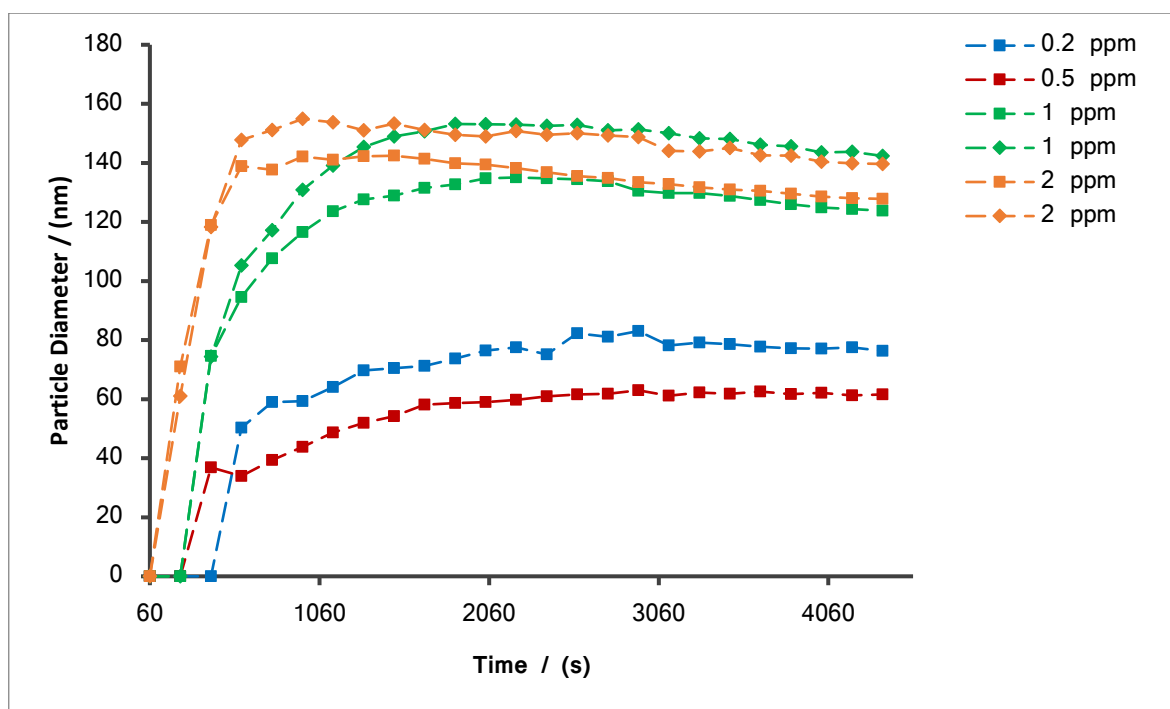


Figure 66: Mean particle diameter vs. time; [ozone] = 0.10 ppm; varying enone concentrations detailed by legend.

There is a marked difference between the particle evolutions as the intended enone concentration increases from 0.20 to 1.0 ppm, even whilst ozone concentration remains constant. Particle mass concentration increases with increasing enone excess, indicating that complete reaction of the ozone has not yet been achieved for the intended enone concentrations of 0.20 and 0.50 ppm, which in turn suggests that the true concentration of the enone within the chamber, for these experiments, lies below that of the ozone; that is, below 0.10 ppm. For ease of discussion, when referring to enone concentrations herein, the concentration referred to is the intended concentration in the static chamber, not necessarily the true concentration achieved.

For the 1.0 ppm enone experiments, the peak mass concentration lies at  $28.2 \pm 1.0 \mu\text{g m}^{-3}$ , slightly below that of  $34.1 \pm 1.0 \mu\text{g m}^{-3}$  for the set with initial enone concentration of 2.0 ppm. As expected, the experiments carried out at a higher initial enone concentration proceed at a faster rate, and the peak mass concentration is observed at 600 s, compared to 2040 s for both of the 1.0 ppm enone data sets. Then, when the data are corrected for wall loss (see section 2.4.1 for method), the peak mass concentrations look strikingly similar:  $40.4 \pm 1.0 \mu\text{g m}^{-3}$  for the 1.0 ppm data, and  $41.7 \pm 0.2 \mu\text{g m}^{-3}$  for the 2.0 ppm data.

This suggests that, at and above 1.0 ppm enone, an excess has been achieved, and ozone is now the limiting reagent. The low uncertainties in both sets of data further support this conclusion since, if an enone excess had not been achieved, the uncertainty in enone concentration would be expected to cause a greater variance in the resulting aerosol mass evolutions.

The number concentrations for the two data sets at 2.0 ppm enone peak from 240–420 s, much earlier than the 1.0 ppm data sets, which peak at 600–780 s. This is as expected, since the higher initial enone concentration will result in a faster rate of reaction, and thus an earlier ‘burst’ of particle nucleation. Both data sets at an initial enone concentration of 2.0 ppm show good reproducibility in their number concentrations, to within  $\pm 9\%$  throughout, aside from the initial nucleation burst at 240 s, where variability is slightly higher at 20 %. One of the experiments performed at an enone concentration of 1.0 ppm shows good agreement after 600 s—although initially lower due to the slower rate of reaction. The other experiment performed at 1.0 ppm enone produced a number concentration which remained approximately 33 % lower throughout the course of the experiment. This is not unexpected since, as noted in the previous chapter, the number concentrations tend to show the lowest reproducibility.

Some curious behaviour is observed for the number concentration and mean particle diameters when increasing from 0.20 to 0.50 ppm enone. The higher initial enone concentration results in a significantly higher particle number concentration, as might be expected, peaking at  $1.5 \times 10^4 \text{ cm}^{-3}$ , approximately 10 $\times$  higher than the  $1.6 \times 10^3 \text{ cm}^{-3}$  observed for the lower enone concentration. Conversely, the lower initial enone concentration resulted in larger particles, achieving a mean particle diameter of 77 nm after 4000 seconds, compared to 62 nm for the higher initial enone concentration. However, since these experiments were clearly conducted under unrefined conditions—that is, with an excess of ozone, and thus with no certainty as to the initial enone concentration—it is not prudent to draw any conclusions based on these results.

The experiments performed here suggest that, due to the large uncertainties associated with the initial enone concentration in the static chamber, any further experiments

should be conducted under at least an apparent 10:1 excess of enone:ozone. Since concentration of the low-volatility enone within the chamber could not be accurately measured—as measured pressures were only partially due to enone, and the limited amount of custom-synthesised enone did not allow for full investigation to resolve this particular issue— this ensured that the amount of enone which reacted could still be controlled by simply using ozone as the limiting reagent, and therefore mass yields may be accurately calculated.

#### **4.4 Comparison of the Enone to $\alpha$ -Pinene**

The crux of this chapter is a comparison of the ozonolysis behaviour of the enone derivative to that of  $\alpha$ -pinene. To this end, a number of static chamber experiments were performed between ozone (0.10 ppm) and either  $\alpha$ -pinene or the enone (1.0 ppm). The results of these are presented in Figure 67 – Figure 69, alongside the enal ozonolysis data reported by Hoare<sup>2</sup> for experiments performed under identical conditions. It should be noted that the enal also has a low vapour pressure, though not so low as the enone, and therefore reported concentrations may not be accurate, in a similar fashion to the enone. Hoare also reported some, very limited enone data—however, these were particularly unreliable, which the author attributes to difficulty in introducing the enone into the reaction chamber, and resulted in a particularly large scatter across experimental repeats. This is the same problem as that encountered in this work, which was discussed in section 4.3. However, the use of excess enone conditions in this work resulted in far more reliable and reproducible results than those obtained by Hoare (see Figure 67 – Figure 69).

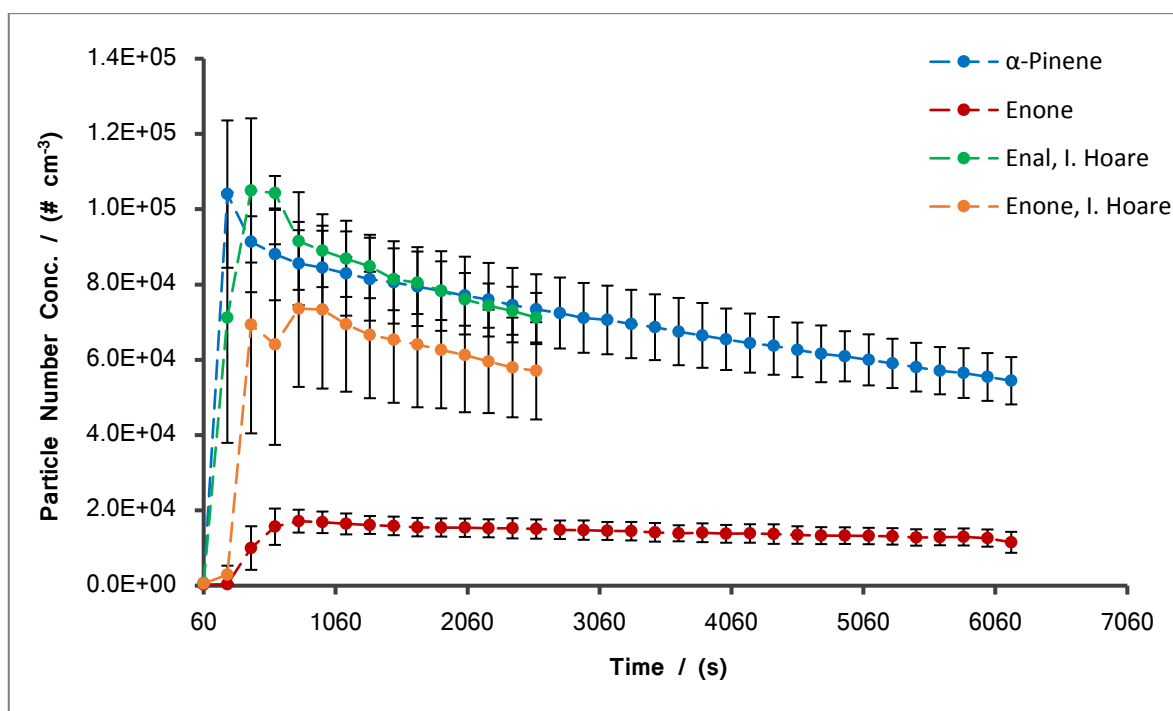


Figure 67: Particle number concentration vs. time; [ozone] = 0.10 ppm, [enone;  $\alpha$ -pinene; enal] = 1.0 ppm. Labelled data from Hoare.<sup>2</sup>

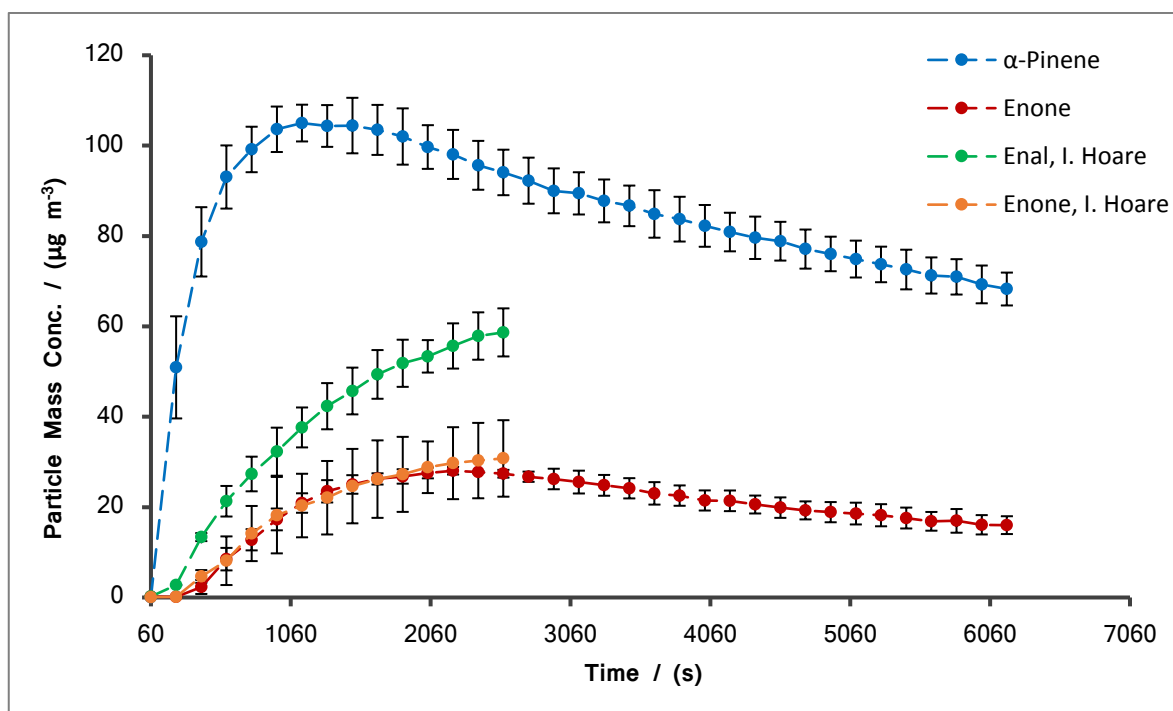


Figure 68: Particle mass concentration vs. time; [ozone] = 0.10 ppm, [enone;  $\alpha$ -pinene; enal] = 1.0 ppm. Labelled data from Hoare.<sup>2</sup>

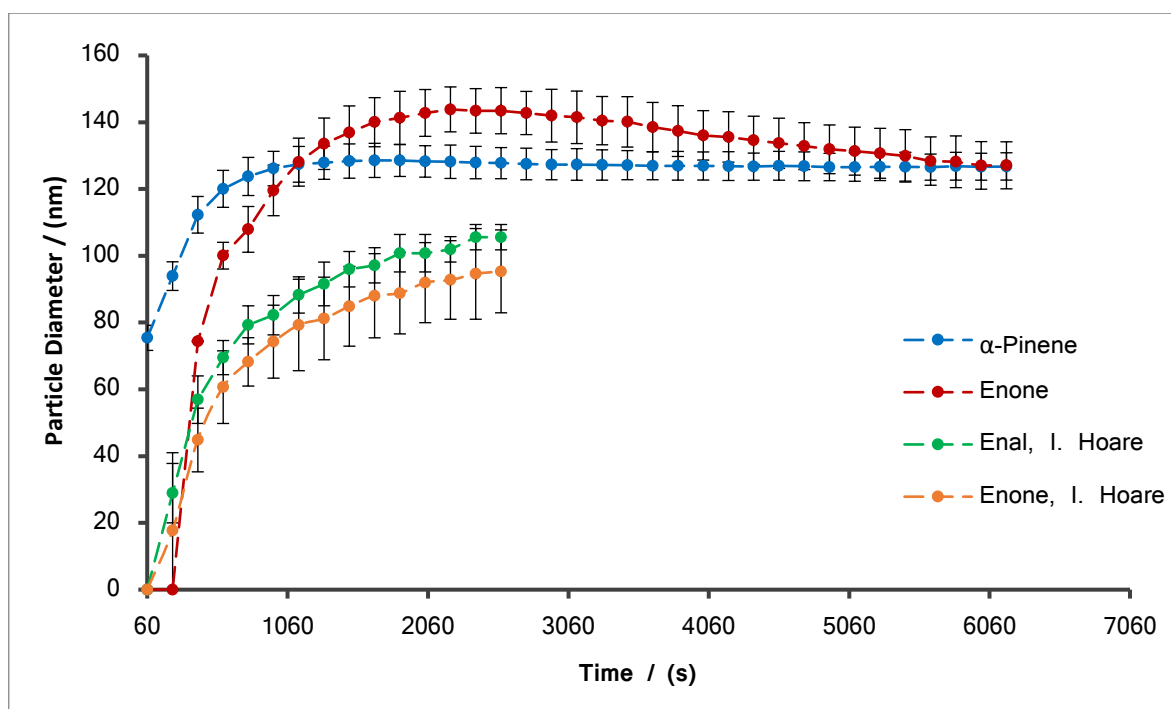


Figure 69: Mean particle diameter vs. time; [ozone] = 0.10 ppm, [enone;  $\alpha$ -pinene; enal] = 1.0 ppm. Labelled data from Hoare.<sup>2</sup>

There are a number of immediate differences between the SOA evolution profiles of the enone ozonolysis when compared to the  $\alpha$ -pinene ozonolysis. Immediately obvious is the initial rate of aerosol formation, which is much faster for  $\alpha$ -pinene than for the enone. The rate constant for ozonolysis of the enone will be calculated in section 4.5. Key data obtained are summarised in Table 16:

VOC	[VOC] (ppm)	[Ozone] (ppm)	Scavenger	RH (%)	Peak Number Conc. (cm <sup>-3</sup> )	Max. Mass Conc. (μg m <sup>-3</sup> )	Mean Dia. at 45 mins (nm)
$\alpha$ -Pinene	0.2	0.1	Cyclohexane	0	$1.04 \pm 0.19 \times 10^5$	$105.6 \pm 5.1$	$128 \pm 5$
Enone	0.2	0.1	Cyclohexane	0	$1.76 \pm 0.37 \times 10^4$	$28.3 \pm 0.7$	$144 \pm 9$
Enal <sup>a</sup>	0.2	0.1	Cyclohexane	0	$51.12 \pm 0.07 \times 10^5$	$58.7 \pm 9.4$ <sup>b</sup>	$106 \pm 4$

Table 16: Summary of experimental conditions and results for ozonolysis of  $\alpha$ -pinene and its derivatives.

<sup>a</sup> Enal data from Hoare.<sup>2</sup> <sup>b</sup> This is the maximum mass concentration achieved during the timeframe reported by Hoare. It is likely that, had data collection continued further, the maximum mass concentration would be higher.

The number concentrations of the aerosol formed from each compound are markedly different (see Figure 67). The enone produces significantly fewer particles, reaching a peak of  $1.76 \pm 0.37 \times 10^4$  cm<sup>-3</sup>, compared to  $1.04 \pm 0.19 \times 10^5$  cm<sup>-3</sup> for  $\alpha$ -pinene. Mean

particle diameters (Figure 69) are similar for both compounds, although the enone shows poorer reproducibility. They reach maxima of  $128 \pm 5$  nm and  $144 \pm 9$  nm for  $\alpha$ -pinene and the enone, respectively. This suggests formation of slightly larger particles from the enone ozonolysis. However, upon ageing of the aerosol, that formed from  $\alpha$ -pinene maintains a consistent mean particle diameter, whereas the mean diameter of that formed from the enone slowly falls. By 5000 s, the two are similar, and lie within error of one another.

Whilst the number concentrations and mean particle diameters of the enone ozonolysis products show some variability, the mass concentrations (Figure 68) are remarkably reproducible. They reach their maxima of  $28.3 \pm 0.7 \mu\text{g m}^{-3}$  after 2040–2400 seconds—considerably below the peak mass concentration for the  $\alpha$ -pinene ozonolysis of  $106 \pm 5 \mu\text{g m}^{-3}$ . This is in agreement with the  $30.8 \pm 8.5 \mu\text{g m}^{-3}$  reported by Hoare, under identical (intended) conditions, with a substantially smaller uncertainty.<sup>2</sup>

In this work, only the enone derivative was synthesised and ozonised, since sufficient data has already been reported for the enal derivative of  $\alpha$ -pinene. Comparing the enone data presented here to the enal data reported by Hoare,<sup>2</sup> the enone typically produces significantly fewer particles (see Figure 67); the enal number concentration peaks at  $1.12 \pm 0.07 \times 10^5 \text{ cm}^{-3}$ , comparable to the  $\alpha$ -pinene data, which peak at  $1.04 \pm 0.19 \times 10^5 \text{ cm}^{-3}$ . The particles produced by the enone are typically larger (see Figure 69), peaking at  $144 \pm 9$  nm, compared to  $106 \pm 4$  nm for the enal, although the particles formed from the enal do appear to still be growing at the end of the analysis time. The mass concentration of the enal-produced aerosol is significantly higher than that of the enone, reaching a maximum of  $58.7 \pm 9.4 \mu\text{g m}^{-3}$  after 2580 s, although the mass concentration also appears to still be increasing at this point. Continued measurement of the enal SOA evolution over a longer timeframe would have been desirable to facilitate better comparison. Unfortunately, Hoare did not extend data collection past this point, and therefore more data were not available.

The results suggest that, in the  $\alpha$ -pinene ozonolysis scheme, products of CI 2 are primarily responsible for particle nucleation, with a small contribution from CI 1. This is thought to be due to differences in yields of pinic and pinonic acid from each CI, the rationale for

which is discussed in detail in section 4.6. Products of both CIs are expected to contribute to the subsequent growth of those particles, with perhaps a greater contribution from CI 2, evidenced by the larger mass concentration achieved. This will again be discussed in greater detail in section 4.6.

#### 4.5 Gas-Phase Kinetics

The reaction rate constant for ozonolysis of the enone was estimated according to the simulation method introduced in section 3.4. An example of the comparison between experimental and simulated data is presented:

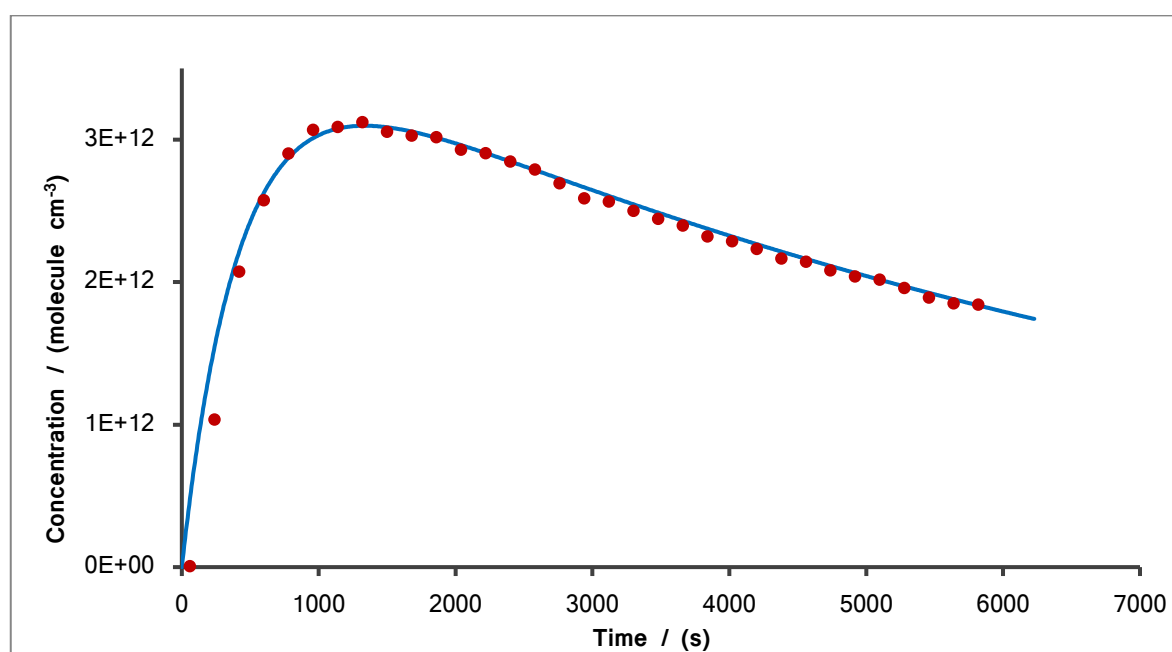


Figure 70: Calculation of a reaction rate constant. Red circles = experimental data; Blue line = simulated data.

The best fit for the data in Figure 70 was achieved for a value of  $k = 3.8 \times 10^{-17} \text{ cm}^3 \text{ molecule}^{-1} \text{ s}^{-1}$  (see highlighted row in Table 17). The data obtained for all experiments are summarised in Table 17, and these range from  $2.6\text{--}7.5 \times 10^{-17} \text{ cm}^3 \text{ molecule}^{-1} \text{ s}^{-1}$ .

[Ozone] / (ppm)	[Enone] / (ppm)	$k$ / ( $10^{-17} \text{ cm}^3 \text{ molecule}^{-1} \text{ s}^{-1}$ )
0.1	1	2.8
0.1	1	2.6
0.1	1	3.2
0.1	1	2.8
0.1	2	4.8
0.1	2	5.5
0.2	2.5	4.4
0.2	2.5	5.1
0.2	2.5	7.5
0.15	1.83	6.5
0.15	2.5	4.0
0.15	2.5	3.8
0.12	2	3.2
Average		4.3 $\pm$ 0.9

Table 17: Summary of mixing ratios and calculated reaction rate constants for the enone ozonolysis. Highlighted row indicates experiment displayed in Figure 70.

Calculation of the rate constant by this method gives a value of  $k = 4.3 \pm 0.9 \times 10^{-17} \text{ cm}^3 \text{ molecule}^{-1} \text{ s}^{-1}$ . When the uncertainties are combined, this agrees with the rate constant suggested by Hoare, who reported a value of  $2.4 \pm 1.0 \times 10^{-17} \text{ cm}^3 \text{ molecule}^{-1} \text{ s}^{-1}$ .<sup>2</sup>

However, a review of the data suggests a degree of unreliability in measurement of the rate constant reported by Hoare. The method used was the same as that employed here, but because aerosol mass data was only collected for 2500 s, the data were extrapolated to fit the simulated curve, introducing an additional uncertainty. Comparison to the enal ozonolysis rate constant reported by Hoare,  $k = 1.51 \pm 0.21 \times 10^{-17} \text{ cm}^3 \text{ molecule}^{-1} \text{ s}^{-1}$ , suggests a faster rate constant for the enone ozonolysis.

The relatively large uncertainty associated with the calculated rate constant for enone,  $k$ , is likely due to uncertainty regarding the determination of the initial concentration of enone, as a result of the difficulties discussed regarding its introduction to the chamber.

A number of studies in the literature have reported a linear relationship between energy of the highest occupied molecular orbital (HOMO) and  $-\log(k)$ , for symmetric alkenes.<sup>10, 11</sup> Johnson *et al.*<sup>12</sup> further report that, for more complex alkenes, the greater the degree of asymmetry, the smaller the rate constant. They suggest that this is due to the nature of ozone as a reactant—the concerted attack at both carbons of the double bond, leading to the formation of a cyclic transition state, can be hindered by the nature of the local environment surrounding the double bond. An asymmetric molecule will result in a



difference between the HOMO orbital coefficients at each of the carbon atoms. The larger this difference, the smaller the achievable HOMO-LUMO overlap between the alkene and ozone, and thus the lower the reactivity.

The ionisation potential (IP), and hence the energy of the highest occupied molecular orbital ( $E_{HOMO}$ ) for the enone was calculated using Gaussian 03<sup>13</sup> at the semi-empirical level, using the PM3 parameterisation of atomic wavefunctions. These calculations were performed by Prof. George Marston (Northumbria University). This yielded a value of  $E_{HOMO} = 10.28$  eV.

$E_{HOMO}$  was calculated in the same way (again, by Prof. George Marston) for a number of symmetric alkenes: ethene, E-butene, Z-butene & 2,3-dimethylbut-2-ene. The enone can be thought of as a 1-alkene, and therefore calculation of  $E_{HOMO}$  for a range of 1-alkenes (propene, 1-butene, 1-pentene, 1-hexene, 1-heptene & 1-octene) was also performed. Table 18 summarises the calculated  $E_{HOMO}$  values for each compound, in addition to their ozonolysis rate constants.

Compound	$E_{HOMO}$ / (eV)	$k$ / ( $10^{-18} \text{ cm}^3 \text{ molecule}^{-1} \text{ s}^{-1}$ )	$-\log(k)$
Ethene	10.64	1.59 <sup>7</sup>	17.8
E-butene	9.64	1.90 <sup>7</sup>	15.7
Z-butene	9.7	125 <sup>7</sup>	15.9
2,3-dimethylbut-2-ene	9.07	1140 <sup>7</sup>	14.9
Propene	10.11	10.1 <sup>7</sup>	17.0
1-methylbutene	10.03	9.64 <sup>7</sup>	17.0
1-methylpentene	10.03	9.97 <sup>7</sup>	17.0
1-methylhexene	10.03	11.5 <sup>7</sup>	16.9
1-methylheptene	10.04	11.6 <sup>7</sup>	16.9
1-methyloctene	10.04	11.4 <sup>7</sup>	16.9
Enone	10.28	44.0	16.4

Table 18: Summary of ozonolysis rate constants and calculated  $E_{HOMO}$  values. Rate constants from Atkinson.<sup>14</sup>

The data in Table 18 are plotted in Figure 71, and a line of best fit is drawn for the symmetric alkenes.

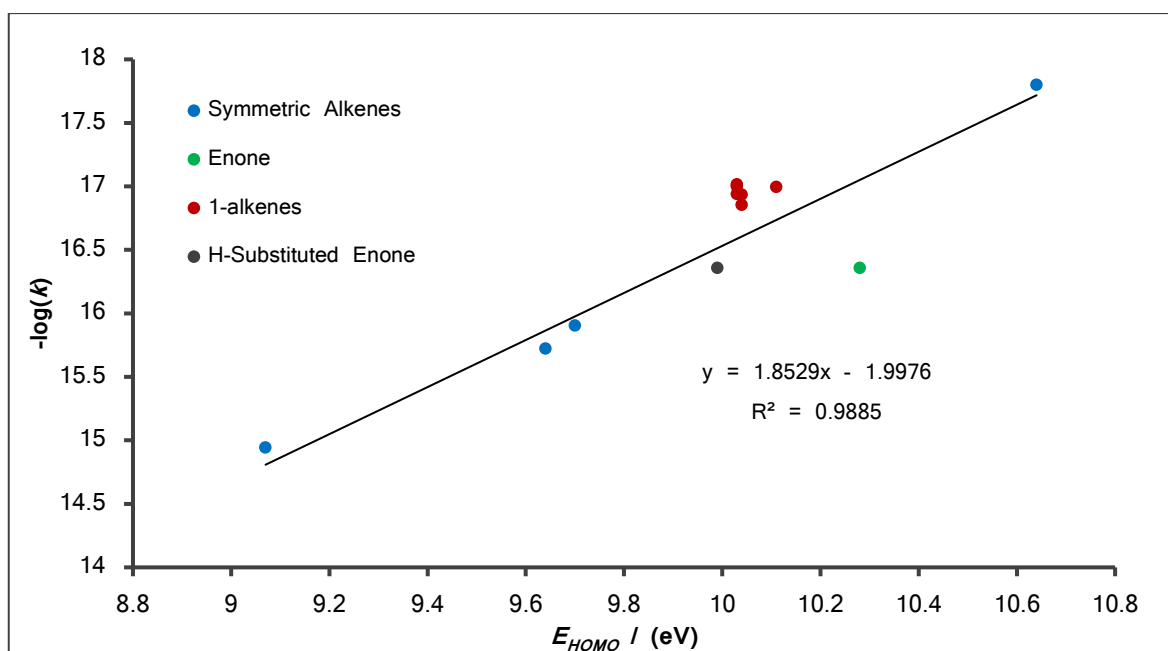


Figure 71: Plot of  $-\log(k)$  vs.  $E_{HOMO}$  for a range of alkenes. H-substituted enone refers to the calculated  $E_{HOMO}$  when the enone carbonyl is replaced by two hydrogen atoms.

All of the 1-alkenes are seen to lie above the line of best fit—that is, their rate constants are smaller than would be predicted for a symmetric alkene with the same  $E_{HOMO}$ . The enone, however, reacts substantially more quickly than expected. On average, the 1-alkenes have rate constants approximately 45 % of those predicted by the fit. On this basis, a predicted rate constant for the enone would be  $k = 4.1 \times 10^{-18} \text{ cm}^3 \text{ molecule}^{-1} \text{ s}^{-1}$ —approximately 10 % of that calculated experimentally. This is a large difference between the experimental value and that predicted by theory.

Replacing the carbonyl group on the enone with two hydrogen atoms, to better compare to the 1-alkenes, caused a reduction in calculated  $E_{HOMO}$  to 9.99 eV—evidence that the carbonyl group has a significant impact on  $E_{HOMO}$ . The predicted rate constant for this alkene, based on the value for  $E_{HOMO}$ , would then be  $1.4 \times 10^{-17} \text{ cm}^3 \text{ molecule}^{-1} \text{ s}^{-1}$ —approximately a third of the experimental value for the enone. This suggests that the experimental rate constant determined is still faster than might be expected. However, there is no discernible reason as to why the experimental rate constant would be larger than that predicted by the IP.

#### **4.6 Aerosol Mass and Mass Yields**

The question posed at the beginning of this chapter was: to what extent does each Criegee intermediate contribute to the total SOA yield from the  $\alpha$ -pinene ozonolysis? To answer this, an understanding of the relationship between aerosol mass concentration and mass fraction for each CI must be established. Hoare reported slightly elevated mass yields for the enal ozonolysis compared to that of  $\alpha$ -pinene, and potentially slightly reduced mass yields for the enone, although the author notes that this may lie within experimental error.<sup>2</sup> However, very little data were reported for the enone, and the range of aerosol mass concentrations investigated was particularly narrow.

To provide more conclusive evidence of the contribution of the enone (CI 1) to the total SOA yield of  $\alpha$ -pinene, a number of static chamber experiments were conducted using the optimised setup detailed previously. Ozone concentrations in these experiments ranged from 0.10 to 0.20 ppm and apparent enone concentrations were typically 10–20 $\times$  higher to ensure an excess. The resulting aerosol mass concentrations are plotted against their corresponding aerosol mass fractions in Figure 72. Also plotted are the basis-set fit for  $\alpha$ -pinene produced by Presto and Donahue,<sup>15</sup> the  $\alpha$ -pinene data reported in Chapter 3 of this work, and the enal and enone data reported by Hoare.<sup>2</sup>

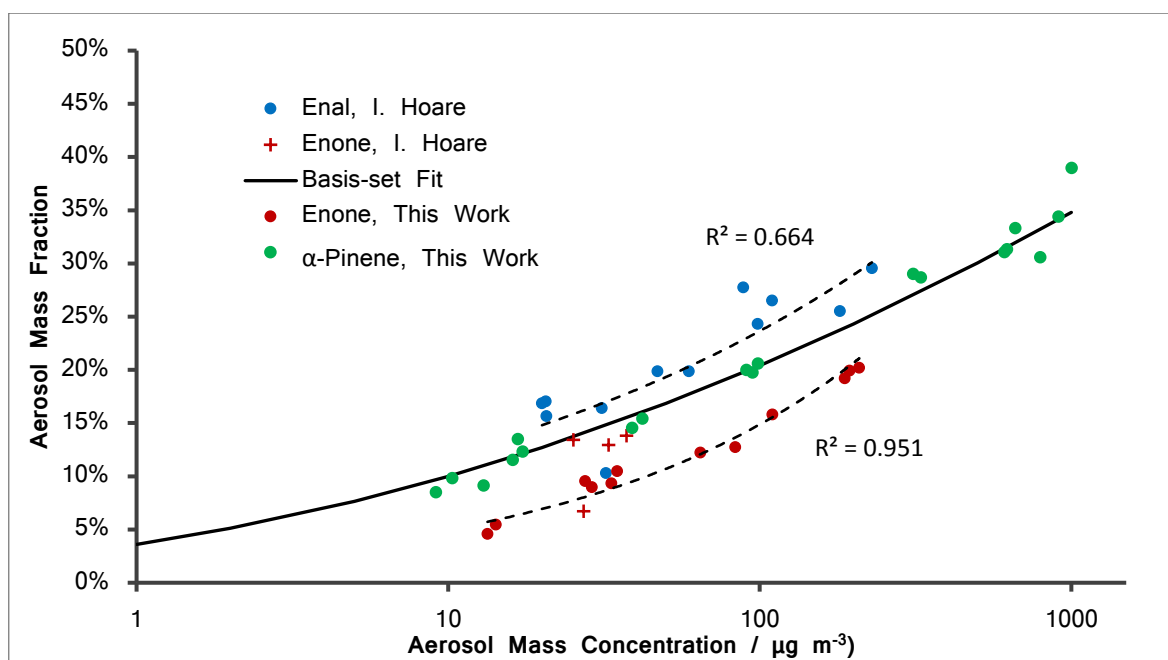


Figure 72: Aerosol mass fraction as a function of observed aerosol mass concentration, for  $\alpha$ -pinene and enone experiments, plotted against the basis-set fit from Presto and Donahue,<sup>15</sup> and the enal and enone data from Hoare.<sup>2</sup> Fits to the enal and enone data are also plotted as dashed lines.

Calculation of the mass yield by equation (47) requires knowledge of the initial reactant concentrations. In the case of the enone experiments performed here, initial concentration of the enone was uncertain—hence the excess conditions employed. However, this uncertainty had little effect on the calculated mass yields.  $F$ , the correction factor, is calculated from the simulated product concentration (see equation (45)), which in turn is calculated from both  $k$ , the reaction rate constant, and  $[\text{enone}]$ , the concentration of enone (see equation (44)). If  $[\text{enone}]$  decreases,  $k$  must in turn increase to produce a good fit, resulting in minimal impact on the mass yield calculated.

The correlation coefficient,  $R^2$ , is 0.95 for the fit to the enone data presented here, suggesting a good fit.  $R^2$  for the enal data reported by Hoare<sup>2</sup> is only 0.66, suggesting a poorer fit due to the greater scatter in the data.

The enone data produced in this work all lie below the basis set fit, and also below the  $\alpha$ -pinene data produced in this work. This suggests that CI 1 is responsible for a smaller proportion of the aerosol mass produced by the ozonolysis of  $\alpha$ -pinene, compared to CI 2. This agrees well with the data for the enal reported by Hoare,<sup>2</sup> which all lie slightly above the trend line, suggesting that CI 2 is responsible for more than 50 % of  $\alpha$ -pinene SOA. CI

1, therefore, must produce a greater quantity of low volatility products, which are incorporated into the aerosol, than CI 2.

It is interesting to note that, whilst the enone produces consistently lower mass yields than  $\alpha$ -pinene, and the enal consistently higher, the proportional contribution of each is not constant. Across the range of aerosol mass concentrations investigated, the enone produces mass yields consistently 5–7 percentage points below those of  $\alpha$ -pinene, and the enal 3–5 percentage points above (aside from outlier), although with much greater scatter across the data obtained by Hoare.<sup>2</sup> Therefore, as mass yield increases, the proportional contribution of CI 1 also increases and that of CI 2 decreases, trending asymptotically toward a 50:50 split (see Figure 73).

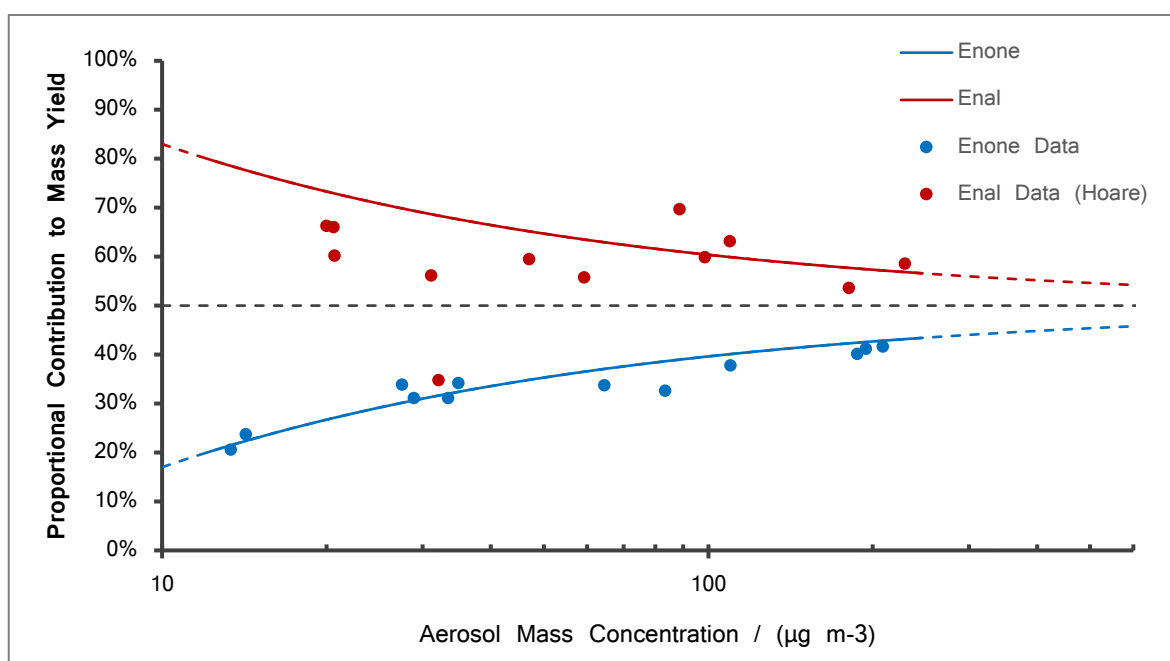


Figure 73: Proportional contribution of each CI to the overall aerosol mass yield vs. aerosol mass concentration. Enone data represented by red circles, enal data (Hoare)<sup>2</sup> represented by blue circles. The red line corresponds to the hypothesised curve for the enone (CI 1), and the blue line to that for the enal (CI 2). Red and blue dashed lines represent extrapolations of these curves outside the measured range.

The hypothesised curve for the proportional contribution of the enone (Figure 73) shows good agreement with the enone data, also plotted in Figure 73. The enal shows poorer agreement, due to the large degree of scatter in the data reported by Hoare.<sup>2</sup> Therefore, the hypothesised curve presented here for the proportional contribution of the enal is simply calculated as the difference between 100 percent and the percentage contribution of the enone, since the contributions from both CIs must total 100 % of  $\alpha$ -pinene yield.

This trend suggests that the contribution of each CI to the observed aerosol mass produced by the ozonolysis of  $\alpha$ -pinene is strongly dependent on local concentrations of reactants, with an increasing proportional contribution from CI 1 products as reactant concentrations increase, although products of CI 2 always contribute the greater proportion.

As was previously discussed in section 3.1, pinonic acid<sup>1</sup> and pinic acid<sup>16</sup> may potentially be likely candidates for the initial nucleation of aerosol particles in chamber experiments due to their low vapour pressures, of  $7 \times 10^{-5}$  and  $3.2 \times 10^{-5}$  Pa,<sup>17</sup> respectively. Referring to Figure 61, whilst pinonic acid is produced by both Criegee intermediates, and thus may be responsible for particle nucleation in both cases, pinic acid is only formed from CI 2. Molar yields of pinonic and pinic acid from the enal ozonolysis are 3.5 % and 1.5 % respectively,<sup>18</sup> in the presence of cyclohexane as a scavenger. For the lowest reactant concentration reported by Hoare,<sup>2</sup> 0.10 ppm, pinonic and pinic acid may therefore be expected to be formed in mixing ratios of approximately 3.5 and 1.5 ppb, respectively. These equate to partial pressures of  $3.5 \times 10^{-4}$  and  $1.5 \times 10^{-4}$  Pa, significantly higher than their respective vapour pressures. Molar yield of pinonic acid from the enone ozonolysis is not reported. It therefore seems likely that the difference in behaviour between enal and enone, particularly with regards to the quantity of low ( $< 10 \mu\text{g m}^{-3}$ ) volatility products formed, may be in large part due to this distinction between yields of pinic and pinonic acid.

This rationale may also explain the difference in particle number concentrations of the aerosol formed from ozonolyses of enal and enone, reported in section 4.4. Formation of higher concentrations of these two very low volatility compounds from the enal channel, compared to the enone, is likely to lead to nucleation of more particles, and may explain the higher number concentration formed from the enal ozonolysis. Hydroperoxides are also thought to be important for particle nucleation.<sup>19</sup> However, there is no discernible reason as to why the influence of hydroperoxides should vary between the enal and enone ozonolyses, and therefore the conclusion is that differences in product yields, particularly those of pinic and pinonic acid, are responsible for the difference, reported here for the first time.

## 4.7 Conclusions

The enone derivative of  $\alpha$ -pinene was synthesised in moderate yield (37 %), and the structure elucidated by  $^1\text{H}$  and 2D-COSY- $^1\text{H}$  NMR. Ozonolysis of the enone allowed for calculation of a reaction rate constant,  $k = 4.3 \pm 0.9 \times 10^{-17} \text{ cm}^3 \text{ molecule}^{-1} \text{ s}^{-1}$ , approximately 40 % of that of  $\alpha$ -pinene + ozone. This is in agreement with that reported by Hoare,<sup>2</sup> but with smaller uncertainty, likely due to inaccuracies introduced by extrapolation of the data in Hoare's work.

Ozonolysis of  $\alpha$ -pinene and its enone derivative were carried out under apparent identical conditions (both in excess with respect to ozone), and the resulting aerosol evolution profiles compared both to one another and to that of the enal derivative reported by Hoare.<sup>2</sup> This comparison highlighted some stark and interesting differences between the behaviours of the three compounds. Ozonolysis of the enone produced significantly fewer, larger particles than the enal, and a considerably lower aerosol mass concentration than either the enal or  $\alpha$ -pinene itself. Comparison of  $\alpha$ -pinene to its enal derivative was difficult, since the enal data reported by Hoare do not cover a timeframe wide enough to encompass the peak mass concentration, making extrapolation and estimation the only possibility. It has been shown that products of the enal (CI 2) may be responsible for the majority of particle nucleation in the  $\alpha$ -pinene ozonolysis, and that products of both Criegee intermediates contribute to subsequent growth of those particles. This is in agreement with the conclusions of Hoare, who noted the same trend between the enone and enal, despite lacking conclusive data on the enone ozonolysis.

A comparison of the aerosol mass yields of each compound was particularly interesting. The data produced in this work for the enone are conclusive—mass yields are consistently 5–7 percentage points below those of  $\alpha$ -pinene, across a range of aerosol mass concentrations from approximately 10–200  $\mu\text{g m}^{-3}$ . Reported data by Hoare for the enal are less conclusive, but appear to lie around 3–5 percentage points above those of  $\alpha$ -pinene. These results suggest that, while products of both Criegee intermediates contribute to the aerosol mass formed by the ozonolysis of  $\alpha$ -pinene, CI 2 contributes the greater proportion. Interestingly, the proportional contribution from each CI changes as aerosol mass concentration increases, suggesting an increased importance of CI 1 at

higher concentrations. This suggests that CI 2 forms a greater proportion of low volatility products than CI 1, and it is suggested that the acid products, pinic and pinonic acid, may be an important factor in the exhibited behaviours.



## 4.8 References

1. Y. Ma, A. T. Russell and G. Marston, *Phys. Chem. Chem. Phys.*, 2008, **10**, 4294-4312.
2. I. D. Hoare, *Physical Properties of Aerosol from the Ozonolysis of  $\alpha$ -Pinene and some of its Synthetic Derivatives*, University of Reading, Ph.D., 2013.
3. J. Marrero and R. Gani, *Fluid Phase Equilibria*, 2001, **183-184**, 183-208.
4. B. E. Poling, J. M. Prausnitz and J. P. O'Connell, *The properties of gases and liquids*, McGraw-Hill, New York, USA, 2001.
5. M. Capouet and J.-F. Müller, *Atmos. Chem. Phys.*, 2006, **6**, 1455-1467.
6. T. E. Daubert and R. P. Danner, *Physical and Thermodynamic Properties of Pure Chemicals Data Compilation*, Taylor and Francis, Washington, D.C., 1989.
7. P. J. Ziemann and R. Atkinson, *Chem. Soc. Rev.*, 2012, **41**, 6582-6605.
8. E. S. C. Kwok and R. Atkinson, *Atmos. Environ.*, 1995, **29**, 1685-1695.
9. J. Peeters, W. Boullart, V. Pultau, S. Vandenberg and L. Vereecken, *J. Phys. Chem. A*, 2007, **111**, 1618-1631.
10. M. D. King, C. E. Canosa-Mas and R. P. Wayne, *Phys. Chem. Chem. Phys.*, 1999, **1**, 2231-2238.
11. E. Grosjean and D. Grosjean, *Int. J. Chem. Kinet.*, 1996, **28**, 911-918.
12. D. Johnson, A. R. Rickard, C. D. McGill and G. Marston, *Phys. Chem. Chem. Phys.*, 2000, **2**, 323-328.
13. Gaussian 03, *Revision C.02*, M. J. Frisch, G. W. Trucks, H. B. Schlegel, G. E. Scuseria, M. A. Robb, J. R. Cheeseman, J. A. Montgomery, Jr., T. Vreven, K. N. Kudin, J. C. Burant, J. M. Millam, S. S. Iyengar, J. Tomasi, V. Barone, B. Mennucci, M. Cossi, G. Scalmani, N. Rega, G. A. Petersson, H. Nakatsuji, M. Hada, M. Ehara, K. Toyota, R. Fukuda, J. Hasegawa, M. Ishida, T. Nakajima, Y. Honda, O. Kitao, H. Nakai, M. Klene, X. Li, J. E. Knox, H. P. Hratchian, J. B. Cross, V. Bakken, C. Adamo, J. Jaramillo, R. Gomperts, R. E. Stratmann, O. Yazyev, A. J. Austin, R. Cammi, C. Pomelli, J. W. Ochterski, P. Y. Ayala, K. Morokuma, G. A. Voth, P. Salvador, J. J. Dannenberg, V. G. Zakrzewski, S. Dapprich, A. D. Daniels, M. C. Strain, O. Farkas, D. K. Malick, A. D. Rabuck, K. Raghavachari, J. B. Foresman, J. V. Ortiz, Q. Cui, A. G. Baboul, S. Clifford, J. Cioslowski, B. B. Stefanov, G. Liu, A. Liashenko, P. Piskorz, I. Komaromi, R. L. Martin, D. J. Fox, T. Keith, M. A. Al-Laham, C. Y. Peng, A. Nanayakkara, M. Challacombe, P. M. W. Gill, B. Johnson, W. Chen, M. W. Wong, C. Gonzalez, and J. A. Pople, *Gaussian, Inc.*, Wallingford CT, 2004.
14. R. Atkinson, *J. Phys. Chem. Ref. Data*, 1997, **26**, 215-290.

15. A. A. Presto and N. M. Donahue, *Environ. Sci. Technol.*, 2006, **40**, 3536-3543.
16. T. S. Christoffersen, J. Hjorth, O. Horie, N. R. Jensen, D. Kotzias, L. L. Molander, P. Neeb, L. Ruppert, R. Winterhalter, A. Virkkula, K. Wirtz and B. R. Larsen, *Atmos. Environ.*, 1998, **32**, 1657-1661.
17. M. Bilde and S. N. Pandis, *Environ Sci Technol*, 2001, **35**, 3344-3349.
18. Y. Ma, T. R. Willcox, A. T. Russell and G. Marston, *Chem. Comm.*, 2007, 1328-1330.
19. K. P. Wyche, P. S. Monks, A. M. Ellis, R. L. Cordell, A. E. Parker, C. Whyte, A. Metzger, J. Dommen, J. Duplissy, A. S. H. Prevot, U. Baltensperger, A. R. Rickard and F. Wulfert, *Atmos. Chem. Phys.*, 2009, **9**, 635-665.

# Chapter 5

## Ozonolysis of $\alpha$ -terpinene

---

### 5.1 Introduction

The previous chapters focused on  $\alpha$ -pinene ozonolysis, and the subsequent formation of aerosol. A highly abundant species,  $\alpha$ -pinene is clearly a very important compound in atmospheric chemistry, worthy of the widespread attention it has garnered from various research groups. There are, however, such a multitude of biogenic VOCs that it is important to look beyond the most abundant and widely-researched compounds, and also consider the potential of others to produce SOA.

This chapter will look at the ozonolysis of  $\alpha$ -terpinene (Figure 74), another monoterpene sharing the chemical formula  $C_{10}H_{16}$ , upon which far fewer studies have been carried out. Emissions of  $\alpha$ -terpinene are substantially lower than those of  $\alpha$ -pinene, although to our knowledge no estimate of the global emissions of  $\alpha$ -terpinene has been published, although emissions of  $\alpha$ - +  $\gamma$ -terpinene are estimated at approximately  $1 \text{ Tg yr}^{-1}$ .<sup>1</sup>

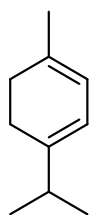


Figure 74: Chemical structure of  $\alpha$ -terpinene.

It is well-known that the emission patterns of different plants are specific to their species,<sup>2</sup> and there have been a number of studies in the literature which make mention of  $\alpha$ -terpinene emissions from specific sources. Both total monoterpene emissions and fractional contribution of each monoterpene to the whole are highly dependent on the season, availability of light, and temperature.<sup>2, 3</sup> With this in mind, emissions of  $\alpha$ -terpinene vary significantly over the course of a year.

The most prominent source-species of  $\alpha$ -terpinene, by percentage of total monoterpene emissions, appears to be Pitch pine (*Pinus rigida*), which is native to South Korea, China, Japan, Russia and the north-east US.<sup>4,5</sup> Emissions of  $\alpha$ -terpinene from this species are negligible in the spring, and low during the summer, accounting for approximately 2 % of total monoterpene emissions. However, this increases substantially in the autumn, when  $\alpha$ -terpinene makes-up 27 % of monoterpene emissions from *Pinus rigida*, before falling back to 10 % of the whole in the winter.<sup>4</sup> This remarkable increase in the percentage contribution of  $\alpha$ -terpinene is partially offset by an overall fall in monoterpene emissions across the seasons. Terpene emissions measured by Son *et al.* showed an average monoterpene leaf level emission rate (measured as the emission rate of VOC per unit weight of leaf matter) of approximately  $1.2 \mu\text{gC g}^{-1} \text{h}^{-1}$  in spring, which fell to around  $0.6 \mu\text{gC g}^{-1} \text{h}^{-1}$  in summer and autumn, and again to approximately  $0.1 \mu\text{gC g}^{-1} \text{h}^{-1}$  in the winter.<sup>4</sup> By simple calculation, this corresponds to an  $\alpha$ -terpinene emission rate of around  $0.15 \mu\text{gC g}^{-1} \text{h}^{-1}$  at its peak in the autumn. For comparison,  $\alpha$ -pinene emissions from *Pinus rigida* peak at around  $0.36 \mu\text{gC g}^{-1} \text{h}^{-1}$  in the spring.

Another study, by Rivoal *et al.*, characterises the monoterpene emissions of *Cistus monspeliensis* L., a widespread shrub species native to the Mediterranean region.<sup>3</sup> Total monoterpene emissions for this species were  $3.192 \mu\text{gC g}^{-1} \text{h}^{-1}$  in spring, of which  $0.197 \mu\text{gC g}^{-1} \text{h}^{-1}$  is  $\alpha$ -terpinene. For comparison,  $\alpha$ -pinene emissions from *Cistus monspeliensis* L. in springtime were measured as  $1.413 \mu\text{gC g}^{-1} \text{h}^{-1}$ . This study also characterised emissions across the other seasons, but no  $\alpha$ -terpinene was detected.

Further plant species which release  $\alpha$ -terpinene into the atmosphere include, but are not limited to, European beech (*Fagus sylvatica* L.),<sup>2,6</sup> Mediterranean oak (*Quercus ilex* L.)<sup>7</sup> and Ponderosa pine (*Pinus ponderosa* L.).<sup>8</sup>

Ham *et al.*<sup>9</sup> investigated the concentrations of various terpenes in different forests in South Korea. A large proportion of trees in South Korean coniferous forests are of the *Pinus rigida* species which, according to Son *et al.*,<sup>4</sup> is a prominent source-species of  $\alpha$ -terpinene. It seems, then, that this should provide a reasonable estimation of the upper-end of  $\alpha$ -terpinene concentrations globally. They measured a mixing ratio of

0.524  $\mu\text{g m}^{-3}$   $\alpha$ -terpinene, corresponding to a background concentration of 0.1 ppb. This compares to a value of 1.693  $\mu\text{g m}^{-3}$  for  $\alpha$ -pinene.

Kesselmeier *et al.*<sup>10</sup> also measured ambient terpene concentrations, this time in the Amazonian rainforest. Concentrations of  $\alpha$ -terpinene observed were again low, below 0.1 ppb. They comment that this is likely a consequence of both a low emission rate, and also a particularly fast rate of removal through reaction. For comparison,  $\alpha$ -pinene concentrations were around 2.4 ppb.

One study in the literature, by Hov *et al.*, attempts to quantify ground-level concentrations of terpenes including terpinene.<sup>11</sup> Unfortunately, the authors make no distinction between  $\alpha$ - and  $\gamma$ -terpinene in their measurements, instead referring to “terpinene” as a whole. Still, they identify terpinene concentrations in coniferous forest air of 0.9–14.1 ppb throughout June and August. This is a much higher estimate of terpinene concentrations than those measured by Ham *et al.* and Kesselmeier *et al.* However, the authors do acknowledge that their observations show higher concentrations than other studies in the literature. They attribute this to their method, whereby terpenes were collected within 10 cm of the tree species, within the canopy itself. Thus, little oxidation is able to occur before collection and measurement of the species.

$\alpha$ -Terpinene is known to undergo rapid ozonolysis at ground level; the IUPAC preferred rate constant for the reaction of  $\text{O}_3 + \alpha$ -terpinene is:  $k = 1.9 \pm 0.20 \times 10^{-14} \text{ cm}^3 \text{ molecule}^{-1} \text{ s}^{-1}$ .<sup>12</sup> This is an average of the values of  $k = 1.5 \pm 0.4 \times 10^{-14}$  and  $k = 2.18 \pm 0.23 \times 10^{-14} \text{ cm}^3 \text{ molecule}^{-1} \text{ s}^{-1}$  reported by Witter *et al.*<sup>13</sup> and Shu and Atkinson,<sup>14</sup> respectively. Another, earlier study<sup>15</sup> reported a higher rate constant. However, the rate constants reported in that study, for both  $\alpha$ -terpinene and other terpenes, are judged to be systematically high, and therefore are not taken into account. This reaction is again known to proceed via attack of the ozone molecule onto one of the double bonds in  $\alpha$ -terpinene, forming a primary ozonide which then decomposes into Criegee intermediates, as shown in Figure 75.<sup>16</sup> Subsequent ozonolysis of the alternate carbon-carbon double bond may form further Criegee intermediates,<sup>16</sup> but these are not included for clarity.

The structure of  $\alpha$ -terpinene contains two conjugated C=C bonds, held *cisoid* to each other by the 6-membered ring conformation (see Figure 74). Lewin *et al.*<sup>17</sup> experimentally determined the ozonolysis rate constants of a number of conjugated dienes, and observed a clear difference between the rate constants of the *trans*-dienes vs. the *cis*-dienes.

It is well established that, for a single class of compounds, ozonolysis rate constants may be reasonably estimated by a plot of  $E_{\text{HOMO}}$  vs.  $-\log K$ <sup>18</sup> (see section 4.4 for a more detailed discussion). Lewin *et al.*<sup>17</sup> perform a corresponding regression analysis for a group of *trans*-dienes, and report a linear relationship between  $E_{\text{HOMO}}$  and  $-\log k$ . However, they note that the rate constants of *cis*-dienes, such as  $\alpha$ -terpinene, are not well described by the fit for *trans*-dienes, and that *cis*-dienes react approximately one order of magnitude faster than would be expected based on the trend for *trans*-dienes. The authors conclude that it is uncertain as to why the cyclic *cis*-dienes react significantly more rapidly than the *trans*-dienes. Particularly interesting to note is the observation that, for all dienes, ozone attacks preferentially at the less substituted double bond. This directly opposes the trend observed for monoterpenes, for which increased alkyl substitution increases reactivity.<sup>17</sup>

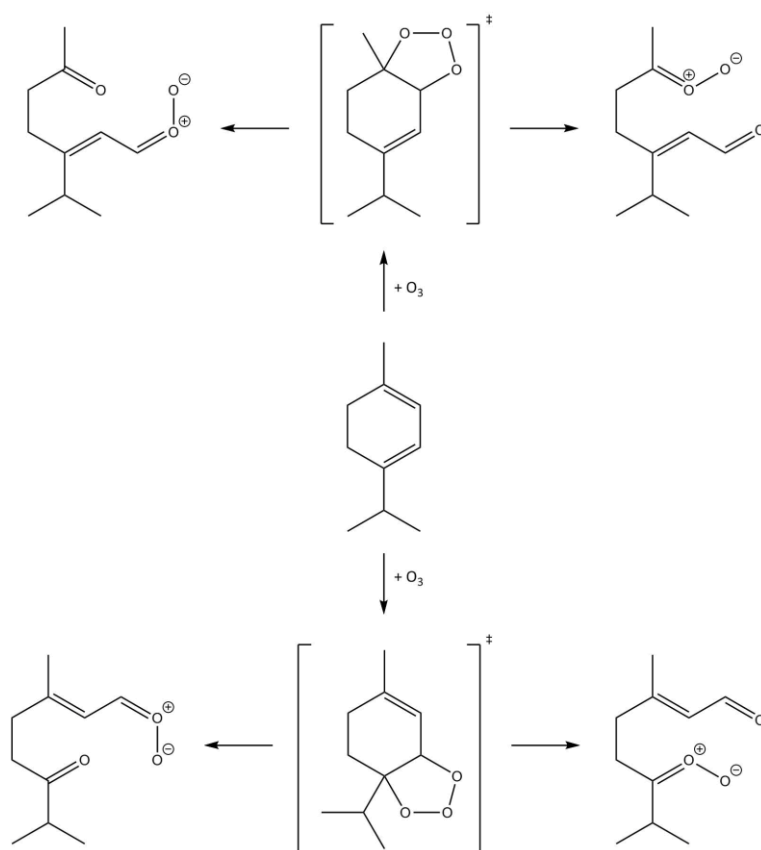
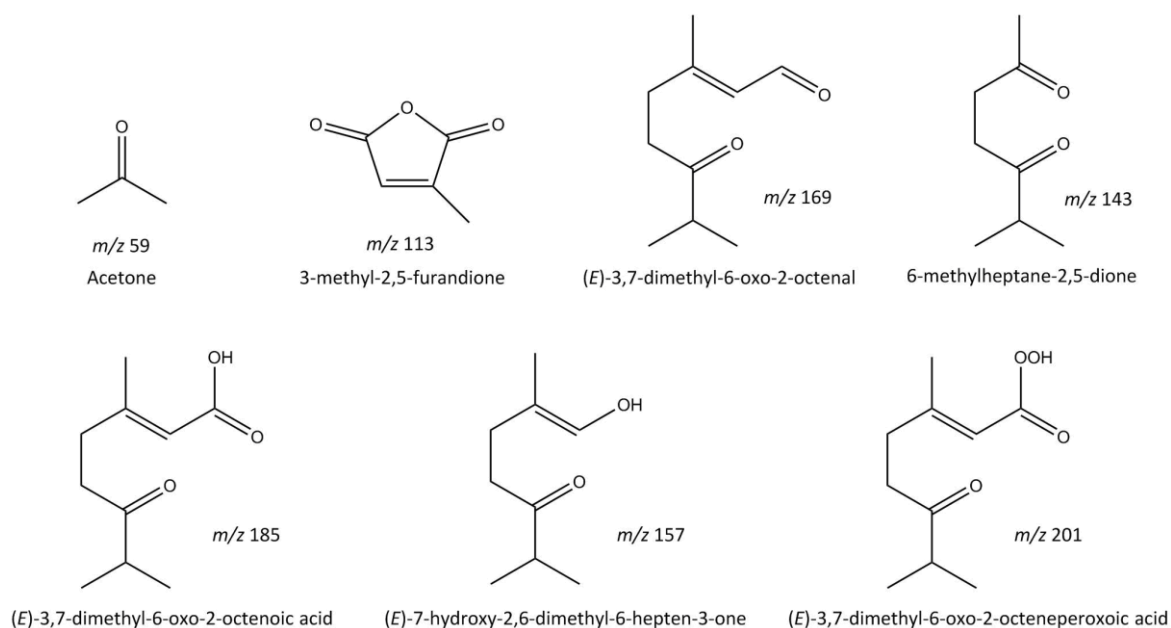


Figure 75: Criegee intermediate formation from the ozonolysis of  $\alpha$ -terpinene.<sup>16</sup>

Ozonolysis of  $\alpha$ -terpinene is complex. In the literature, PTR-MS studies observed at least 21 different product ions, for nine of which structures have been proposed. Seven of these are reproduced in Figure 76.<sup>16</sup> The literature states that there are a number of possible, multi-step reaction pathways to account for their formation, but details are not provided. Both  $\text{HO}_2$  and  $\text{RO}_2$  radicals are involved in the formation of some of these products. Table 19 describes the participation of each radical in the formation of each of the products.

For the other two product ions,  $m/z$  151 & 139, structures are not provided. Instead, they are listed alongside  $m/z$  169 & 157, respectively. This constitutes a difference of 18 amu for each unidentified compound, which suggests a loss of one H and 2 O atoms. Unfortunately, mechanistic details are not provided for the formation of the final structures and, with the evidence available, it would not be reasonable to infer those structures.

Figure 76: Products of the ozonolysis of  $\alpha$ -terpinene, reproduced from Lee *et al.*<sup>16</sup>

$m/z$	RO <sub>2</sub>	HO <sub>2</sub>
59		
113	✓	
143	✓	
157	✓	
169		
185	✓	
201		✓

Table 19: Participation of the HO<sub>2</sub> and RO<sub>2</sub> radicals in formation of the ozonolysis products, according to Lee *et al.*<sup>16</sup>  
See Figure 76 for compound structures.

To our knowledge, only one group in the literature (Lee *et al.*<sup>16</sup>) have studied the potential of  $\alpha$ -terpinene ozonolysis products to form SOA. They report a high aerosol yield of  $47 \pm 1$  %, for an initial terpene concentration of  $164 \pm 1 \mu\text{g m}^{-3}$ , under low (3.4 %) RH conditions, and using cyclohexane as a scavenger. The use of (NH<sub>4</sub>)<sub>2</sub>SO<sub>4</sub> as a seed aerosol suppressed nucleation in their experiments. Particle size distributions and number concentrations were measured using a cylindrical scanning electrical mobility spectrometer. This suggests that  $\alpha$ -terpinene is much more efficient as an SOA precursor than  $\alpha$ -pinene, which, according to the basis-set fit offered by Presto and Donahue<sup>19</sup> (see section 3.5), gives approximately 24 % SOA mass yield under equivalent conditions.



Thus, it seems logical that the SOA-forming potential of  $\alpha$ -terpinene and its ozonolysis products warrants further investigation, and this will be addressed in this chapter.

## 5.2 Aerosol Mass and Mass Yields: Initial Investigation

As mentioned in SECTION 3.4, an important result is the relationship between aerosol mass concentration and mass yield. In this work, this relationship was initially probed through static chamber experiments, according to the method described in section 2.3.2. Experiments were carried out using concentrations of  $\alpha$ -terpinene ranging from 5–25 ppb, in a 1:1 ratio with ozone. This concentration range lies in accordance with the measured ground level concentrations reported by Hov *et al.*<sup>11</sup> Cyclohexane was again employed as an OH scavenger, under low RH conditions. Temperature was monitored throughout and remained between 293 and 297 K for all results reported here. Experiments were carried out in the absence of UV radiation.

Data collection for each experiment was allowed to continue for one hour after the reaction neared completion (> 95 % reacted, calculated according to rate constant,  $k = 1.5 \pm 0.4 \times 10^{-14} \text{ cm}^3 \text{ molecule}^{-1} \text{ s}^{-1}$ )<sup>13</sup>, and wall loss rate constants calculated for each individual experiment, as described in section 2.4.1. Mass yields were calculated from the corrected values, according to equation (47), and plotted versus aerosol mass concentration in Figure 77.

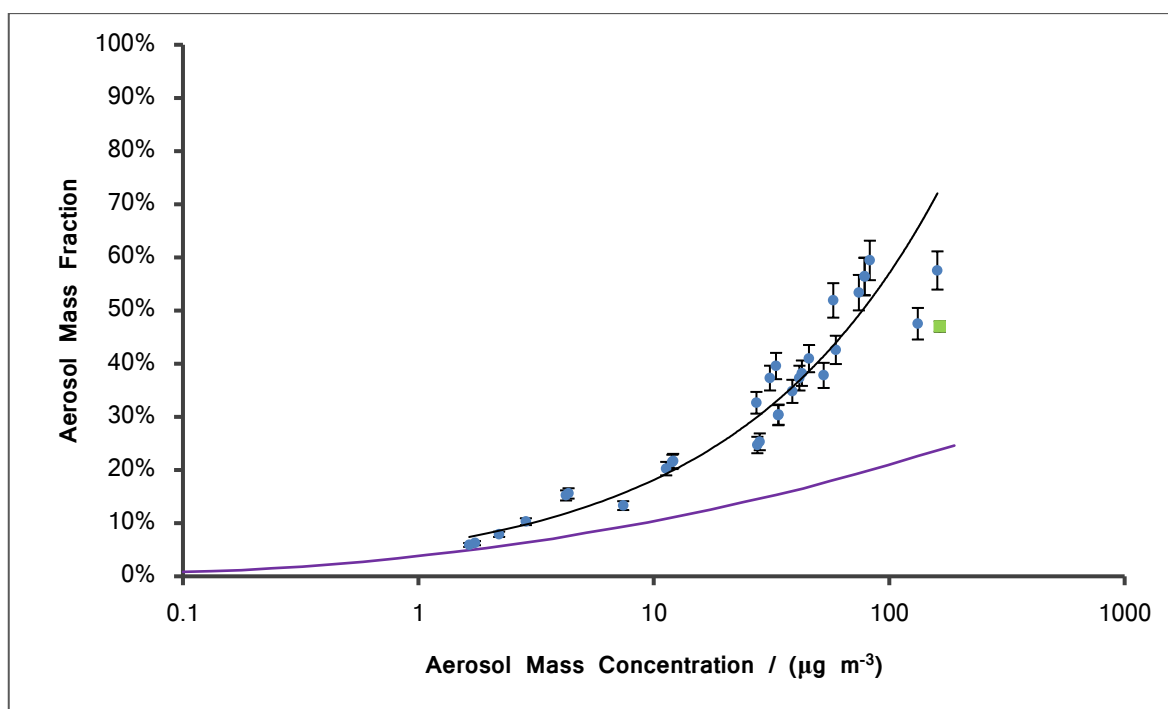


Figure 77: Aerosol mass fraction as a function of aerosol mass concentration, for  $\alpha$ -terpinene ozonolysis products. Blue circles are data from this work; black line corresponds to fit to data presented in this work; green square is from Lee *et al.*<sup>16</sup> purple line = literature fit to  $\alpha$ -pinene ozonolysis data.<sup>20</sup>

The results of these experiments, displayed in Figure 77, show a rapid increase in mass yield across the range 10–100  $\mu\text{g m}^{-3}$ . The lone result available in the literature<sup>16</sup> is plotted alongside, represented by the green square, and shows some similarity to the results of this work. Both Lee *et al.*<sup>16</sup> and the results presented here agree that  $\alpha$ -terpinene ozonolysis produces a high aerosol yield, though Lee *et al.* report a lower yield of  $47 \pm 1\%$ , compared to that of  $57 \pm 3\%$  in this work at a similar mass concentration of 160  $\mu\text{g m}^{-3}$ . Both sets of data employed cyclohexane as a scavenger, and were performed at 293 K under low RH conditions.

However, the data presented here show a significant scatter toward higher mass concentrations, which may account for this difference. Two data points show better agreement with that reported by Lee *et al.* than with the other experimental data. There was nothing unusual about either of these experiments to suggest such a shift. The increased scatter is likely due to uncertainty in reactant concentrations. Experiments performed at higher concentrations used only one dilution in the preparation of the  $\alpha$ -terpinene sample, whereas those at lower concentrations used two dilutions. The

pressure gauge used afforded a resolution of 0.1 Torr. Therefore, by performing two dilutions rather than one, the uncertainty introduced by the resolution of this pressure gauge was minimised. An increased uncertainty in reactant concentration would manifest in an increased uncertainty in mass yield. Also, since only one data point is provided by Lee *et al.*, it is not possible to infer whether this is in fact an outlier for their experimental system.

Lee *et al.* state that sufficient ozone was introduced to their chamber to exceed the terpene concentration by 3 $\times$ , thus employing excess ozone conditions, even when taking into consideration the two double bonds present in  $\alpha$ -terpinene. Thus, it may be more suitable to the data presented later in this work, in section 5.5.

Comparing the  $\alpha$ -terpinene SOA yields to those of  $\alpha$ -pinene, it is clear that  $\alpha$ -terpinene ozonolysis produces compounds of significantly lower volatilities than those of  $\alpha$ -pinene ozonolysis. The difference appears particularly pronounced for compounds with volatilities in the range 10–100  $\mu\text{g m}^{-3}$ , evidenced by the rapidly divergent trends over this range.

### 5.3 Aerosol Mass and Mass Yields: Flow Tube Investigation

To supplement the static chamber experiments, additional experiments were carried out using a flow tube as the reaction vessel, as described in section 2.6. This allowed for study of the initial stages of SOA evolution, through ‘selection’ of specific timeframes, and also provided a clearer idea of the volatility behaviour of the SOA.

#### 5.3.1 Comparison of Flow Tube and Static Chamber Techniques

As previously mentioned, the flow tube technique was introduced to supplement experimental work using the static chamber method, and to provide a clearer picture of the initial stages of SOA evolution. In order to do this, it is important to compare the two techniques, to ensure that data obtained from both are in good agreement.

With this in mind, a number of static chamber experiments were carried out between  $\alpha$ -terpinene and ozone. Experiments were undertaken at various concentrations, with reactants in a 1:1 ratio. Cyclohexane was used as a scavenger, and low RH conditions employed. Temperatures for these experiments lie between 295 and 298 K.

A number of flow tube experiments were undertaken with identical conditions to the static chamber experiments (reactant concentrations, scavenger, temperature and RH), according to the method described in section 2.6. Pressure within the flow tube was 920–940 mbar. Thus, the results of the flow tube experiments should be directly comparable to the static chamber experiments, and provide a good basis for a comparison of the two techniques. The mean results of at least three experimental repeats from both experimental sets are displayed in Figure 78 – Figure 81:

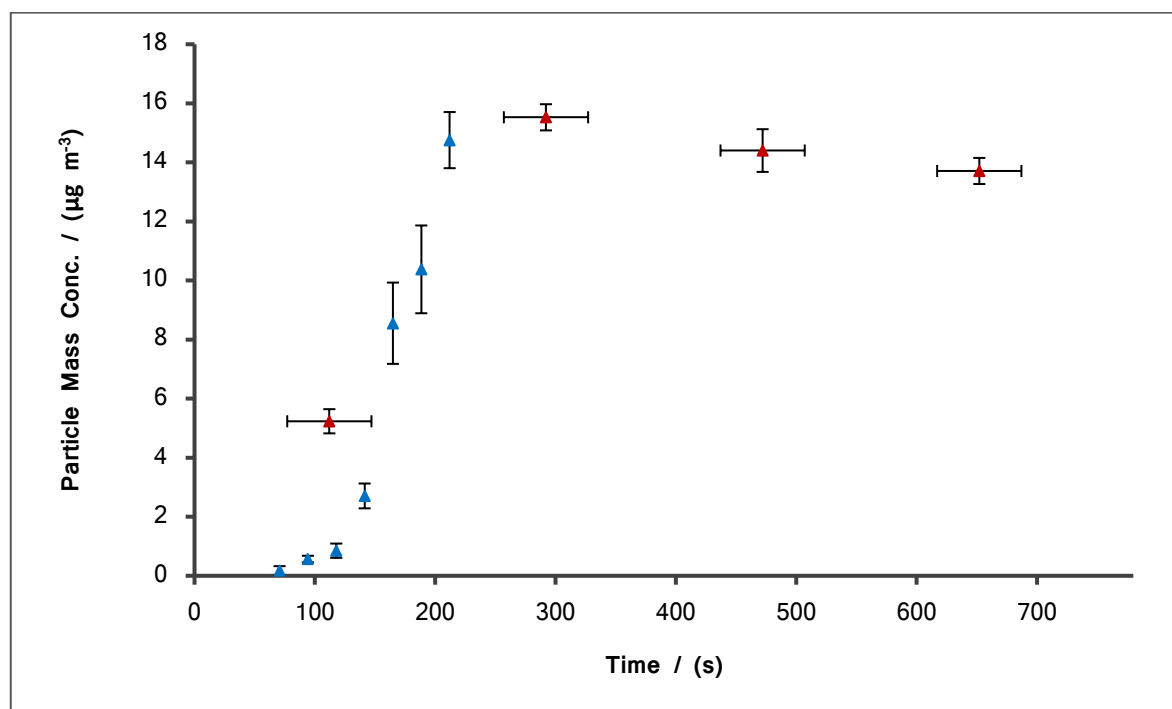


Figure 78: Particle mass concentration vs. time; [ $\alpha$ -terpinene] = [ozone] = 11 ppb. Flow tube data depicted by blue triangles; static chamber data by red triangles.

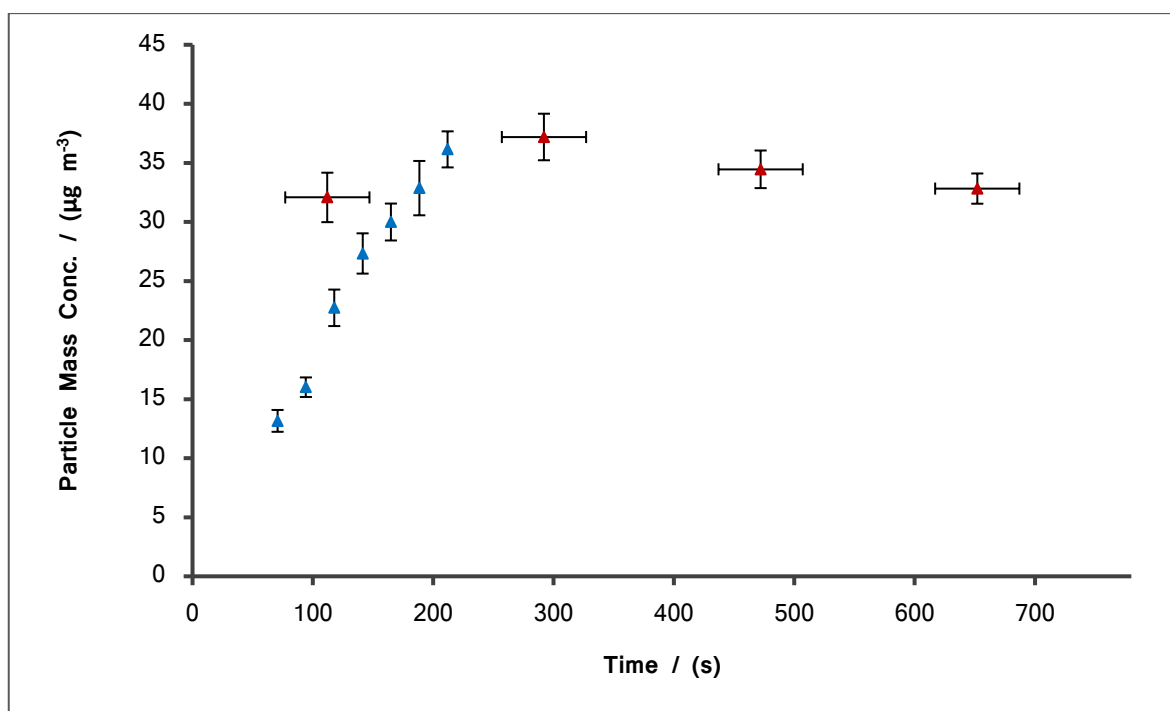


Figure 79: Particle mass concentration vs. time;  $[\alpha\text{-terpinene}] = [\text{ozone}] = 19 \text{ ppb}$ . Flow tube data depicted by blue triangles; static chamber data by red triangles.

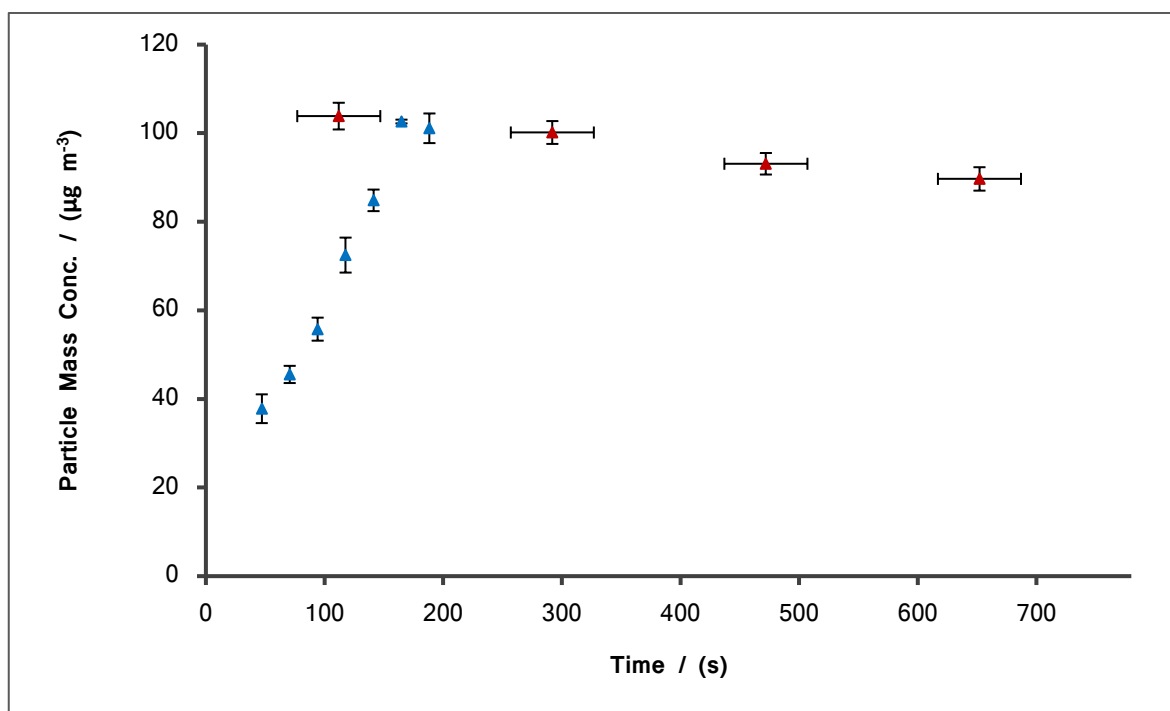


Figure 80: Particle mass concentration vs. time;  $[\alpha\text{-terpinene}] = [\text{ozone}] = 38 \text{ ppb}$ . Flow tube data depicted by blue triangles; static chamber data by red triangles.

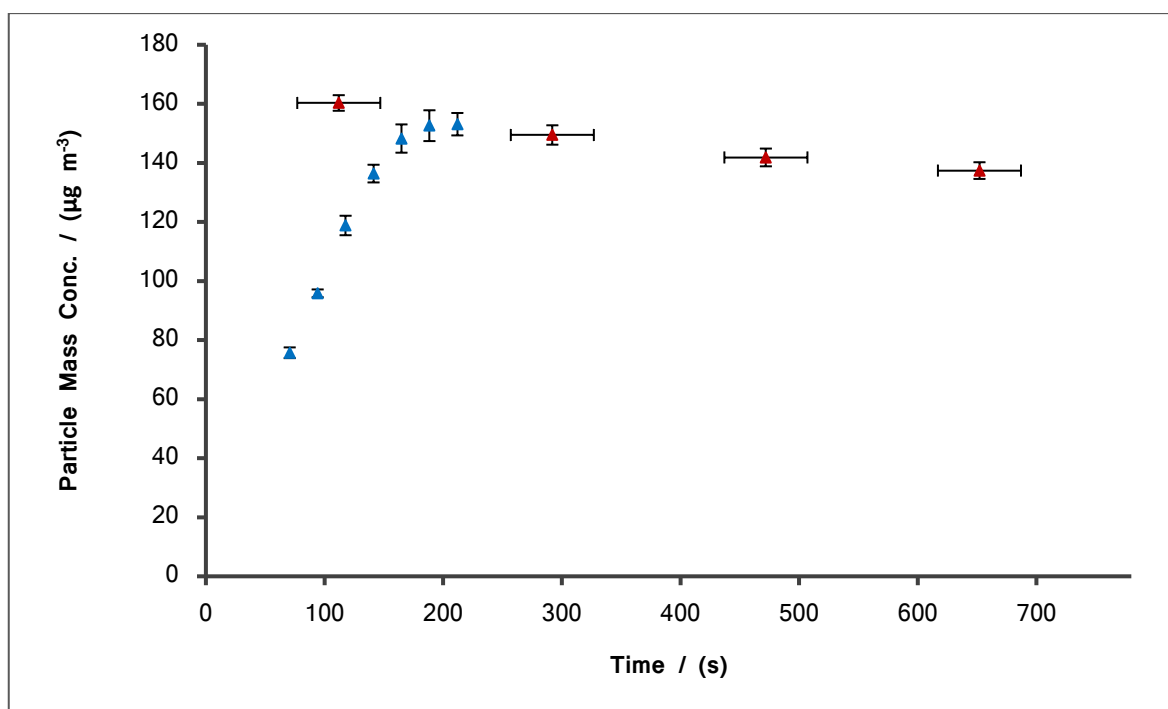


Figure 81: Particle mass concentration vs. time;  $[\alpha\text{-terpinene}] = [\text{ozone}] = 46$  ppb. Flow tube data depicted by blue triangles; static chamber data by red triangles.

Horizontal error bars for the static chamber experiments are due to the scan time of the SMPS instrument. One scan through all particle diameters takes 135 seconds. For the data here, each data point lies at the time corresponding to the mean particle diameter. The error bars for each point are sufficiently wide to encompass  $> 95\%$  of all particle mass detected at that time (typically 35 seconds in both the positive and negative directions). Vertical error bars for both experimental sets are a standard deviation calculated across all experiments under those conditions (typically 3–5 individual runs).

The two experimental techniques show generally good agreement on the maximum mass obtained, across the range of conditions investigated, and always lie within 5 % of one another. The main difference between the two techniques is the observed rate of SOA growth—SOA produced via the static chamber method consistently results in a faster observed growth rate. The reason for this is not clear. One likely contributing factor is the uncertainty regarding the exact point in time at which the static chamber data are measured. In these comparisons, each data point is plotted at the time corresponding to the mean particle diameter, with an uncertainty either side. However, since the number of particles follows a roughly Gaussian distribution, a greater proportion of particle mass

may therefore be attributed to particles of larger diameter than the mean. Since the SMPS scans upwards through particle diameters, this would therefore mean that the centre of the particle mass concentration distribution would be at a slightly later time—shifted toward the right of the error bars in the graphs.

However, this alone cannot fully explain the profound difference between the rates at which SOA is initially observed to form between the two techniques. It is likely that mixing of the different species plays a pivotal role in the early stages of SOA formation, and thus it seems reasonable that formation in a static chamber is accelerated in comparison to the flow tube. While mixing cannot be controlled within the static chamber, it seems likely that it is turbulent, since introduction of ozone to the chamber is at quite a high flow rate ( $7 \text{ L min}^{-1}$ ). Also, once ozone introduction is complete, the static chamber must be moved across the laboratory, resulting in some agitation of the chamber, which again encourages mixing.

Conversely, mixing in the flow tube can be well defined for a simple system with a single-point gas injection. According to equation (30), with a flow rate of  $2 \text{ L min}^{-1}$  as for these experiments, the mixture will produce a homogeneously mixed, laminar flow 15 cm after the sliding injector, or 35 seconds. It was also noted that, due to the design of the injector head, laminar flow may be achieved as early as 8.5 cm, or 20 seconds, after the injector head. This should facilitate faster mixing of the chemical species within the tube, but it proves difficult to quantify the exact mixing time. The data plotted assume a mixing time of 35 seconds. However, it is likely that the mixing time is considerably lower than this, due to the multi-point injection head; see Figure 30. Also, some reaction between the species will be expected to occur before a homogeneously mixed, laminar flow is achieved. This uncertainty has not been included in the graphs because separate error bars would imply that each data point may lie anywhere within the range, whereas in reality, mixing time should be independent of the position of the injector head, and thus all points should be translated toward lower times by the same number of seconds.

### 5.3.2 Gas-Phase Kinetics

Calculation of the reaction rate constant was performed in the same way as for  $\alpha$ -pinene, according to the simulation method described in section 3.4. However, since the ozonolysis of  $\alpha$ -terpinene occurs rapidly, static chamber experiments were not appropriate for calculation of a value for  $k$ . Instead, experiments were carried out in a flow tube, according to the method in section 2.6, using a 1:1 reactant ratio and cyclohexane as a scavenger.

As discussed in section 5.3.1, there is an uncertainty of up to 35 seconds associated with the mixing times in flow tube experiments. Therefore, two analyses were performed for each experiment: one using the minimum possible mixing time of the species, and the other using the maximum, resulting in a lower and upper bound for the rate constant. It seems likely that the true mixing time lies closer to the minimum possible, due to the design of the multi-point injector head, and also since reaction of species will begin before formation of a homogeneously mixed, laminar flow system. An example of each are given in Figure 82 and Figure 83. Initial reactant concentrations for this reaction were 46 ppb, for both  $\alpha$ -terpinene and ozone.



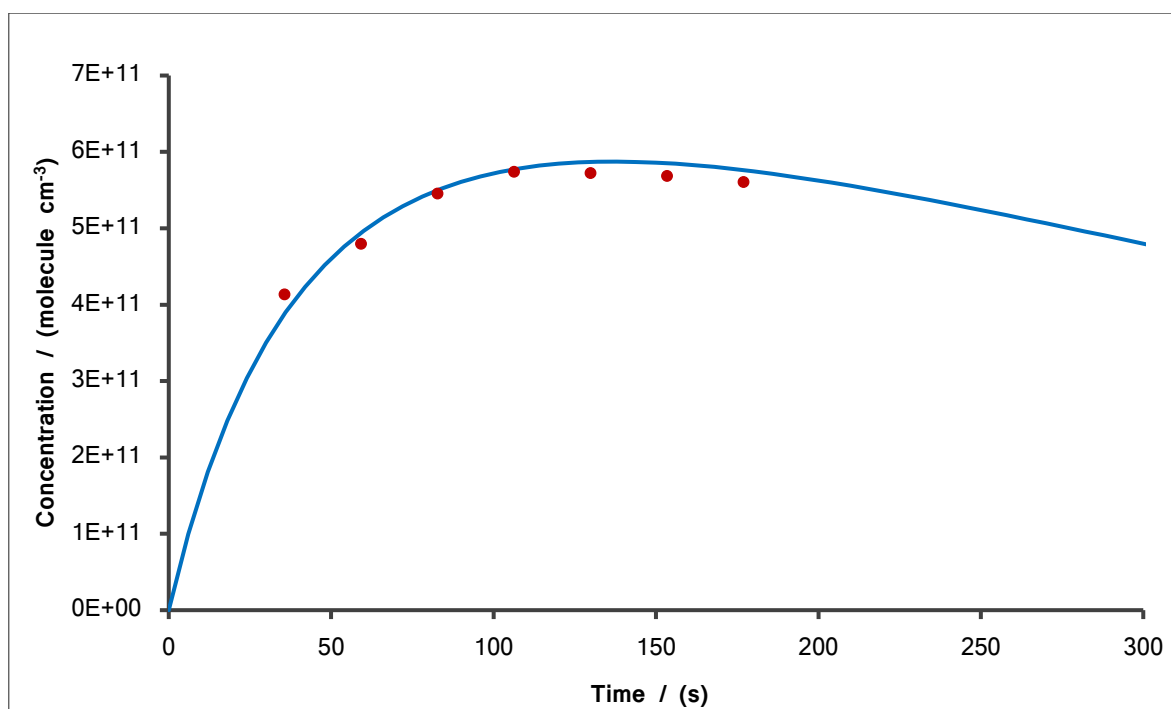


Figure 82: Calculation of a reaction rate constant. Red circles = experimental data; Blue line = simulated data.  
Minimum possible mixing time, assuming instantaneous mixing.

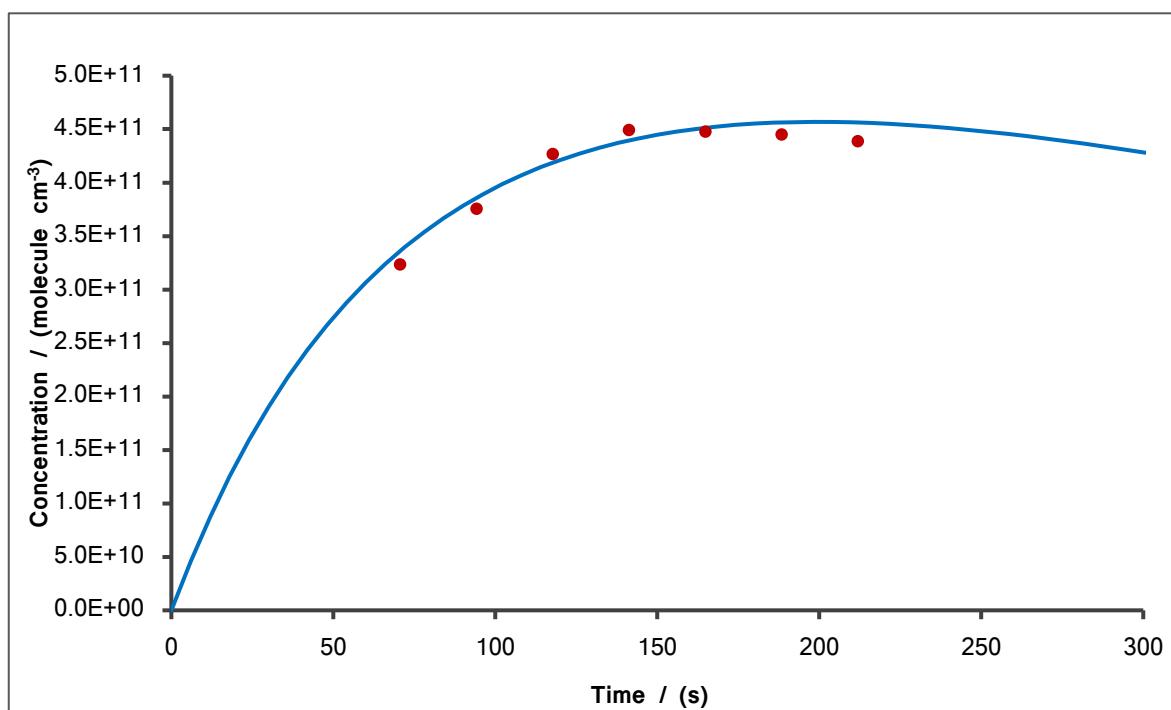


Figure 83: Calculation of a reaction rate constant. Red circles = experimental data; Blue line = simulated data.  
Assuming maximum possible mixing time of 35 s.

Reactions were performed across a range of concentrations, and upper and lower bounds for the reaction rate constant calculated from each. The results are summarised in Table 20:

Concentration / (ppb)	Lower bound $k$ / ( $10^{-15} \text{ cm}^3 \text{ molecule}^{-1} \text{ s}^{-1}$ )	Upper bound $k$ / ( $10^{-15} \text{ cm}^3 \text{ molecule}^{-1} \text{ s}^{-1}$ )
19	10	19.8
30	10	17.3
38	7.9	14.5
46	5.9	13.3
<b>Average</b>	<b><math>8.5 \pm 2.0</math></b>	<b><math>16.2 \pm 2.9</math></b>

Table 20: Reaction rate constants for the  $\alpha$ -terpinene ozonolysis.

The calculated rate constant,  $k$ , must therefore lie between  $8.5 \pm 2.0 \times 10^{-15}$  and  $1.6 \pm 0.3 \times 10^{-14} \text{ cm}^3 \text{ molecule}^{-1} \text{ s}^{-1}$ . The upper bound is in agreement with the IUPAC preferred rate constant of  $k = 1.9 \pm 0.20 \times 10^{-14} \text{ cm}^3 \text{ molecule}^{-1} \text{ s}^{-1}$ ,<sup>12</sup> and with the value of  $k = 1.5 \pm 0.4 \times 10^{-14} \text{ cm}^3 \text{ molecule}^{-1} \text{ s}^{-1}$  reported by Witter *et al.*<sup>13</sup> It is slightly below, yet comparable to the value of  $k = 2.18 \pm 0.23 \times 10^{-14} \text{ cm}^3 \text{ molecule}^{-1} \text{ s}^{-1}$  reported by Shu and Atkinson.<sup>14</sup> This suggests that mixing time within the flow tube is considerably lower than 35 seconds.

### 5.3.3 Aerosol Mass and Mass Yields: Flow Tube Results

As determined in section 5.3.1, the flow tube technique offers very similar results to the static chamber technique with regards to the maximum aerosol mass concentration achieved. Thus, flow tube experiments were carried out to complement this work, and potentially provide results with a lesser degree of scatter. The experiments described here were carried out between  $\alpha$ -terpinene and ozone in a range of concentrations from 5 to 50 ppb, in a 1:1 ratio. Again, cyclohexane was used as a scavenger, temperatures were maintained between 295 and 298 K, and pressure in the flow tube was between 920 and 940 mbar, ensuring that conditions were as similar as possible to those previously used in section 5.2.

The resulting aerosol mass concentrations were corrected for wall loss, according to the method in section 2.6.1. The corrected mass concentrations are plotted alongside their calculated mass yields and are presented in Figure 84, alongside the data previously reported in Figure 77:

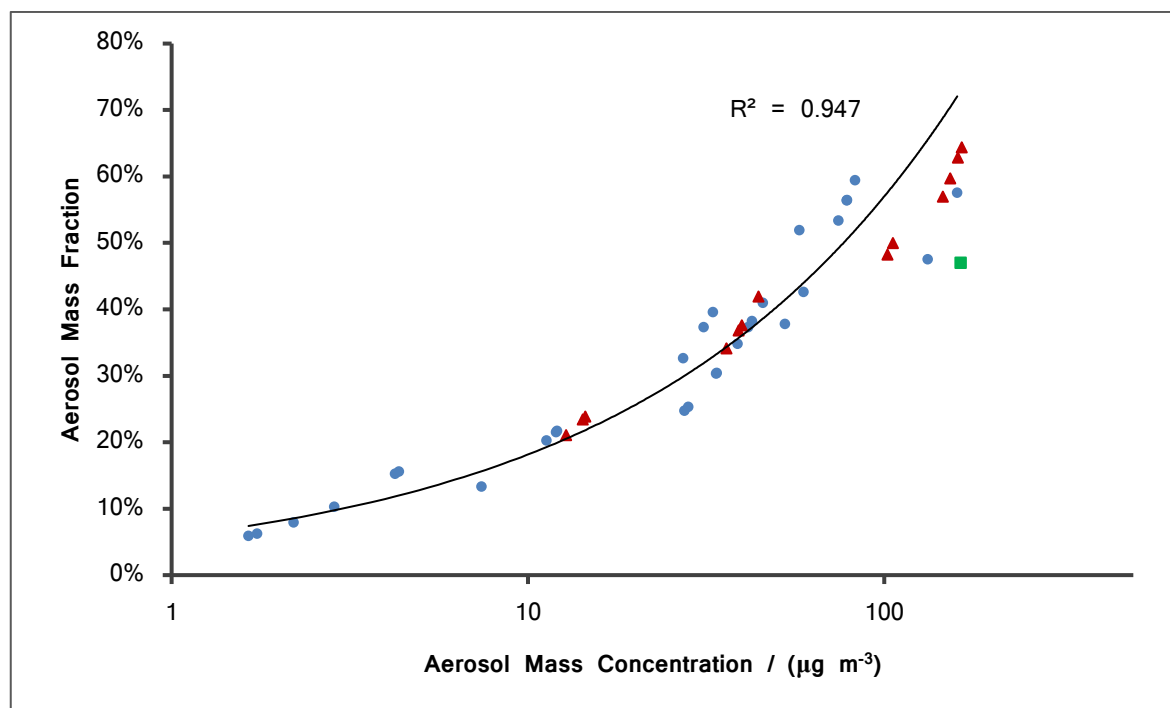


Figure 84: Aerosol mass fraction as a function of aerosol mass concentration, for  $\alpha$ -terpinene ozonolysis products. Blue circles = static chamber data; red triangles = flow tube data; green square = Lee *et al.*<sup>16</sup> Fit to data is only for the static chamber results.

The flow tube data agree well with the fit previously ascertained in section 5.2, particularly at lower mass concentrations. There is some deviation from the fit at higher mass concentrations of above around  $80 \mu\text{g m}^{-3}$ . However, there is significant scatter observed in this region for the static chamber data, which was discussed earlier in this chapter. The flow tube data, on the other hand, show a much smaller degree of scatter, and more closely agrees with Lee *et al.*<sup>16</sup>

If we were to exclude those data points which show a large degree of scatter—those above around 45 % mass yield for the static chamber experiments, where the determination of concentration was affected by inaccurate pressure readings—and fit a curve to the remaining points (including those from flow tube data), we obtain Figure 85:

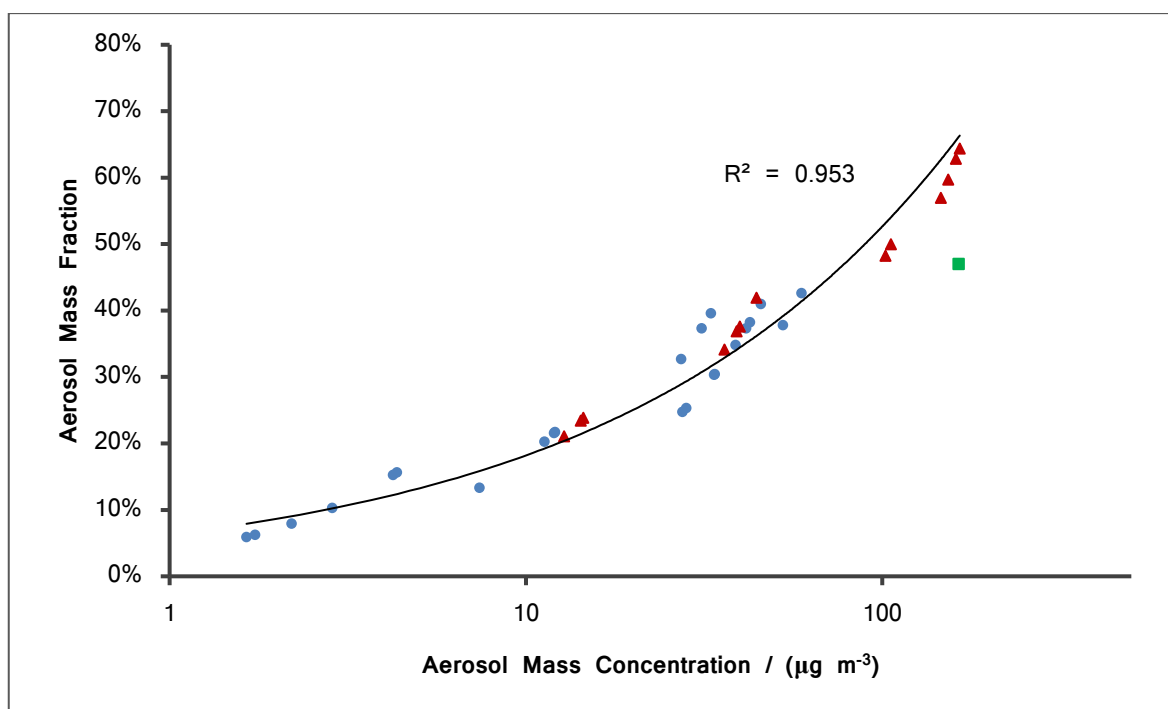


Figure 85: Aerosol mass fraction as a function of aerosol mass concentration, for  $\alpha$ -terpinene ozonolysis products. Blue circles = static chamber data; red triangles = flow tube data; green square = Lee *et al.*<sup>16</sup> Fit to data excluding static chamber region of high uncertainty ( $> 45\%$  mass fraction).

The curve shows a good fit to the data when both experimental approaches are combined in this way, and a slightly improved coefficient of determination,  $R^2$ . The one available reference point from the literature<sup>16</sup> also does not lie far from the curve, suggesting that this is indeed closer to the true relationship. These results suggest that a large proportion of the product mass have volatility in the range  $10\text{--}150\ \mu\text{g m}^{-3}$ , since the observed mass fraction increases dramatically over this range, and, extrapolating, that less than 5 % have volatility  $< 1\ \mu\text{g m}^{-3}$ .

Compared to the  $\alpha$ -pinene system previously studied (see Chapter 3), the products of  $\alpha$ -terpinene are of much lower volatility. This is an important result because, whilst  $\alpha$ -terpinene emissions are significantly lower than those of  $\alpha$ -pinene, if its potential to form SOA is far higher then it may still be an important source of SOA within the atmosphere. Furthermore, this system would be unrealistic within the atmosphere itself, where one would expect a mixture of terpenes, rather than a single species. In a more realistic, mixed system, the low volatility of the  $\alpha$ -terpinene ozonolysis products could lend them to behaving as nucleating agents, forming clusters. Essentially acting as a seeding particle,

this may cause an increase in SOA formation by providing a base onto which the higher volatility products from other terpene ozonolyses may condense.

#### 5.4 Varying Ozone Excess

Since local concentrations of reactants vary according to their environment, it is important to quantify how an excess of one reactant might affect the nature of the SOA produced. Local concentrations of  $\alpha$ -terpinene can vary across the globe, dependent on the type of land-use and vegetation. As previously mentioned, Hov *et al.* measured background levels of 0.9–14.1 ppb terpinene in coniferous forests.<sup>11</sup> Local concentrations of ozone are also known to vary according to the local environment and level of pollution. The current global background is approximately 30–40 ppb,<sup>21</sup> whilst rural areas are exposed to daily maximums of 50–120 ppb ozone.<sup>22</sup>

Therefore, it seems particularly prudent to investigate the impact of an ozone excess on the formation of SOA. This may be especially true in the case of  $\alpha$ -terpinene, which is host to two endocyclic double bonds, both of which may undergo reaction with ozone.

To this end, a number of static chamber experiments were undertaken, according to the method described in section 2.3.2. Initial experiments were carried out between  $\alpha$ -terpinene and ozone in equal concentrations of 10 ppb, using cyclohexane as a scavenger and at 0 % RH. Further experimental sets were carried out with ozone in 2:1 and 3:1 excess with respect to  $\alpha$ -terpinene (20 and 30 ppb of ozone, respectively). The resulting SOA evolutions are plotted in Figure 86 – Figure 88. Data presented are averages across a minimum of three experimental repeats. Due to the huge difference in number concentrations between the experimental sets, contour plots were not appropriate to represent this data.

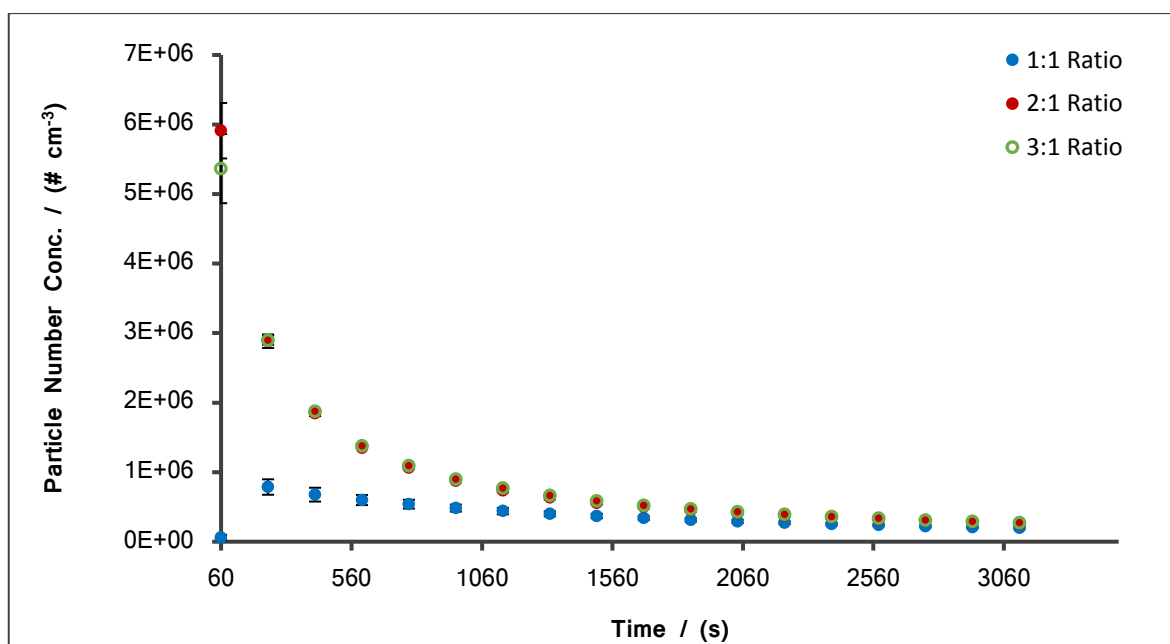


Figure 86: Particle number concentration as a function of time; varying ozone excess. Blue circles = 1:1 ratio; red circles = 2:1 ratio; green circles = 3:1 ratio.

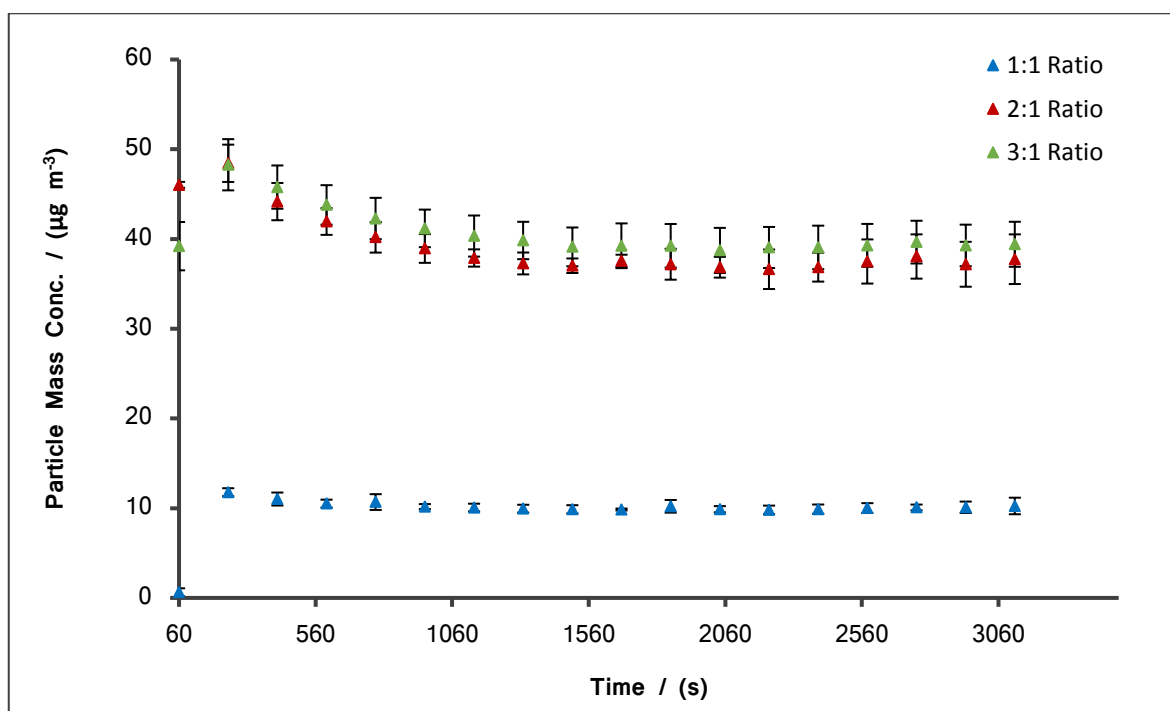


Figure 87: Particle mass concentration as a function of time; varying ozone excess. Blue triangles = 1:1 ratio; red triangles = 2:1 ratio; green triangles = 3:1 ratio.

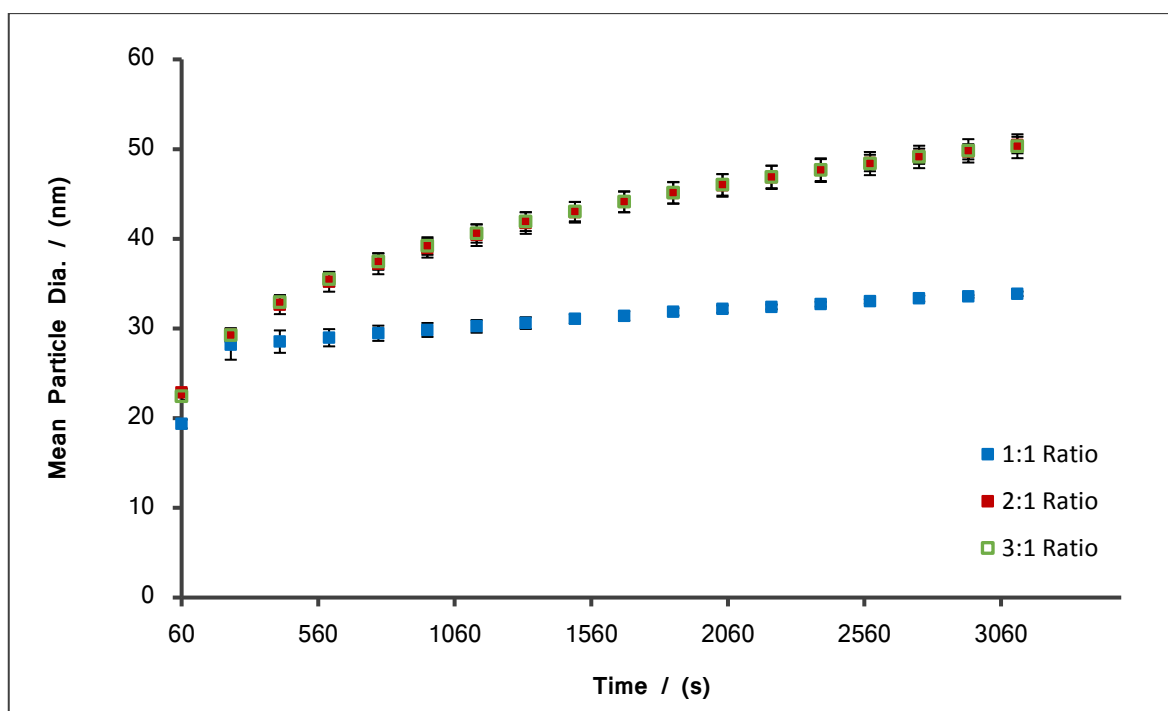


Figure 88: Mean particle diameter as a function of time; varying ozone excess. Blue squares = 1:1 ratio; red squares = 2:1 ratio; green squares = 3:1 ratio.

Looking at Figure 86, the initial appearance of SOA is clearly accelerated by the increased concentration of ozone. Using the 1:1 mixture, peak particle number concentration is not observed until the second SMPS scan, at approximately 240 seconds (though this is not to say that it does not occur before 240 seconds, sometime between the two scans).

Conversely, for the 2:1 and 3:1 mixtures, peak particle number concentration is observed during the first SMPS scan. Key data obtained from these experiments are summarised in Table 21:

[ $\alpha$ -Terpinene] (ppb)	[Ozone] (ppb)	Scavenger	RH (%)	Peak Number Conc. ( $\text{cm}^{-3}$ )	Peak Mass Conc. ( $\mu\text{g m}^{-3}$ )	Mean Dia. at 52 mins (nm)
10	10	Cyclohexane	0	$7.8 \pm 1.77 \times 10^5$	$11.8 \pm 0.4$	$33.9 \pm 0.3$
10	20	Cyclohexane	0	$5.70 \pm 0.40 \times 10^6$	$48.4 \pm 2.1$	$50.3 \pm 0.8$
10	30	Cyclohexane	0	$5.37 \pm 0.50 \times 10^6$	$48.3 \pm 2.9$	$50.1 \pm 1.4$

Table 21: Summary of experimental conditions and results for ozonolysis of  $\alpha$ -terpinene with varying [ozone].

Increasing ozone concentration from the 1:1 to 2:1 mixture causes a huge increase in particle number concentration. Peak number concentrations observed were

$7.86 \pm 1.77 \times 10^5$  and  $5.70 \pm 0.40 \times 10^6 \text{ cm}^{-3}$ , respectively (see Figure 86). Number concentrations fell after this point, particularly rapidly in the case of the 2:1 mixture, due to coagulation of the aerosol. Particle mass concentrations (see Figure 87) similarly increased, from  $11.8 \pm 0.4$  to  $48.4 \pm 2.1 \mu\text{g m}^{-3}$ , which equate to mass yields of  $21.1 \pm 0.8 \%$  and  $87.8 \pm 3.0 \%$ . Mean particle diameter (see Figure 88) for the 1:1 mixture rose slowly throughout the course of the experiment, reaching  $33.9 \pm 0.3 \text{ nm}$  after 52 minutes. Mean particle diameter for the 2:1 mixture began at approximately the same size, but increased more rapidly over the course of the reaction, reaching  $50.3 \pm 0.8 \text{ nm}$  after 52 minutes. This was due to increased coagulation of aerosol particles, as also evidenced by the more rapid decrease in number concentration over the same period.

It is apparent from the graphs that no clear difference between the SOA formed by the 2:1 and 3:1 mixtures was observed. Peak particle mass concentrations were  $48.4 \pm 2.1 \mu\text{g m}^{-3}$  and  $48.3 \pm 2.9 \mu\text{g m}^{-3}$  respectively, which lie well within error of one another. Particle diameters remained within 2 % for the duration of the experiments. Number concentrations initially showed some variance, but quickly converged, again remaining within 2 % of one another for the duration of the experiments.

An increase in mass yield as the ozone concentration increases is perfectly logical. With the 1:1 mixture, and each  $\alpha$ -terpinene molecule containing two double bonds, there is only enough ozone available to react with half of the double bonds, resulting in incomplete oxidation. We might expect a wide range of products formed—with one, the other, or both carbon-carbon double bonds having undergone ozonolysis. With the 2:1 mixture, there is now enough ozone in the system to potentially react with all double bonds present, allowing for complete oxidation of the terpene. With more of the terpene able to react, the amount of condensable material formed must therefore increase, which may then be incorporated into the aerosol, increasing mass yield. It is also possible that the availability of ozone may encourage formation of some products over others—perhaps those which are formed through two separate ozonolyses. If these more-favoured products are of lower volatility than their precursors, this would, at least in part, explain the huge increases in number and mass concentrations observed.



There is no significant difference between the SOA formed by the 2:1 and 3:1 mixtures, suggesting that the 2:1 ratio is indeed sufficient to cause complete oxidation of the terpene.

To probe the suggestion that the increased SOA yield may be due to a change in product yields, a further experimental set was carried out, with  $\alpha$ -terpinene and ozone in equal concentrations of 20 ppb. A comparison between this setup and the 2:1 mixture used previously ( $[\alpha\text{-terpinene}] = 10$  ppb;  $[\text{ozone}] = 20$  ppb) should provide some insight as to whether a change in product yields is the culprit for the increase in SOA yield observed at higher  $\text{O}_3$  concentration. The results of these two experimental sets are presented in Figure 89 – Figure 91. Data are averages across a minimum of three experimental repeats.

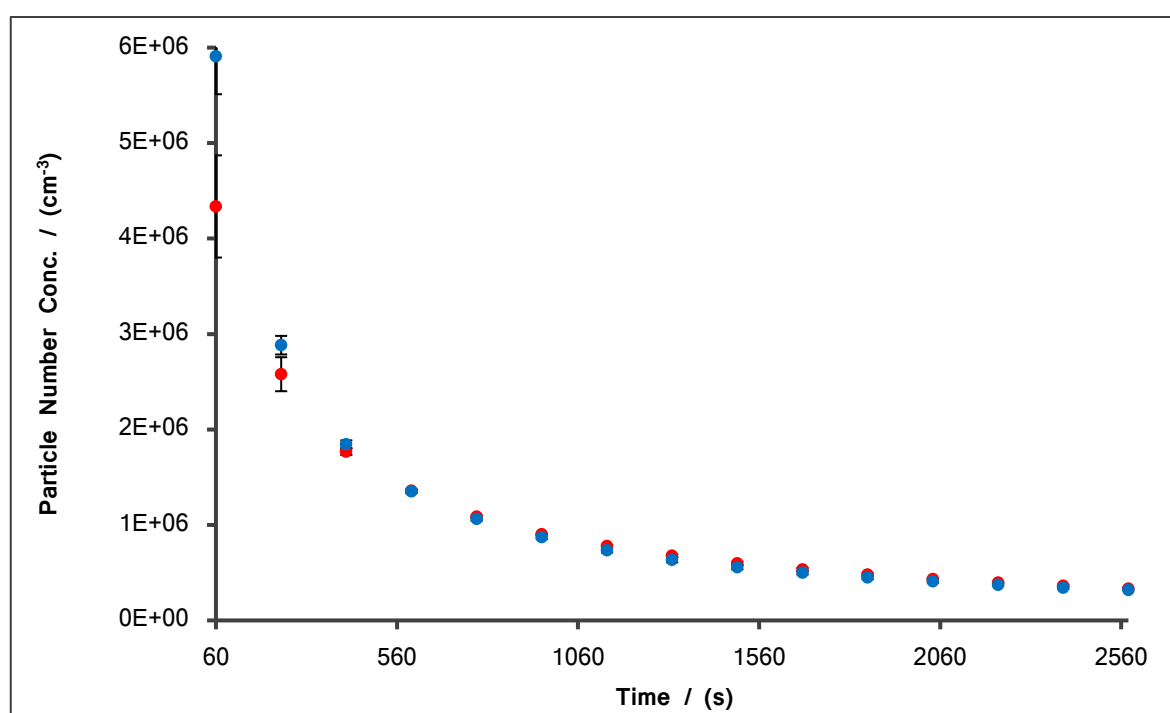


Figure 89: Particle number concentration as a function of time.  $[\text{Ozone}] = 20$  ppb. Blue circles,  $[\alpha\text{-terpinene}] = 10$  ppb; red circles,  $[\alpha\text{-terpinene}] = 20$  ppb.

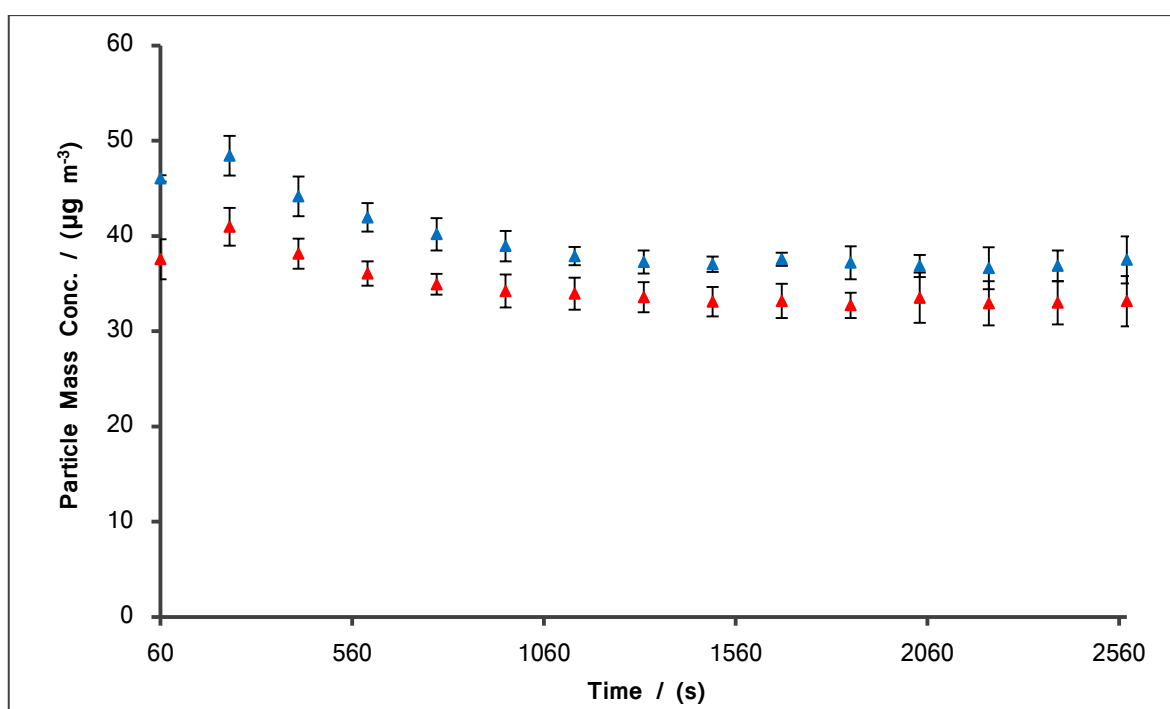


Figure 90: Particle mass concentration as a function of time. [Ozone] = 20 ppb. Blue triangles, [ $\alpha$ -terpinene] = 10 ppb; red triangles, [ $\alpha$ -terpinene] = 20 ppb.

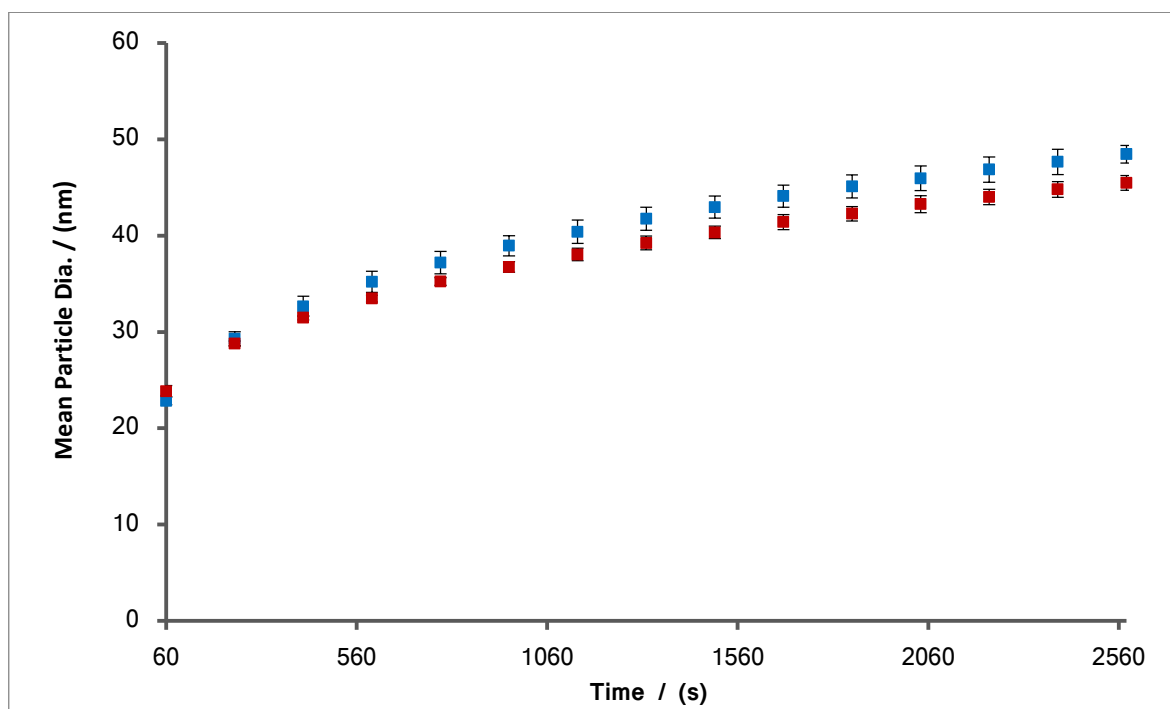


Figure 91: Mean particle diameter as a function of time. [Ozone] = 20 ppb. Blue squares, [ $\alpha$ -terpinene] = 10 ppb; red squares, [ $\alpha$ -terpinene] = 20 ppb.

The results from these two experimental sets show a similar SOA evolution profile. The 20/10 ppb mixture initially showed a slightly increased number concentration compared

to that of the 20/20 ppb mixture. However, after 600 seconds, the two converged, and remained within error of one another throughout the rest of the experiments. The 20/10 ppb mixture did, however, show a slight increase in both mean particle diameter and particle mass concentration, which persisted throughout the timeframe investigated. The 20/20 ppb mixture produced a peak mass concentration of  $41.0 \pm 2.1 \mu\text{g m}^{-3}$ , a decrease of approximately 20 % on the  $48.4 \pm 2.1 \mu\text{g m}^{-3}$  produced by the 20/10 ppb set. Errors are sufficiently small to suggest that this is a significant difference between the two data sets, and not the result of overlapping uncertainties. This difference in SOA mass concentrations was driven by a difference in mean particle diameters between the two data sets—particles formed by the 20/10 ppb mixture were approximately 7 % larger than those formed by the 20/20 ppb mixture, whilst particle number concentrations were within error. The key data from both experimental sets are summarised in Table 22:

[ $\alpha$ -Terpinene] (ppb)	[Ozone] (ppb)	Scavenger	RH (%)	Peak Number Conc. ( $\text{cm}^{-3}$ )	Peak Mass Conc. ( $\mu\text{g m}^{-3}$ )	Mean Dia. at 45 mins (nm)
10	20	Cyclohexane	0	$5.70 \pm 0.40 \times 10^6$	$48.4 \pm 2.1$	$48.5 \pm 0.9$
20	20	Cyclohexane	0	$4.34 \pm 0.54 \times 10^6$	$41.0 \pm 2.1$	$45.5 \pm 0.8$

Table 22: Summary of experimental conditions and results for ozonolysis of  $\alpha$ -terpinene with varying [ $\alpha$ -terpinene].

This may initially seem surprising—that increasing the concentration of one reactant decreases the mass yield of SOA. However, since ozone is the limiting reagent in both cases, the total number of double bond sites which may react doesn't change. What does change is that, by increasing the concentration of  $\alpha$ -terpinene, incomplete oxidation of the terpene is encouraged over the complete oxidation allowed by the lower concentration. Since the complete oxidation set showed a marked increase in particle mass concentration, this lends credence to the theory that second-generation oxidation products are in fact more suitable to being incorporated in aerosol. This suggests that the second-generation oxidation products are of lower volatility than the first-generation products, likely as a result of either higher molecular mass or a greater degree of oxygenation.

## 5.5 Aerosol Mass and Mass Yields: Complete Oxidation

With the results of section 5.4 in mind, which suggested that increasing ozone concentration results in a huge increase in SOA mass yield, it seemed prudent to revisit the relationship between aerosol mass and mass yield. A new set of static chamber experiments were carried out between  $\alpha$ -terpinene (in concentrations ranging from 1.5–10 ppb) and ozone, which was always in 2:1 excess (e.g. 10 ppb ozone to 5 ppb  $\alpha$ -terpinene). Cyclohexane was present as a scavenger, and low RH conditions were employed. Temperatures were 295–298K. The new results are presented in Figure 92, alongside the data from the 1:1 mixtures presented in section 5.3.

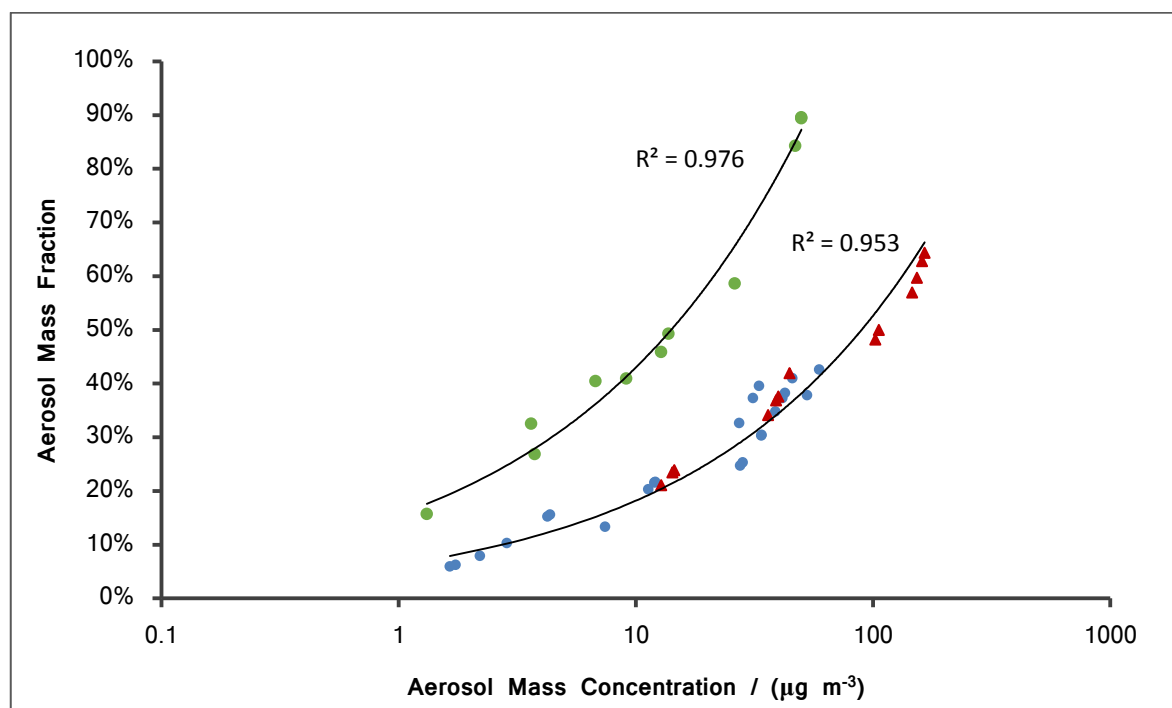


Figure 92: Aerosol mass fraction as a function of aerosol mass concentration.  
Blue circles = static chamber data, 1:1 mixture; red triangles = flow tube data, 1:1 mixture;  
green circles = static chamber data, 2:1 mixture.

These results show clearly that an increased ozone concentration, in conditions more likely to mirror those found in the atmosphere, results in a marked increase in mass yield. The curve shows a good fit to the data, which lends confidence to the incredibly high yield observed.

As mentioned previously, Lee *et al.*<sup>16</sup> reported a lower SOA yield from  $\alpha$ -terpinene ozonolysis than that observed here. This is especially surprising given the results

presented in this section, which suggest a considerable increase in mass yield with an increase in ozone concentration. Lee *et al.* reportedly carried out their experiment with sufficient ozone to exceed the terpene concentration by 3 $\times$ . However, compared to the data reported here, the yield they obtained is below that expected of even the 1:1 reactant ratio, and substantially below the yields obtained from complete oxidation, reported in Figure 92. There is no discernible reason as to why this might be— both experiments employed cyclohexane as a scavenger, and were carried out at 293 K under low RH and low NO<sub>x</sub> conditions. However, since Lee *et al.* report only one data point, it is difficult to make any inferences regarding the reliability of their data.

To ensure that complete oxidation had been achieved, a further data set was collected, under identical conditions, but with a 3:1 ozone: $\alpha$ -terpinene excess. These results are presented in Figure 93. Presented alongside these is the literature fit for the volatility behaviour of the  $\alpha$ -pinene ozonolysis products over the same mass concentration range, from Hallquist *et al.*,<sup>20</sup> previously presented in Figure 44.

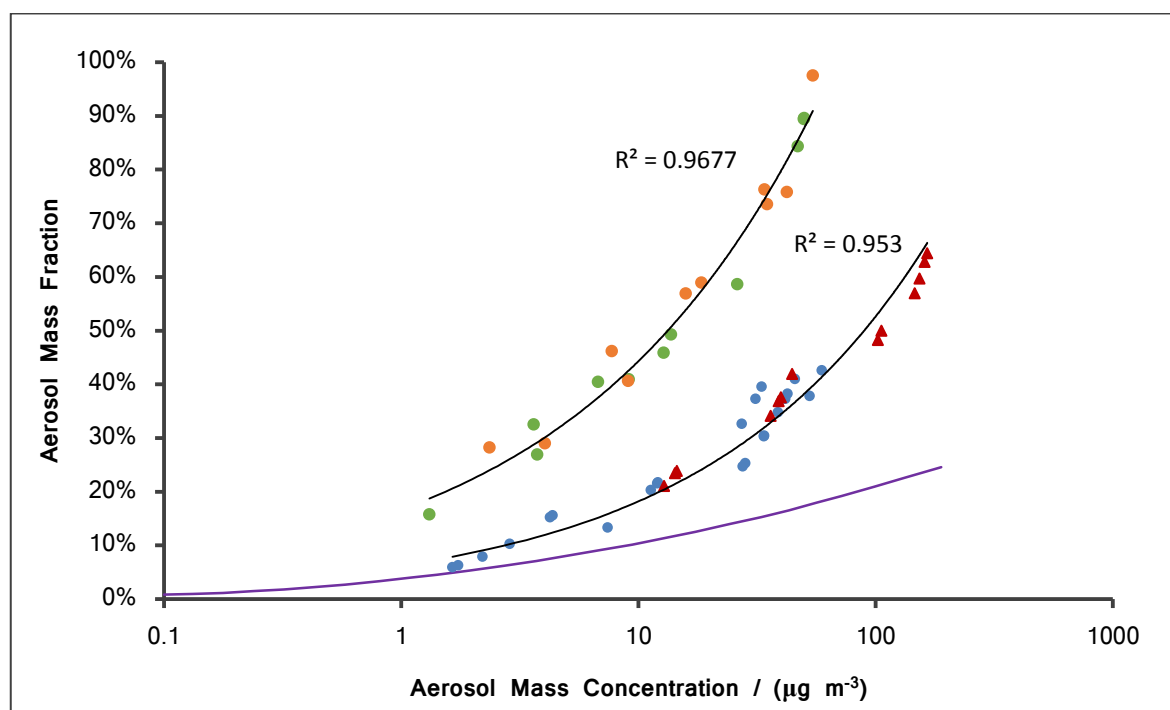


Figure 93: Aerosol mass fraction as a function of aerosol mass concentration.  
 Blue circles = static chamber data, 1:1 mixture; red triangles = flow tube data, 1:1 mixture;  
 green circles = static chamber data, 2:1 mixture; orange circles = static chamber data, 3:1 mixture;  
 purple line = literature fit to  $\alpha$ -pinene ozonolysis data<sup>20</sup> (see Figure 44 for individual literature data points).

The SOA yields of the 3:1 mixture lie, as expected, along the curve of the 2:1 data, suggesting again that complete oxidation was achieved by the 2:1 mixture. It is very interesting that the yield achieved is so high under these conditions since, as detailed in section 5.4, these are more likely to mirror those conditions found in the ground-level atmosphere. The results suggest that a large proportion of the product mass have volatility in the range  $1\text{--}10\ \mu\text{g m}^{-3}$ , and that the vast majority have volatility  $< 100\ \mu\text{g m}^{-3}$ .

An important note as mass yield approaches 100 % is that, when calculating mass yields, it is assumed that the products have identical molecular mass to  $\alpha$ -terpinene,  $136\ \text{g mol}^{-1}$ . This is an underestimation, and products with molecular mass as high as  $200\ \text{g mol}^{-1}$  have been identified in the literature.<sup>16</sup> Still, the very high proportion of products with low volatilities under these conditions suggests that SOA formation from the  $\alpha$ -terpinene ozonolysis is highly relevant under atmospheric conditions, and may be a particularly strong candidate for cluster nucleation, onto which more volatile vapours, perhaps formed from other biogenic species, may condense.

Comparison with the volatility behaviour of  $\alpha$ -pinene ozonolysis products further highlights the efficiency of  $\alpha$ -terpinene as a precursor to SOA. The proportion of products with lower volatilities, particularly in the  $10\text{--}100\ \mu\text{g m}^{-3}$  range, is significantly higher for the  $\alpha$ -terpinene ozonolysis, as evidenced by the higher aerosol yields observed over this range for  $\alpha$ -terpinene compared to  $\alpha$ -pinene.

## 5.6 Impact of Relative Humidity

The impact of relative humidity on the  $\alpha$ -pinene ozonolysis was discussed in the previous chapter, using static chamber experiments, and a number of rationales for the observed change in SOA evolution were proposed.

In this section, the evolution of SOA from the  $\alpha$ -terpinene ozonolysis under low and high RH conditions was characterised using the flow tube technique. Total flow rate within the flow tube was  $2.00\ \text{L min}^{-1}$ , and concentrations of  $\alpha$ -terpinene and ozone within the flow tube were 30 ppb each. Cyclohexane was employed as a scavenger. Pressure within the flow tube was 920–940 mbar, and temperatures were 295–298 K. High RH conditions

were achieved by introducing the air flow to the flow tube via the triple-Dreschler bottle setup described in section 2.1. Air flow within the flow tube was  $1.70 \text{ L min}^{-1}$ , resulting in relative humidity conditions of 85 %.

The mean SOA evolution profiles under low and high RH conditions are presented in Figure 94 and Figure 95. Note that the data presented in these contour plots are made-up of a number of cross-sections at different times during the evolution. However, due to the nature of the plots, they appear as a continuous data set, which is not the case (see line artefacts, e.g. Figure 96).

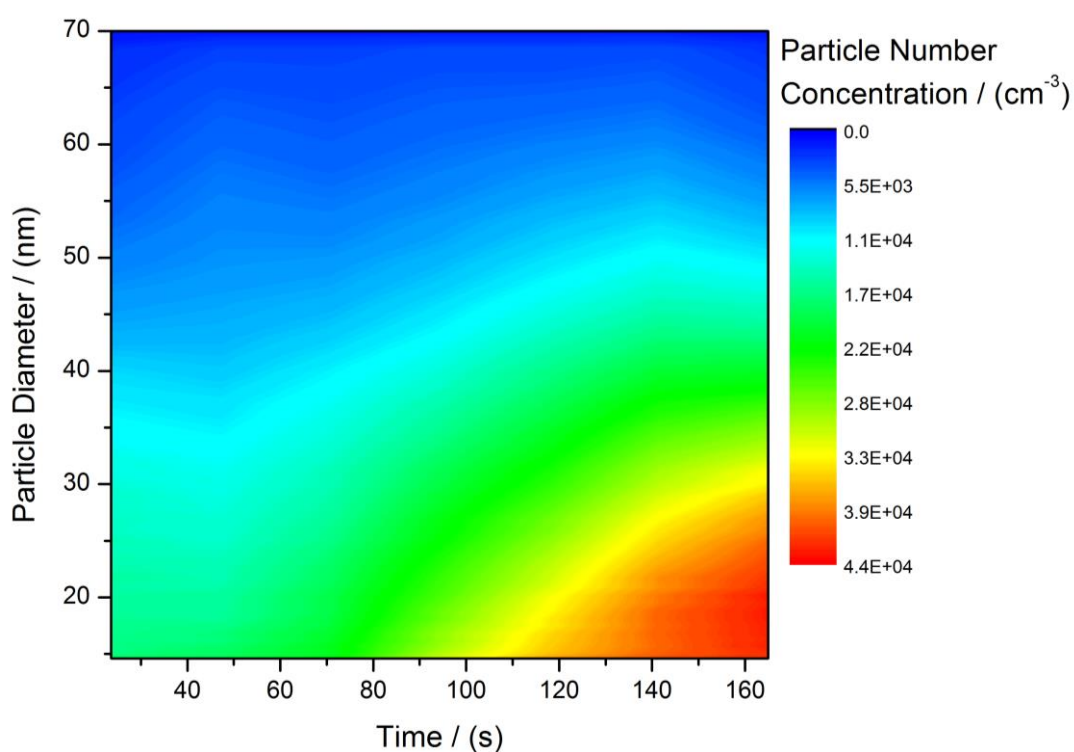


Figure 94: Particle number concentration as a function of diameter vs. time;  $[\alpha\text{-terpinene}] = [\text{ozone}] = 30 \text{ ppb}$ ; 0 % RH.

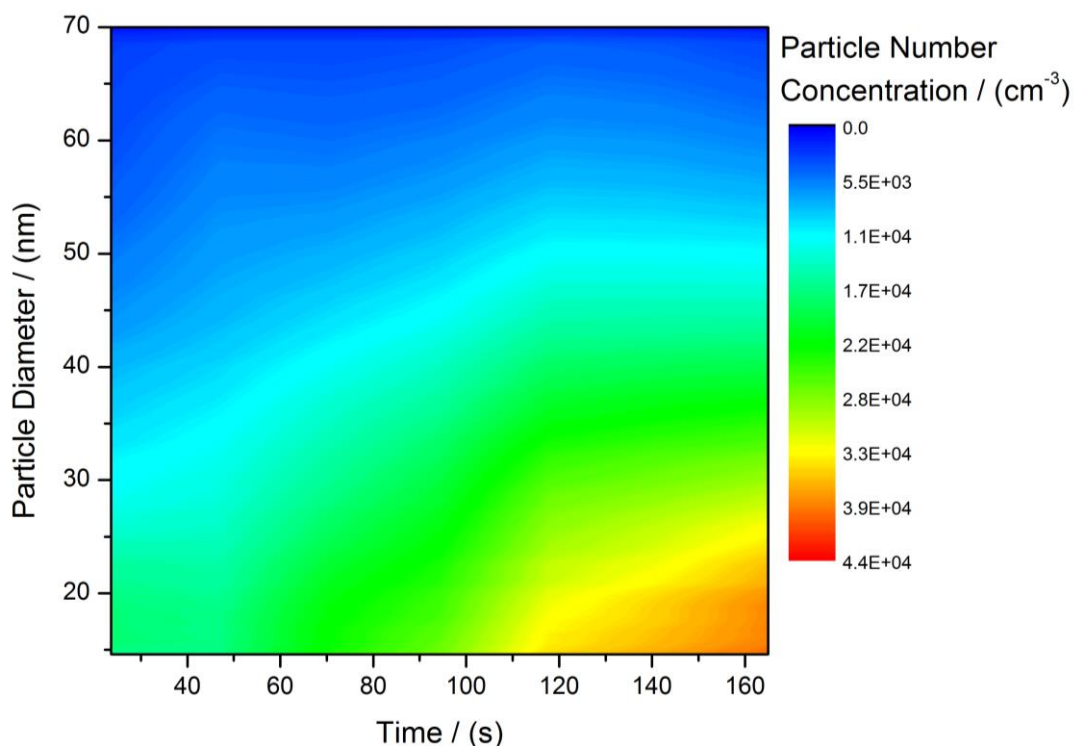


Figure 95: Particle number concentration as a function of diameter vs. time; [ $\alpha$ -terpinene] = [ozone] = 30 ppb; 85 % RH.

On initial observation, it is immediately clear that an increase in relative humidity appears to cause a decrease in observed particle number concentration toward the later stages of the experiment, although no obvious difference is observed in the initial stages. This is in agreement with some of the conclusions for the  $\alpha$ -pinene ozonolysis, presented in section 3.7.3, which suggested a decrease in number concentration with increasing RH. There appears to be little change in particle diameter, with perhaps a slight upward shift observed, which, again, is in agreement with the conclusions of the  $\alpha$ -pinene ozonolysis results.

To give a clearer picture of the effect of RH on SOA evolution, the particle numbers produced at 85 % RH were subtracted from those produced at 0 % RH (Figure 94 minus Figure 95), and the resulting difference-values are presented in Figure 96.



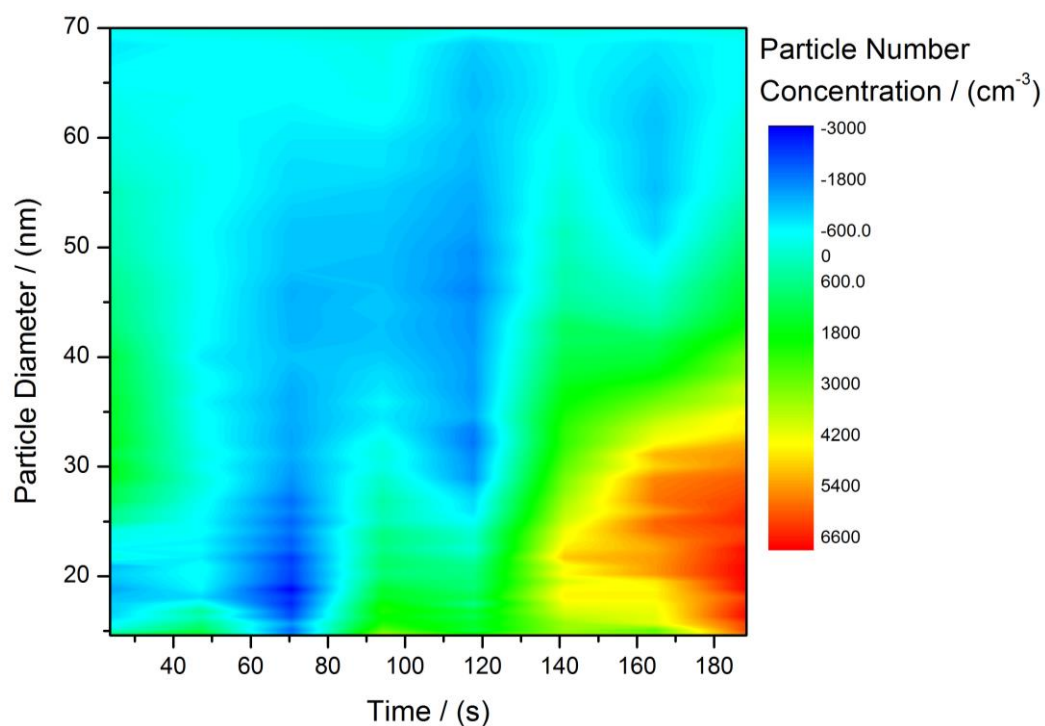


Figure 96: Difference in particle size distributions between 0 and 85 % RH; [ $\alpha$ -terpinene] = [ozone] = 30 ppb.

In this plot, positive values represent more particles of that size formed under low RH conditions, and negative values indicate more particles under high RH conditions. It is strikingly obvious, therefore, that low RH conditions do result in the formation of larger numbers of smaller particles. There is also some evidence to suggest that high RH conditions favour formation of larger particles, evidenced by the blue and teal regions toward the top of the contour plot.

To provide a more quantitative approach, total number and mass concentrations are displayed in Figure 97.

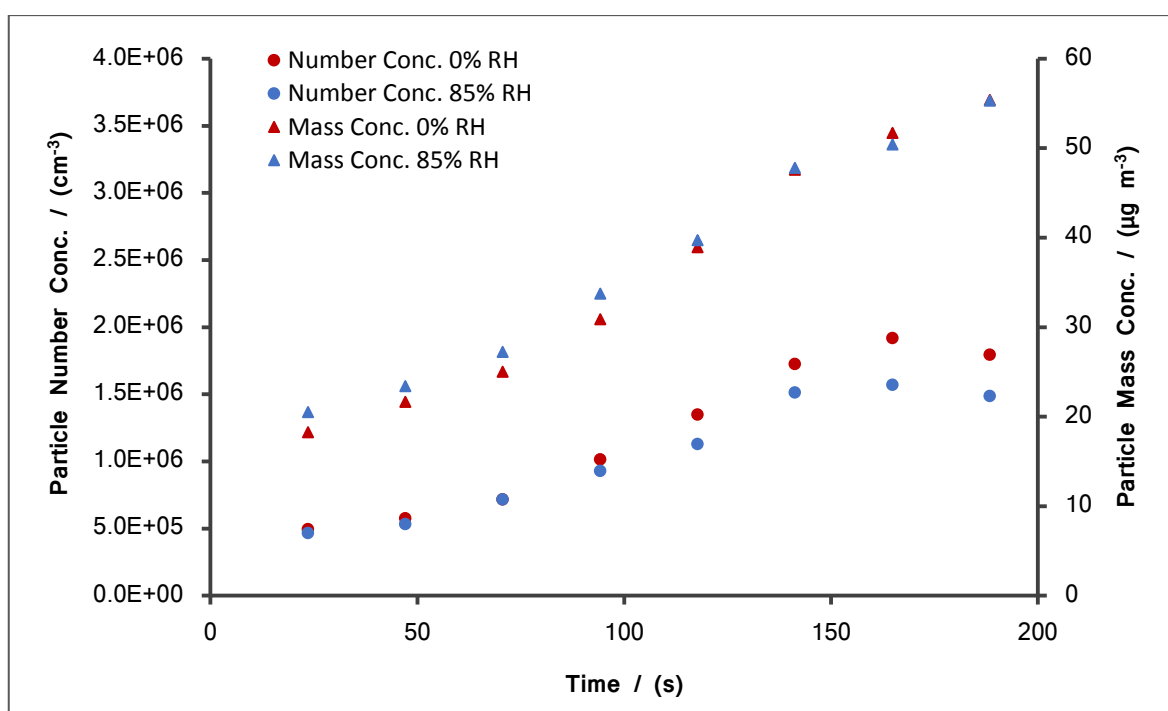


Figure 97: Particle number and mass concentrations vs. time; [ $\alpha$ -terpinene] = [ozone] = 30 ppb.  
 Number concentrations depicted by circles; mass concentrations by triangles.  
 Red data points = 0 % RH; blue data points = 85 % RH.

Quantitatively, increasing RH from 0 % to 85 % appears to result in no change in particle number concentration for the initial 70 seconds of evolution. However, after 93 seconds, the number concentrations for the two systems do begin to diverge, as shown in Figure 97; number concentration of the high RH set becomes significantly lower than that of the low RH set after 117 seconds. They continue to diverge until 165 seconds, at which point rate of formation of new particles is overtaken by coagulation and wall losses, and number concentrations begin to fall. Peak number concentrations are observed after 165 seconds, when they reach  $1.92 \pm 0.05 \times 10^6$  and  $1.57 \pm 0.16 \times 10^6 \text{ cm}^{-3}$  for low and high RH conditions, respectively. This equates to a decrease of 18 % in peak number concentration when increasing RH from 0 % to 85 %.

Particle mass concentrations follow a different trend, with mass concentrations for the high RH system consistently above those for the low RH system for the initial 94 seconds of particle evolution. The increase in observed mass concentrations is  $9.6 \pm 1.8 \%$  for the duration of this period. After 117 seconds, particle mass concentrations produced by the

two systems converge and, while they show a little variation, remain within 2 % of one another for the remainder of the observable period.

Mean particle diameters for SOA produced under high RH conditions were slightly higher than that produced under low RH conditions for the entirety of the observed timeframe, by  $4.9 \pm 1.3$  %. Mean diameters reached 33.8 and 32.6 nm after 165 seconds, under high and low RH conditions, respectively. This slightly increased particle size under high RH conditions accounts for some of the observations made earlier regarding the mass and number concentrations: when particle numbers are equal during the initial stages, the mass concentration of the high RH SOA is greater since the particles are slightly larger, and when number concentration of the low RH aerosol surpasses that of the high RH aerosol, mass concentrations are equal, again due to the smaller particle diameter.

The observed decrease in number concentration with increasing RH may be caused by a couple of different factors. These both concern the potential of water vapour to produce  $\text{HO}_2$ , thus elevating the  $\text{HO}_2 / \text{RO}_2$  ratio.<sup>23</sup> Since the use of cyclohexane as a scavenger is known to produce predominantly  $\text{RO}_2$ ,<sup>24</sup> a new source of  $\text{HO}_2$  may have important consequences for aerosol yield by participating in secondary reactions with products of the  $\alpha$ -terpinene ozonolysis. Jenkin<sup>25</sup> reports that, for  $\alpha$ - and  $\beta$ -pinene ozonolysis, formation of the least volatile products is propagated by permutation reactions of  $\text{RO}_2$  radicals (see section 3.6 for discussion). Ozonolysis of  $\alpha$ -terpinene is expected to result in analogous reaction mechanisms, whereby reactions of  $\text{RO}_2$  form the least volatile products, which are then expected to undergo gas-to-particle partitioning, thereby increasing particle number concentration. A new source of  $\text{HO}_2$  will suppress  $\text{RO}_2$  reactions by providing a competing reaction pathway, thus reducing the amount of low volatility products formed. Previous studies in both this work and the literature<sup>25</sup> have suggested that an elevated  $\text{HO}_2 / \text{RO}_2$  ratio leads to formation of fewer, albeit larger particles than a predominantly  $\text{RO}_2$  system. This may explain the decrease in number concentration observed here, and also contribute to the slight increase in particle diameter.

According to the partial reaction scheme published by Lee *et al*,<sup>16</sup> both  $\text{HO}_2$  and  $\text{RO}_2$  radicals are important species in the formation of various products. A number of products

are identified which are formed through reaction with  $\text{RO}_2$  (see Table 19), but only one ((E)-3,7-dimethyl-6-oxo-2-octeneperoxoic acid,  $m/z$  201, see Figure 98) which requires reaction with  $\text{HO}_2$  (see Table 19). The high molecular weight and degree of oxygenation of this product suggests that it would be a strong candidate for gas-to-particle partitioning, but Lee *et al.* also note that they did not observe this product until nearly one hour after initial ozonolysis. This suggests that (E)-3,7-dimethyl-6-oxo-2-octeneperoxoic acid is not responsible for any effects observed here. If formed, however, (E)-3,7-dimethyl-6-oxo-2-octeneperoxoic acid could participate in a number of the accretion reactions described earlier in Figure 38, and, due to its already high molecular weight, any dimers and oligomers formed could be expected to have particularly low volatilities.

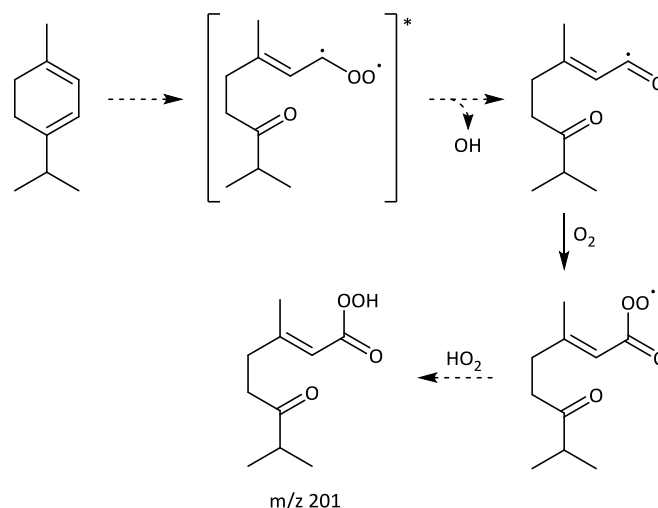


Figure 98: Formation of (E)-3,7-dimethyl-6-oxo-2-octeneperoxoic acid; dashed arrows represent multi-step processes. Adapted from Lee *et al.*<sup>16</sup>

Indeed, since only nine of the products of this reaction have currently been identified in the literature,<sup>16</sup> it is not possible to conclude with any certainty whether a change in  $\text{HO}_2$  /  $\text{RO}_2$  ratio would result in a significant difference in product yields, and hence whether particle number concentration would be affected.

As mentioned previously, the altered  $\text{HO}_2$  /  $\text{RO}_2$  ratio caused by the presence of water vapour may result in an increase in particle diameter. A change in product yields due to increased availability of  $\text{HO}_2$  may also be an influential factor for particle diameter although, due to the current incomplete understanding of the mechanistic details of this reaction to date, it is not possible to conclude with any certainty whether or not this is

the case. The third potential rationale for the observed increase in diameter with increasing RH is direct incorporation of water vapour into the aerosol. As previously discussed in section 3.7.3, water vapour alone cannot form droplets under normal conditions. It may, however, condense onto the surface of other particles, resulting in an increase in particle diameter and consequently in mass concentration.

## 5.7 Conclusions

The SOA-forming potential of the  $\alpha$ -terpinene ozonolysis was investigated, and its status as a high aerosol-yielding terpene confirmed, in the first comprehensive study of its aerosol evolution. This is in agreement with the conclusions of Lee *et al.*<sup>16</sup>, although the much more extensive results presented here suggest a slightly higher aerosol yield. The relationship between aerosol mass concentration and yield was thoroughly explored across a range of atmospherically relevant concentrations. The products of this reaction were found to be of much lower volatility than those of the  $\alpha$ -pinene ozonolysis previously investigated, likely due to the two endocyclic double bonds in the molecule.

Increasing relative ozone concentration was observed to have a profound effect on SOA yield. An increase from a 1:1 ozone: $\alpha$ -terpinene mixture to a 2:1 mixture resulted in a large increase in aerosol yield, due to increased product concentration, but also suggesting that the “double ozonolysis” products are of lower volatility than the products formed from ozonolysis of just one double bond. Aerosol formation in regions of high ozone concentration, such as urban areas or nearby rural areas, is therefore expected to be much more pronounced than in regions of lower concentration.

The use of an atmospheric pressure flow tube for SOA generation was shown to be in good agreement with static chamber experiments, when both data sets are fully corrected for particle losses. The flow tube technique allows for study of the early stages of the reaction with a much better time resolution. This may be particularly useful for studies of SOA formation under higher concentration conditions, where the peak particle concentrations occur earlier, and also for other terpenes which react very quickly with oxidants. Calculation of upper and lower bounds of a rate constant for the  $\alpha$ -terpinene

ozonolysis yielded a range of  $k = 8.5 \pm 2.0 \times 10^{-15} - 1.6 \pm 0.29 \times 10^{-14} \text{ cm}^3 \text{ molecule}^{-1} \text{ s}^{-1}$ . The upper limit is in agreement with literature-published values.

The flow tube was used to study the initial evolution of SOA under low and high RH conditions. An increase in RH resulted in a slight decrease in particle number concentration coupled with a slight increase in particle diameter, equating to no overall change in mass concentration. A reduced number of particles provides fewer sites to act as cloud condensation nuclei, thus resulting in the formation of fewer, but larger droplets in the atmosphere. Larger droplets are known to have a lower albedo than more numerous, smaller droplets, equating to the same aerosol mass.<sup>26</sup> Therefore, we may conclude that an increase in RH during the formation of these particles may lead to a decrease in the magnitude of the radiative forcing effect. A wide range of RH conditions are observed within the atmosphere, meaning that a solid understanding of this relationship is vital to provide better estimates of aerosol yields and size distributions. This RH dependence showed good agreement with the  $\alpha$ -pinene studies performed in section 3.7.

## 5.8 References

1. R. J. Griffin, D. R. Cocker, J. H. Seinfeld and D. Dabdub, *Geophys. Res. Lett.*, 1999, **26**, 2721-2724.
2. C. Holzke, T. Dindorf, J. Kesselmeier, U. Kuhn and R. Koppmann, *J. Atmos. Chem.*, 2006, **55**, 81-102.
3. A. Rivoal, C. Fernandez, A. V. Lavoie, R. Olivier, C. Lecareux, S. Greff, P. Roche and B. Vila, *Chemosphere*, 2010, **78**, 942-949.
4. Y.-S. Son, K.-J. Kim, I.-H. Jung, S.-J. Lee and J.-C. Kim, *J. Atmos. Chem.*, 2015, **72**, 27-41.
5. M. Vidaković, *Conifers: morphology and variation*, Grafičko Zavod Hrvatske, Zagreb, 1991.
6. L. Tollsten and P. M. Müller, *Phytochemistry*, 1996, **43**, 759-762.
7. J. Kesselmeier, L. Schäfer, P. Ciccioli, E. Brancaleoni, A. Cecinato, M. Frattoni, P. Foster, V. Jacob, J. Denis, J. L. Fugit, L. Dutaur and L. Torres, *Atmos. Environ.*, 1996, **30**, 1841-1850.
8. N. C. Bouvier-Brown, R. Holzinger, K. Palitzsch and A. H. Goldstein, *Atmos. Environ.*, 2009, **43**, 389-401.
9. K.-J. Ham, K.-Y. Park, M.-S. Kim, J.-M. Song, S.-S. Lee and Y.-S. Ok, *Korean J. Soil Sci. Fertil.*, 2011, **44**, 1226-1231.
10. J. Kesselmeier, U. Kuhn, A. Wolf, M. O. Andreae, P. Ciccioli, E. Brancaleoni, M. Frattoni, A. Guenther, J. Greenberg, P. De Castro Vasconcellos, T. de Oliva, T. Tavares and P. Artaxo, *Atmos. Environ.*, 2000, **34**, 4063-4072.
11. Ø. Hov, J. Schjoldager and B. M. Wathne, *J. Geophys. Res.-Oceans*, 1983, **88**, 10679-10688.
12. R. Atkinson, D. L. Baulch, R. A. Cox, J. N. Crowley, R. F. Hampson, R. G. Hynes, M. E. Jenkin, M. J. Rossi and J. Troe, *Atmos. Chem. Phys.*, 2006, **6**, 3625-4055.
13. M. Witter, T. Berndt, O. Böge, F. Stratmann and J. Heintzenberg, *Int. J. Chem. Kinet.*, 2002, **34**, 394-403.
14. Y. Shu and R. Atkinson, *Int. J. Chem. Kinet.*, 1994, **26**, 1193.
15. E. P. Grimsrud, H. H. Westberg and R. A. Rasmussen, *Int. J. Chem. Kinet.*, 1975, **1**, 183.
16. A. Lee, A. H. Goldstein, M. D. Keywood, S. Gao, V. Varutbangkul, R. Bahreini, N. L. Ng, R. C. Flagan and J. H. Seinfeld, *J. Geophys. Res.-Atmos.*, 2006, **111**, n/a-n/a.
17. A. G. Lewin, D. Johnson, D. W. Price and G. Marston, *Phys. Chem. Chem. Phys.*, 2001, **3**, 1253-1261.
18. I. Fleming, *Frontier Orbitals and Organic Chemical Reactions*, Wiley, New York, USA, 1976.
19. A. A. Presto and N. M. Donahue, *Environ. Sci. Technol.*, 2006, **40**, 3536-3543.

20. M. Hallquist, J. C. Wenger, U. Baltensperger, Y. Rudich, D. Simpson, M. Claeys, J. Dommen, N. M. Donahue, C. George, A. H. Goldstein, J. F. Hamilton, H. Herrmann, T. Hoffmann, Y. Iinuma, M. Jang, M. E. Jenkin, J. L. Jimenez, A. Kiendler-Scharr, W. Maenhaut, G. McFiggans, T. F. Mentel, A. Monod, A. S. H. Prévôt, J. H. Seinfeld, J. D. Surratt, R. Szmigielski and J. Wildt, *Atmos. Chem. Phys.*, 2009, **9**, 5155-5236.
21. K. E. Percy, E. H. Legge and S. V. Krupa, *Air Pollution, Global Change and Forests in the New Millennium*, Elsevier, 2003, vol. 3, 4, p. 85.
22. S. Krupa, M. Nosal and D. L. Peterson, *Environ. Pollut.*, 2001, **112**, 303-309.
23. A. S. Hasson, M. Y. Chung, K. T. Kuwata, A. D. Converse, D. Krohn and S. E. Paulson, *J. Phys. Chem. A*, 2003, **107**, 6176-6182.
24. Y. Ma, A. T. Russell and G. Marston, *Phys. Chem. Chem. Phys.*, 2008, **10**, 4294-4312.
25. M. E. Jenkin, *Atmos. Chem. Phys.*, 2004, **4**, 1741-1757.
26. Myhre, G., D. Shindell, F.-M. Bréon, W. Collins, J. Fuglestad, J. Huang, D. Koch, J.-F. Lamarque, D. Lee, B. Mendoza, T. Nakajima, A. Robock, G. Stephens, T. Takemura and H. Zhang, 2013: Anthropogenic and Natural Radiative Forcing. In: *Climate Change 2013: The Physical Science Basis. Contribution of Working Group I to the Fifth Assessment Report of the Intergovernmental Panel on Climate Change*, [Stocker, T.F., D. Qin, G.-K. Plattner, M. Tignor, S.K. Allen, J. Boschung, A. Nauels, Y. Xia, V. Bex and P.M. Midgley (eds.)]. Cambridge University Press, Cambridge, United Kingdom and New York, NY, USA.



# Chapter 6

## Conclusions and Future Work

---

### 6.1 Conclusions

In this thesis, the physical properties of aerosol formed from the ozonolysis of two different terpenes, together with a custom-synthesised terpene surrogate compound, were thoroughly investigated. Research was primarily conducted using a Scanning Mobility Particle Sizer (SMPS) instrument, coupled to either a static chamber or an atmospheric pressure flow tube system, which enabled measurement of the time-resolved evolution of aerosol particles.

Chapter 3 concerned aerosol products of the ozonolysis of  $\alpha$ -pinene, the most abundant terpene present in the atmosphere. Initial studies focused on characterisation of the system and validation of the experimental setup. Good reproducibility was achieved for particle mass concentrations and mean particle diameters, with slightly poorer reproducibility observed for the particle number concentrations.

An investigation of the relationship between aerosol mass concentration and mass yield showed the expected trend—in good agreement with the literature. The investigation into this relationship was further extended, to provide information on the behaviour of higher volatility products. This gave some surprising results, with higher mass yields observed than might be expected based on an extrapolation of the literature fit, suggesting a significant proportion of additional products with volatilities in the range 1000 to 3000  $\mu\text{g m}^{-3}$ , although these products are not likely to be atmospherically relevant.

By using the mass concentration as a proxy for reaction progress, and comparing this to a simulated product concentration based on a fixed wall loss and a variable reaction rate constant, a value of  $k = 1.05 \pm 0.11 \times 10^{-16} \text{ cm}^3 \text{ molecule}^{-1} \text{ s}^{-1}$  was calculated for the reaction

rate constant of  $\alpha$ -pinene ozonolysis. This compares well to the IUPAC preferred rate constant.

The effect of varying OH scavengers on the size distribution and mass concentration of aerosol formed was investigated. Scavengers producing predominantly RO<sub>2</sub> radicals as by-products were noted to give rise to a large number of smaller particles, whereas an elevated HO<sub>2</sub> / RO<sub>2</sub> ratio produced fewer, larger particles, culminating in a lower mass yield.

The effect of relative humidity (RH) was studied, and some conclusive results obtained. Under both low and high reactant concentrations (2 and 0.2 ppm of  $\alpha$ -pinene), an increase from 0 % to 30 % RH caused no significant change in the properties of the aerosol formed. However, a further increase to 80 % RH resulted in an increase in particle diameter of approximately 10 % in both cases. Under low concentration conditions, a decrease in number concentration was observed, resulting in no significant change in particle mass concentration, whereas under high concentration conditions, no such effect was observed, and mass concentration increased by approximately a third. Potential reasons for these observations were identified, including direct water uptake into the particles, altered product yields, and the Raoult's law effect. However, no discernible reason could be found for the discrepancy between number concentrations at low and high reactant concentrations.

Some experiments were carried out using an Electrical Low Pressure Impactor (ELPI+) instrument, loaned from Dekati Ltd. for a short period. The preliminary results obtained suggest that physical state is independent of relative humidity, for particles formed under RH conditions ranging from 0–80 %. Particles formed under 0, 30 and 80 % RH conditions were all found to behave like crystalline solids. This may have implications for the lifetimes of these particles in the atmosphere, since a solid particle would be expected to be more resistant to penetration by gas-phase oxidants, thus extending its lifetime.

Chapter 4 involved the synthesis of an enone derivative of  $\alpha$ -pinene, which enabled study of the products of one Criegee intermediate (CI) in isolation from the other. Comparisons were drawn between the aerosol formed by the enone derivative and that formed by  $\alpha$ -pinene itself. Further comparisons were also drawn to the aerosol formed by the enal derivative,

reported in the literature. The enone was noted to produce significantly fewer particles than  $\alpha$ -pinene, reaching a peak number concentration of only 17 % that of  $\alpha$ -pinene. The particles formed were of considerably larger diameter, but the total mass concentration was still only 40 % of that produced by  $\alpha$ -pinene. Comparing to the data reported in the literature for the enal derivative, the particle number concentration was similar to that of  $\alpha$ -pinene, but comparison of particle diameter and mass concentration was challenging due to the short timeframe of data reported for the enal. The conclusion drawn was that, whilst products of CI 2 are believed to be primarily responsible for nucleation of aerosol particles, these particles are subsequently grown by inclusion of products from both CIs. It has previously been suggested that pinic and pinonic acid are likely candidates for particle nucleation in chamber experiments such as those described here, and the higher number concentration resulting from the enal supports this.

A comparison of the aerosol mass yields of each compound came to a similar conclusion. The enone data produced in this work resulted in mass yields consistently 5–7 percentage points below those of  $\alpha$ -pinene, whilst the enal data reported in the literature are 3–5 percentage points above. The suggestion, therefore, is that products of both CIs contribute to the total aerosol mass formed by the ozonolysis of  $\alpha$ -pinene, but that CI 2 contributes the greater proportion. Proportional contribution of each CI is dependent on aerosol mass concentration, with an increasing contribution from CI 1 as the aerosol mass concentration increases. Calculation of the rate constant for the ozonolysis of the enone was performed in the same way as for  $\alpha$ -pinene, and resulted in a value of  $k = 4.3 \pm 0.9 \times 10^{-17} \text{ cm}^3 \text{ molecule}^{-1} \text{ s}^{-1}$ , which agreed with the only previous study.

Chapter 5 concerned the ozonolysis of  $\alpha$ -terpinene, a terpene less abundant in the atmosphere than  $\alpha$ -pinene, but one which has been reported, in a single exploratory study, to produce a particularly high aerosol mass yield. The initial investigation focused on the relationship between aerosol mass concentration and mass yield, for a 1:1 ratio of  $\alpha$ -terpinene:ozone, and a fit was proposed. The products of this reaction were noted to be of considerably lower volatility than those of the  $\alpha$ -pinene ozonolysis.

Due to the particularly fast rate of reaction between  $\alpha$ -terpinene and ozone, it proved difficult to accurately measure the peak mass concentration with the static chamber setup

for high initial reactant concentrations due to the unavoidable time lapse from precursor introduction to SMPS analysis in the static chamber setup.

In order to explore the initial aerosol formation, an atmospheric pressure flow tube was characterised, and shown to produce results in good agreement with static chamber experiments. While more experimentally challenging, this technique provided access to the early stages of aerosol formation, with a much-improved time resolution versus that of the static chamber experiments. Use of the flow tube allowed for accurate measurement of the peak mass concentrations produced under high initial reactant concentrations, and was used to supplement the static chamber data. These results suggested a slightly different relationship between mass concentration and yield than that previously suggested, and thus a new, improved fit was proposed.

The mass concentration measured by the flow tube was used in combination with the simulated extent of reaction approach to calculate upper and lower bounds for the reaction rate constant for the ozonolysis of  $\alpha$ -terpinene:  $k = 8.5 \pm 2.0 \times 10^{-15} - 1.6 \pm 0.29 \times 10^{-14} \text{ cm}^3 \text{ molecule}^{-1} \text{ s}^{-1}$ . The upper bound agrees well with the IUPAC preferred rate constant.

The effect of increasing ozone concentration on the aerosol formed was investigated, and found to greatly influence SOA yield. An increase to a 2:1 ratio of  $\alpha$ -terpinene:ozone resulted in a significant increase in aerosol yield. This was as expected since  $\alpha$ -terpinene has two endocyclic double bonds, and by increasing the concentration of ozone there was now enough  $\text{O}_3$  present in the system to react with all of the double bonds, allowing for complete oxidation of the terpene. Therefore, with more terpene able to react, the amount of condensable material formed must also increase, thereby increasing the mass yield. This raised the question of whether the increase in mass yield was simply due to a proportional increase in condensable material, or whether the excess of ozone encouraged formation of some products over others. A further set of experiments was undertaken, which suggested that second-generation oxidation products are more susceptible to being incorporated into aerosol particles, and thus are of lower volatility, than first-generation oxidation products.

The impact of relative humidity on SOA formation was again investigated, but in this case the flow tube was used to provide access to the initial stages of particle formation. High RH

conditions resulted in the formation of slightly larger particles than those formed under low RH conditions. However, increasing RH resulted in the formation of fewer particles, and overall the combination of these two effects resulted in no significant difference in particle mass concentration.

## 6.2 Future Work

The effect of relative humidity on products of the  $\alpha$ -pinene ozonolysis is still not entirely clear. Further experimental investigation of SOA yields under varying RH conditions would be useful to more definitively make conclusions about its impact. Only limited RH conditions were investigated in this work, and a study of the effect of varying RH within the parameters explored here would be of use—that is, further studies between 30–80 % RH. Perhaps an exploration of the effects of varying RH with an alcohol or no scavenger as opposed to cyclohexane, as proposed in section 3.7.3, might yield some interesting results. The presence of water vapour is known to encourage formation of  $\text{HO}_2$  radicals. Therefore, by using an alcohol scavenger such as methanol, that produces solely  $\text{HO}_2$  radicals (no  $\text{RO}_2$ ), the influence of RH on the  $\text{HO}_2$  /  $\text{RO}_2$  ratio can be effectively nullified. Thus, comparing the effect of varying RH on methanol-scavenged experiments with its effect on cyclohexane-scavenged experiments will allow for investigation of the hypothesis that elevated an  $\text{HO}_2$  concentration, resulting from high-RH conditions, has a substantial effect on aerosol formation.

Clearly, there is more work to be done on this system using the ELPI+ instrument. Due to the time constraints of the instrument loan period, both instrument calibration and experimental repeats were limited in this work. The results presented here suggest solid particle formation across the range 0–80 % RH, albeit with a decreasing bounce factor. Further repeats would be useful to confirm, and also to investigate the effect of humidity on particles of various diameters.

It would be interesting to carry out further work using the enone derivative, particularly looking at the effect of different scavengers and varying RH on the aerosol evolution, to see if the same trend as for  $\alpha$ -pinene is exhibited. Synthesis of the enal derivative, and

investigation in a similar fashion, would also be of interest. Also, analogous experiments to those carried out with the enone, but instead carried out with the enal derivative would be useful, with extended run times so that the full SOA evolution, and maximum mass concentration, could be observed. This would remove the need for extrapolation of the data, discussed in section 4.7, greatly increasing the reliability of these results.

Little is known about the SOA evolution of the  $\alpha$ -terpinene system, and there is great scope for expansion on the work presented here. This thesis noted a significant dependence of aerosol yield on ozone concentration, but only looked at three reactant ratios. Future investigations might look at varying ozone concentrations in smaller graduations, and determine whether this is a linear relationship or a curve.

In section 3.7.1, the possible existence of a critical RH value was suggested. Further experiments under RH conditions between 30 and 80 % may allow for validation of this conclusion and, assuming that validation is successful, may allow the critical value to be narrowed down substantially.

The identification of products from this system is incomplete, and mechanistic details lacking. Future studies might focus on identification of a greater proportion of products through GC-MS experiments, and on any change in product yields as a result of varying RH and scavenger. This would potentially provide mechanistic detail, and may assist in understanding the effect of RH on SOA yield.

Finally, a study of the effects of different scavengers on the SOA evolution from  $\alpha$ -terpinene ozonolysis would be useful. It would be interesting to note whether this system behaves in the same way as the  $\alpha$ -pinene ozonolysis.

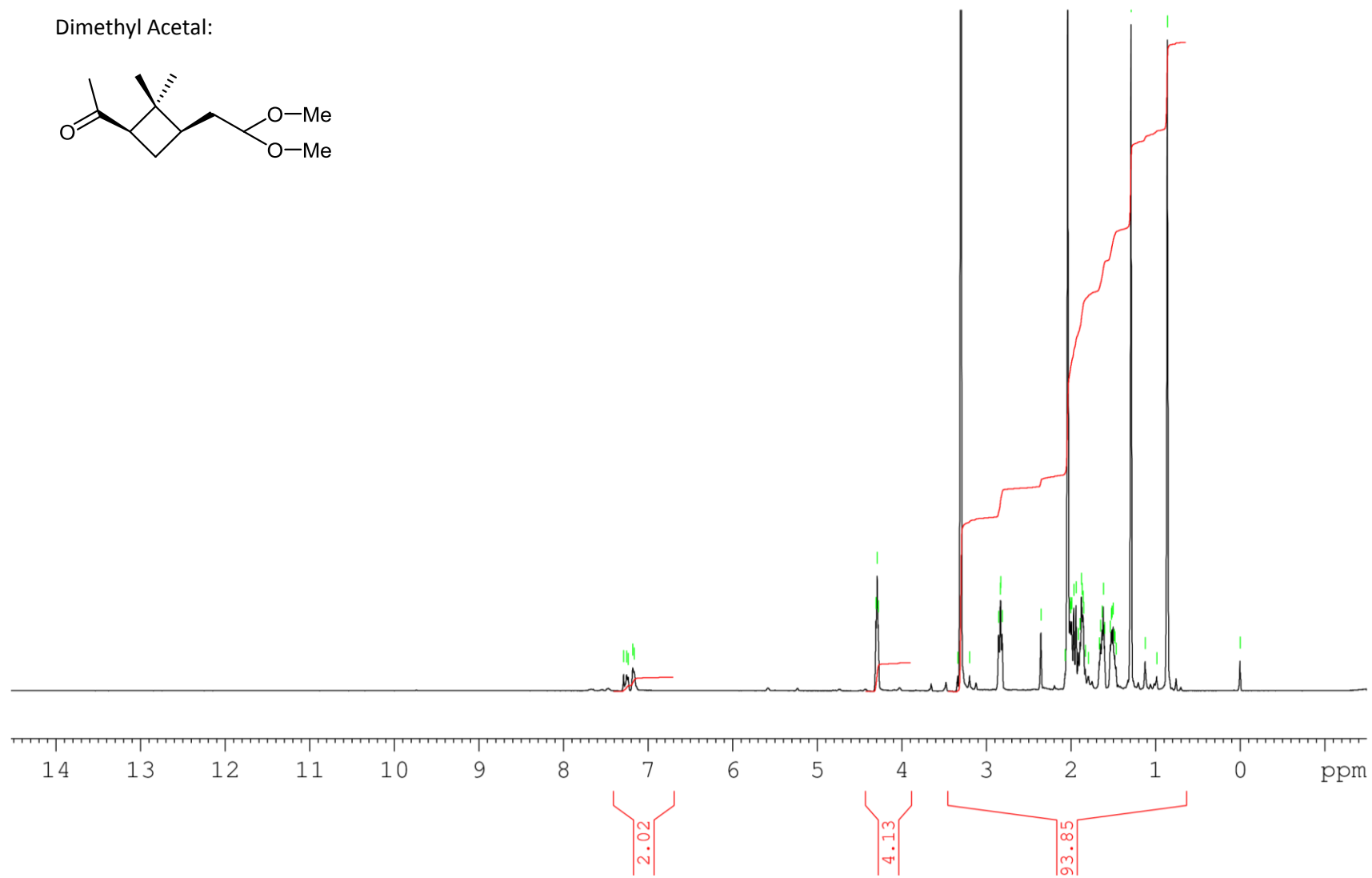
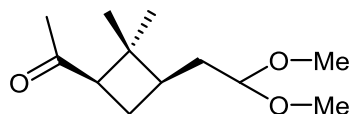
# Appendix

---

## A.1 Spectra Relevant to Chapter 4

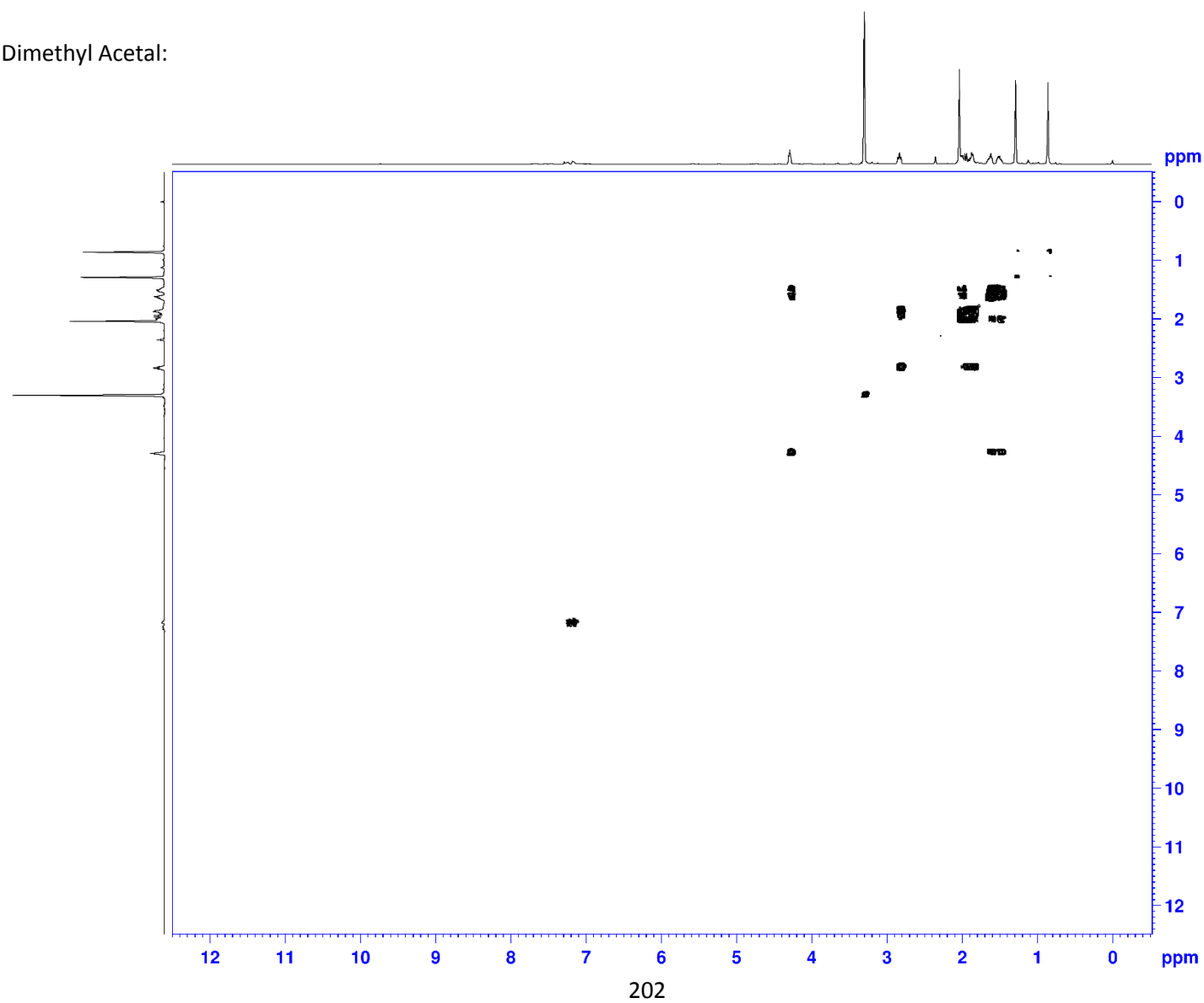
In this section, the  $^1\text{H}$  and 2D-COSY- $^1\text{H}$  NMR spectra for the enone and intermediate compounds synthesised in section 4.2 are presented.

Dimethyl Acetal:

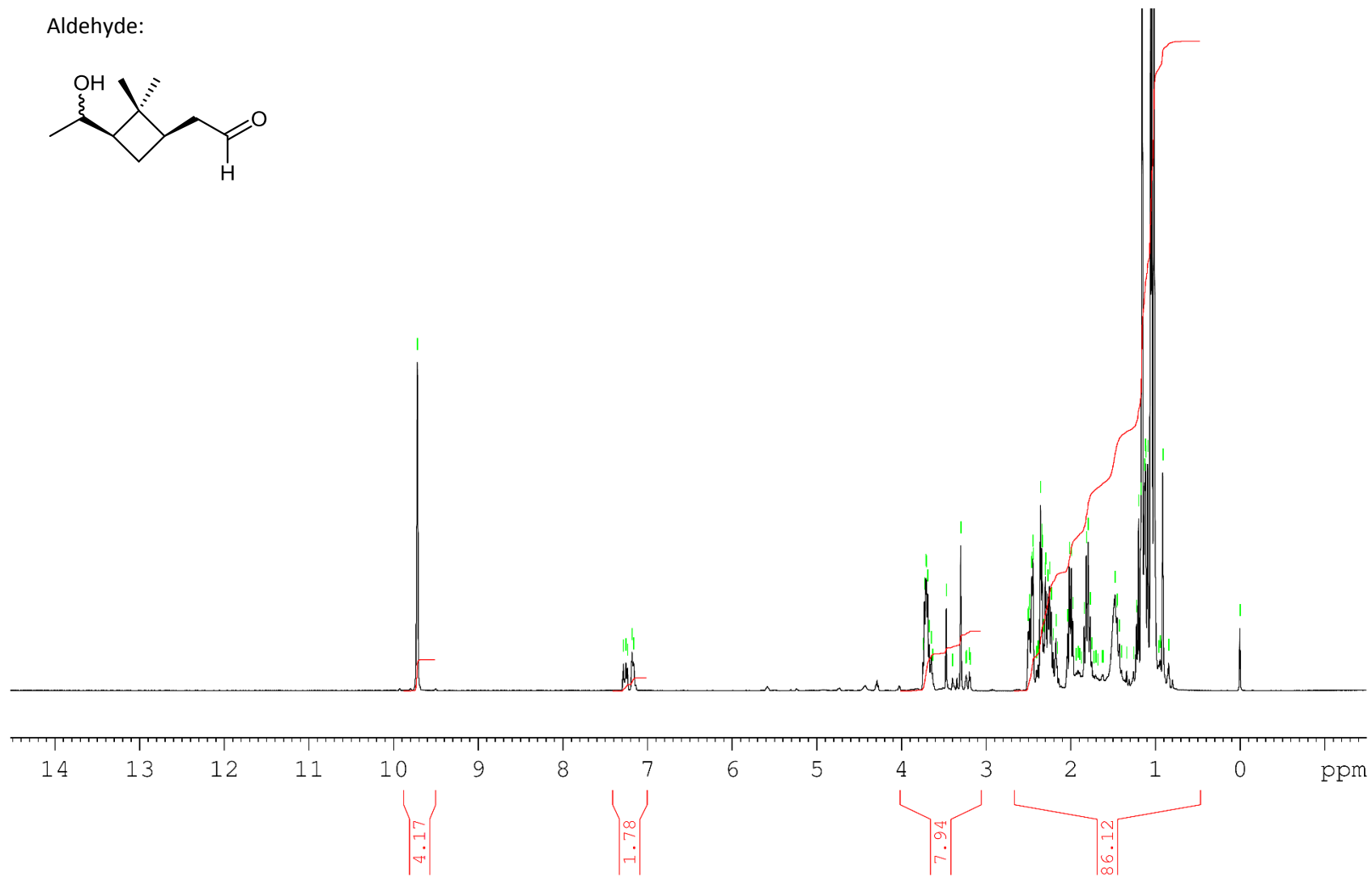
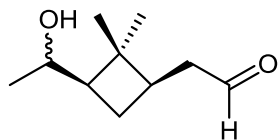




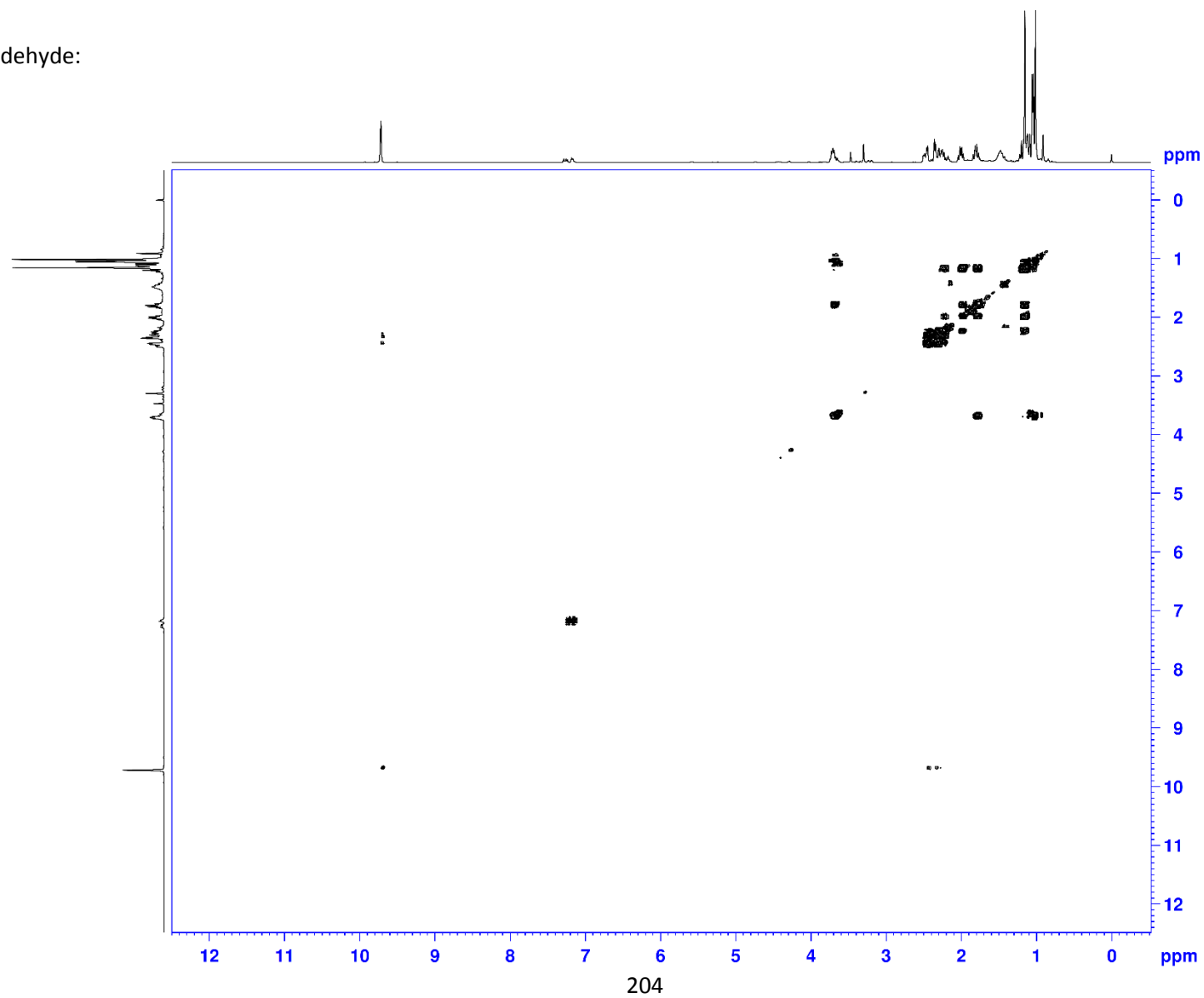
Dimethyl Acetal:



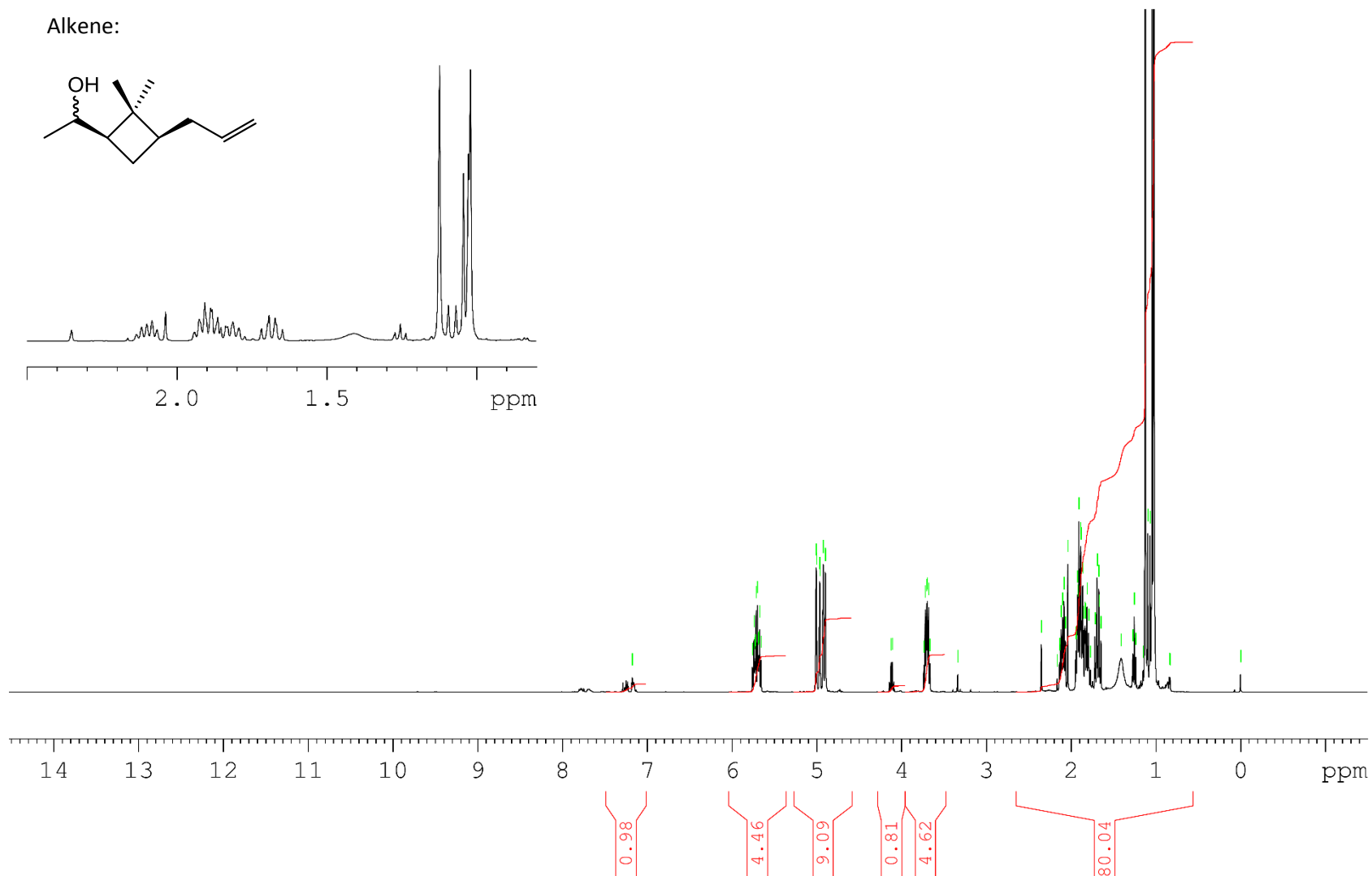
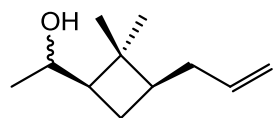
Aldehyde:



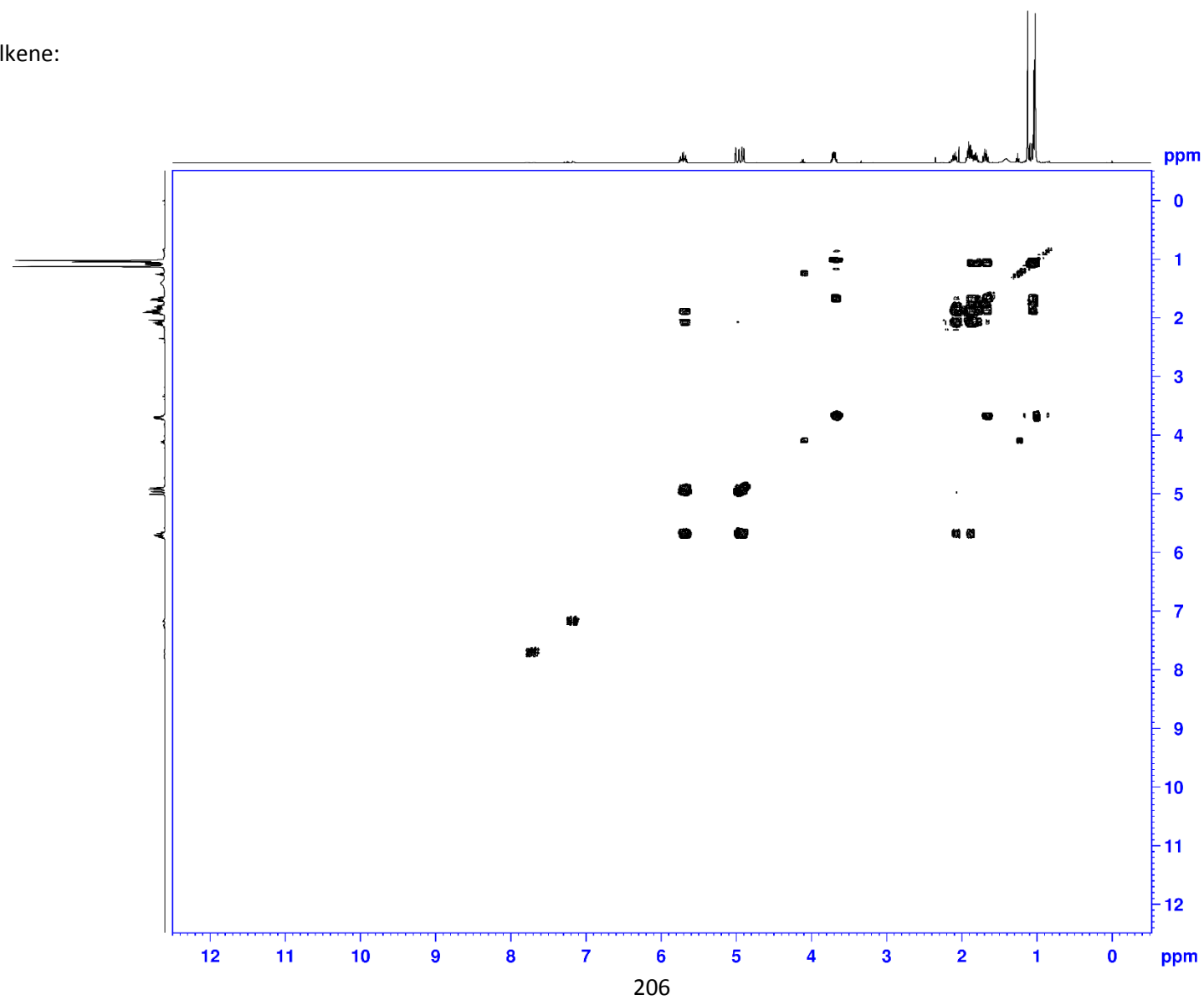
Aldehyde:



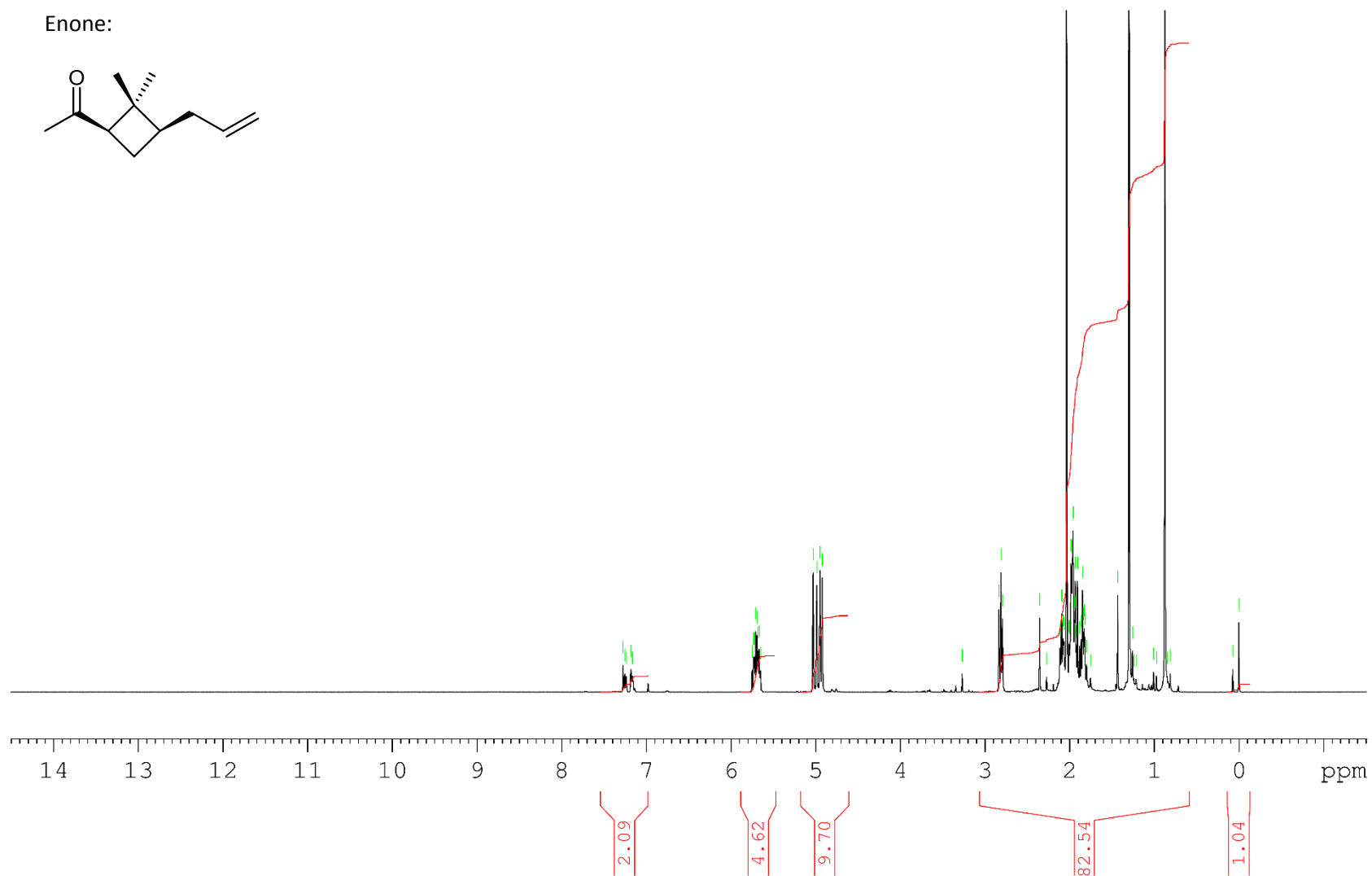
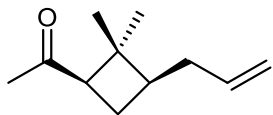
Alkene:



Alkene:



Enone:



Enone:

